

The University of Adelaide  
School of Chemical Engineering  
Cooperative Research Centre for Clean  
Power from Lignite

Physical Modelling of Mixing Between  
Rectangular Jets Present in Tangentially  
Fired Brown Coal Boilers

Ph.D. Thesis

Alessio Angelo Scarsella

# Chapter 1

## 1. Introduction

### 1.1. Background and Motivation

This project aims to investigate the mixing phenomenon that occurs with adjacent rectangular nozzles utilised in many tangentially fired boilers. One example is in the Latrobe valley where banks of rectangular jets are used to burn the brown coal that is readily available in the area. The brown coal used in the boilers cannot combust until oxygen in the air is brought into contact with the fuel, hence all combustion processes take place in the following stages:

#### ***MIXING – IGNITION - CHEMICAL REACTION - DISPERSAL OF PRODUCTS***

The rate of combustion is dependant on the slowest of the above stages. In most industrial combustion systems the mixing is slow whilst the other stages are fast. The rate and the completeness is therefore controlled by the rate and completeness of air/fuel mixing. Insufficient fuel/air mixing produces un-burnt CO in the flue gases, wasting fuel energy potential. For good combustion it is necessary to ensure that adequate air is supplied for complete mixing and that the burner is designed to mix the fuel and air streams effectively and efficiently. The rate and completeness of combustion is controlled by the rate of completeness of fuel air mixing. Hence, a saying of combustion engineers:

#### ***IF IT'S MIXED IT'S BURNT***

As well as controlling the fuel burn rate the mixing process also controls the heat transfer from the flame. Knowledge of the mixing process will allow for prediction of the heat release rates and flame length (Mullinger *et al.*, 2002) and consequently allow for the formulation of complete boiler modelling, so that they can be either modified or re-designed to accommodate new fuels such as dewatered lignite (Clayton *et al.*, 2003), reducing fuel requirements, CO<sub>2</sub> emission and fouling rates.

The burner nozzles used in the Loy Yang and the Yallourn Power Stations are rectangular. The mixing of adjacent rectangular jets is poorly understood. The purpose of this project is to experimentally study mixing in adjacent rectangular jets.

These measurements will allow prediction of jet fluid concentration in the axial and radial directions of each burner, allowing for combustion modelling in coal fired boiler systems and characterisation of flame shape and heat release characteristics. Modelling is important for the effective implementation of coal de-watering technology, currently being developed by the Cooperative Research Centre for Clean Power from Lignite.

The purpose of the current project is to deliver a mixing model which predicts the oxygen content in the jets. This model can then be used as a basis of input for a combustion model for the use in tangentially fired brown coal boilers which needs the oxygen concentration to calculate the reaction rate. The nozzles used in the boilers are categorised as bluff jets, one central 'primary jet with AR (aspect ratio) =1.2 and two adjacently placed secondary jets with AR=2.2 precisely spaced apart. The nature of the flow means that both the primary and secondary streams which are representative of the fuel and air streams must be studied and their mixing characteristics quantified separately. The best way to do this is to investigate the concentration of both primary and secondary jets. It is also important to quantify the concentration distribution of entrained fluid or re-circulated flue gas, as this gas will dilute oxygen concentration, thus altering the combustion characteristics of the flame.

## **1.2. Utilisation of De-watered Lignite in Existing Technologies**

A primary objective of the Co-operative Research Centre for Clean Power for Lignite is to improve the efficiency of existing boilers. Boilers in the Latrobe valley use Victorian brown coal, which has a very high water content. Table 1.1 illustrates typical moisture contents in several Latrobe valley coals.

Under combustion conditions the water content significantly reduces the effective calorific value of the fuel, due to the high latent heat of vaporisation of water. This implies that fuel requirements for a given process will be greater than that for a de-watered lignite. Figure 1.1 displays the approximately linear relationship between the calorific value of different lignites versus the moisture content. The current high fuel requirements also mean each brown coal

boiler is releasing high quantities of greenhouse gases. The issues related with global warming, clean power production and climate change have been given an enormous amount of attention by the Federal and State Governments as-well as the main stream media. Consequently, a shift in doctrinal thinking on the power generation process and policymaking is imminent in the near future. In order to continue to deliver a reliable supply of electricity using Victorian lignite, new techniques in coal drying and combustion and boiler design are required.

Several techniques exist for the reduction of water content in coal, such as steam drying, solar drying, electro de-watering and mechanical press de-watering (Durie, 1991). Mechanical Thermal Expression (MTE), which is a non-evaporative mechanical press de-watering technique, has been identified as the most effective process for commercial development (Jackson, 2003). A continuous MTE system has been designed and successfully commissioned on a laboratory scale and is capable of reducing moisture from 65-75% to 37-39% (Banks and Burton, 1985; 1989, Guo *et al.*, 1999). The implementation of a de-watered coal in existing boilers is untried and unproven, thus considerable research and development is required to make this process viable.

Dewatered coal is effectively a new fuel representing a similar, or greater, change in calorific value than experienced when converting from bituminous coal to oil or from oil to natural gas. A change in fuel will alter heat release rates and, with it, the heat flux profiles to boiler walls. Insufficient heat flux may result in a process that does not reach the specified requirements. Conversely, extremely high heat fluxes may cause significant damage to heat transfer surfaces. Figure 1.2 illustrates calculated heat flux profiles for different fuels for a particular process. Note that every system is different and that most industrial equipment can only tolerate a limited range of heat flux profiles. Water tube boilers used for electricity generation are no exception and determining heat flux profiles will be critical in the successful implementation of de-watered coal in existing boilers. Smith *et al.*, (2001) made an initial assessment on the effects of pre-dried coal on brown coal fired boilers using Hottel's 0-D model (Hottel, 1961), (using the baseline conditions of the Yallourn W stage 1 furnace). Figures 1.3 and 1.4 show the trends in temperature and heat flow for the whole boiler as a function of coal moisture content. In Figure 1.3 the adiabatic flame temperature rises from 1032 to 1557°C as the coal moisture content is reduced from 66% to 0%. Figure 1.4 shows how a reduction in moisture content reduces the amount of sensible heat, leaving (presumably through convection) and causing an increase in radiative heat transfer.

Although the use of the  $0$ -D model is useful for conducting preliminary studies, a  $3$ -D model is required in order to conduct a more detailed assessment on the effect of de-watered coal on boiler performance. A 1:30 scale Perspex model of the Yallourn W stage 1 boiler was built and operated under isothermal conditions with water using the acid alkali technique. This technique provided information on the influence of stoichiometry and velocity on flame shapes and permits the mapping of the region in which the fuel and air streams interact, which corresponds to the flame reaction zone (Rhine and Tucker, 1991). The knowledge of the position of the reaction zone of the furnace is a fundamental input into the  $3$ -D combustion model. The other fundamental input is the current work, which aims to develop a  $3$ -D mixing model so as it can be used in the  $3$ -D combustion model. The  $3$ -D mixing model will help determine ignition distances and location of flame fronts relative to surfaces. The success of the  $3$ -D combustion model will also enable design of the changes in flow-rates and possible burner geometry, so that pre-dried coal can be used in existing furnaces.

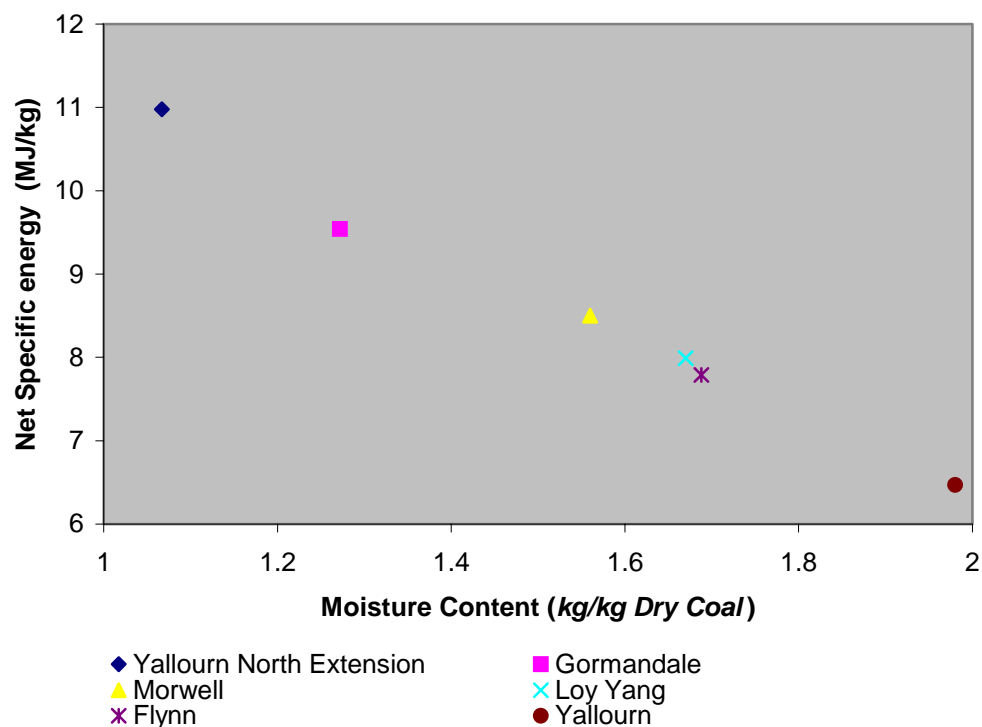


**Figure 1.1:** Variation of net specific energy with bed moisture content for Latrobe Valley brown coals (Durie, 1991).

NOTE: This figure is included on page 5 of the print copy of the thesis held in the University of Adelaide Library.

**Figure 1.2:** Effect of different fuels on heat flux patterns in a combustion system (Jenkin and Moles, 1981).

NOTE: This figure is included on page 5 of the print copy of the thesis held in the University of Adelaide Library.

**Figure 1.3:** Effect of using pre-dried coal, on mean boiler operation. Illustrated are the 0-D model outputs of the adiabatic flame temperature and flue gas temperature versus coal moisture content (Smith *et al.*, 2001).

NOTE: This figure is included on page 6 of the print copy of the thesis held in the University of Adelaide Library.

**Figure 1.4:** Effect of using pre-dried coal, on mean boiler operation. Illustrated are the 0-D model outputs of the radiative and sensible heat transfers versus coal moisture content (Smith *et al.*, 2001).

Field	% moisture (% w/w)	kg water / kg dry coal
Yallourn	66.6	1.99
Morwell	60.9	1.56
Loy Yang	62.6	1.67
Yallourn North Extension	51.7	1.07

**Table 1.1:** Moisture Content of Brown Coal Fields in Victoria (Durie, 1991).

### 1.3. Tangentially Fired Boilers

The boilers used in power stations in the Latrobe Valley are tangentially fired pulverised coal boilers. These boilers are the heart of the power generating process. Figure 1.5 is a schematic diagram of the power generating facility at Loy Yang Power which requires 6000 tonnes of mined pulverised coal per day to power four, 500 MW boilers which provide superheated steam in order to turn four turbo generators, as shown in Figure 1.5.

The Loy-Yang boilers are balanced-draft tower units with superimposed vortex circulation (Perry and Pleasance, 1983a, Hart, 2001). A tangentially fired boiler is quite complex and consists of a total of eight “groupings” of rectangular slots, two on each corner of the boiler

(Figure 1.6), with typically six operating at a time. The burners in some of the boilers form a 60-degree angle to the furnace wall. These angled burners produce a central vortex or fireball (Figure 1.6).

The raw wet coal is fed into the system with hot furnace gas typically at 1100 °C introduced with the coal. The hot gases/coal are then fed to the milling section where the coal is ground into fine particles increasing specific surface area and enhancing evaporation of moisture (Figure 1.7a). The de-watered coal/air/furnace gas/water vapour mixture leaves the mill at 120 C and is then split, with most of the coal being fed to the main burner section whilst the remaining mixture is fed to the vapour burners (Figure 1.7b). It is the geometry of the main burners, rather than the vapour burners, that are of interest in this study.

After a period of operation the heat transfer surfaces in boilers may become coated with various deposits arising from dust and condensable vapours, carried with combustion gases passing over the heat exchanging surfaces. This coating represents additional resistance to heat flow and thus results in decreased performance, this phenomena is more commonly referred to as ‘fouling’. Several fouling mechanisms were found to be responsible for the reduction of boiling efficiency in the Yallourn W boilers, which have a very similar configuration to the Loy Yang boilers. For instance, in the stage 1 boiler, ash particles tend to deposit a sticky sulphatic layer on boiler tubes and furnace walls (Perry and McIntosh, 1985), whereas in the stage 2 boilers, incompletely oxidised ash particles tend to stick to the furnace walls inducing corrosion. The formation of ash and fouling products is a direct consequence of the inorganic constituents of the coal and combustion conditions, such as flow-rate, fuel and oxidant mixing, velocity profiles of fuel, oxidants, temperature and concentration of limiting reactants, especially oxygen.



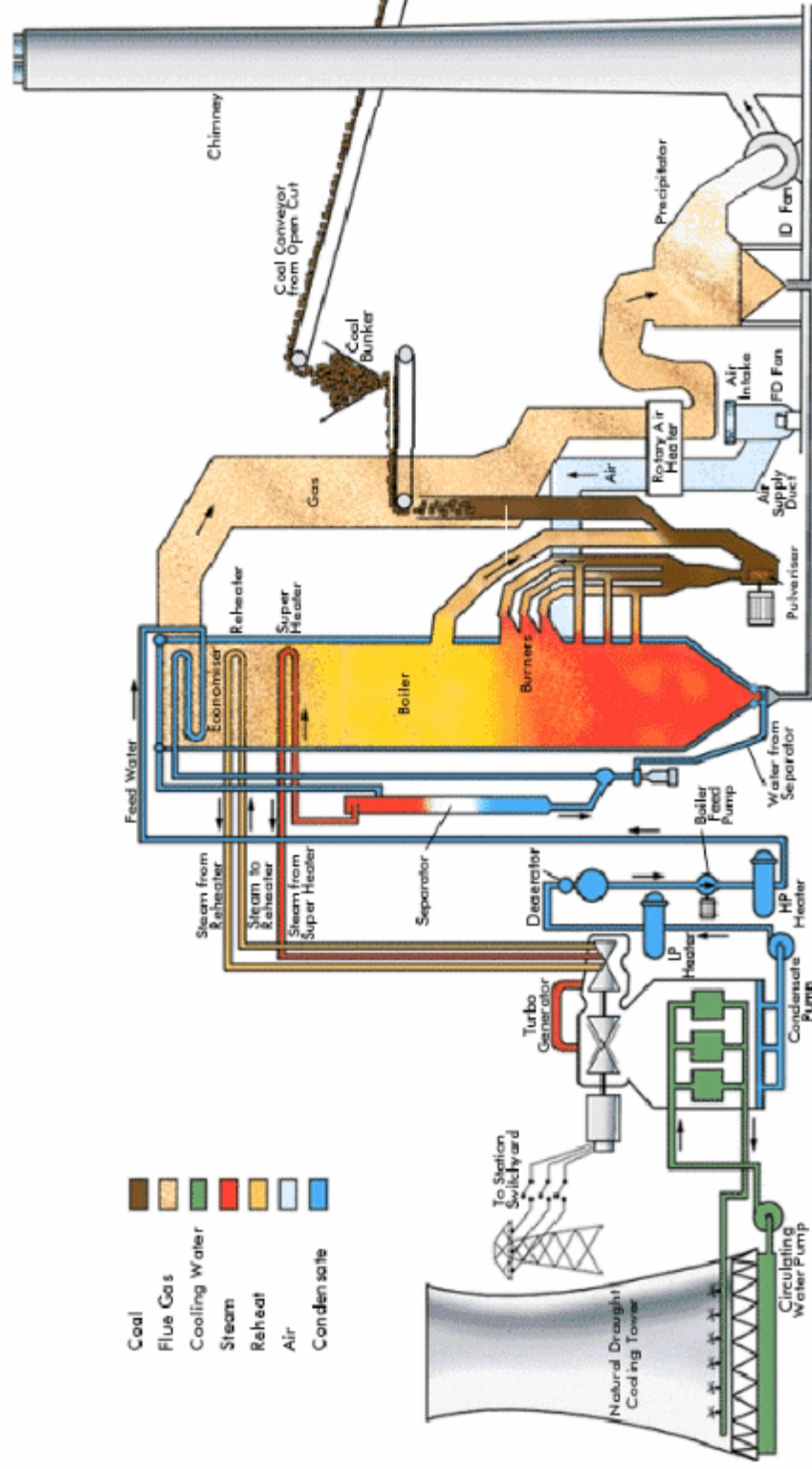


Figure 1.5: Power generation cycle from brown coal for The Loy Yang Power Station.

NOTE: This figure is included on page 9 of the print copy of the thesis held in the University of Adelaide Library.

**Figure 1.6:** Schematic diagram of a typical tangentially fired boiler with cross sectional view of the main central vortex, source: (Hart, 2001).

NOTE: This figure is included on page 9 of the print copy of the thesis held in the University of Adelaide Library.

**Figure 1.7:** Schematic diagram of typical coal drying and milling system used in Victorian coal fired power stations a) together with a fireside view of the burners b) (Mullinger *et al.*, 2002).

#### 1.4. Rectangular Slot Burners

During the 1980's, the Victorian State Electricity Commission performed extensive studies of the aerodynamics of slot burner systems with slight variations in the geometries (Perry and Pleasance, 1983b). Three basic geometries were identified by boiler manufacturers (Perry and Pleasance, 1983b) as being the most commonly constructed. Figures 1.8a), b) and c) illustrate these geometries. The primary jet (P) stream is designated for the conveying of coal, the conveying fluid being re-cycled flue gas with small quantities of leakage air and evaporated water from the coal and the secondary jet (S) supplying the majority of the air.

The burner banks at Loy Yang and Yallourn consist of 3 groups of primary and secondary rectangular jets. Each group is comprised of a central primary and two secondary jets; this can be seen in Figure 1.9.

Refractory cooling air is injected 'crosswise' through the exit plane of the primary flow (Figure 1.10a) and can be seen in the photograph of the main burners in Figure 1.10b). It has been found that the flow from the refractory jets slightly suppresses a vortex shedding between jets but may be omitted for the purpose of modelling due to the minimal effect it has on the flow field (Perry and Hausler, 1982).

Most other industrial burner systems are co-annular circular jets (Figure 1.11). As a result the structural (Duraio and Whitelaw, 1973, Ribeiro and Whitelaw, 1976), entrainment (Wall *et al.*, 1980) and scalar properties (Forstall and Shapiro 1950, Alpinieri 1964, Grandmaison *et al.*, 1996) have been the focus of much research. The interaction of multiple rectangular jets, however has been the subject of little investigation and is consequently poorly understood. The current project aims to address this lack of knowledge. Quantification of mixing between primary and secondary streams, as well as furnace gases, is fundamental to development of a full boiler heat transfer model (Jenkins and Moles, 1981).

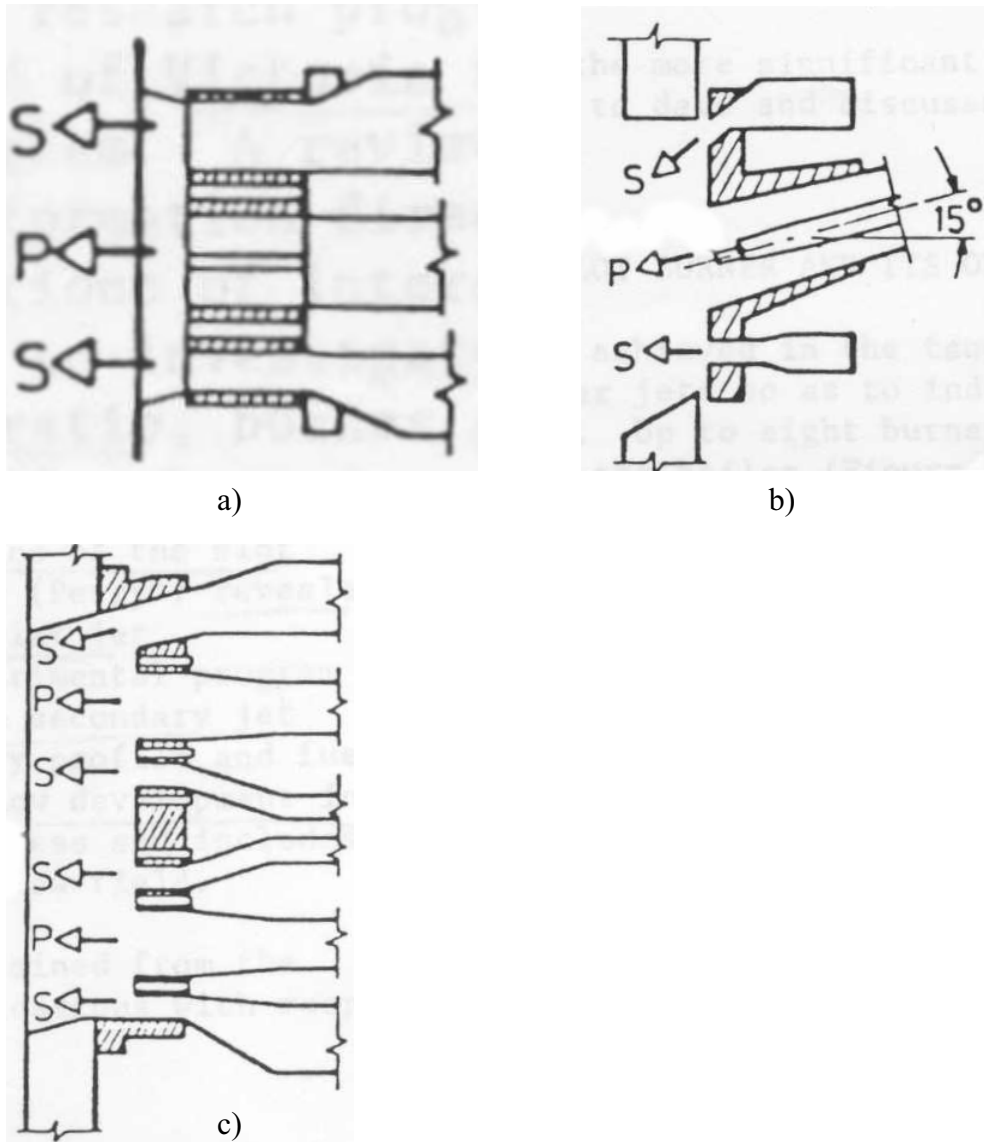


**Figure 1.8:** Basic used burner geometries. P – primary Jet, S – secondary jet a) Type I burner, b) Type II burner and c) Type III burner.

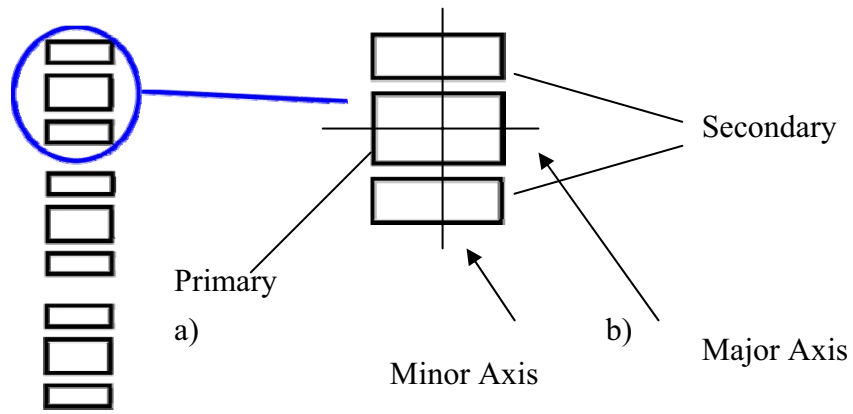


**Figure 1.9:** Schematic diagram of the front view of a Loy Yang burner bank a) and a magnified view of a single burner illustrating primary and secondary jets b).

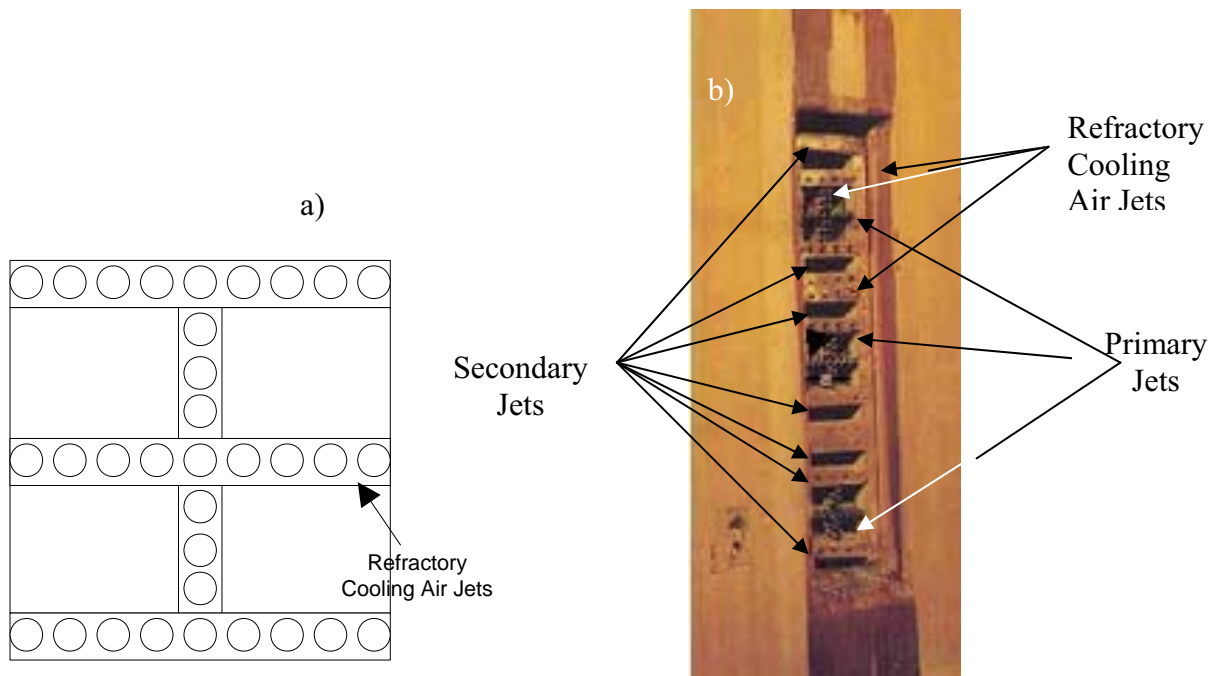


**Figure 1.10:** Orientation of refractory cooling Air Jets a) and photograph refractory jet position with respect to the main burners b).

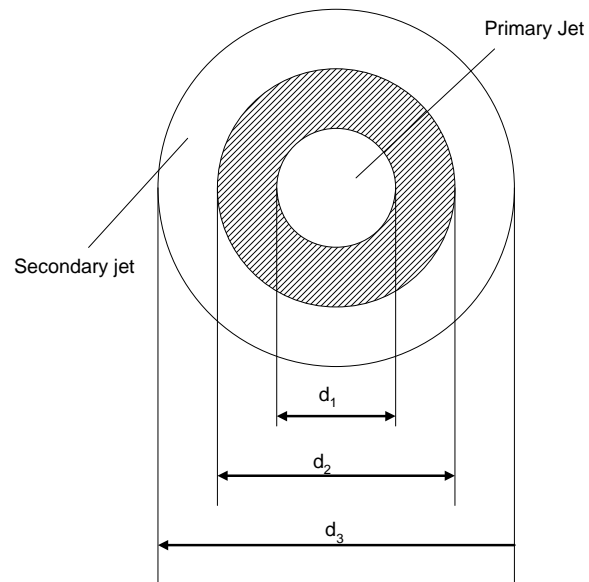


**Figure 1.11:** Schematic diagram of a circular co-axial jet configuration typically used in many other combustion systems, illustrating primary and secondary streams.

# Chapter 2

## 2 Literature Review

Turbulent flow is characterised by fluctuations of all flow properties, such as velocity, pressure and, in non-isothermal cases, temperature (Holland, 1995). Motion is caused by vortices, commonly known as “eddies” which do not necessarily have circular motion (Holland, 1995). The magnitude of the eddies depends on the characteristic dimension of the system (e.g. pipe diameter for pipe flow or wall length for flat-plate flow).

### 2.1 Scales of Turbulence

Eddies in turbulent jet flow may grow in length scale but they can also generate smaller scale structures that dissipate. This results in a release in energy which is adsorbed by smaller eddies, where the rate at which the smaller eddies receive energy is equal to the rate they dissipate energy due to viscous heating.

Hence, according to Kolomogrov, (1942) the characteristic length of the smallest eddies will depend on;

The rate of dissipation of energy from larger to smaller eddies

$$\varepsilon = -\frac{dk}{dt} \tag{Equation 2.1}$$

where  $\varepsilon$  is the rate of dissipation and  $k$  the turbulent kinetic energy. However, the dissipation rate is commonly expressed as;

$$\varepsilon \approx \frac{1.5(u'_{rms})^3}{l_o} \tag{Equation 2.2}$$

where  $l_o$  is the value of the integral scale and  $u'_{rms}$  is the root mean square of the velocity fluctuation.

Four main turbulent velocity length scales, are frequently cited in the literature (Turns, 1996);

- Characteristic width of flow or macro scale;
- Integral length or turbulence macro scale;
- Talyor micro scale; and
- Kolmogrov micro scale.

**The Characteristic width or Macro scale ( $L$ )** represents the largest eddies in the turbulent system and scales with the characteristic length for that particular system (ie; pipe diameter in pipe flow or jet width in jet flow for a given axial position).

**Integral scale or Turbulence Macro scale ( $l_o$ )** represents the mean size of the large eddies in turbulent flow; i.e. in eddies with low frequency and large wave lengths (Turns, 1996). The Integral scale is obtained by integrating the correlation coefficient for the fluctuating velocities between two points, implying that it may also be defined as a statistical measurement of the large scale structures in the flow.

$$l_o = \int_0^{\infty} R(x) dr \quad \text{Equation 2.3}$$

where

$$R(x) = \frac{\overline{u'_{r=0} u'_r}}{u'_{rms,r=0} u'_{rms,r}} \quad \text{Equation 2.4}$$

where  $u'$  is the velocity fluctuation,  $u'_{rms,r=0}$  is the root mean square of the velocity fluctuation at an initial point  $r=0$  and  $u'_{rms,r}$  is the root mean square of the velocity fluctuation at a measured point  $r$ .

**Taylor Micro scale ( $\lambda_T$ )** This is an intermediate length scale between the integral scale and the Kolomogrov scale and is related to the mean rate of strain.



$$\lambda_T = \frac{u'_{rms}}{\left(\left(\frac{\partial u}{\partial x}\right)^2\right)^{0.5}} \quad \text{Equation 2.5}$$

**Kolomogrov Micro Scale** This is the smallest length associated with turbulent flow at which turbulent kinetic energy dissipates into the flowing fluid in the form of viscous heating.

$$\lambda_K = \left(\frac{\nu^3}{\varepsilon}\right)^{1/4} \quad \text{Equation 2.6}$$

where  $\nu$  is the kinematic viscosity.

Batchelor introduced an equivalent expression for scalar (concentration) length scales which is known as the **Batchelor Scale**;

$$\lambda_B = \lambda_K Sc^{-0.5} \quad \text{Equation 2.7}$$

where  $Sc$  is the turbulent Schmidt number which is the ratio between the kinematic viscosity ( $\nu$ ) and molecular diffusivity ( $D_f$ ). The low diffusivity in water implies that the Batchelor scale could be anything up to 50 times smaller than the Kolomogrov scale. Using gases as the working fluids results in  $Sc \approx 1$ , implying that Kolomogrov and Batchelor scales are of similar length.

Several other semi-empirical models for turbulent scale estimations exist without determination of the rate of dissipation for different flow systems.

## 2.2 Equations of Motion

The equations of motion are a coupling of macroscopic mass and momentum balance, which describe all flows in differential form and are more commonly known as the equations of continuity and the Navier-Stokes Equations. These equations represent any flow condition for any specified geometry.

Analytical solutions of these equations is possible for one dimensional steady and unsteady laminar flow in any geometry. However, the resolution of three dimensional steady or unsteady laminar flow requires approximation using numerical techniques (ie, finite differences, finite volume and finite element) and is easily solved with 4 dependant variables; (3 directional velocities and 1 pressure term) and 4 equations.

Similar equations have also been developed for multi-component systems and are applicable for a moving fluid being issued into another moving or stagnant fluid (Bird, 1960). The equation of continuity of a component A diffusing into another component B is;

$$\frac{\partial C}{\partial t} = -\left(\frac{\partial(C * u)}{\partial x} + \frac{\partial(C * v)}{\partial y} + w \frac{\partial(C * w)}{\partial z}\right) + D_f \left(\frac{\partial^2 C}{\partial x^2} + \frac{\partial^2 C}{\partial y^2} + \frac{\partial^2 C}{\partial z^2}\right) \quad \text{Equation 2.8}$$

where  $C$  is the concentration of fluid at any particular point of component A and  $D_f$  the molecular diffusivity of substance A into substance B. Equation 2.8 may be solved in conjunction with the continuity and Navier-Stokes equations and give accurate results for steady and unsteady laminar conditions using similar numerical techniques.

### 2.3 Velocity and Concentration under Turbulent Conditions

A graph of the instantaneous axial velocity plotted against time for flow in a pipe under turbulent conditions is shown in Figure 2.1. The diagram shows rapid fluctuations of the axial velocity. The mean velocity is obtained by averaging the instantaneous value over a sufficient period of time. If the average value is constant of a given time period the flow conditions may be defined as steady turbulent flow (Holland 1995).

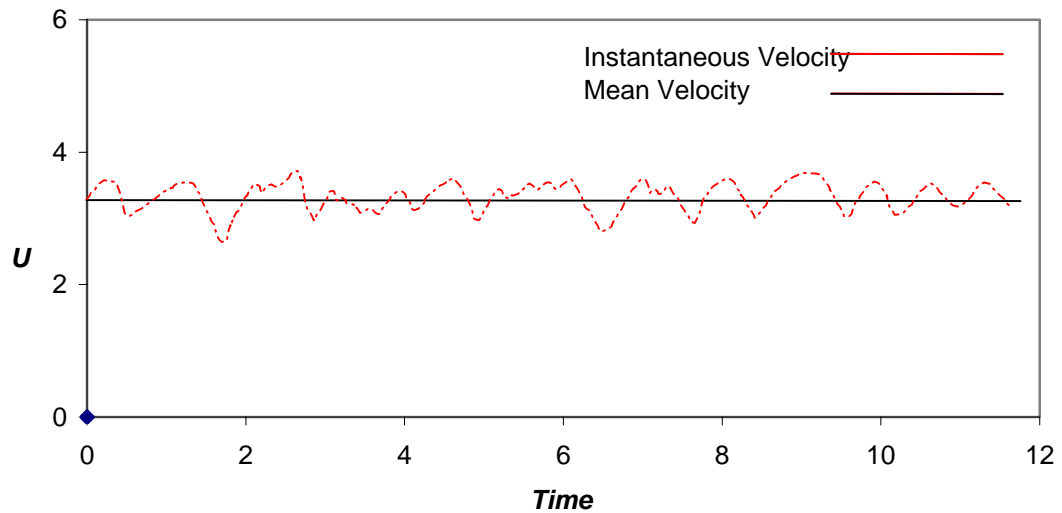


**Figure 2.1:** Eulerian description of the variation of the single point velocity component  $u$  in turbulent flow.

It can be deduced that the instantaneous velocity at a given point is the sum of the mean velocity and fluctuating component as shown in equation 2.9.

$$u = \bar{u} + u' \quad \text{Equation 2.9}$$

Similarly pressure and concentration profiles manifest the same turbulent fluctuations;

$$P = \bar{P} + P' \quad \text{Equation 2.10}$$

$$C = \bar{C} + C' \quad \text{Equation 2.11}$$

Any mean variable over a given time span is defined as:

$$\bar{U} = \frac{1}{N} \sum_1^N U_i \quad \text{Equation 2.12}$$

where  $N$  is the number of measurements.

Substitution of Equations 2.9 to 2.11 into the continuity, Navier Stokes equations and Equation 2.8 and use of the rules of Reynolds averaging (Bird, 1960) yields a series of relationships which describe turbulent incompressible flow.

Resolution of these equations cannot be done using conventional numerical techniques, as there are nine variables and only five equations. This problem of closure is encountered in all turbulent computational fluid dynamic modelling and requires several semi-empirical models in-order to solve these equations. These models often enough are capable of solving non-complex systems (ie, constant density and non-reacting). Several models have been developed and have become increasingly useful throughout the years with the development of processing technology, which range from the early Boussinesq and Prandtl mixing length theories to the more recent one and two equation models and the Reynolds stress model. These are only a few of the several closure models in circulation for computation of turbulent flows.

## 2.4 Turbulent Jets

Several interpretations of the definition of jets exist; for example

*“When a fluid emerges from a nozzle it interacts with fluid from the surroundings to form a jet”* (Beer, 1972).

or

*“A free jet upon leaving an outlet, will entrain the surrounding fluid, expand and decelerate”* (Perry, 1997).

Jets are classified as fully separated flows, and, after separation from a nozzle, the solid surface no longer plays a direct role in flow development. A free jet is defined as a fluid issuing from a nozzle into a stagnant fluid, which has no confining walls or the influence of a confining wall is negligible. From numerical studies and experimental data, it can be shown that free jets have the following characteristics in the far field (Rhine, 1991):

- The dimensionless concentration (or mixture fraction) of a nozzle fluid is independent of the nozzle diameter and is expressed in terms of nozzle diameters down-stream ( $x/D$ ).

- The ratio of the concentration of a jet fluid at any point on that axis at the same distance  $x$  from the nozzle is the same when given as a function of  $r/x$  (where  $r$  is the radial coordinate).

In the case that the free jet criteria is not met and the supply of secondary fluid is restricted, it will be rapidly depleted through entrainment and subsequently an external re-circulating zone will establish itself as a dominant flow feature (Figure 2.2). This phenomenon is utilised in confined jets and the re-circulating flows is used to assist flame stability. Several parameters have been formulated to define these jets such as the Craya-Curtet similarity criterion (Rhine, 1991).

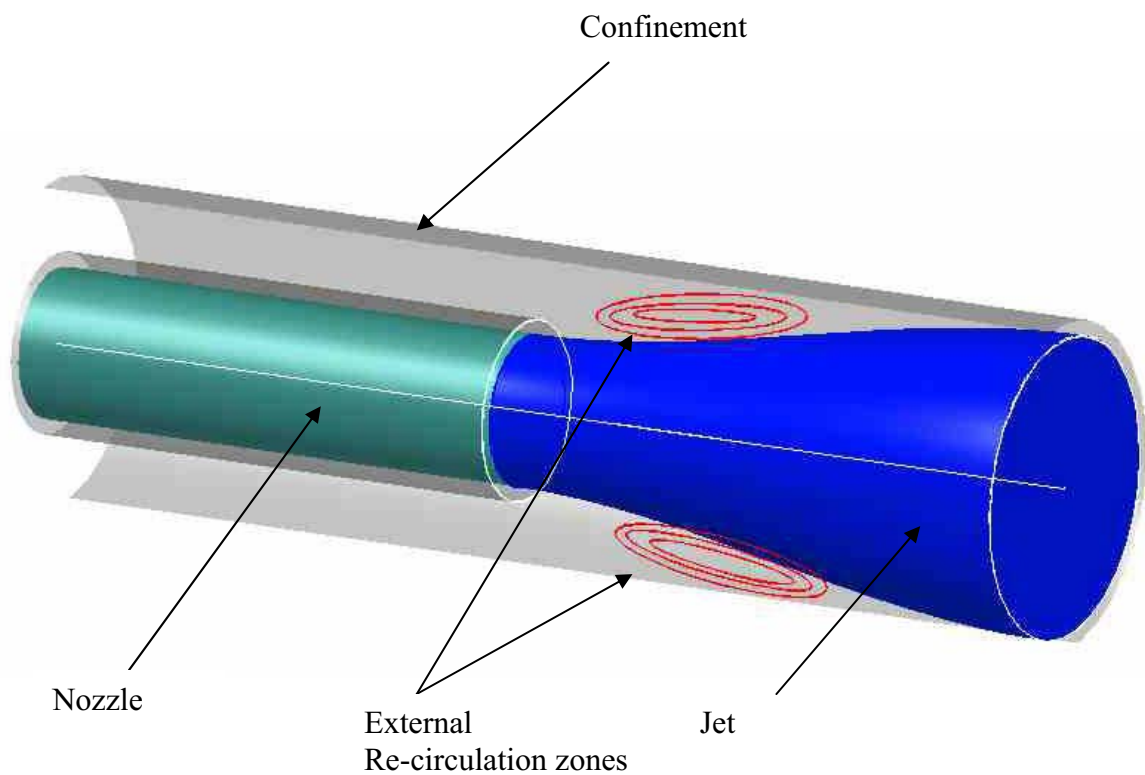


**Figure 2.2:** Diagram of a confined jet with external recirculation zone highlighted

### 2.4.1 Circular Jets

By far the largest body of research of reference to burner aerodynamics has been done on circular jets. Four regions exist in singular, round turbulent free jets and are illustrated in Figure 2.3.

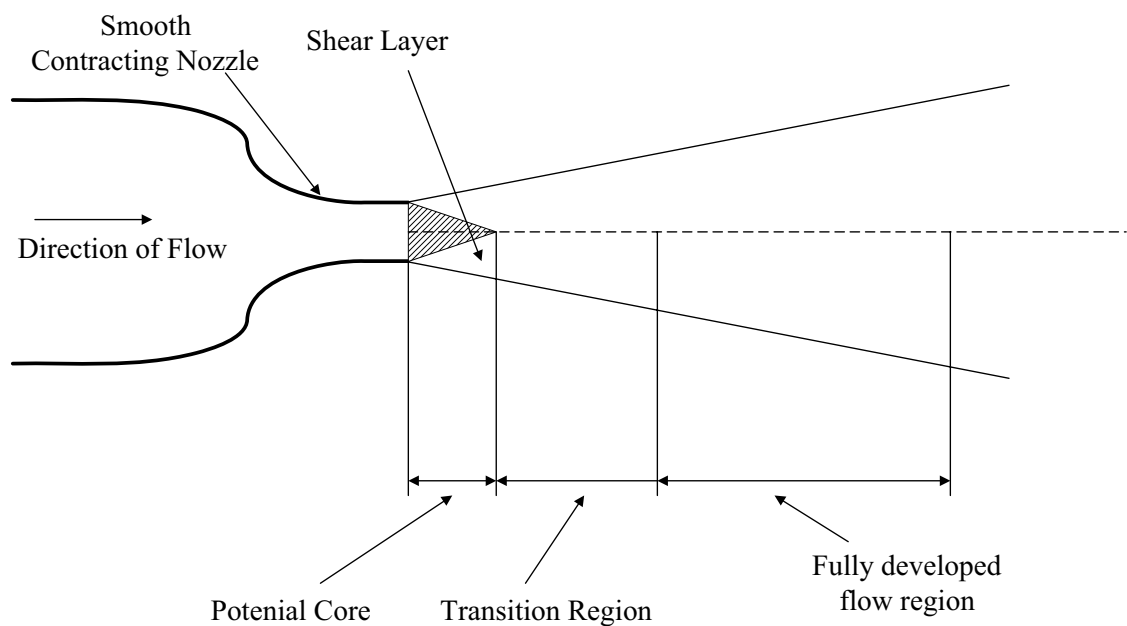


**Figure 2.3:** Schematic diagram of the developing regions of a round turbulent jet issuing from a smooth contraction.

- **Potential Core:** Region of uniform velocity and concentration and low turbulent intensity where potential flow theory applies. The potential core is found only in jets issuing from smooth-contractions or with top-hat velocity profiles at the nozzle exit plane (Mi *et al.*, 2001a; 2001b).
- **Mixing or Shear Layer:** A region in which mass and momentum are transferred from ambient fluid perpendicularly to the direction of the flow into the jet and is situated on the edge of the potential core.
- **Transition Region:** This region is between the end of the potential core and the start of the fully developed flow region. It is a region where mass is being continuously transferred from the external fluid into the jet, with a variable velocity profile in the radial direction.

- **Fully Developed Flow Region:** This region exhibits a normalised centreline velocity proportional to distance whilst still growing in size and entraining surrounding fluid. The fully developed flow region also exhibits a constant dimensionless normalised concentration versus dimensionless radial distance for any downstream distance  $x/D$ .

A great deal of disagreement exists within the literature concerning the occurrence and length of each specific region. Rhine, (1991) specifies that the length of the potential core is approximately 4-5 nozzle diameters and the transition region is approximately 10 nozzle diameters. Contrarily, Wygnanski and Fielder, (1969) stated that the round jet achieves a fully developed flow only after  $x/D = 20$  while Mi *et al.*, (2001b; 2001b) found that occurrence and duration of the potential core, transition and fully developed flow regions are all functions of the initial flow conditions.

Near field studies of the round turbulent jet by Boguslawski and Popiel, (1979) described the first 4 nozzle diameters of flow as a wedge shaped mixing sub-region from which short interfacial waves increase the thickness of the mixing layer, after which a tenuous train of large scale vortices appear at constant frequencies. Boguslawski and Popiel, (1979) believed that a fully developed flow is achieved only after 8 nozzle diameters.

The Centreline velocity decay of an isothermal round jet is found to be inversely proportional to axial distance from the nozzle and encapsulates part of the transition and all of the fully developed flow regions. It is also commonly referred to as the self-similar flow region. The self-similar flow region is defined by the region in which either the centreline velocity or concentration steadily decreases at a constant rate with axial distance ( $x/D$ ). Equation 2.13 is an example of descriptive velocity decay.

$$\frac{\overline{u_0}}{\overline{u_x}} = C_1 \left( \frac{x-a}{D} \right) \quad \text{Equation 2.13}$$

where  $\overline{u_0}$  is the mean velocity at the exit plane of the nozzle,  $\overline{u_c}$  is the jet centreline velocity,  $D$  is the nozzle diameter,  $C_1$  is a constant of proportionality and  $a$  the virtual origin .

Expressions have also been developed for radial velocity and concentration profiles, which are approximated to a Gaussian error curve distribution.

$$\frac{\bar{u}}{u_x} = \exp\left(-C_2\left(\frac{r}{x}\right)^2\right) \quad \text{Equation 2.14}$$

where  $C_2$  is a constant and  $r$  is the radial co-ordinate in the radial direction.

Albertson, (1950) assumed that for the purpose of modelling, all round jets have two axial flow regions and that the transition between these two is immediate, rather than gradual, and denoted these near and far regions as the zone of flow establishment and the zone of established flow. His analysis yielded the two distinct relationships for the prediction of the mean velocity in these regions. Albertson, (1950) also determined relationships for entrainment of ambient fluid into the jet for the zone of flow establishment and established flow regions.

For the zone of flow establishment:

$$\frac{Q}{Q_0} = 1 + 2(\sqrt{2\pi} - 2)C_3 \frac{x}{D} + 4(3 - \sqrt{2\pi})C_3^2 \left(\frac{x}{D}\right)^2 \quad \text{Equation 2.15}$$

and for the zone of established flow:

$$\frac{Q}{Q_0} = 4C_3 \frac{x}{D} \quad \text{Equation 2.16}$$

where  $Q$  is the volumetric flow-rate of a jet at a given axial distance and  $Q_0$  is the volumetric flow of the jet at the nozzle exit, and  $C_3$  is an experimentally determined constant.

Ricou and Spalding, (1961) experimentally measured the rate of entrainment using a porous wall technique and obtained the following expression for the volumetric flow ratio of a round turbulent free jet issuing from a smooth radially contracting nozzle:

$$\frac{Q}{Q_0} = 0.32 \frac{x}{D} + 1 \quad \text{Equation 2.17}$$



The value of 0.32 was later more commonly known as the entrainment coefficient. Hill, (1972) developed an expression for the entrainment coefficient using dimensional analysis and validated it using Ricou's direct entrainment measurement technique;

$$C_E = \frac{d\dot{m}}{dx} \frac{1}{\sqrt{M\rho_s}} \quad \text{Equation 2.18}$$

where  $M$  is the initial momentum flux of the jet and  $\rho_s$  is the ambient fluid density. The entrainment coefficient was measured for a series of Reynolds numbers and at different downstream stations ( $x/D$ 's). Wall *et al.*, (1980) similarly to Albertson (1950) analytically derived an expression for the entrainment of the ambient fluid for the near field of round turbulent jet, as follows.

$$\frac{Q}{Q_0} = A\left(\frac{x}{D}\right) + B\left(\frac{x}{D}\right)^2 \quad \text{Equation 2.19}$$

where the coefficients  $A$  and  $B$  are defined as;

$$A = 2 \left( \frac{\int_0^\infty f(\eta) d\eta}{\int_0^\infty f^2(\eta) d\eta} - 1 \right) \quad \text{Equation 2.20}$$

$$B = 2 \left( 1 + 2 \frac{\int_0^\infty \eta f(\eta) d\eta}{\int_0^\infty f^2(\eta) d\eta} - 2 \frac{\int_0^\infty f(\eta) d\eta}{\int_0^\infty f^2(\eta) d\eta} \right) \quad \text{Equation 2.21}$$

and the term  $f(\eta)$  is the velocity profile and  $\eta$  the dimensionless radial distance ( $y/x$ ), with  $y$  being the radial coordinate. The values of  $A$  and  $B$  were numerically determined by Wall *et al.*, (1980) using different empirical expressions of radial velocity profile and also evaluated experimentally by using the porous wall technique (Ricou and Spalding, 1961) which yielded  $A = 0.128$  and  $B = 0.004$ .

Wynanski and Fielder, (1969) measured the rate of entrainment in the near nozzle region using hot wire anemometry and obtained a constant entrainment coefficient over the first 12 nozzle diameters;

$$\frac{Q}{Q_0} = 0.183 \frac{x}{D} + 1 \quad \text{Equation 2.22}$$

These findings distinctly contradict those of Hill, (1972) who found that the entrainment coefficient varies exponentially rather than linearly over the initial region of the flow field.

The importance of concentration (as a jet parameter) is fundamental to the current project. It is important to understand the work to date on simple circular turbulent jets. The concentration of a jet is known as a “scalar” meaning that, unlike velocity, which is defined by magnitude and direction, concentration is only identified by magnitude. Pressure and temperature are also scalars present in turbulent jets. The latter has shown to have similar physical properties as concentration itself in heated, non reacting flows (Van Der Hegge, 1958, Mi and Nathan, 2003). The concentration of a non-reacting jet is conserved, whereas for a reacting system this is not the case.

Several models have been developed to describe the centreline mean concentration (or scalar) in the self-similar region for the round turbulent free jet. However, the most widely used relationship for describing the centreline concentration decay of the round jet is the inverse power law;

$$\frac{1}{\bar{\xi}_c} = \frac{1}{K_1} \left( \frac{x - x_{0,1}}{D_\varepsilon} \right) \quad \text{Equation 2.23}$$

where  $\bar{\xi}_c$  is the centreline mixture fraction of jet fluid,  $K_1$  is an experimentally determined decay constant,  $x$  is the axial coordinate,  $x_{0,1}$  is the virtual origin of the jet and  $D_\varepsilon$  is the equivalent jet momentum diameter, defined as;

$$D_\varepsilon = \frac{2m_0}{(\pi\rho_\infty J_o)^{0.5}} \quad \text{Equation 2.24}$$

where  $m_o$  is the mass flow rate of jet fluid at the nozzle,  $J_o$  is the momentum flux, and  $\rho_\infty$  is the density of surrounding fluid. For a round jet from a smooth contraction issuing into a fluid of equivalent density, then  $D_\varepsilon = 0.99D$ , for a pipe jet  $D_\varepsilon = 0.97D$ .

The spreading of the jet is widely quantified by determining the concentration half-width,  $b$ ; this term is defined as being the radial distance at which the concentration is half that on the centreline. In similar fashion to the centreline mixture fraction decay, the concentration half-width of a jet in the self-similar region is expressed as;

$$\frac{r_{1/2}}{D_e} = K_2 \left( \frac{x - x_{o,2}}{D_e} \right) \quad \text{Equation 2.25}$$

where  $K_2$  is a constant determined by experiment and  $x_{o,2}$  is the jet spread virtual origin.

The analysis of Becker *et al.*, (1967) is the first to perform extensive scalar studies on the concentration of a round jet issuing from a smooth contraction. His analysis found that the experimental coefficients  $K_1$  and  $K_2$  have values of 5.59 and 0.106 respectively and both virtual origins had values of 2.4. Birch *et al.*, (1978) found  $K_1$  to be 4.44 and  $K_2$  0.097. Lubbers *et al.*, (2001) performed direct numerical simulation of a turbulent round jet using a working fluid with a unity Schmidt number and found the experimental constant  $K_1$  to be 5.5. Xu and Antonia, (2002) used temperature as the measured scalar and found  $K_1$  to be 4.6.

A wide range of experimental studies on the concentration of round jets issuing into both stagnant and moving surroundings have been conducted, with different fluids and different experimental techniques that have different spatial and temporal resolutions. Table 2.1 is a summary of experimental studies on the scalar quantities of the round, turbulent jet from a range of authors, including boundary conditions Schmidt numbers and experimental techniques. Most of the Authors cited in Tables 2.1-2.4 report different values of centreline and half-width scalar constants with different conditions such as Schmidt number, co-flow and density ratio. However, none of these took into account the effects of the upstream conditions. The studies of Mi *et al.*, (2001a; 2001b) and Xu and Antonia, (2002) are the only ones to observe the effects of velocity exit profile on the scalar mixing field on round turbulent jets.

Author	Technique	$\rho_{\infty}/\rho_0$	$U_{\infty}/U_0$	Sc	$Re_d$	$K_1$	$x_{0.1}/D_e$	$K_2$	$x_{0.2}/D_e$
Richards and Pitts (1993)	Rayleigh Scattering	1.552	0	$\sim 1$	25,000	4.76	1.6	0.113	3.6
Dowling and Dimotakis (1990)	Rayleigh Scattering	1.05	0.4%	1.2	16,000	4.73		0.114	
Grandmaison <i>et al.</i> , (1982)	Mie Scattering	1.0	0	0.7	27,000	5.43	1.67	0.105	1.67
Becker <i>et al.</i> , (1967)	Mie Scattering	1.1	0	0.7	54,000	5.59	2.4	0.106	2.4
Mi <i>et al.</i> , (2001a)	Hot wire	1	0	$\sim 1$	16,000	4.64	4.25	0.11	1.0
Chua and Antomia (1986)	Cold Wire	0.85	0	0.7	17,700	4.63	-2.3	0.106	-1.4
Corrsin and Kislter (1955)	Cold Wire	0.65		0.7	55,000	5.26	2.16	0.143	3
		0.95	0	0.7	55,000	3.66	2.6	0.086	0
<b>Average</b>						<b>4.21</b>	<b>2.1</b>	<b>0.095</b>	<b>1.8</b>

**Table 2.1:** A comparison of the scalar mixing statistics measured by previous experimentalists from simple axisymmetric smooth contraction jets with low Schmidt number.

Author	Technique	$\rho_{\infty}/\rho_0$	$U_{\infty}/U_0$	Sc	$Re_d$	$K_1$	$x_{0.1}/D_e$	$K_2$	$x_{0.2}/D_e$
Kristmanson and Danckwerts (1964)	Acid Alkali	1	$\sim 0$	500	10,000	4.75	0	0.112	0
Papanicolaou and List, E.J.(1987)	Thermometry	0.98-1.0	$\sim 0$	$\sim 1000$	16,700	5.49		0.096	
Papanicolaou and List, E.J.(1988)	LIF	0.98-1.0	$\sim 0$	$\sim 1000$	11,000	6.34	4.35	0.115	2.51
<b>Average</b>						<b>5.52</b>	<b>2.2</b>	<b>0.112</b>	<b>1.3</b>

**Table 2.2:** A comparison of the scalar mixing statistics measured by previous experimentalists from simple axisymmetric smooth contraction jets with high Schmidt number.

Author	Technique	$\rho_d/\rho_o$	$U_d/U_o$	Sc	$Re_d$	$K_1$	$x_{o,1}/D_e$	$K_2$	$x_{o,2}/D_e$
Birch <i>et al.</i> , (1978)	Raman Scattering	0.56	0	0.7	16,000	4.44	5.8	0.097	0
Richards and Pitts (1993)	Rayleigh Scattering	1.552	0	~1	25,000	4.81	2.1	0.104	4.2
Pitts <i>et al.</i> , (1991)	Rayleigh Scattering	1.02	4.3%	~1	3,960	4.42	-0.35		-0.35
Pitts and Takashi, K.(1984)	Rayleigh Scattering	0.55	3.3%	~1	4,130	4.5	-1	0.104	0
Mi <i>et al.</i> , (2001a)	Hot wire	1	0	~1	16,000	4.62	4.91	0.102	-1.3
<b>Average</b>						<b>4.56</b>	<b>1.79</b>	<b>0.097</b>	<b>0.87</b>

**Table 2.3:** A comparison of the scalar mixing statistics measured by previous experimentalists from simple axisymmetric pipe jets with low Schmidt number.

Author	Technique	$\rho_d/\rho_o$	$U_d/U_o$	Sc	$Re_d$	$K_1$	$x_{o,1}/D_e$	$K_2$	$x_{o,2}/D_e$
Nakamura <i>et al.</i> , (1982)	Dye Absorption	1	0	~1000	5,000			0.114	4.37
Dahm and Dimotakis (1990)	LIF	1	0	~1000	5,000	5.41	0		
Law and Wang (2000)	LIF	1	0	~1000	12,700	5.26	0	0.108	0
<b>Average</b>						<b>5.33</b>	<b>0</b>	<b>0.11</b>	<b>2.18</b>

**Table 2.4:** A comparison of the scalar mixing statistics measured by previous experimentalists from simple axisymmetric pipe jets with high Schmidt number.

### 2.4.2 Concentric (co-annular) jets

Concentric jets are more common in industrial practice than parallel rectangular jets and, although the velocity properties of concentric jets have been widely studied, their scalar characteristics however have only been studied by a few authors. The flow structure of the dual concentric jet system has some similarities to the round free turbulent jet but is severely affected by the thickness of the wall separating the centre (primary) and outer (secondary) jets as well as the velocity ratio. Durao and Whitelaw (1973) stated that the distance at which self-similarity is attained is a function of nozzle geometry and velocity ratio; the distance required to achieve self-similarity increases with decreasing wall thickness. For large wall thicknesses rapid flow development is observed. According to Riberio and Whitelaw (1976) the flow is characterised by the fact that a re-circulation vortex is established in the vicinity of the wake of the wall; this vortex is enhanced for  $\lambda > 1$  (secondary to primary jet velocity ratio) where the momentum of the inner jet is less than that of the annulus, causing the jet to reach a self-similar state further upstream. Also the turbulent intensity around the vortex region increases as the vortex overlaps with the shear layer due to the shortening of the potential core.

Very few relationships exist in literature that quantitatively describe the entrainment field of concentric jet systems. Wall *et al.*, (1980) analytically derived and experimentally validated an expression for entrainment into the concentric annular jet system. The rate of entrainment into the primary (central) and secondary (annulus) jets of ambient fluid is defined as;

$$\frac{Q_{1+2}}{Q_{0,1+2}} = \frac{\frac{Q_2}{Q_{2,0}} - 1}{1 + \frac{1}{\lambda A_r}} + 1 \quad \text{Equation 2.26}$$

where  $Q_{1+2}$ , is the total flow of primary, secondary and entrained fluid,  $\lambda$ , is the secondary to primary velocity ratio,  $A_r$  is the secondary to primary area ratio,  $Q_{0,1+2}$  is the primary and secondary flows at the nozzle exit plane and  $\frac{Q_2}{Q_{2,0}}$  is the secondary flow plus entrained fluid to secondary flow ratio and is defined as;

$$\frac{Q_2}{Q_{2,0}} = A \left( \frac{d_{1r}^2 + A_r}{A_r} \right)^{0.5} \left( \frac{x}{d_2} \right) + B \left( \frac{d_{1r}^2 + A_r}{A_r} \right) \left( \frac{x}{d_2} \right)^2 \quad \text{Equation 2.27}$$

where  $d_2$  is the outer diameter of the annulus, and  $d_{1r}$  is the ratio of the inner and outer diameter of the primary tube,  $d_{1r} = \frac{d_{01}}{d_{i1}}$ , where  $d_{01}$  is the outer diameter of the central jet and  $d_{i1}$  is the inner diameter of the outer jet. Experimentally the values of  $A$  and  $B$  were determined to be 0.128 and 0.004 for concentric jets issuing from long pipes.

Grandmaison *et al.*, (1996) investigated centreline concentration and half-width of a round concentric system by varying the secondary to primary velocity ratios from 5.3 to 1.92 and 1.09 and observed no significant change in  $K_I$  and  $x_{o,l}/D_e$ . Contrarily the work of Forstall and Shapiro, (1950) also sought to quantify the effect of velocity ratio on the scalar mixing field and performed scalar measurements of the primary jet at velocity ratios of 0.5 and 0.25, yielding values of  $K_I = 13.35$  and 8.1, and  $x_{o,l}/D_e = 8.99$  and 3.45. Alpinieri (1964) and Forstall and Shapiro, (1950) stated that together with turbulent intensity at the exit plane and boundary conditions it may be concluded that velocity ratios are very important variables which dictate the concentration profiles and half width. Momentum ratio is also a fundamental variable as shown in the comparison of the axial data of Alpinieri, (1964) with the data of Chigier and Beer, (1964) in Beer and Chigier, (1972). The operating conditions of Chigier and Beer, (1964) were identical to that of Alpinieri, (1964) but air was substituted with the carbon dioxide/hydrogen system, thus altering the momentum ratios and found that with an increase in momentum ratio caused the rate of decay (scalar) of the jet to increase in the far field region,  $5 < x/D < 12$ .

### 2.4.3 Rectangular jets

Little research has been done on singular rectangular or multiple rectangular jet flows. Rajaratnam (1976) classified rectangular jets into three different categories based on aspect ratio (AR) which is the ratio between the width and height of the jet:

- 1) Plane Jets  $AR \rightarrow \infty$
- 2) Three dimensional or slender Jets  $\infty \gg AR \geq 5$
- 3) Bluff jets  $AR < 5$

The rectangular jets of interest in brown coal fired boilers will fall under the Bluff Jet category. The long side of the rectangular jet is known as the major or spanwise axis and assigned the 'y' coordinate; the short side is commonly known as the minor or transverse axis and assigned the 'z' coordinate. An equivalent diameter is used when quantifying relationships for the rectangular jets and is defined as;

$$D = \sqrt{\frac{4A}{\pi}}$$

Equation 2.28

where  $A$  is the jet cross sectional area.

As with circular jets several regions of interest have been established. Trentacoste and Sforza (1967) represented the dynamic profile of a singular rectangular jet in three distinct regions based on velocity (Figure 2.4): However, more recent investigations by Deo, (2005) and Mi *et al.*, (2005) showed that the potential core is only present when a top-hat velocity profile is encountered at the nozzle exit plane, very similar to that found from jets issuing from a smooth contraction. This finding coincides with that of Mi *et al.*, (2001a; 2001b) for round jets.

- **Potential Core:** Very similar to the potential core found in the round jet, the mixing initiated around the jet boundary has not yet permeated the entire flow, with the region having a nearly uniform velocity profile. As for the round jet the potential core is a characteristic from rectangular jets issuing from smooth contractions or with top-hat velocity profiles (Deo, 2005).
- **Characteristic Decay:** The velocity decay in this region depends on the aspect ratio of the jet. According to Trentacoste and Sforza (1967), the velocity profiles on the plane of the minor axis are regarded to be 'similar' and those on the plane of the major axis are 'non-similar'. Marsters (1980) states that the mixing over this region is relatively independent from the three dimensional geometry of the jet.
- **Axisymmetric Decay:** Velocity decay is axisymmetric in nature, where the flow approaches axisymmetry. The start of the axisymmetric region varies linearly with the width and length of the rectangular nozzle. Quinn (1994) described this region of the flow as having great similarity to that of a round free turbulent jet.



Rajaratnam (1976) demonstrated that the axisymmetric decay region for plane jets does not occur transitionally, but immediately and bluff jets do not experience a characteristic decay region but a very brief transition from the potential core to the axisymmetric decay region.

Krothpalli *et al.*, (1981) also enforces the three regions of flow concept, stating however that their transition points for each region depend on the aspect ratio as well as the magnitude of turbulent intensity at the exit plane. Sfeir (1976) and Sforza *et al.*, (1979) used temperature as a conserved scalar and compared it to velocity measurements and found that, although dimensionless centreline temperature decay behaves similarly to velocity in the potential core, this characteristic decay region and axisymmetric region occur slightly upstream, which lead Sfier to believe that mass was diffused at a slightly faster rate than momentum and concluded that the transition from the scalar characteristic decay region to the axisymmetric decay region occurs at a downstream distance of;

$$\frac{x}{W} \approx \frac{(K_1')^2}{K_1''} \frac{4AR}{\pi} \quad \text{Equation 2.29}$$

where  $W$  is the nozzle width,  $K_1'$  and  $K_1''$  are the slopes of the inverse mixture fraction on the centreline for the axisymmetric decay region and the characteristic decay region respectively and AR is the aspect ratio of the rectangular nozzle.

Hart *et al.*, (2004) who performed large eddy simulations on rectangular jets found that entrainment is heavily controlled by the geometry, especially in the near field. Large-scale turbulent structures responsible for the entrainment of fluid into the shear layer are called ‘rings’. They induce a low pressure region causing stagnant fluid to be drawn towards the jet. Secondary structures are present in each corner called ‘braids’ and are a resultant of the deformation of the ring, causing jet fluid to be expelled through the sides of the major axis. The expulsion of jet fluid by the secondary structures and entrainment by the rings causes the jet’s aspect ratio to change (Sau, 1999, Quinn 1994). When the major axis has become shorter than the minor one ‘axis switching’ has occurred. According to Abramovich, (1982 and 1983) large counter rotating vortices are responsible for an oscillating pressure field. The magnitude of the local time-averaged pressure depends on the distance between the shear layers and these vortices. The shear layer (major axis plane) in proximity to these vortices forms a lower pressure region and a

high pressure region for shear layers further away (minor axis plane) which means an overflow of fluid from the high to low pressure region. This difference in pressure results in a straining motion on different sides of the vortices, which results in the shortening of the major axis and lengthening of the minor.

Abramovich (1963) used first principles to determine the mean velocity and scalar properties on the centreline of a rectangular jet to determine that velocity, conserved temperature and concentration gradients are all inversely proportional to the square-root of axial distance.

$$\bar{u}_c - \bar{u} = \frac{C_u}{\sqrt{x}} \quad \text{Equation 2.30}$$

$$\bar{T}_c - \bar{T} = \frac{C_T}{\sqrt{x}} \quad \text{Equation 2.31}$$

$$\bar{C}_c - \bar{C} = \frac{C_{conc}}{\sqrt{x}} \quad \text{Equation 2.32}$$

where the subscripts  $C$ ,  $u$ ,  $T$  and  $conc.$ , represent centreline, velocity, temperature and concentration.

This theory has been used by a number of experimentalists to model both velocity and scalar trends in the characteristic decay region only (Sfier, 1979 and Grandmaison Pollard, 1991). However, the inverse square root power law has been contested by Sfier (1979) who claims that an exponent of 0.35 for the  $x$  term in Equations 2.30-32 in lieu of the square root is more appropriate. Velocity and scalar centreline decay in the axisymmetric region is accurately modelled using the inverse power law (Equation 2.23, Grandmaison and Pollard 1991).

Abramovich, (1963) initially claimed that velocity profiles in the radial direction of a rectangular jet are very similar on both axes and assume a Gaussian error curve profile. More recent publications such as Sfier, (1976) Sforza *et al.*, (1979) Grandmaison *et al.*, (1991) and Tsuchiya *et al.*, (1986) showed that this statement is only true in part, that the radial velocity (and consequently scalar) profile is Gaussian throughout the flow only for small aspect ratio jets; larger aspect ratio bluff jets experience a so called “saddle back” profile effect on the plane of

the major axis. Figure 2.5 illustrates the saddle back profiles of the dimensionless temperature versus radial position where a ‘hump’ is distinctly observed close to the jet centreline. The existence of this hump depends on the fact that the planes on the minor axes entrain at greater rates than the planes on the major axes. What is not as clear is at what aspect ratio does the saddle back effect appear? Grandmaison and Pollard (1991) state that for  $AR \geq 3$  saddle back profiles are observed, and similarly Sfier (1976) for  $AR \geq 5$ , whereas Tsuchiya *et al.*, (1986) observes this phenomena for much larger aspect ratios ( $AR = 10$ ) and also states that it is significantly enhanced by the upstream geometry prior to the jet exit plane. Sforza *et al.*, (1979) observes this characteristic for Slender rectangular jets of  $AR \geq 40$ . Consequently, there is no true agreement in the literature about the saddle back profile phenomena because there is no consistency between the upstream geometries. Marsters and Fotheringham (1980) studied a range of aspect ratios between 3 and 12 and different upstream geometries and states that the ‘saddle back’ effect is only present in the higher aspect ratio orifice type rectangular jet and rectangular jets with a non uniform velocity distribution at the exit plane and that the ‘saddle back’ peaks which merge at a down stream distance correspond to the transition from the characteristic decay region to the axisymmetric decay region. Comparison of radial velocity profiles of two free sharp edged turbulent rectangular jets with two different aspect ratios ( $AR = 2$  and  $10$ ) revealed that the ‘saddle back’ phenomena only occurs for the higher aspect ratio in the potential core region of the spanwise or major axis plane (Quinn, 1991). Studies of the minor axis plane by the same author show that the radial profiles reach a self-similar state almost immediately and, hence have a very small potential core. Comparison of the radial profiles of a transverse or minor axis planes of a jet of  $AR = 10$  to that of  $AR=2$  in Figure 2.7 reveal that the higher aspect ratio jet reaches a self similar state further upstream, indicating that jet development is favoured by a higher aspect ratio. Once the flow develops the humps observed for velocity and scalars in the radial direction (note that in Figure 2.5 only one radial face is showing) tend to merge, reverting the profiles back to a typical Gaussian form.

Few measurements of entrainment have been reported of a rectangular jet and ambient fluid. Entrainment of ambient fluid is evaluated by normalising the mass flow at a given downstream distance with the initial mass flow conditions. The ratio is plotted as a function of dimensionless downstream distance  $x/D$ . Grinstein (2001) performed large eddy simulation on jets of different aspect ratios ( $AR = 1, 2$  &  $3$ ) and concluded that the square jet ( $AR = 1$ ) entrains more in the first few diameters than the rectangular conformations but less downstream (Figure 2.6). Grinstein (2001) in his simulations assumes a top hat, plug flow velocity profile at the nozzle exit plane similar to that achieved from experimental jets issuing from smooth contractions. Trentacoste

and Sforza (1967) reported the normalised mass flux ratio rather than the mass flow ratio of a rectangular jet of aspect ratio  $AR = 10$  with a fully developed velocity profile. When compared to mass flux profiles for the round axisymmetric jet (Ricou and Spalding, 1961) it was found to entrain greater volumes of fluid in the near nozzle region. However, as the rectangular jet reaches a self-similar state, entrainment characteristics are very similar. Miller *et al.*, (1995) performed direct numerical simulation on a series of jets of different geometries. This included a square jet and a rectangular jet of a 2:1 aspect ratio with a plug-flow velocity profile. They concluded that, axis switching enhances mixing, a rectangular jet of  $AR = 2$ , will switch axis at  $x/D = 6.3$ , whereas high aspect ratios will switch closer to the nozzle exit thus increasing near field entrainment. Elrod (1954) developed computational charts for peak velocity and entrainment ratios for free three-dimensional jets of virtually any aspect ratio. The charts were developed around Reichart's similarity hypothesis (Reichart, 1941) where momentum is hypothesised to diffuse with distance from a source in the same manner that heat diffuses through a solid. Hence average velocities may be postulated in the same manner as the three dimensional heat diffusion equation for solids. Results depicted in Figure 2.6 were compared with the modern numerical results obtained by Miller *et al.*, (1995) and Grinstein, (2001) and show that there is a great error involved when using the assumption made by Elrod (1954). Use of the Reichardt's hypothesis in quantifying momentum transport by Elrod, (1954) is very simplistic and does not accommodate for different nozzle exit conditions, hence yielding erroneous estimation of the normalised mass flow in Figure 2.6.

Very little information exists in the literature dealing with concentration characteristics from rectangular jets. The most complete scalar analysis was compiled by Grandmaison and Pollard (1991) who investigated the mixing characteristics of a  $AR = 10$  rectangular jet. Sfier, (1976) Sforza *et al.*, (1979) and Tsuchiya *et al.*, (1986) all performed studies on the scalar mixing field of the rectangular turbulent free jets, using temperature as the passive scalar.

Grandmaison and Pollard (1991) developed correlations to predict the mixture fraction along the centreline of the jet for different regions of the flow. The near field region of the mean mixture fraction was described by using the model initially derived by Abramovich (1963) and described in Equation 2.32 which approximately corresponds to the 'Characteristic Decay' region of the flow.

for

$$1.4 \leq \frac{x}{D} \leq 8.4, \left( \frac{1}{\xi_c} \right)^2 = 1.24 \left( \frac{x}{D} + 1.01 \right) \quad \text{Equation 2.33}$$

Beyond this region two different versions of the inverse power law had to be used for  $8 \leq x/D \leq 25$ , and  $x/D \geq 25$

$$8 \leq \frac{x}{D} \leq 25, \left( \frac{1}{\xi_c} \right)^2 = 0.267 \left( \frac{x}{D} + 4.87 \right) \quad \text{Equation 2.34}$$

$$\frac{x}{D} \geq 25, \left( \frac{1}{\xi_c} \right)^2 = 0.382 \left( \frac{x}{D} - 3.74 \right) \quad \text{Equation 2.35}$$

Grandmaison and Pollard (1991) described the scalar jet spreading by fitting a linear curve to half-width versus axial distance. When comparing the spreads of the major and minor axes, they show very different characteristics in not only the decay constants but in the region in which the half-widths assume a linear profile. The minor axis half widths ( $z$ ) are approximated by the following relationships;

$$\frac{x}{D} \geq 2.8, \frac{r_{1/2z}}{D} = 0.13 \left( \frac{x}{D} + 0.54 \right) \quad \text{Equation 2.36}$$

whereas the major ( $y$ ) half width can be approximated linearly only at a further downstream distance;

$$\frac{x}{D} \geq 14, \frac{r_{1/2y}}{D} = 0.152 \left( \frac{x}{D} - 5.0 \right) \quad \text{Equation 2.37}$$

Upstream to this on the major plane the half width actually decreases parabolically and then increases linearly. Figure 2.7 is a summary of the scalar half widths obtained from Grandmaison and Pollard, (1991) Sforza *et al.*, (1979) and Tsuchiya *et al.*, (1986). Tsuchiya *et al.*, (1986) investigated velocity and Scalar spread for a range of rectangular jets having not only different aspect ratios (AR = 2, 3, 4 and 5) but with different upstream geometries, such as rectangular

orifices, smooth rectangular contractions and rectangular channels. Figure 2.7 distinctly shows a cross-over feature between the half widths of the major and minor planes. Sforza *et al.*, (1979) indicates that the cross-over point approximates the beginning of the axisymmetric decay region. Marsters (1980) who only observed velocity measurements, states that a sort of ‘vena contracta’ effect causes the negative spreading on the major plane (hence reduction in velocity and consequently scalar half width) by virtue of the motion of fluid toward the jet centreline on the upstream face on the jet nozzle. Consequently, the peaks in that give rise to the ‘saddle back’ effect are caused by major transport of fluid. Sfier (1979) also observed a change in cross over points of the velocity half-widths between orifice and smooth contraction rectangular jets. In the case of the orifice jet the cross over point is located closer to the nozzle exit plane, implying that the length of the axisymmetric decay region is shorter and a 15- 20 % minimum drop in initial half-width is observed with respect to a 5% drop of the rectangular jet issuing from a smooth contraction.

The average radial concentration profiles obtained by Grandmaison and Pollard (1991) and Sfier, (1976) are reported in Figures 2.8 and 2.9 at different axial stations for the major and minor directions respectively. Grandmaison and Pollard (1991) used the following generic Gaussian error curve to curve fit scalar radial distribution in both  $y$  and  $z$  directions;

$$\frac{\bar{C}_c}{C} = \exp\left(-0.693 * \left(\frac{y,z}{r_{1/2,y,z}}\right)^n\right) \quad \text{Equation 2.38}$$

where  $n$  is an empirical constant. Table 2.5 illustrates the various values of  $n$  obtained by Grandmaison for different downstream intervals on the  $y$  and  $z$  directions. The data in Table 2.2 also indicates that the Gaussian error curve is an unsuitable model to predict scalar radial profiles in the near field on the major plane ( $y$ -direction) for large aspect ratio jets, and orifice jets due to the ‘saddle back behaviour’.

Direction	Interval	$n$
$z$	$2.8 < x/D < 14$	1.93
$z$	$x/D > 19.6$	1.6
$y$	$8.4 < x/D < 14$	2.03
$y$	$19.6 < x/D < 42$	1.38

**Table 2.5:** Empirical values of  $n$ , derived from experimental data for concentration profiles for a rectangular turbulent jet (Grandmaison and Pollard, 1991).

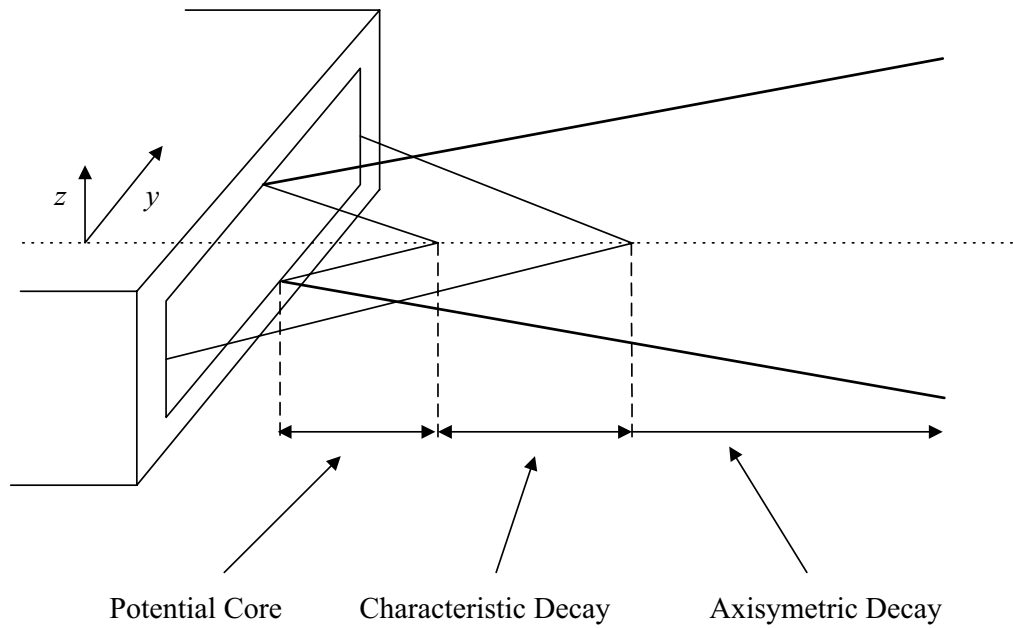


**Figure 2.4:** Developing regions of a rectangular turbulent jet (Trentacoste and Sforza, 1967). However, it has been noted by Deo, (2005) and Mi *et al.*, (2005) that the potential core only arises when a top-hat velocity profile is encountered similar to that of a smooth contraction.

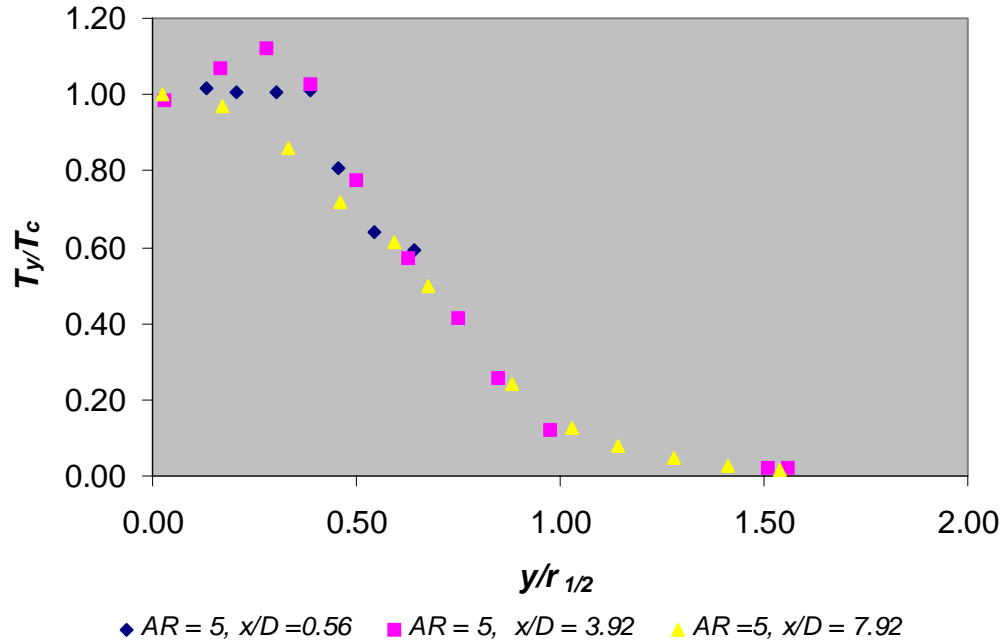


**Figure 2.5:** Dimensionless scalar profiles of a rectangular orifice jet in the radial direction with emphasis on the “saddle back” profile effect on the scalar in the near field where  $T_c$  is the centreline temperature,  $T_y$  is the temperature at a radial position,  $y$  is the coordinate on the major axis (spanwise plane) and  $r_{1/2}$  is the temperature half width (Tschuyia *et al.*, 1986).

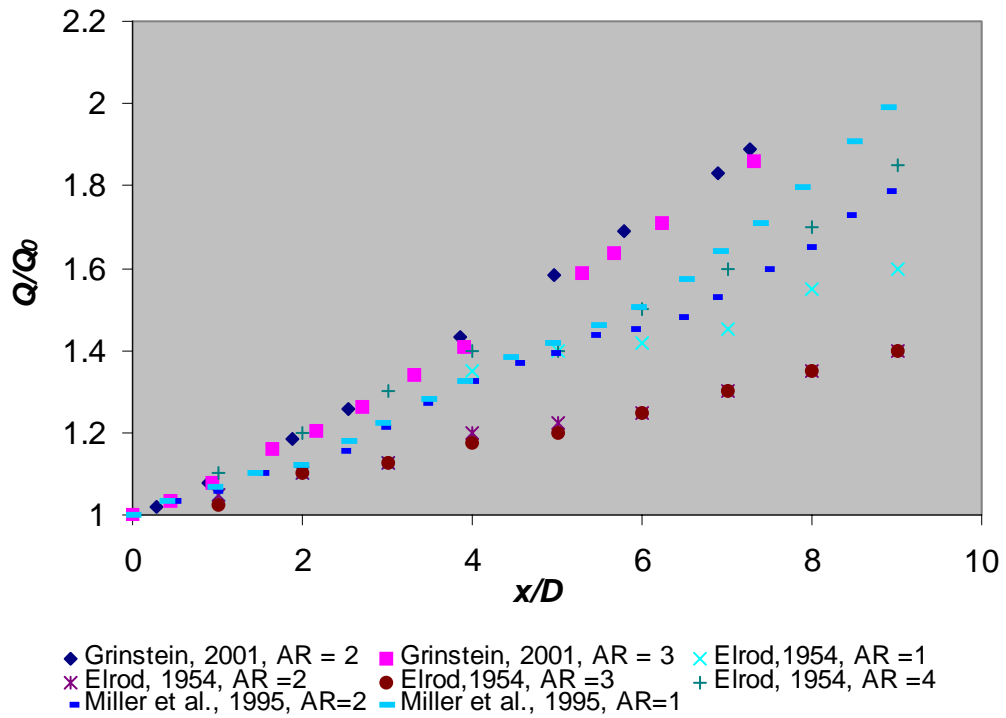


**Figure 2.6:** Predicted dimensionless entrainment ratios versus axial distance for rectangular free jets of different aspect ratios of  $AR = 1, 2, 3$  and  $4$  (Elrod, 1954, Trentacoste and Sforza 1967, Miller *et al.*, 1995, Grinstein, 2001).

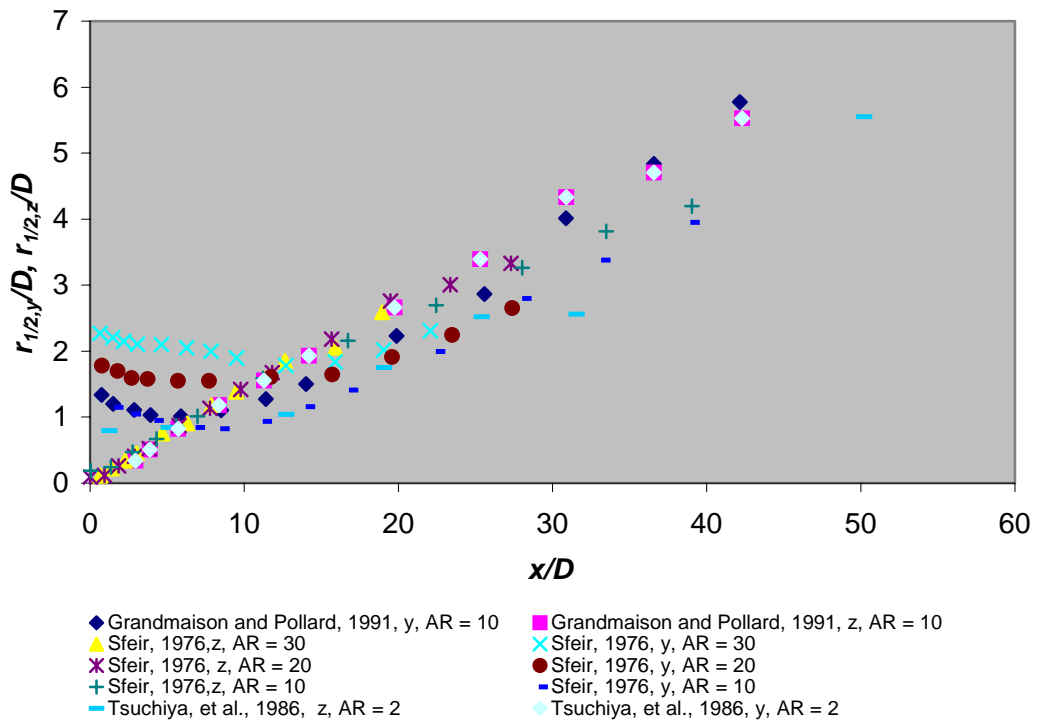


**Figure 2.7:** Experimental spanwise (major axis) and transverse (minor axis) half widths for a series of turbulent rectangular jets of aspect ratios of  $AR = 2, 10$  and  $30$  (Sfeir 1976, Grandmaison *et al.*, 1991, Sforza *et al.*, 1979 and Tsuchiya *et al.*, 1986).



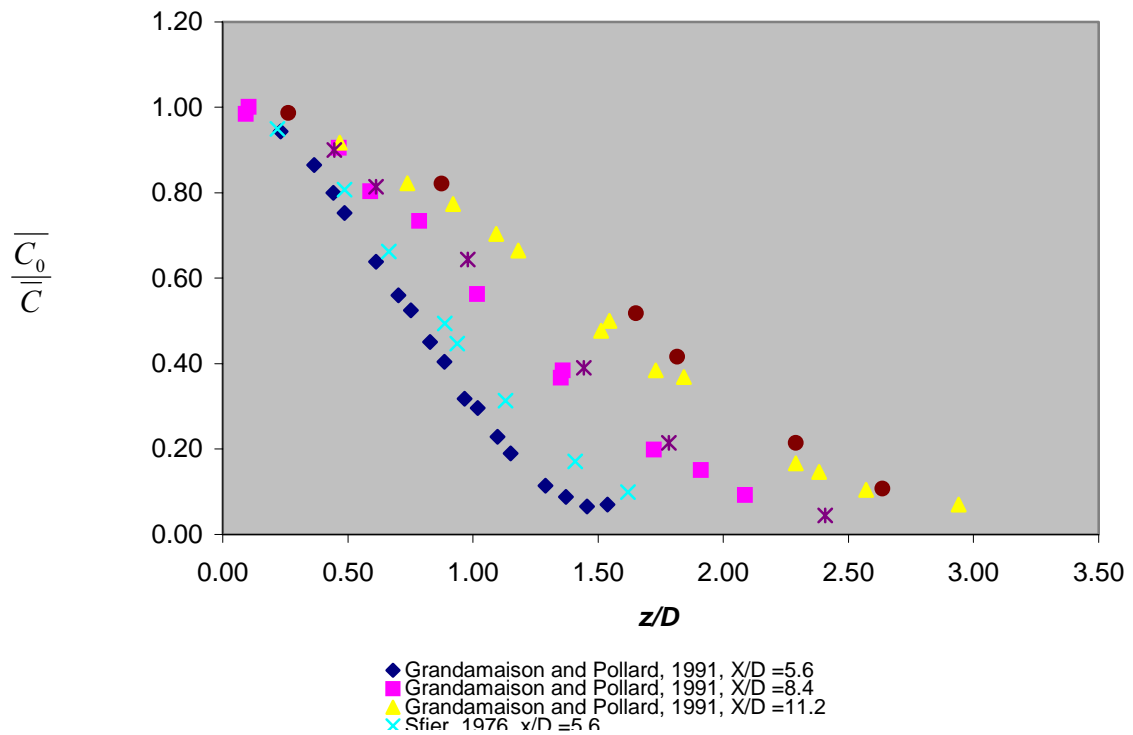


**Figure 2.8:** Comparison of Experimental dimensionless scalars versus dimensionless radial distance in the transverse (minor axis) direction at axial stations of  $x/D = 5.6, 8.4$  and  $11.2$  for a rectangular turbulent jet with  $AR = 10$  (Grandamaison and Pollard 1991, Sfier 1976).

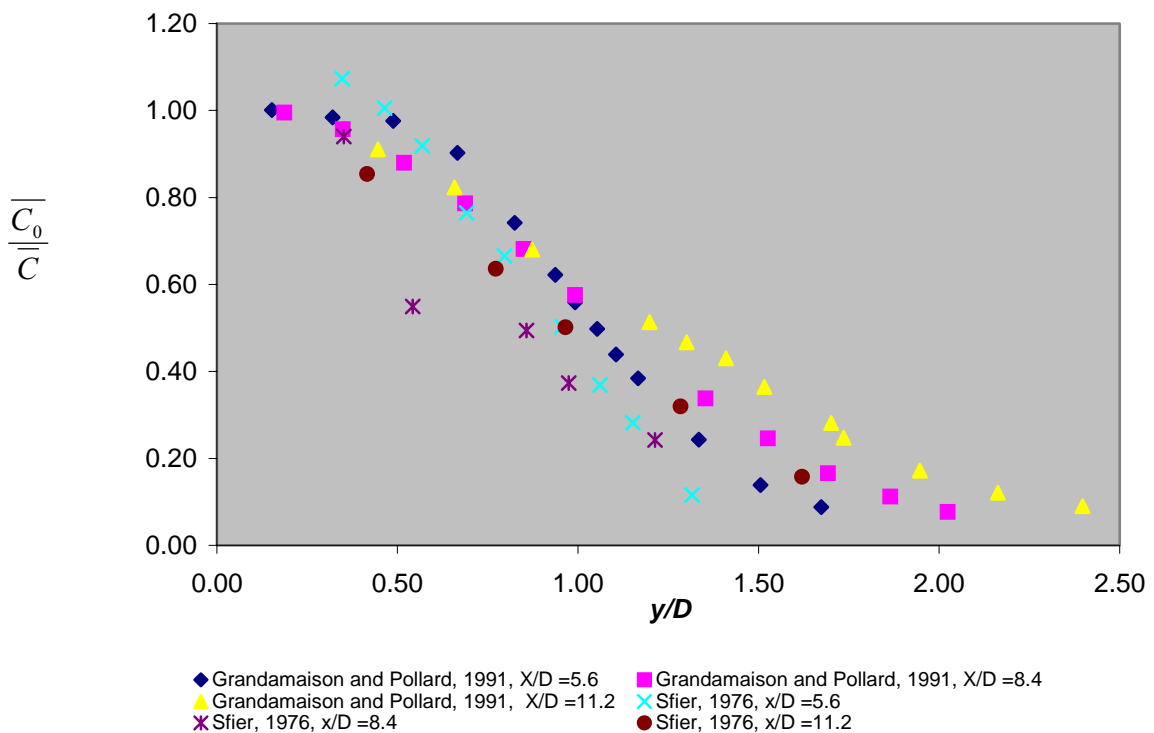


**Figure 2.9:** Comparison of Experimental dimensionless scalars versus dimensionless radial distance in the spanwise (major axis) direction at axial stations of  $x/D = 5.6, 8.4$  and  $11.2$  for a rectangular turbulent jet with  $AR = 10$  (Grandamaison and Pollard 1991, Sfier 1976).

#### 2.4.4 Multiple jets

Very little data exists on the study on the scalar mixing field from multiple Bluff jets. Most of the studies of interest have focused on velocity of multiple Slender or Plane jets.

Lin and Sheu (1991) performed velocity measurements on two parallel rectangular jets of an aspect ratio of 90 at different spaced intervals of  $S/D = 2.8, 3.2$  and  $3.73$  where  $S$  is the spacing between jets and  $D$  is the jet equivalent diameter. Lin and Sheu (1991) identified three regions in the flow field which are illustrated in Figure 2.10:

- **The Converging Region:** This region is characterised by a low pressure region between the jet exit plane and the reattachment point, creating a re-circulating flow between them.
- **Merging Region:** The flow downstream from the recirculation developed by the low-pressure region, and a strong interaction between the two jets causing the velocity profiles to merge.
- **Combined region;** this stage of the flow is self explanatory, where the velocity profiles combine to form a jet with characteristics similar to that of a single jet.

Elbanna *et al.*, (1983) investigated a dual rectangular system with two jets of both having an aspect ratio of 9 and  $s/D = 0.47$  and  $1.73$ . Results confirmed Lin's findings that mutual entrainment of the surrounding fluid creates a sub-atmospheric region between the two jets. This causes the jets to merge to form a single jet with the centreline, radial and half-width velocity measurements exhibiting very similar characteristics to a single turbulent jet.

Krothpalli *et al.*, (1980) investigated 5 rectangular jets, each having an aspect ratio of 16.7 with a spacing  $s/D = 1.73$ . They state that upstream the jets do not interact, they behave as singular free jets. The length of this region of 'independent flow' is a function of jet spacing and only in the merging region do they behave differently. Krothpalli *et al.*, (1980) also states that the three zone region for singular free rectangular jets (Sforza *et al.*, 1966) is still applicable in a multiple jet arrangement as long as each jet has not yet interacted. Miller *et al.*, (1960) Marsters, (1977) and Yuu *et al.*, (1979) stated that a low pressure region established between the jets subsequently

dictates the flow patterns and also claims that the combined region of flow behaves as a single free jet.

Mostafa *et al.*, (2000) performed  $k-\varepsilon$  simulations and experiments of the velocity of a 3 rectangular jet system consisting of a central jet of  $AR = 4$  and outer jets of  $AR = 8$ , operating velocity ratio of 6.34 and concluded that the interaction of the jets depends heavily on the jet spacing, and the nature of the re-circulation zone in the converging region is also heavily dependant on this. Mostafa *et al.*, (2000) also states that the geometrical flow conditions and degree of upstream turbulence dictate the level of mixing in the converging zone and the axial extent of the converging and merging regions. It was also found that rapid merging by the three jets is enhanced by operating at higher velocity ratios.

Tanaka, (1970) studied the flow field of dual rectangular jets with an aspect ratio of 6 and observed the effects of varying the spacing between the two jets ( $0.97 < S/D < 3$ ). Tanaka (1970) focussed on the low pressure region created between the two jets and concluded that entrainment was enhanced due to the increase in turbulent intensity from the re-circulation region between the jets. Tanaka, (1974) also examined the combined region of the two parallel jets, illustrating how it showed very similar mean velocity and half width characteristics to a single jet. Tanaka and Nakata, (1975) qualitatively investigated the same system, paying particular attention to the effects of the variation of secondary to primary velocity ratio (Equation 2.39).

$$\lambda = \frac{\overline{u_2}}{\overline{u_1}} \quad \text{Equation 2.39}$$

where  $\overline{u_2}$  and  $\overline{u_1}$  are the time averaged velocity of the secondary and primary jets. At lower velocity ratios ( $\lambda = 0.602$ ) the two outer jets are drawn towards the central jet (Figure 2.11a). At a velocity ratio of  $\lambda = 0.865$  the central jet is entrained equally into the two outer jets (Figure 2.11b). As the velocity of the outside jet is increased the central jet must overcome the re-circulation vortex or negative pressure zone and is deflected to one of the outer jets, constricting the system into a 2 jet transitional state which then combines to form a single jet (Figure 2.11c).

At higher velocity ratios the initial point of junction of the merging region is pushed further upstream because of the greater entrainment capabilities of the outer jet. Unstable flow was

observed for velocity ratios above 1.15, where the reverse flow caused by the two outer jets is equal to that of the central jet.

Very little data exists in the description of the scalar-mixing field of parallel multiple rectangular jets. The few exceptions are Grandmaison and Zettler (1989) and NG and Grandmaison (1989) who performed scalar measurements of the mean and fluctuating field of triple parallel slender jets with an equal aspect ratio of 40 and a spacing of  $s/D = 0.14$ . NG *et al.*, (1989) observed the effect of varying the velocity ratio and observed that low velocity ratios enhance dilution of centre jet fluid on the centreline.

Grandmaison and Zettler (1989) used the inverse power law to describe the centreline mixture fraction for various velocity ratios and splined it for different regions of the flow field. The centreline concentration decay model in Equation 2.23 and concentration half-width spread model in Equation 2.25 were used to curve fit the jet spread. The values of  $K_1$ ,  $K_2 x_{o,1}/D$  and  $x_{o,2}/D$  for each velocity ratio are reported in Table 2.6.

NOTE: This table is included on page 43 of the print copy of the thesis held in the University of Adelaide Library.

**Table 2.6:** Model data for centreline mixture fraction and jet spread as a function of secondary to primary velocity ratio for a three plane jet system,  $AR = 40$ ,  $s/D = 0.56$  (Grandmaison and Zettler, 1989).

NOTE: This figure is included on page 44 of the print copy of the thesis held in the University of Adelaide Library.

**Figure 2.10:** Schematic Diagram of the three flow regions for a multiple plane jet system, highlighting the converging, merging and combined regions (Lin *et al.*, 1991).

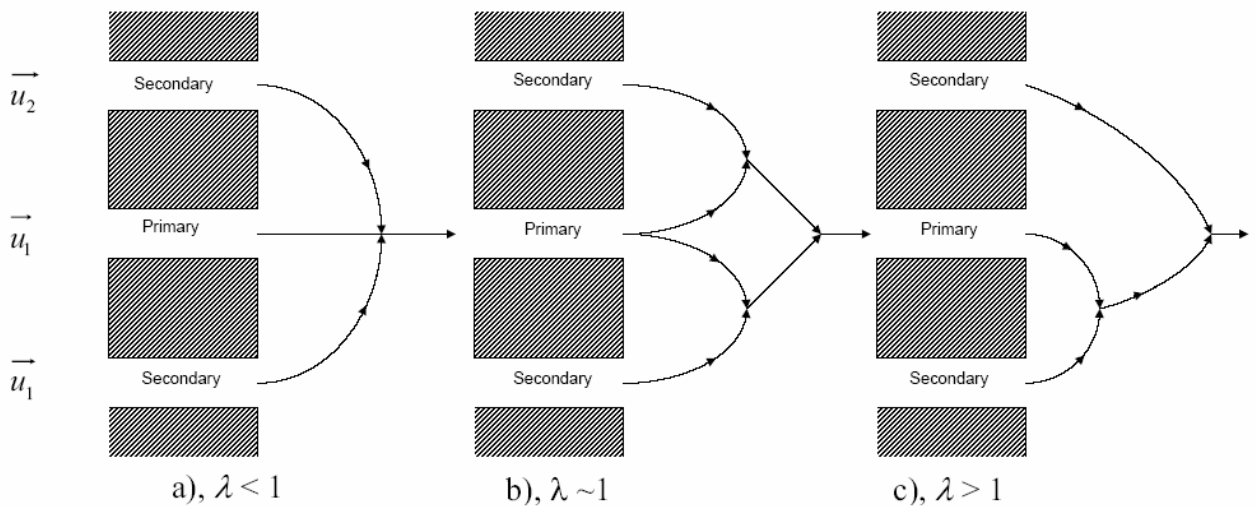


**Figure 2.11:** Models of flow patterns of three parallel plane jets described by Tanaka *et al.*, (1975) for operating at different velocity ratios: a) for  $\lambda < 1$  both secondary jets are entrained into the primary, b) for  $\lambda \sim 1$  the primary jet is equal entrained into the secondaries which merge further downstream and c)  $\lambda > 1$ , where the primary merges first into one secondary and the resultant into the other.

### 2.4.5 Rectangular Jets Studies on Multiple Rectangular Jets Commonly found in Brown Coal Fired Boilers

The Victorian State Electricity Commission sought to optimise the combustion stability and minimise fouling of brown coal fired boilers by performing an investigation of the aerodynamic mixing of a pair of rectangular slots (Perry *et al.*, 1982; 1983a; 1983b; 1984; 1985; 1986) so as to “lay the foundations” for a mathematical model of an entire boiler to include a suitable combustion model. Axial and radial velocity measurements (through different planes of flow) were performed on groups of rectangular slots of different geometries, similar to those found in the Yallourn stage 1 and 2 boilers (Perry *et al.*, 1982; 1983a; 1983b; 1984; 1985; 1986). The basic geometry which is illustrated in Figure 2.12 consists of a primary jet ( $AR=1.28$ ) centrally positioned which is a pulverised coal stream pneumatically transported by recycled flue gas and two adjacent secondary jets ( $AR=2.2$ ) which model the air supply. Perry *et al.*, (1982) performed studies on a singular primary rectangular jet system and conventional primary/secondary rectangular jet systems normal to a jet wall (Figure 2.13, Geometry A). The experimental program was extended to accommodate several other nozzle geometries commonly found in brown coal fired boilers. The geometries included primary and secondary jets perpendicular to the wall (Figure 2.13, Geometry A) at 60 degrees to the wall (Geometry B) at 60 degrees to the wall with dividing walls between each stream terminated at a short distance upstream from the boiler wall, (Geometry C) and a final geometry with a diverging side and end walls bounding the burner exit plane as well as being 60 degrees with boiler wall and having the dividing walls removed upstream (Geometry D). The dimensions of the model rectangular jets were geometrically scaled down 1:27 from the jets present in the brown coal fired boilers of the Yallourn ‘stage W’ boilers. Refractory cooling air is injected through jets arranged crosswise across the exit plane of the primary flow as illustrated in Figure 2.14, and can be seen in the photograph of the main burners in Figure 2.15. Perry *et al.*, (1982) concluded that the core flow slightly suppresses vortex shedding between the plates but may be omitted for the purpose of modelling due to the minimal effect it has on the flow field.

Qualitative flow visualisation (Marker Nephelometry) and quantitative hot wire anemometry measurements were performed on the above geometries up to  $x/D = 12$  (Perry *et al.*, 1982; 1983a; 1983b; 1984; 1985; 1986) over an extensive range of velocity ratios. Initial observations showed

that velocity ratio had very little effect on Geometries A and B but has significant effects on recessed burners such as Geometries C and D with in the first few diameters of flow.

### **Geometry A**

A wide range of velocity ratios were investigated. Fluid from Geometry A was found to be entrained around the perimeter of all three jets. It was also found that the axial velocity decayed at lower rates than Geometries C and D (Figure 2.16).

### **Geometry B**

It was found that changing the angle of the burner to the wall affected the jet's entrainment characteristics. Entrainment characteristics for Geometry B are similar to that of A, except that the majority of fluid is entrained from the side of the nozzle at 120 degrees to the furnace wall. Even though there is a geometrical difference between Geometries A and B there was no significant difference in velocity profiles (Figure 2.16).

### **Geometry C**

For Geometry C, initial velocities are higher with respect to A and B due to the low pressure at the burner mouth caused by the removal of separation plates. The velocity decays more rapidly in geometry C than for geometries A and B. Within the recess the decay is caused by velocity diffusion within the cavity.

It was found that, for secondary to primary jet velocity ratios ( $\lambda$ ) between 1 and 1.5, the three jets merge inside the recess, so that the emerging jets have a defined velocity profile by the time they reach the furnace wall. As the velocity ratio is increased to 3 the primary jet separates from the major axis wall. For velocity ratios greater than 7, the primary jet seems to be symmetrically entrained almost immediately into each secondary stream.

### **Geometry D**

The velocity profiles of Geometries C and D at relatively high and low velocity ratios were compared. For low velocity ratios experienced in geometry D ( $1 < \lambda < 1.5$ ) all three jets are separated from the major axis wall with the secondary jets attached to the walls on the minor

axis. As the velocity ratio increases from 3 to 4.5, entrainment of primary fluid into the secondary stream occurs to the extent that they merge whilst still in the cavity. Higher velocity ratios ( $7 < \lambda < 9.27$ ) show similar results to Geometry C with the primary jet splitting almost immediately into both secondary streams.

The influence of secondary to primary velocity ratio was only assessed in detail for Geometries C and D based on earlier conclusions that the effect of velocity ratio on Geometries A-B is negligible. Figure 2.17 is a comparison for axial velocity decay of the primary jet for Geometries C and D operating at different velocity ratios. It is evident that geometry D seems to experience large rates of decay for  $x/D = 2$ , at a velocity ratio of  $\lambda = 3$ .

The only existing study of scalar properties of the triple jet system was performed by Mullinger *et al.*, (2002) who compared the scalar jet spread of a 1:30 scale model of the triple rectangular jet system of the Yallourn Stage W boilers with a concentric jet arrangement of the same primary and secondary cross sectional areas and equivalent wall. It was concluded that changes in velocity ratio had no effect on jet spread, and that the rectangular jet generally entrained less fluid than the co-annular system.

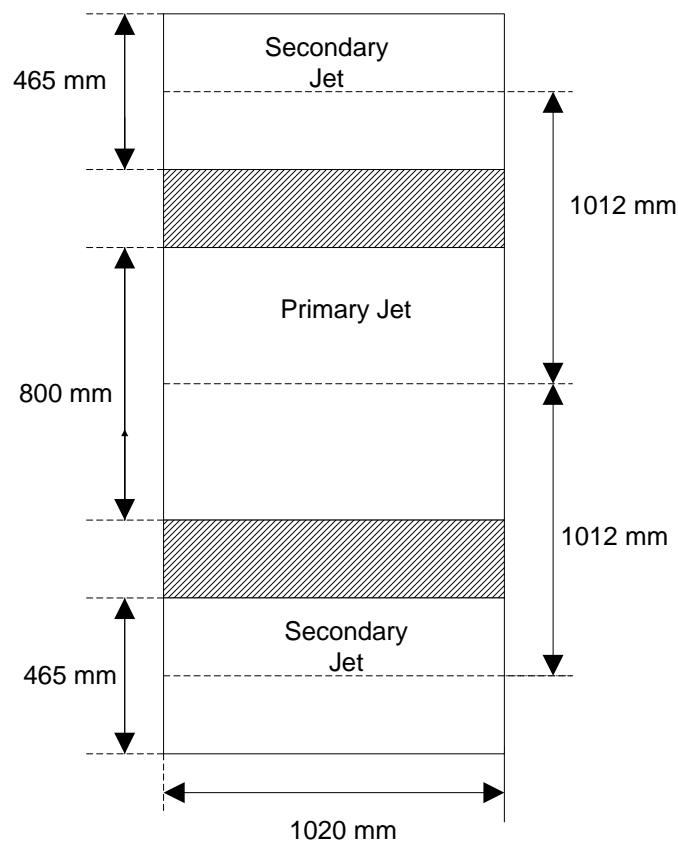


**Figure 2.12:** Schematic diagram of the triple jet configuration present in the Yallourn W boilers



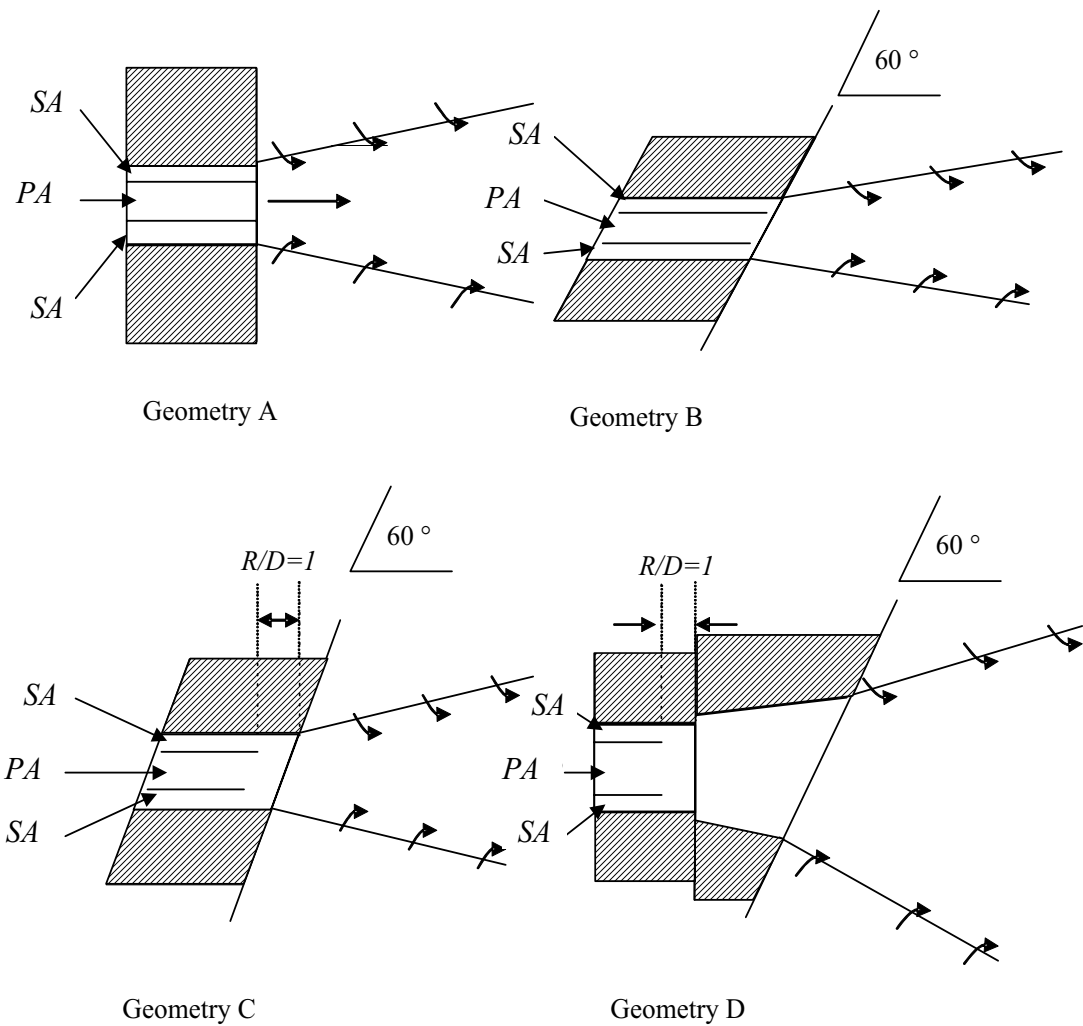


**Figure 2.13:** Diagram of different geometries used in the study conducted by Perry and Pleasance (1983b) Geometry A; perpendicular to wall, Geometry B; at 60 degrees to the wall, Geometry C with the removed separation plates at 60 degrees to wall, Geometry D, with removal of separation plates as well as an expanded recess.

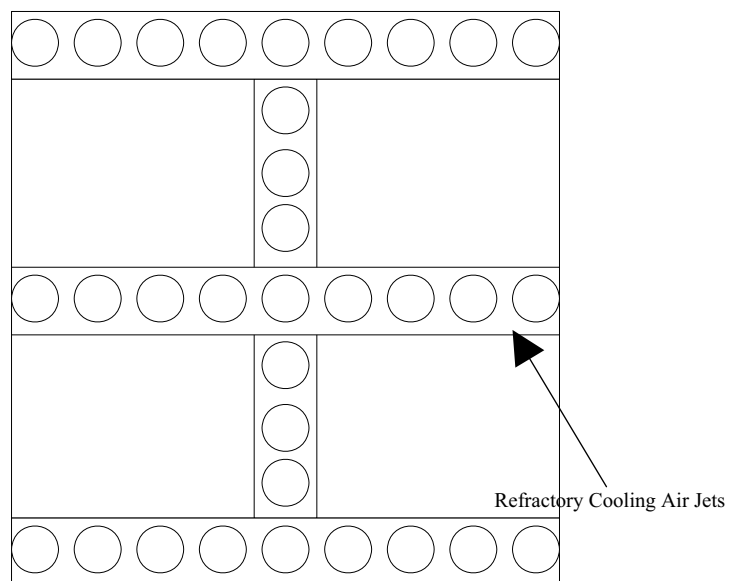


**Figure 2.14:** Schematic of Refractory cooling Air Jets

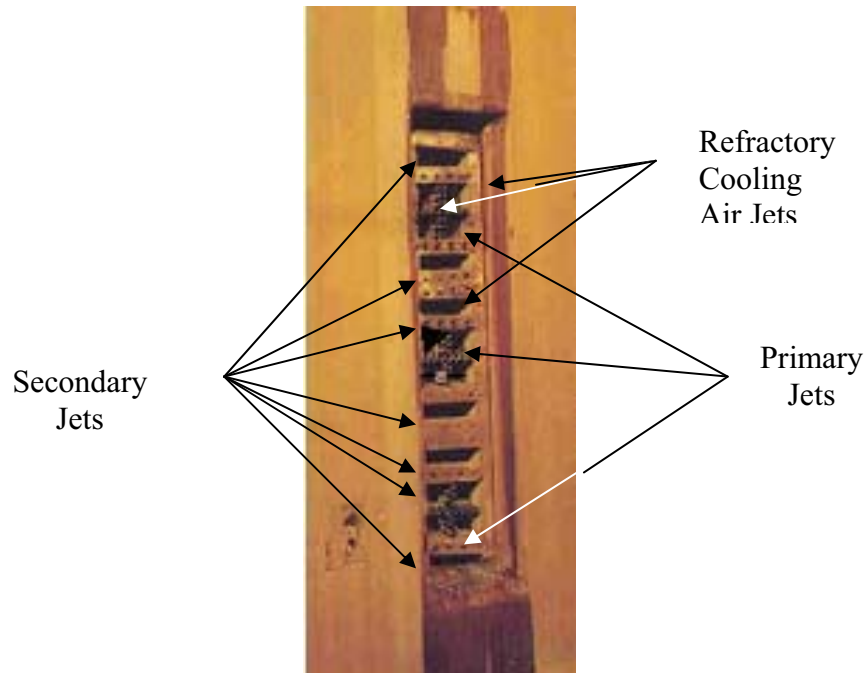


**Figure 2.15:** Photograph of Rectangular Jets Present in a Brown Coal Fired Boiler, illustrating the primary and secondary jet pairings and refractory cooling air jets (Loy Yang Power Station, Courtesy of Loy Yang Power).

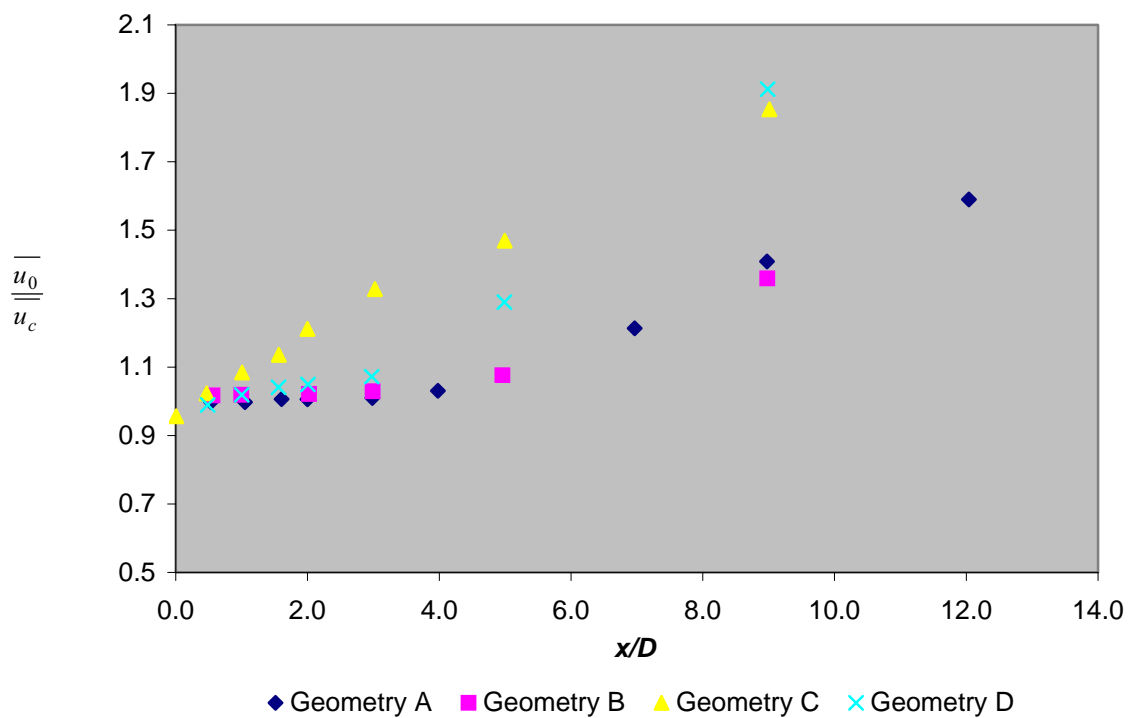


**Figure 2.16:** Dimensionless centreline jet velocity versus dimensionless axial distance for Geometries A, B, C and D, at  $\lambda = 1$  (Perry *et al.*, 1982)  $\overline{u_0}$  is the source velocity and  $\overline{u_c}$  is the centreline velocity.

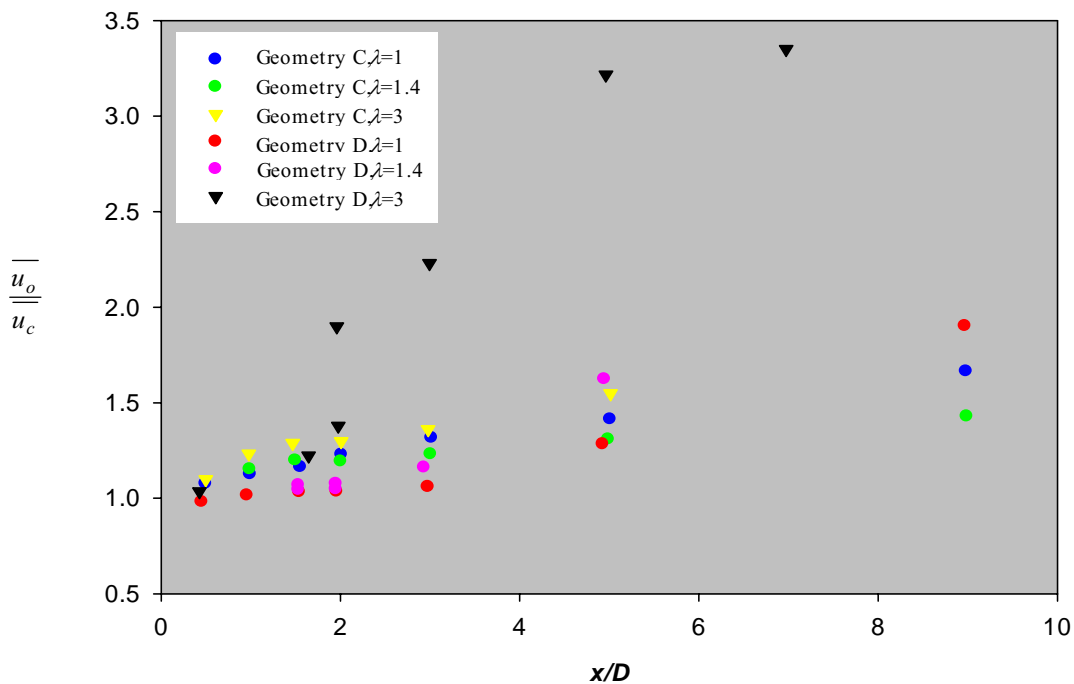


**Figure 2.17:** Dimensionless centreline jet velocity versus dimensionless axial distance for Geometries C and D, at  $\lambda = 1$ ,  $\lambda = 1.4$  and  $\lambda = 3$  (Perry *et al.*, 1986).

## 2.5 Scaling Analysis of the Aerodynamic Trajectories of Coal Particles in Brown Coal Fired Boilers

A Scaling Analysis is a useful way to identify which are the dominant physical processes in two phase flow systems. It is important to determine the dimensionless parameters, which identify broad regimes of flow behaviour. A scaling analysis allows for quick order of magnitude assessments to be made on the importance of a specific phenomenon. A Scaling analysis is not a definitive assessment for a given phenomenon and cannot provide quantitative prediction or a detailed optimisation.

The dominant dimensionless groups in two phase flow systems are the flow Reynolds number  $Re_f$ , Particle Reynolds number  $Re_p$  and the Stokes number,  $St$ .  $Re_f$  is used to characterise the flow regime, ie turbulent, laminar or transitional.  $Re_p$  is used to characterise coefficient of a particle and  $St$  is used to characterise how closely particles follow turbulent motions. The flow Reynolds number and particle Reynolds number are defined as;

$$\text{Re}_p = \frac{\rho_f L \bar{u}_s}{\mu} \quad \text{Equation 2.40}$$

$$\text{Re}_f = \frac{\rho_f d_p \bar{u}}{\mu} \quad \text{Equation 2.41}$$

where  $\rho_f$  is the fluid density,  $d_p$  is the particle diameter,  $\mu$  is fluid viscosity,  $L$  is the characteristic flow length,  $\bar{u}$  is the fluid velocity and  $\bar{u}_s$  the relative velocity between fluid and particle. For a particle Reynolds numbers less than 0.1 the flow behind the particle is deemed creeping flow, where the particle moves throughout the fluid without deforming it. For a  $\text{Re}_p < 20$ , the flow in the wake of the particle is considered to be in the stokes regime or laminar where minimal wake effects are observed and the separation of the boundary causes the formation of small scale low-intensity eddies. For  $\text{Re} > 20$ , the separation of the boundary layer moves towards the rear of the particle causing larger size eddies to form; this region is the turbulent flow regime.

The stokes number is defined as the ratio of response time of a particle ( $\tau_p$ ) to a fluid structure ( $\tau_f$ );

$$\text{St} = \frac{\tau_p}{\tau_f} = \frac{\rho_f \bar{u} (d_p)^2}{18 \mu L} \quad \text{Equation 2.42}$$

For  $\text{St} \ll 1$  a particle is fully able to respond to a turbulent structure of length scale  $L$  and follows the streamlines exactly. For  $\text{St} \gg 1$  the particle trajectory is completely unaffected by the eddy. For  $\text{St} \sim 1$ , particles partially respond to fluid motions. Eaton and Fessler (1994) have used this analysis to explain particle clustering for a range of fluid flows such as free shear flows, Plane Mixing layers, wake flows and jets.

The rectangular jets of the Yallourn W1 main burners (Perry and Pleasance, 1983a) will provide the basis for the determination of the Length scales of the flow, fluid velocity and fluid temperature. The values of  $L$  are the equivalent diameter of the particle laden primary jet which is 1019 mm and the equivalent diameter of the secondary jet is 777 mm. Two other important length scales have also been identified. They are the major and minor widths of the spacing

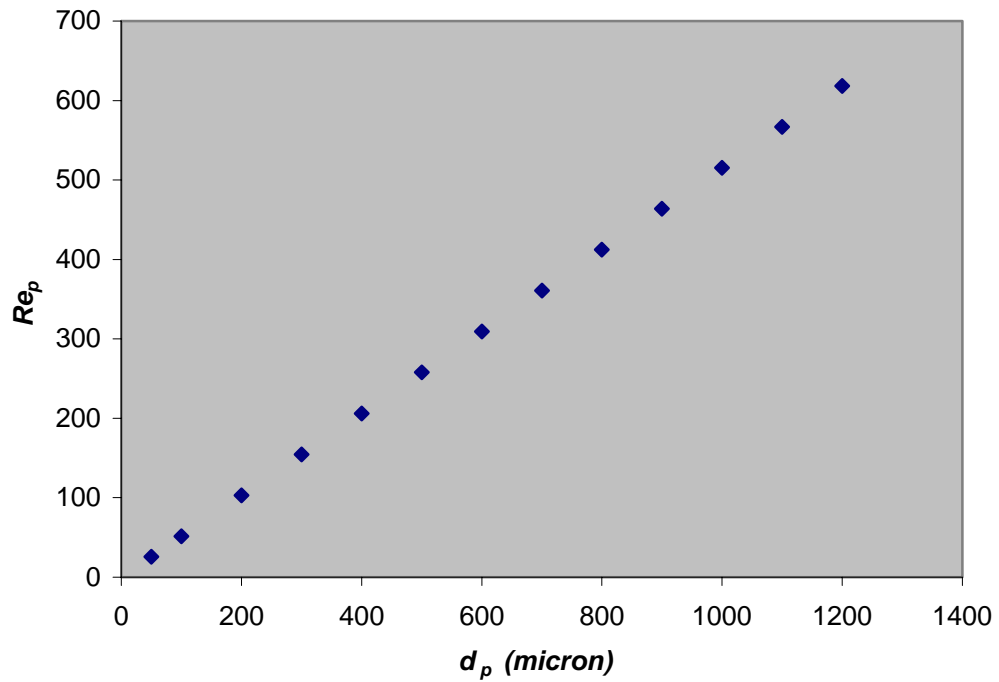
between the primary and secondary jets which is 1020 and 388 mm. The flow Reynolds number is  $4.6 \times 10^5$ , the primary jet temperature is  $122^\circ\text{C}$  and  $\bar{u} = 14.9$  m/s. It is assumed that the viscosity of primary transport fluid is similar to that of air at the same temperature ( $\mu = 2.2 \times 10^{-5}$  Pa s). The density of a brown coal particle was found to be  $1114 \text{ kg/m}^3$  (Durie, 1991). The particle sizes of brown coal particles being pneumatically transported to the primary jets were assessed by Salter and Nguyen, (2001). Their particle size distribution is tabulated in Table 2.7

Figure 2.18 is an assessment of the particle Reynolds number versus particle diameter for the Yallourn W1 main burners. Figure 2.18 clearly illustrates that the particles are in the turbulent flow regime. All particles smaller than 170 micron represent more than 80 % of the particles, these however still move at Reynolds number of greater than 50.

Figure 2.19 is the relationship between the Stokes number and particle diameter for the four different length scale identified in the Yallourn W1 main burners. For the four length scales, the majority of the particles have  $d_p < 90 \mu\text{m}$ . This implies that  $0.1 < St < 0.26$ , according to this the particles will respond sufficiently to large scale eddies in the flow. Particles with  $d_p \sim 170 \mu\text{m}$ , have Stokes numbers ranging in between  $0.41 < St < 1.1$ . This implies that the particles will only partially respond to eddies. For  $d_p \geq 170 \mu\text{m}$  Stokes range from 4 and reach 50 however according to the particle size distribution in Table 2.7. These larger size particles only account for a small percentage of total coal particles fed to the system.

NOTE: This table is included on page 52 of the print copy of the thesis held in the University of Adelaide Library.

**Table 2.7:** Average particle size distribution of coal particles feed to Yallourn W power station boilers, Salter and Nguyen, (2001).



**Figure 2.18:** Dependence of Particle Reynolds number on particle size for coal particles fed to the Yallourn W1 boilers.

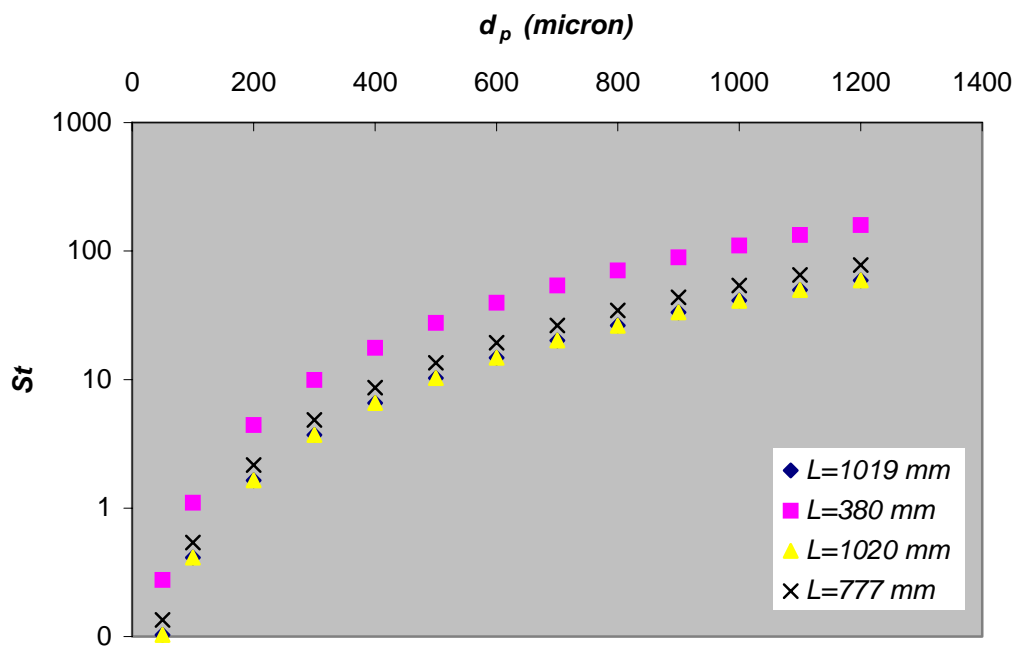


**Figure 2.19:** The effect of particle diameter on the Stokes number of the particle calculated for four characteristic length scales.

## 2.6 Conclusion

The purpose of the current project is to deliver a mixing model which predicts the oxygen content in the jets. This model can then be used as a basis of input for a combustion model for the use in tangentially fired brown coal boilers which needs the oxygen concentration to calculate the reaction rate. The nozzles used in the boilers are categorised as bluff jets, one central 'primary jet with AR =1.2 and two adjacently placed secondary jets with AR=2.2 precisely spaced apart. The nature of the flow means that both the primary and secondary streams which are representative of the fuel and air streams must be studied and their mixing characteristics quantified separately. The best way to do this is to investigate the concentration of both primary and secondary jets. It is also important to quantify the concentration distribution of entrained fluid or re-circulated flue gas, as this gas will dilute oxygen concentration, thus altering the combustion characteristics of the flame.

The previous studies performed on multiple rectangular jet arrangements has mostly focussed on the turbulent characteristics of plane jets (Lin and Sheu, 1991, Elbanna and Gahin 1983, Krothpalli *et al.*, 1980, Tanaka, 1970; 1974, Tanaka and Nakata 1975) with some focussing on the scalar characteristics (Grandmaison and Zettler 1989, NG and Grandmaison 1989). No official studies to date have been done on the scalar properties of a series of multiple bluff-jets. The studies performed by Perry and Hausler (1982), Perry and Pleasance (1983b) who focussed more on the turbulent characteristics of these jet arrangements paid very little attention to the effect of secondary to primary velocity on the nature of the flow.

It is the purpose of this thesis to provide qualitative and quantitative information on the flow field as well as the scalar characteristics of the primary/secondary rectangular jet arrangement similar to that used by Perry and Hausler (1982) and Perry and Pleasance (1983b) with variation in the secondary to primary velocity ratio. The retrieved quantitative information will formulate the basis of a three-dimensional mixing model.

Although Perry *et al.*, (1982; 1983a; 1983b; 1984; 1985; 1986) did conclude that velocity ratio has little effect on the flow field characteristics on a simple case geometry such as Geometry A, their evidence is insufficient and inconsistent with other experimentalists such as Tanaka *et al.*, (1975) and (Grandmaison and Zettler, 1989) who varied the velocity ratio for other multiple rectangular jet systems and observed both quantitative and qualitative changes in the flow field.

A Scaling analysis determined that over half of the particles fed to the primary jet will fully respond to turbulent structures in the fluid. However, nearly 30 % of the remaining particles will only partially respond and 18-20% will not respond at all. Although this is not a definitive conclusion on the two-phase flow characteristics of the rectangular burners, it is important to state that investigating the fluid-dynamic nature of the flow is of first order importance.



# Chapter 3

## 3 Experimental

### 3.1 Isothermal Jet Modelling

Experimental measurements on full-scale boilers and burners is a tedious and expensive process. Physical models offer a quick and an inexpensive route to provide information necessary for development and design. However, success in physical modelling requires similarity between the model and prototype (Spalding, 1963). Several categories of similarity exist:

#### *Geometric Similarity*

The simplest and most commonly used modelling for studying incompressible non-reacting isothermal flow. Geometric similarity is maintaining consistent ratios of the geometric parameters between model and prototype.

#### *Kinematic Similarity*

The case where the fluid and or solid particles in the model and prototype traverse a geometrically similar path in corresponding intervals of time, e.g.; velocity ratios between the model and prototype are constant.

#### *Dynamic Similarity*

The ratio of forces causing acceleration of mass are similar for the model and the prototype.

#### *Thermal Similarity*

Flow of heat and kinetic energy ratios are maintained constant, or temperature ratios maintained constant, with other parameters adjusted through the mechanical energy equation

The above forms of similarity may be extracted from dimensional analysis or by creating non-dimensional relationships in differential equations governing mass and momentum conservation. In experimental modelling, it is necessary to hold certain dimensionless variables constant whilst varying others one at a time and assessing the end effect this has on the model.

This approach is not always feasible however: Therefore, critical selection is required to determine the parameters, which affect the system in a greater way than others. This technique is known as ‘partial modelling’ (Spalding, 1963, Beer, 1966).

Combustion modelling is extremely difficult as there are significantly more independent variables than degrees of freedom. Therefore, knowledge of which variables to ‘float’ requires experience. In turbulent flame modelling the following variables may be ‘relaxed’:

- The Reynolds number need not be replicated in the model when operating under fully turbulent conditions provided that the model is also turbulent.
- Two Phase flow effects are negligible if the settling time of a particle is significantly lower than the residence time over a given length. Particle settling is strongly dependant on the squared value of the particle diameter (see section 2.5).
- If the density change associated with combustion is not large, then it is not necessary to maintain constant the density ratio.

### 3.2 Quantification of Mixing

The definition of mixing of fluids is simple. According to the Oxford Dictionary (1987) for a batch system mixing is defined as:

*‘to combine or put together two or more substances so that the constituents of each are diffused among the others’.*

In the realm of turbulent combustion the above substances may be interpreted as fuel and air, or reacting species. For the current project the participating substances consist of pneumatically transported coal, air and entrained furnace gas. How may the pneumatically transported coal, air and entrained furnace gas be quantified using a mathematical model or function? Knowledge of the concentration of coal is a function of space and time. Two common methods have been identified in the combustion community, which deal with the turbulent mixing of jets;

- a) Quantification of entrainment, or how much fluid is being entrained per unit time as a function of space.

- b) Quantification of the concentration of a particular constituent as a function of space and time.

Entrainment is the volumetric flux of a fluid into a moving fluid. In jets entrainment is a consequence of momentum exchange between the jet and fluid surroundings. Entrainment can be measured directly (Ricou and Spalding, 1961, Hill, 1972, Becker and Yamazaki, 1978 and Han and Mungal, 2001) and is useful when quantifying mixing in systems where there is only one working fluid (such as a jet) and only one entrained fluid (such as stagnant or moving surroundings) where the amount of entrained fluid per unit time is reported as a function of downstream distance. When three different streams are interacting such as the current one, it is insufficient to assess the mixing by defining entrainment; consequently the concentration of each individual component must be assessed. Concentration of different species can be distinguished and mapped as a function of space and time.

In order to model the concentration of different fluids in a multi jet system, it is important to understand which variables exist and each role they play in the mixing and whether they are required for the current project. The assessment of the variables can be achieved through dimensional analysis. A set of scaled rectangular nozzles such as those shown in Section 3.4, have several important physical parameters which will alter the flow, these being, jet height,  $H$ , Primary and Secondary jet width,  $W_1$  and  $W_2$ , jet spacing  $S$  and equivalent jet diameter  $D$ . A set of spatial and temporal variables need to be considered;  $x$ ,  $y$ ,  $z$  as the directional components, and  $t$ , time. Also included into the initial model are flow parameters such as the time-averaged velocity of the primary and secondary jet at the nozzle exit planes  $\overline{U}_1$ ,  $\overline{U}_2$  as well as fluid properties such as, viscosity  $\mu_1$ ,  $\mu_2$ ,  $\mu_3$  and density  $\rho_1$ ,  $\rho_2$ ,  $\rho_3$  where the subscripts denote the fuel jet (1), air jet (2) and furnace gases (3). Combining such variables will yield the following expression;

$$\overline{C} = F(x, y, z, D, S, H, W_1, W_2, D, \overline{U}_2, \overline{U}_1, \rho_1, \rho_2, \rho_3, \mu_1, \mu_2, \mu_3, t) \quad \text{Equation 3.1}$$

where  $\overline{C}$  is the time averaged fluid concentration. Application of Buckingham Pi's Theorem reduces Equation 3.1 to;

$$\frac{\bar{C}}{\rho} = F\left(\frac{x}{D}, \frac{y}{D}, \frac{z}{D}, \frac{S}{D}, \frac{H}{D}, \frac{W_1}{D}, \frac{W_2}{D}, \frac{\bar{U}_2}{U_1}, \frac{\rho_1 \bar{U}_1 D}{\mu_1}, \frac{tD}{U_1}, \frac{\rho_2}{\rho_1}, \frac{\rho_3}{\rho_1}, \frac{\mu_2}{\mu_1}, \frac{\mu_3}{\mu_1}\right) \quad \text{Equation 3.2}$$

$\frac{\bar{C}}{\rho}$  for a non-reacting fluid is actually the time-averaged mixture fraction  $\frac{\bar{C}}{C_o}$  ( $\bar{\xi}$ ) and the last

three terms in Equation 3.2  $\frac{\bar{U}_2}{U_1}$ ,  $\frac{\rho \bar{U}_1 D}{\mu}$  and  $\frac{tD}{U_1}$  are the secondary to primary velocity ratio ( $\lambda$ ),

Reynolds number ( $Re$ ) of the primary jet and the Strouhal number ( $St$ ). A number of these variables were relaxed such as the Reynolds number, owing to the fact that, if sufficient turbulence is generated, the fluid-dynamic characteristics do not change. The Strouhal number is representative of the instantaneous characteristics of a flow field. Time dependant fluctuating statistics are not entirely necessary when modelling a flame, however their presence in a combustion or mixing model will increase the accuracy of predictions. In this project reliable time-averaged data is of first order importance. Industrial furnace models require mean data and many are not capable of higher order accuracy, even with the inclusion of time dependant statistics (Jenkins, 1998, Jenkins and Moles 1988). In this project the time averaged data from a wide range of conditions were assessed and considered of first order importance to the model. Consequently, the instantaneous characteristics were not included. This does not mean however that the time-dependant statistics are not of relative importance and have their place in many combustion model applications. Modelling of the mixing characteristics is best achieved in a cold-flow environment and has been done by many experimentalists. Consequently, the density and viscosity ratio terms were dropped from Equation 3.2, similarly for the Strouhal number. This does not mean that viscosity and density ratio do not have their effect on the flow; in fact density ratio does have a significant effect on turbulent mixing (Corrsin and Uberoi, 1949). However, at this stage, understanding of the basic mixing mechanisms with few variables as possible is also of first order importance. The lack of knowledge on the mixing of rectangular jets in this arrangement has conditioned the physical modelling process to closely look at one geometry only. Consequently, the spacing between the jets, the height and the width of the primary and secondary jets were also omitted reducing Equation 3.2 to ;

$$\bar{\xi} = F\left(\frac{x}{D}, \frac{y}{D}, \frac{z}{D}, \lambda\right) \quad \text{Equation 3.3}$$

In conclusion, it is the primary objective of this study to define the function  $F$ . The term  $x$  is the axial component and  $y$  and  $z$  are the radial components in the direction of the major and minor axes respectively. The scaled diagram of the jets in Figure 3.2 illustrates the directional components as well as the point of origin which is positioned at the centre of the primary jet.

### 3.3 Range of Experimental Variables

#### 3.3.1 Downstream Distance

The range of downstream distance corresponds to the range of  $x/D$ . The projected distance of the rectangular jets from inside the recess to the other side of the boiler is approximately 12 nozzle diameters, as illustrated in Figure 3.1.  $D$  is the equivalent diameter of the combined primary and secondary jets:

$$D = \sqrt{\frac{4(W_1^* H + W_2^* H)}{\pi}}$$

Equation 3.4

The notion of free jets is no longer valid for approximately  $x/D > 5-6$  because at this stage large scale vortical motion based on the total furnace diameter dominates the flow field. Consequently, only up to eight nozzle diameters were to be studied. The transverse experiments, Chapter 6 which supplies quantitative data, is only able to measure one axial position at a time; experiments were conducted at axial stations of  $x/D = 0.1, 0.2, 0.5, 1, 2, 4, 6, 8$ . The nature of the transverse experiments will be explained in more detail in section 3.5.3. Figure 3.2 is a schematic diagram of the orientation of the burner banks in the boilers and the primary and secondary nozzles which constitute the banks.

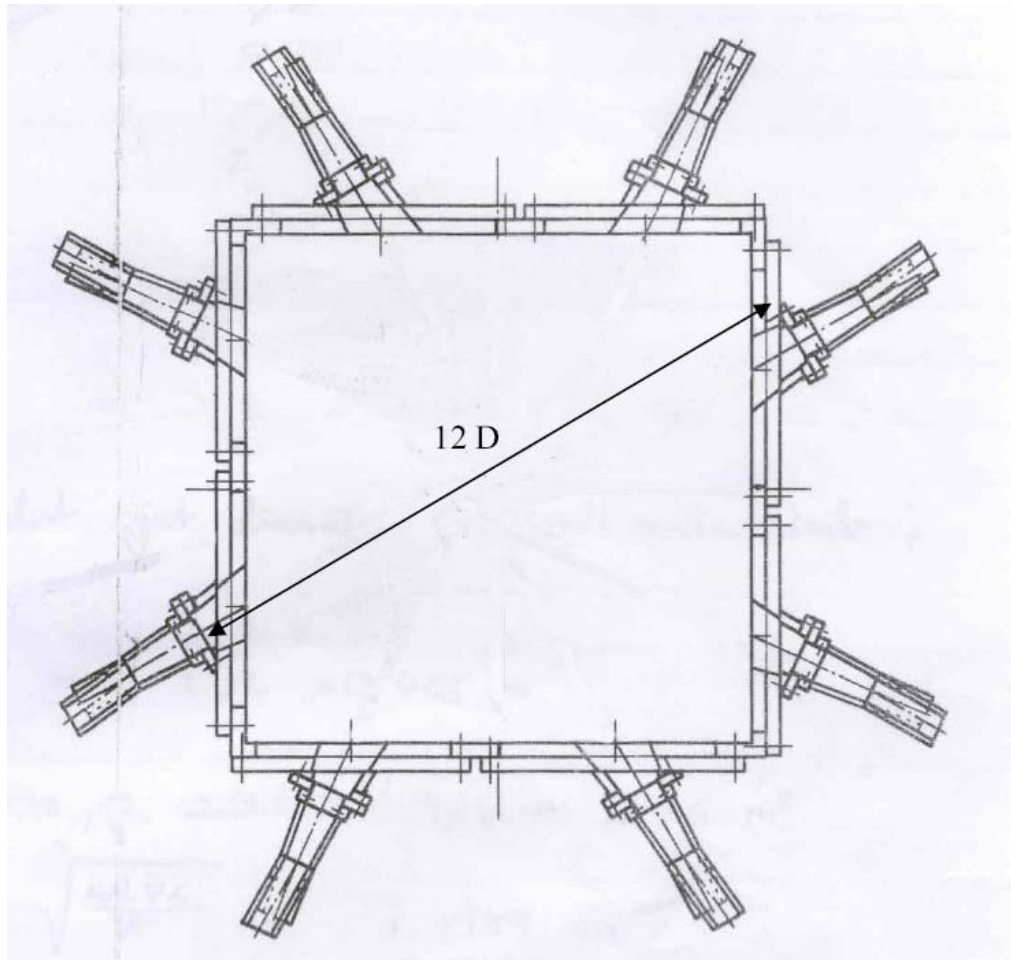


**Figure 3.1:** Top view of a tangentially coal fired boiler, with reference to the projected distance of the rectangular jets.

NOTE: This figure is included on page 61 of the print copy of the thesis held in the University of Adelaide Library.

**Figure 3.2:** Top view of a tangentially fired boiler indicating jet directions of 8 burner banks a). Front on view of a single burner bank b). Front view of a single burner indicating primary and secondary jets and position of the Cartesian coordinates  $y$  and  $z$ . Source of diagram: Goodhand *et al.*, (2001).

### 3.3.2 Range of Velocity Ratios in the Yallourn W1 Furnace

A preliminary investigation by Mullinger *et al.*, (2002) looked into the scalar mixing between multiple rectangular jets and Co-annular jets at velocity ratios of  $\lambda = 0, 0.5, 1$  and  $1.5$ . The selection of velocity ratios in that study was arbitrary and not based on any prior knowledge of the current operating velocity ratios of the main burners in the Yallourn W1 furnace. Consequently, the velocity ratios of the next phase of the experimental program were changed so that they were more representative of the actual operating conditions.

It was necessary to calculate the current velocity ratio of the main burners in the Yallourn W1 furnace. Although data was readily available for the amount of coal issuing through the primary jets it was unclear how much fluid was being used as the transport medium. The primary fluid is a mixture of recycled flue gas, evaporated lignite water and leakage air from the feed supply system (Simpson and McIntosh, 1998). Figure 3.3 is a basic block diagram of the unit operations involved in the pneumatic transport of coal to the primary burners. The recycled flue gas ( $F_6$ ) heated the coal to  $120^\circ\text{C}$  and reduced the coal moisture to 15% as it is being pneumatically transported (Simpson and McIntosh, 1998).

The mass flow rate of the recycled flue gas was determined by performing mass and energy balances around the coal feeder and milling section (red section in Figure 3.3) using flue gas composition and raw coal composition (Simpson and McIntosh, 1998). A detailed experimental methodology is given in Appendix A and the results of the mass and energy balances given in form of the mass flow rate of each stream in Table 3.1.

The air flow rates to main burners or secondary jets of the Yallourn 'W' boilers were measured over a period of three months between January and April 2001; (Yallourn Energy Pty. Ltd., 2004) values of air flow rates are also given in Simpson and McIntosh (1998). Knowledge of the flow rates to the primary and secondary nozzles in the burners will then permit calculation of the secondary to primary velocity ratio ( $\lambda$ ). Table 3.2 is the calculated velocity ratio using these sources of measured air flow rates.

Table 3.2 are the operating velocities and the secondary to primary velocity ratios depending on the measured and referenced values of air flow. The experimental velocity ratios were

consequently set around the operating flows. Velocity ratios of  $\lambda = 0.55, 1.4, 2.8$  and  $3.6$  were selected as well as  $\lambda = 0$  and  $\infty$  so as the effects of having a secondary or primary jet shut may be observed. The experimental jet flow rates were calculated based upon the selected velocity ratios and the Reynolds number of the primary jet which was kept constant at 10,000, consistent with the experiments of Mullinger *et al.*, (2002). The experimental flow rates are tabulated in Table 3.3.

Stream	Flow, tph	Temperature, °C
Coal Feed, $F_1$	576	15
Leakage air in, $F_2$	131	15
Secondary Air, $F_3$	1476, 1300, 1289, 1340	300
Dry coal conveying gas, $F_4$	1368	120
Leakage air in, $F_5$	633	15
Recycled flue gas, $F_6$	889	1000

**Table 3.1:** Operating Flow rates of coal feed system to Millourne 'W' Boilers (Simpson and McIntosh, 1998 and Millourne Energy Pty. Ltd., 2004).

Mass flow-rate, kg/s of Air to secondary nozzles	Secondary to primary velocity ratio, $\lambda$
416 <sup>i</sup>	2.82
361 <sup>ii</sup>	2.56
358 <sup>ii</sup>	2.56
372 <sup>ii</sup>	2.677

**Table 3.2:** Operating air flow rates for the main secondary burners in the Millourne W furnace with calculated secondary to primary velocity ratio ( $\lambda$ ) using the calculated primary burner flow rate of 1368 tph (Simpson and McIntosh, 1998, Millourne Energy Pty. Ltd., 2004).

Velocity ratio $\lambda$	Secondary velocity, m/s	Secondary Flow L/min	Secondary Reynolds number
0	0.000	0.00	0.00
0.55	0.214	4.62	3,720
1.4	0.599	12.94	9,712
2.8	1.198	25.87	19,430
3.6	1.540	33.26	24,928
$\infty$	0.57	12.31	10,000

**Table 3.3:** Experimental secondary jet velocities, flow rates and Reynolds numbers, calculated using a constant primary Reynolds number of 10,000 (0.45 L/min) and experimental nozzle geometry (Section 3.4).



NOTE: This figure is included on page 64 of the print copy of the thesis held in the University of Adelaide Library.

**Figure 3.3:** Block diagram of coal conveying process in the Yallourn Power station. (Simpson and McIntosh, 1998).

### 3.4 Experimental Jet Nozzles

#### 3.4.1 Rectangular Jet Nozzles for Qualitative and Quantitative Investigation

##### 3.4.1.1 Free Rectangular Jet Nozzles for Longitudinal and Transverse Investigation

A 1:30 geometrically scaled triple rectangular system was constructed (Figure 3.4) based on the size and geometry of the main burner jets present in the Yallourn 'W' Boilers (Perry *et al.*, 1982; 1983b). The upstream geometry of the models were constructed so that a sudden sharp transition from a round to a rectangular contraction was encountered similar to the upstream geometry of the main burners in the Yallourn 'W' Boilers. The model primary and secondary nozzles have inner dimensions of 16x20 mm and 9.6x20 mm respectively, and spacing ( $S$ ) between of 7.2 mm.

Figure 3.4 presents a scaled front section of the experimental nozzles, with physical dimensions and a coordinate system associated characteristic length with the origin placed at the centre of the primary jet. Figure 3.5 presents a side view; the most important dimensions are tabulated in Table 3.4. Figures 3.6 a), b) and c) are close-ups of the internal transition from round to

rectangular piping through symmetrical planes of the major and minor axes and cross section of the primary jet. Similarly, Figures 3.7 a), b) and c) are close-ups of the internal transition from round to rectangular piping through symmetrical planes of the major and minor axes and cross section of the secondary jet.

### 3.4.1.2 Rectangular Jet Nozzles for Investigation of Wall Effects

The same rectangular nozzles shown in Figures 3.4 to 3.7 for the investigation of free rectangular jets were attached to a 100x100 mm metal base plate, positioned flush with the exit plane. Figure 3.8 is a side view of the experimental nozzles with base plate; associated dimensions are the same as those tabulated in Table 3.4.

### 3.4.1.3 Rectangular Jet Nozzles for Investigation of Wall Inclination

The rectangular nozzles shown in Figures 3.4 for the investigation of free rectangular jets were attached to a 10x10 cm metal base plate at an angle of 60 degrees to one of the minor axes of the nozzles exit plane as illustrated in Figure 3.9. The remaining faces were covered by two 27 x 47 x 40 mm triangular plates and a 40 x 56 mm rectangular plate. Figures 3.9 a) and b) present side views of the experimental nozzles with the base plate. Associated dimensions are also tabulated in Table 3.4.

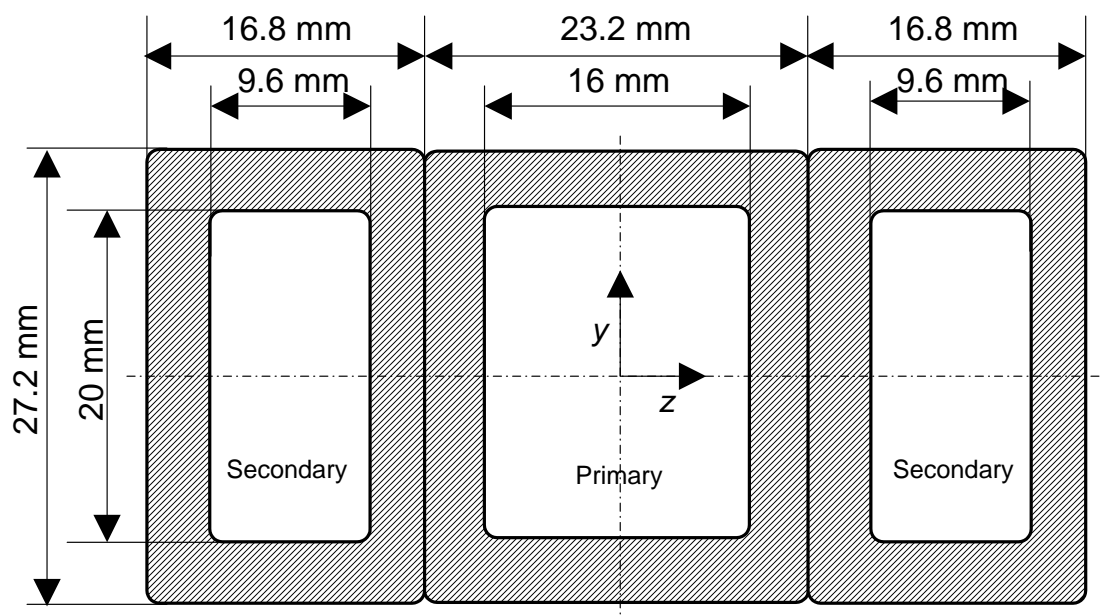


**Figure 3.4:** Schematic of cross sectional view of the rectangular jet system.

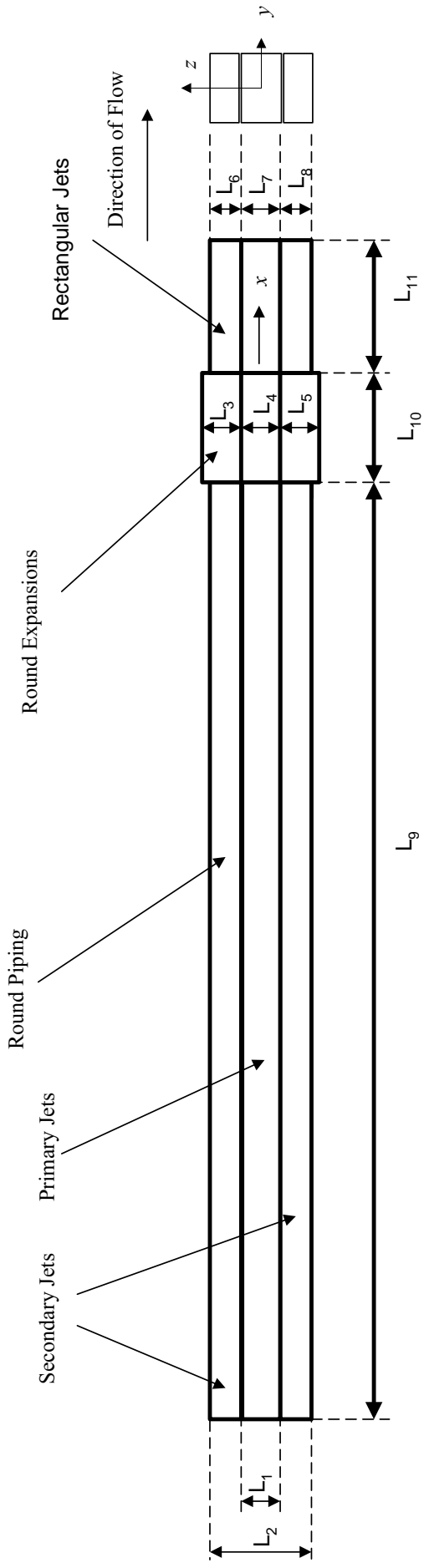


**Figure 3.5:** Schematic of side view of free the rectangular jet system with base plate angled at 60 degrees, top view with associated characteristic lengths in Table 3.4.

Symbol	Length, mm	Symbol	Length, mm
L <sub>1</sub>	22	L <sub>8</sub>	16
L <sub>2</sub>	51	L <sub>9</sub>	25
L <sub>3</sub>	21	L <sub>10</sub>	685
L <sub>4</sub>	24	L <sub>11</sub>	76
L <sub>5</sub>	21	L <sub>12</sub>	25
L <sub>6</sub>	16	L <sub>13</sub>	27
L <sub>7</sub>	23		

**Table 3.4:** Values of characteristic lengths for Figures 3.5, 3.8 and 3.9.

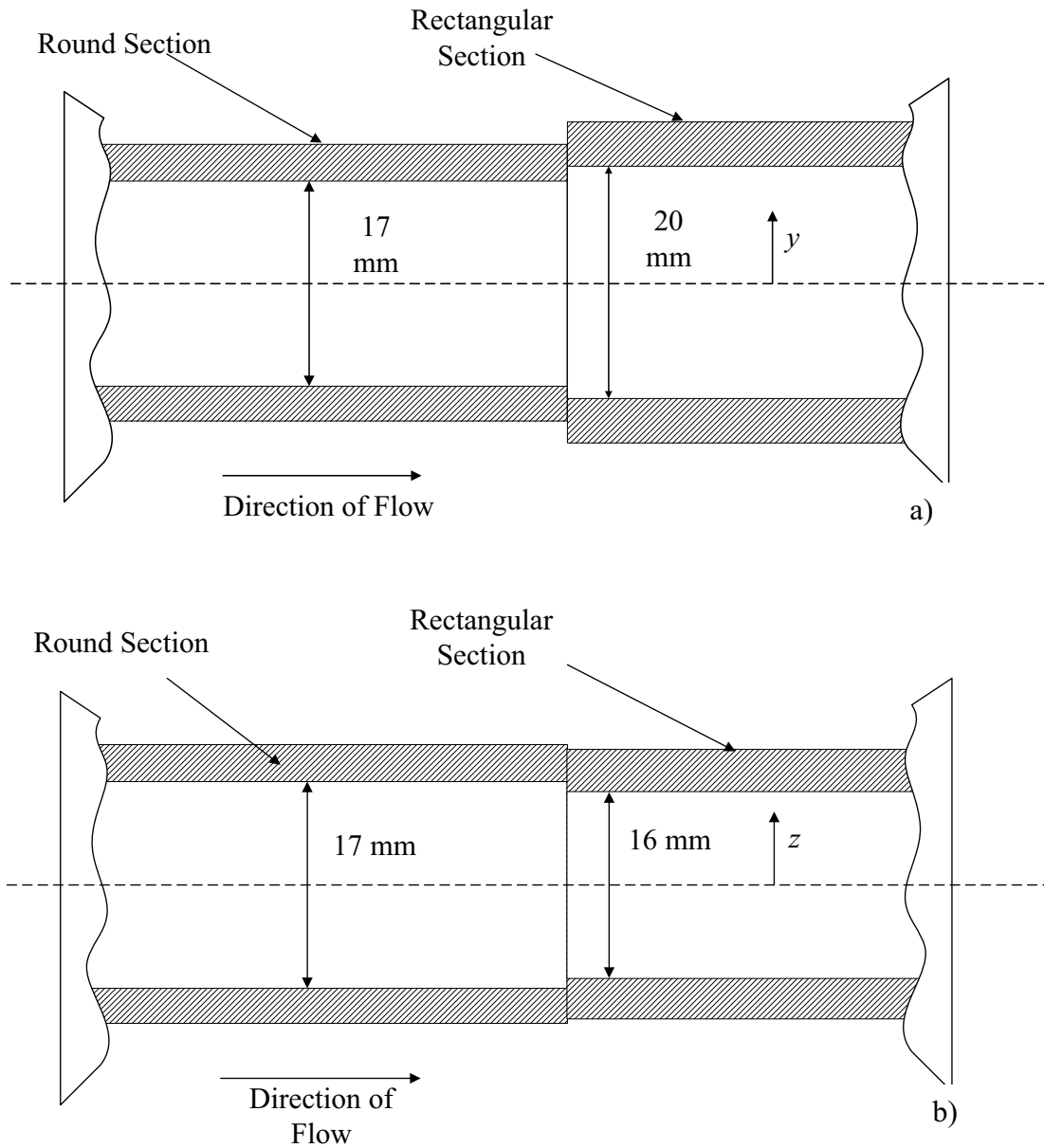


**Figure 3.6:** Major axis a), minor axis b) and cross sectional c) views of the round to rectangular transition encountered in the primary experimental nozzles.

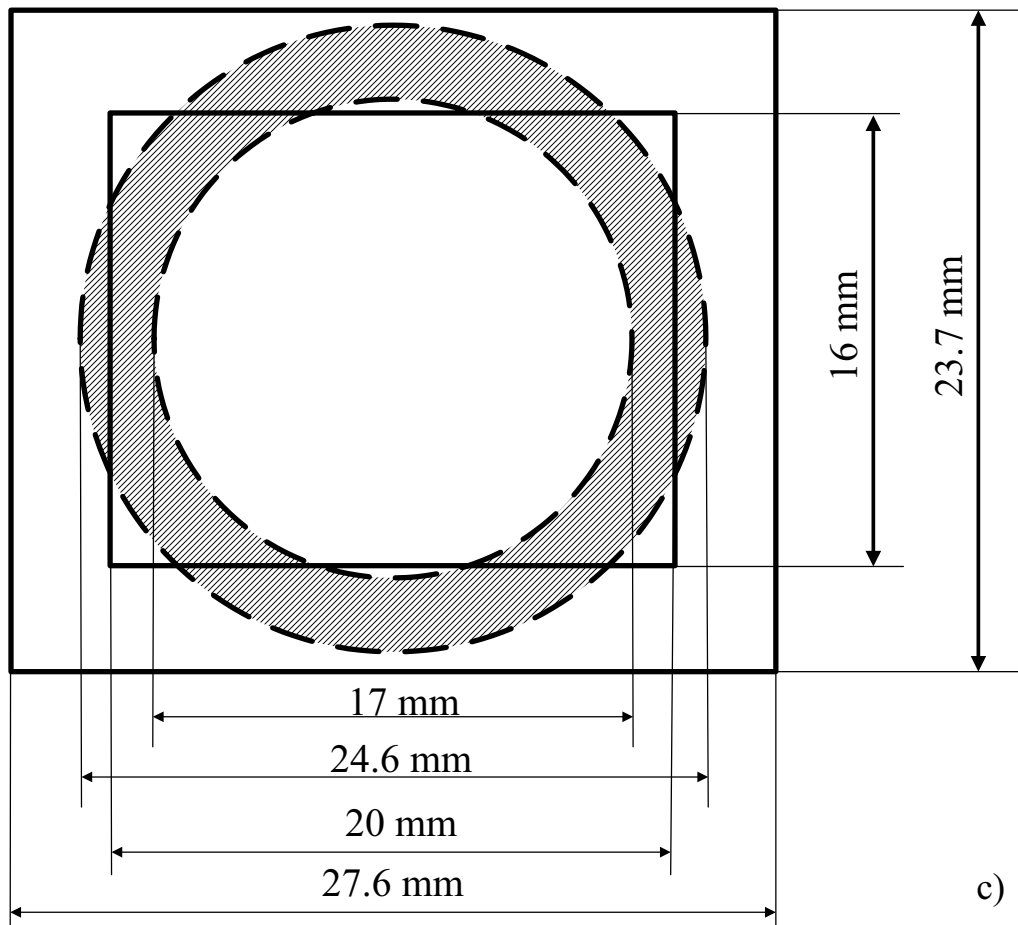


**Figure 3.6:** Major axis a), minor axis b) and cross sectional c) views of the round to rectangular transition encountered in the primary experimental nozzles.

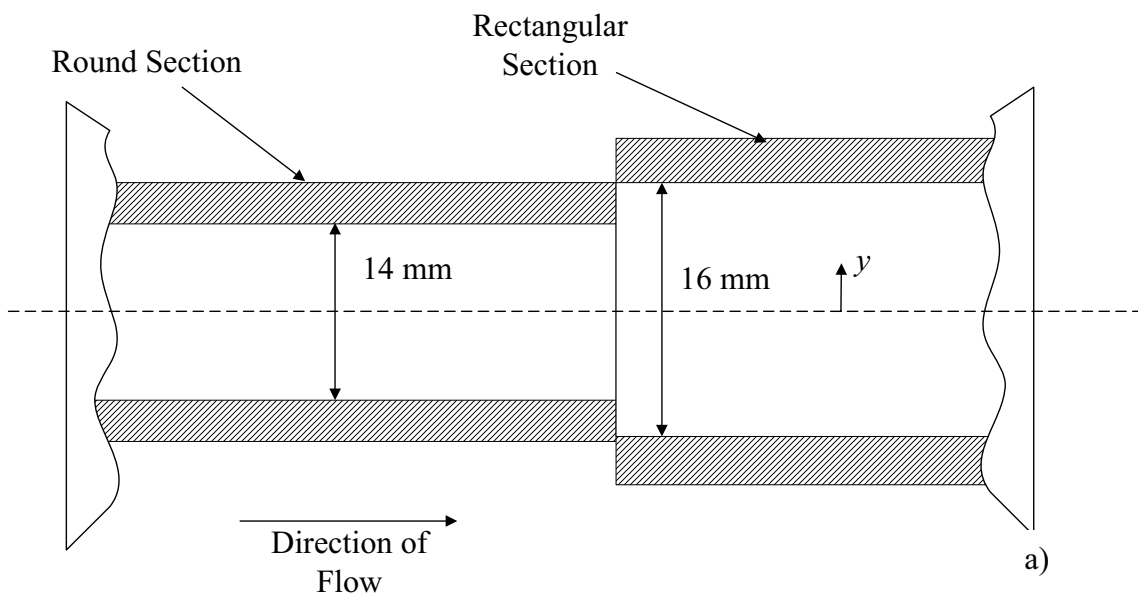


**Figure 3.7:** Major axis a), minor axis b) and cross sectional c) views of the round to rectangular transition encountered in the secondary experimental nozzles.

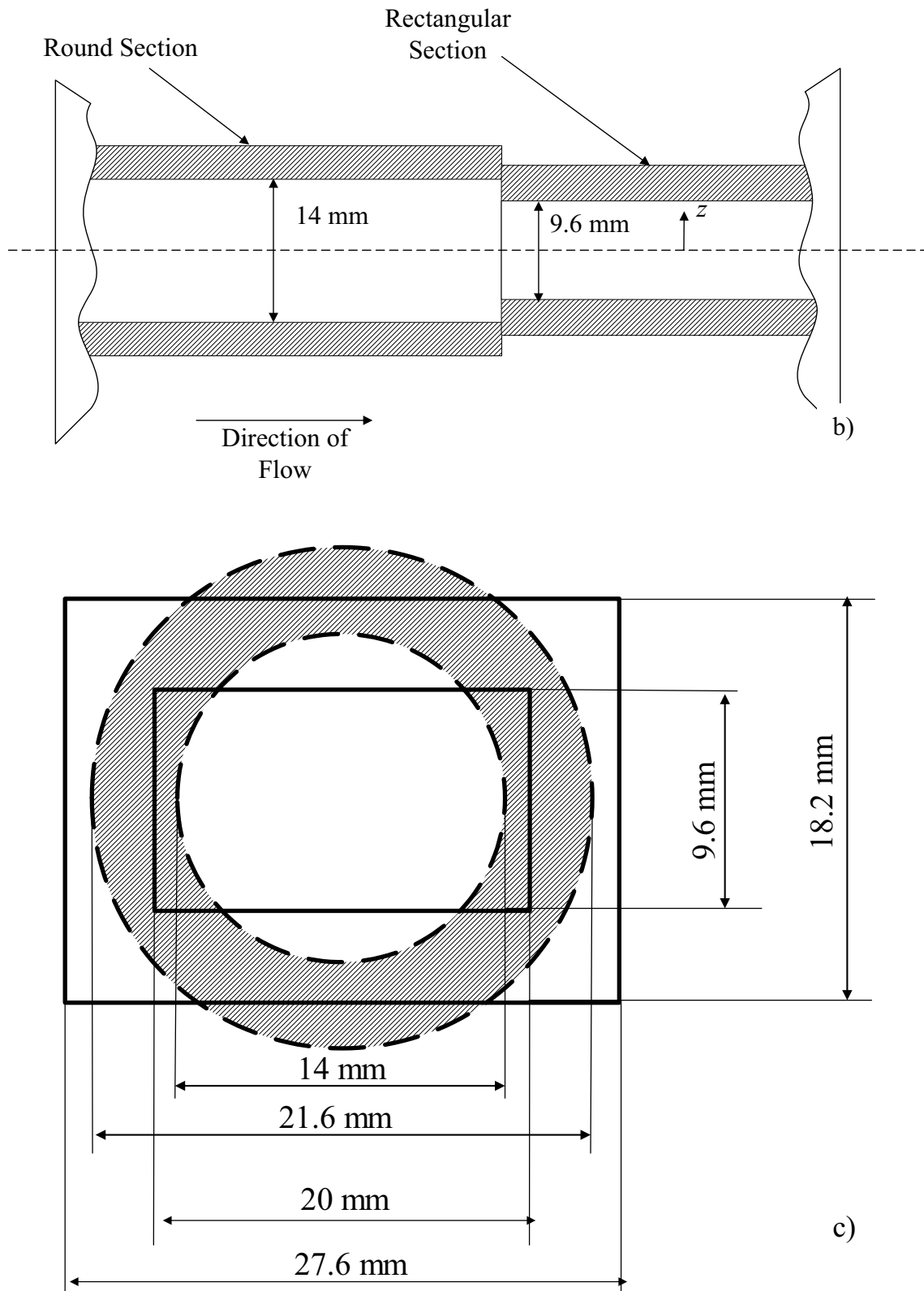


**Figure 3.7:** Major axis a), minor axis b) and cross sectional c) views of the round to rectangular transition encountered in the secondary experimental nozzles.

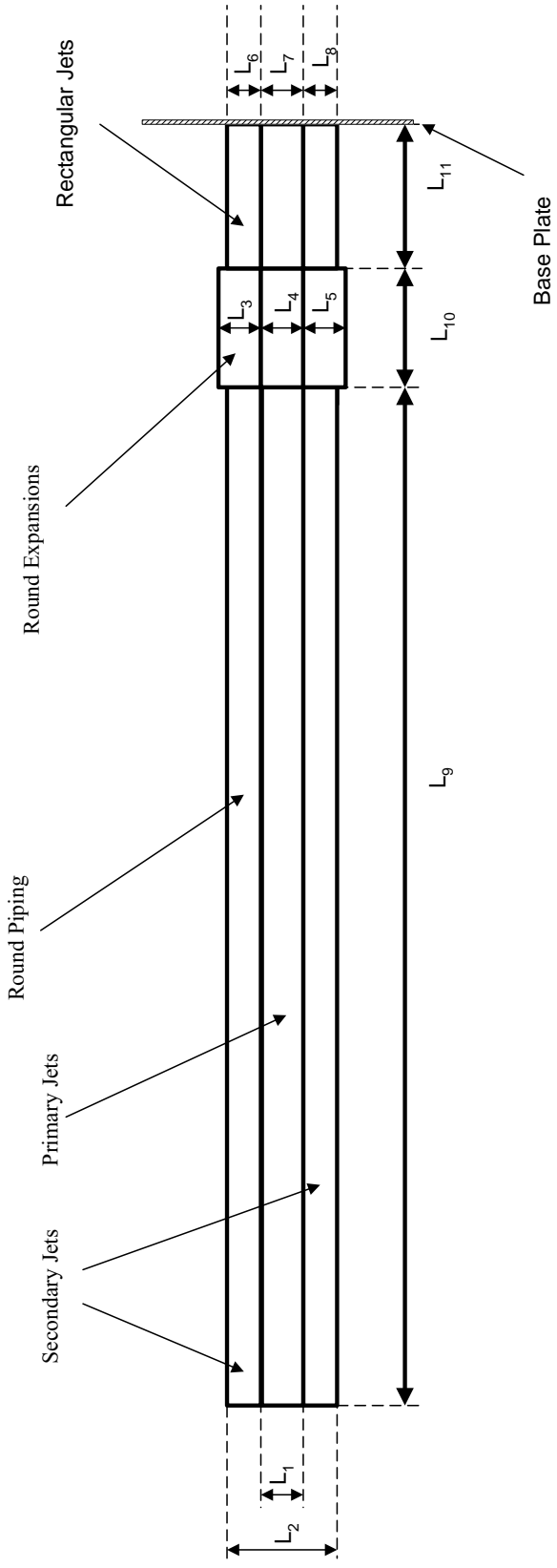


**Figure 3.8:** Schematic of side view of the rectangular jet system with associated characteristic lengths in Table 3.4.

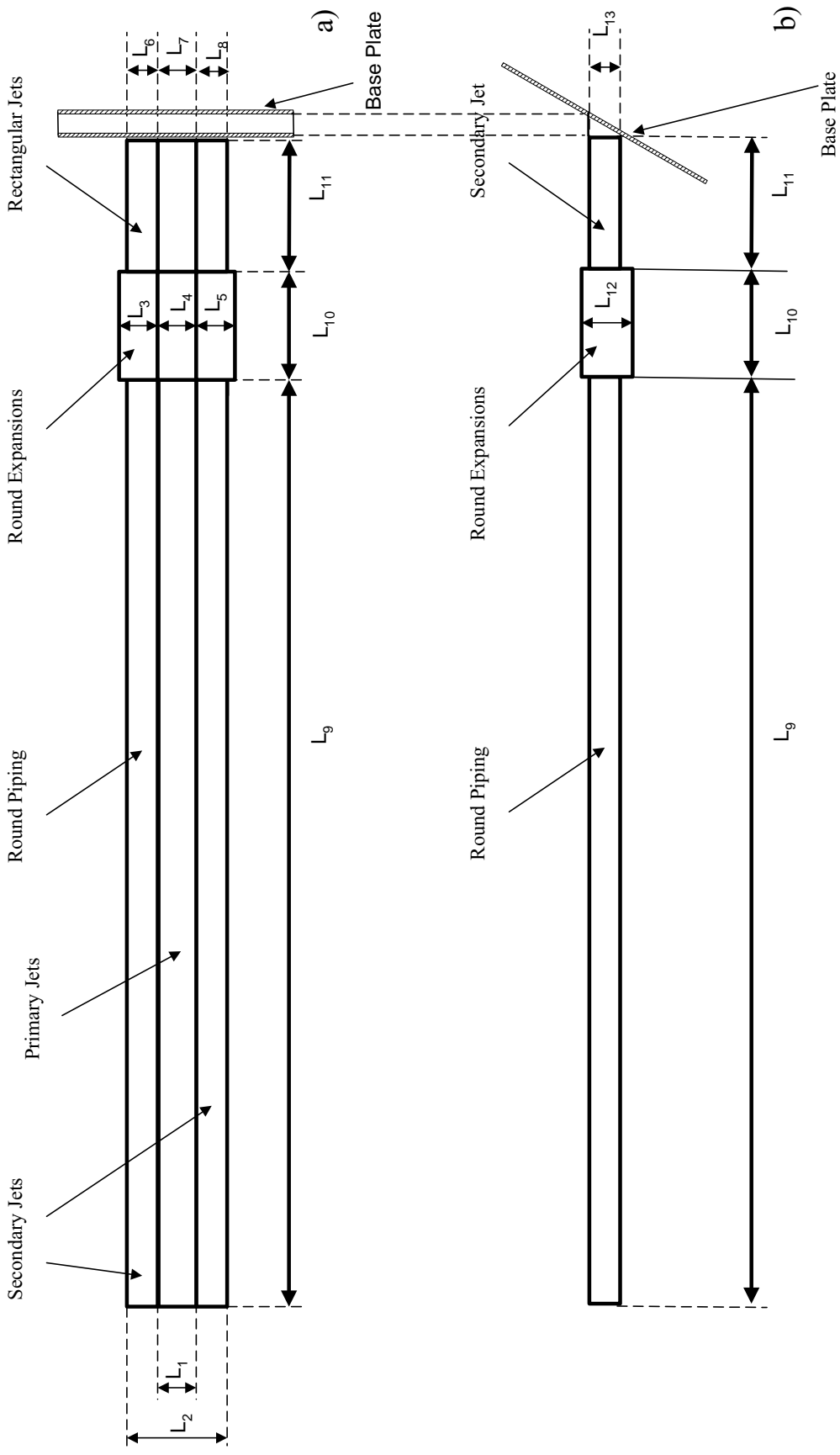


**Figure 3.9:** Schematic of side view of the rectangular jet system with base plate angled at 60 degrees, top view a), side view, b).



### 3.4.2 Conventional Jet Nozzles

Due to the large amount of experimental data available on the time averaged scalar characteristics for the round turbulent jet for a wide range of boundary conditions and Schmidt numbers, a 120 mm long and 15 mm internal diameter pipe jet was cut and used for validating the experimental technique. The edges of the pipe jet were slightly rounded off removing any exposed filaments that may effect the flow.

## 3.5 Isothermal Experiments

### 3.5.1 Selection of Diagnostic Techniques

#### 3.5.1.1 Invasive Techniques

Physical probing of gas fluid was one of the early techniques used in the 1950's to determine the scalar field of a jet, where the jet was marked with a tracer (e.g., Helium, Forstall and Shapiro, 1950) and sampled by physically inserting a probe into the stream and analysing it. This technique was time consuming, and the dimensions of the probe ensured very poor spatial resolution. Consequently alternatives were required.

Anemometry similarly requires physical probing of the flow field and senses changes in the temperature of a heated or cooled fluid as it mixes with ambient fluid at a different temperature. Measurement of temperature of a moving non reacting fluid as the working scalar is analogous to measuring concentration itself (Zen, 1958).

#### 3.5.1.2 Non-Invasive Techniques

Laser induced Fluorescence was initially introduced for spectroscopic studies and chemical analysis and has evolved into a powerful flow imaging technique with the potential to monitor concentration, temperature, pressure and velocity. The operating principle behind Laser induced fluorescence is the use of a laser beam to specifically excite a molecule, causing one of the

electrons orbiting on the most outer shell to jump to a higher orbital or energetic state. When the electron ‘relaxes’ and returns to a ground state, energy is released in the form of a ‘photon’. The emitted light is collected by an imaging device (photomultiplier) which generates an electrical current proportional to the amount of light fluoresced, which again is proportional to the concentration of fluid being excited.

The working principle of Mie scattering is very different to Laser induced fluorescence. However, similar experimental equipment is required in order to achieve results. A moving fluid is seeded with a fine emulsion of macroscopic particles which scatters a laser sheet. The scattered light is then captured by a charged coupled device or other optical detection systems. Mie scattering exploits the seeded scattering signals associated with large seed particles, much larger than those used in other scattering techniques such as Rayleigh scattering (Eckbreth, 1988). The scattered light is proportional to the amount of tracer in the fluid (Becker, 1977). Common markers used are dispersed droplets in air such as olive oil or water. The intensity of the scattered light depends on parameters such as droplet particle size, wavelength, the number of particles dispersed per unit volume and refractive index.

Rayleigh Scattering refers to the inelastic scattering of electromagnetic radiation (Pitts *et al.*, 1984) arising from the dipole moment associated with individual molecules and does not involve state to state transitions. Inelastic means that the molecule, after it has been excited by a light source, returns to its initial state and, because there is no energy exchange, the scattered light is at the same frequency as the incident light (Eckbreth, 1988). It also complements Mie scattering and occurs when a particle diameter of the tracing substance has a comparable diameter to the wavelength of the incident beam (Warnatz *et al.*, 1999).

Raman scattering is not only used to quantify mixing fields but is a powerful diagnostic tool for the identification and quantification of several species in a reacting flow. When monochromatic light passes through a flow field, the resulting scattering phenomena may involve elastic and inelastic interactions. The inelastic scattering is more commonly known as Raman scattering. The inelastic scattering is a result of the incident light causing an excited molecule not to return to its initial ground state but to a higher or lower ground state. The higher energy and frequency shift is more commonly known as anti Stokes lines and lower shift Stokes lines. The scattering may be termed to be vibrational or electronic depending on the nature of the energy exchange (Eckbreth, 1988). Figure 3.10 is a schematic of the Stokes and anti-Stokes Raman scattering

phenomena, where the virtual energy state is reached after electromagnetic radiation has either excited vibrationally or electronically (Eckbreth, 1988). The scattered light will have a different energy intensity and frequency; the former permits quantification of a particular species whilst the latter allows their identification.

Other less common non-intrusive techniques exist such as Laser polarisation or Coherent anti-Stokes Raman spectroscopy, but are relatively new and require specialised equipment. All of the above techniques require similar pieces of equipment, such as a laser, collection of optics, and a detector. Figure 3.11 is a schematic diagram of the signal strength of the four mentioned techniques when measuring a conserved scalar (Eckbreth, 1988). Higher signals mean high signal to noise ratios, and low influence of errors. Raman and Rayleigh scattering have low signal strength and require a high powered pulsing laser such as a Nd:Yg, with a synchronised camera (8 –12bit) with suitable gain control. The unavailability of a camera with gain control implied that the quality of the imaging would be poor with high-speed flows, hence water was selected as the working fluid. With the availability of a continuous wave Laser only, Laser Induced Fluorescence was the most suitable diagnostic candidate in order to measure scalar quantities in the flow.

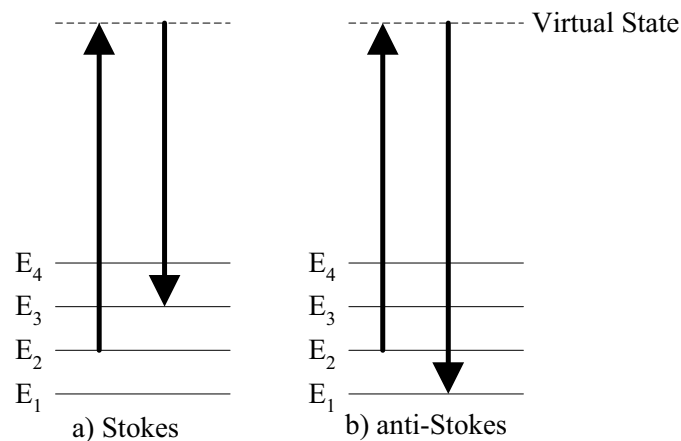


**Figure 3.10:** Illustration of the basic process involved in Stokes a) and anti-Stokes b) Raman scattering (Warnatz *et al.*, 1999).

NOTE: This figure is included on page 75 of the print copy of the thesis held in the University of Adelaide Library.

**Figure 3.11:** A comparison for different signal strength laser diagnostic Techniques (Eckbreth 1988).

### 3.5.1.3 Laser Induced Fluorescence Fundamentals

While laser induced Fluorescence was initially introduced for spectroscopy studies and chemical analysis (Skoog *et al.*, 1996) it has evolved into a powerful flow imaging technique with the potential to monitor concentration, temperature, pressure and velocity.

The operating principle behind Laser induced fluorescence is that an incident laser beam specifically excites a molecule and causes one of the external electrons of a specific atom to jump to a higher orbital or energetic state. When the electron ‘relaxes’ and returns to a ground state energy is released as a form of a ‘photon’ (Walker *et al.*, 1987). The intensity of the fluoresced signal is defined in Equation 3.5 (Hanson, 1986).

$$I_f = I_0 A \phi \varepsilon L C$$

**Equation 3.5**

where  $I_f$  is the fluorescent intensity,  $I_0$ , is the laser power along the beam path before it hits any excitable molecules.  $A$ , is the fraction of light collected.  $\phi$ , is the quantum yield of the fluorescence.  $\varepsilon$ , is the extinction coefficient of the excitable molecule.  $L$  is the length of the laser path and  $C$  is the concentration of excitable fluid.

The emitted light is collected by an imaging device which generates an electrical current proportional to the amount of light fluoresced, which again is proportional to the concentration of fluid being excited (Equation 3.5).

Laser induced fluorescence can be used with either water or air as the working fluids. The type of “excitable” fluid or marker used depends on the type of working fluid and laser (Walker *et al.*, 1987 and Karasso *et al.*, 1997a). The characteristics of the marker for LIF measurements must be adequately chosen; the marker must be stable, be small enough to follow the flow of fluid vortices of the smallest length scale and its absorption and fluorescence spectra must be able to be completely distinguishable.

The dye of choice was Di Sodium (or just Sodium) Fluorescein ( $C_{20}H_{10}O_5N_2$ , Arcoumanis *et al.*, 1990). Sodium Fluorescein is a water soluble compound, meaning that each particle will be of molecular size, hence being highly adequate for flow tracing. A problem with Fluorescein is that it may coalesce over time and hence reduce its fluorescent intensity (Arcoumanis *et al.*, 1990) and also varies with PH (Walker *et al.*, 1987). Alcohol may reduce the rate of coalescence but it also damages Perspex objects. Other more stable dyes do exist such as Rhodamine B and Rhodamine 6G, however these emit weaker signals (Arcoumanis *et al.*, 1990). For the purpose of this project the average residence time of the Fluorescein in aqueous solution is small enough to incur an acceptable error.

High fluorescent intensity is important especially when using continuous wave lasers as opposed to pulsed lasers. Even if most class 4 continuous wave lasers have the same energy output per unit time as pulsed systems, they cannot concentrate the power in a single pulse. The energy released from a pulsed beam is significantly higher and consequently an excitable medium will respond proportionally.

## 3.5.2 Experimental Apparatus

### 3.5.2.1 Water Tank

The nozzles were immersed vertically 600 mm into a 0.75x0.75x1.5 metre perspex water tank. Waves generated on top of the water tunnel had a minimal effect. The Perspex tank has an overflow at the top of the tank, so that in operation, a gentle counter current was generated. The overflow velocity estimate based on area is significantly less than that of the nozzles, hence the effect on the flow will be minimal. The primary and secondary jet fluids were supplied by two independent tanks of 150 litres each, and by two separate 0.5 hp single phase pumps. The flow

of the two streams were monitored and controlled by two Solartron Mobrey 2000 tube and float rotameters. Figure 3.12 shows a layout of the flow facility for the longitudinal investigation used in Chapter 4, with a laser beam orientated so that it symmetrically bisects the flow field. A camera placed normal to the visualised plane acts as the detection device. Figure 3.13 shows a layout of the transverse investigation in Chapter 6, where the laser sheet is orientated normal to the flow and traversed into position with a manual traverse. The fluoresced signal is then sent to a mirror below the tank angled at 45 degrees, which is then directed to a camera also sitting below the tank. The experimental facility was placed in a 25 m<sup>3</sup> tent which was fitted with Brushed Rockel, a light proof material which ensured that background light did not disturb the experiments.

A concentration of 0.1 mg/L was deemed suitable, as it gave a fluorescent signal of reasonable strength, and is well within the linearity limits, where fluorescent light emitted is proportional to dye concentration (Walker *et al.*, 1987), which is slightly higher than the 0.04 mg/L recommended by Arcoumanis *et al.*, (1990). Visual observations at 0.04 mg/L and 0.1 mg/L deemed the fluorescent signal from 0.04 mg/L as too weak.

### 3.5.2.2 Laser Source and Optics

A continuous laser beam was generated at a wavelength of 514 nm using an Argon Ion Laser (Coherent Series Innova 90 Ion Laser). The beam was then focussed into a fibre optic light guide with a 10 mm focussing lens with the fibre optic then placed on a 1500 mm manual traverse and then attached to a 40 mm diameter and an 80 mm focal length focussing lens. This causes the beam to converge. The beam is then passed through a concave lens with focal length of -25mm, causing the beam to diverge into a plane; the resultant is then passed through a convex lens where the thickness of the resultant plane is reduced. The expanded laser sheet had a focal length of 480mm, meaning that sheet thickness was at its thinnest 480 mm from the collection of optics (thickness measured to be 0.8 mm). It was imperative that the focal point of the lens be in line with the axis of the jet of interest, this ensuring that problems associated with probe resolution are kept at a minimum (Mi *et al.*, 2003). Co-linearity between the nozzle and laser sheet was obtained by vertically aligning the nozzle and the manual traverse and optics with a spirit level. Fine adjustments on the verticality of the nozzles was done with a Black and Decker vertical and horizontal laser level which estimates vertical and horizontal horizons with a

relative error of  $\pm 0.1$  degrees. The vertical alignment of the laser sheet was also adjusted with the Black and Decker laser level.

The detection systems for the longitudinal flow visualisation (Chapter 5) was a Sony DCR 8-bit camcorder, operating at maximum aperture, and shutter speeds varying between 30-125 ms according to the flow conditions. The collected footage was then used to retrieve time-averaged data. Instantaneous images were captured with a Canon E60 SLR camera operating at an aperture of 1.8, and shutter speeds between 50 and 150 ms. The Transverse flow visualisation (Appendix C) was imaged with a more powerful Phantom V4.1 camera, an 8 bit system which recorded footage directly to hard disk. The camera has a capability of recording up to 1000 frames per second, but capture rate was restricted to 50 frames per second at a shutter speed of  $1/50^{\text{th}}$  of a second, so that reasonable signal to noise ratios were obtained.

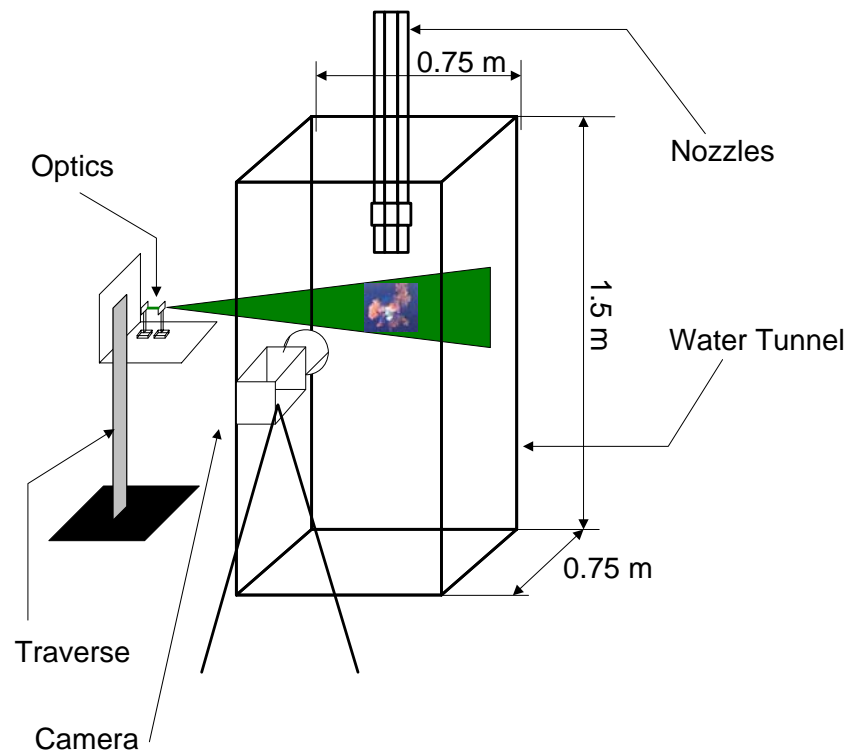


**Figure 3.12** Schematic diagram of experimental setup for longitudinal flow visualisation with rectangular nozzles vertically immersed into the water tunnel, optics orientated giving a vertical sheet with camera position at 90 degrees.

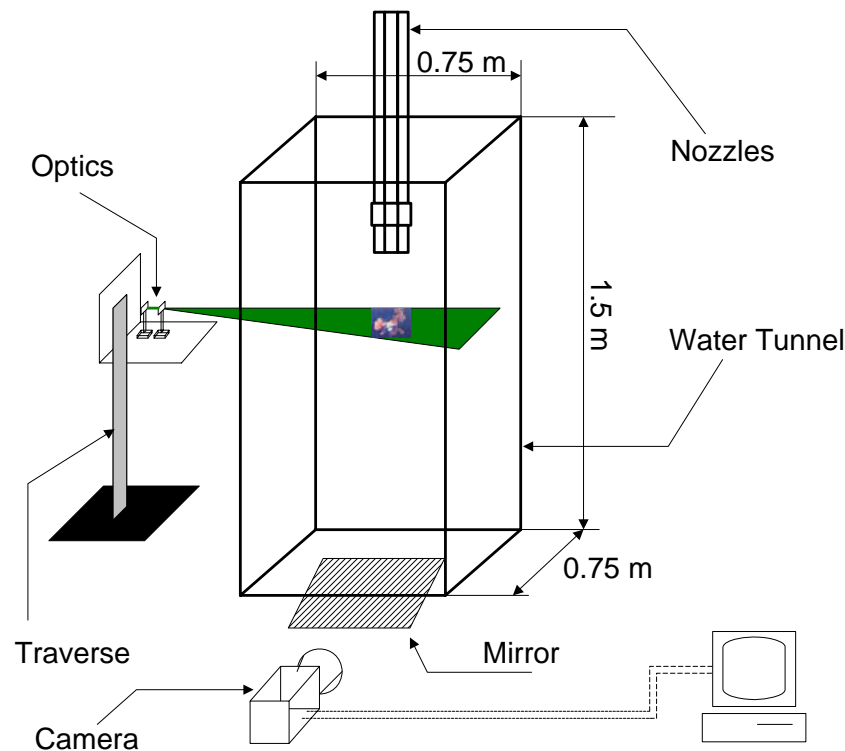


**Figure 3.13:** Schematic diagram of experimental setup for transverse flow visualisation with rectangular nozzles vertically immersed into the water tunnel, optics orientated giving a horizontal sheet delivering a fluorescent signal to a mirror below the tank positioned at 45 degrees to a camera positioned also below the tank.

### 3.5.3 Experimental Procedure

#### 3.5.3.1 Qualitative Measurements

The qualitative measurements reported in Chapter 4 using the experimental setup illustrated in Figure 3.12 consisted of exactly 40 experiments. Each experimental condition depended on which of the two streams were to be marked, laser orientation and velocity ratio. After every second experiment, the water tunnel was emptied and refilled to minimise a build up of background dye. The systematic procedure that was used is illustrated in Table 3.5;

#### 3.5.3.2 Quantitative Measurements

The quantitative measurements reported in Chapters 6 observed the experimental setup in Figure 3.13 consisted of 80 experiments. Before each experiment bubbles were manually removed from



sidewall where the incident laser beam entered the tank, so that as little obstruction as possible was achieved. Each axial position consisted of a block of experiments (10 experiments, primary and secondary seeded separately). This was important as it meant that the optics and camera settings would not need adjustment for each block of experiments. Two experiments at a time were performed before the tank was emptied out and refilled. After the completion of one block of experiments, background corrections for light intensity and fluorescent response were monitored for each axial position in order to perform quantitative data processing. The laser intensity was measured and maintained at 2.28 watts (2.4 watt max) with the laser in ‘light mode’ so that the current would automatically be adjusted to maintain a steady laser power. If the laser was no longer capable of maintaining the desired power, a red light would appear. If so, the experiment was to be halted and repeated at the desired output. More detail on the experimental methodology on the quantitative PLIF technique is given in Chapter 5.

<b>Step</b>	<b>Description</b>
<b>1</b>	The jet was positioned and aligned with the centre of the water tunnel, making such that it was exactly 90 degrees with the horizon. This was achieved firstly with a conventional spirit level and refined with a Black and Decker laser level.
<b>2</b>	The laser sheet was aligned with the geometric axis of the jet and positioned so that the focal point coincided with the jet centreline. The laser sheet traversing system and sheet had to be adjusted with levels so that the laser sheet was completely vertical.
<b>3</b>	The camera focus was adjusted with the lights still on and the laser off.
<b>4</b>	The lights were switched off and the laser switched on and a small amount of flow from the marked stream was released into the tank so that focus and zoom may be further adjusted.
<b>5</b>	The room was re checked for complete darkness, the laser power maximised and experiments commenced. The duration of each experiment was approximately 30 seconds.

**Table 3.5:** Experimental Procedure for the Qualitative Investigation.

# Chapter 4

## 4 Qualitative Longitudinal Flow Visualisation

### 4.1 Introduction

In combustion applications secondary flows and co-flows are commonly used to supply combustion air, to stabilize flames and to alter flame characteristics. The spacing (gap) between co-flowing streams ('bluff bodies') also influence the flow characteristics. Most research on bluff body flows has been performed on axisymmetric devices. Whilst different to the present rectangular arrangement, they provide some important insights. The nature of the current rectangular jets is different to other multiple rectangular jets in the literature; because of the different aspect ratio between the primary and secondary jets and the small bluff body between them.

In the more commonly used co-annular systems the presence of a bluff body between the central primary and outer secondary streams induces re-circulation. Initiated upstream from the recirculation zone the shear layer of the central jet separates from a bluff body. The annular jet then induces a second vortex slightly upstream from the nozzle exit plane, rotating in the opposite direction (Namazian and Kelly 1992). The nature of the recirculation region is dependant on the fluid-dynamic characteristics of the flow, particularly the velocity ratio and momentum ratios. Namazian and Kelly (1992) found that, for a higher ratio of central to annular jet velocity, the central jet had sufficient momentum to penetrate the re-circulation region and somewhat suppress it. Lower ratios of central to annular velocity result in the re-circulation region gaining strength and dictating the near nozzle region flow structure. Varying central to annular velocity ratio can be used to influence the flame shape and lift-off height in co-annular burners (Lin and Faeth, 1999, Li and Tankin 1987) and has many industrial implications, such as altering the heat release profiles and the production of thermal pollutants such as  $\text{No}_x$  (Chen and Driscoll, 1990).

These studies can identify time and length scales as well as directional observations of the larger scale motions (Pascheriet *et al.*,1992).

Planar Laser Induced Fluorescence (PLIF) is a powerful flow visualising tool and has been used by a wide range of researchers. For example, Yoda and Fielder (1996) performed flow visualisation experiments using PLIF to investigate a round turbulent jet in a counter flow. Dahm and Dimotakis (1987) used a similar technique to study the role of large scale structures in the mixing and entrainment process of an axisymmetric free turbulent jet.

Parham *et al.*, (1998,2000) and Newbold *et al.*, (1996) have used this technique for a qualitative study of the fluid-dynamic behaviour of precessing jet flow. The objective of the flow visualisation study in this chapter is to determine the differences in flow features and structure caused by an increase in secondary flow. These complement the quantitative assessment in Chapter 6.

## 4.2 Experimental Conditions

The details of the nozzles and apparatus are described in section 3.4. It is important to establish which planes are to be visualised and which streams to be marked. The planes to be investigated were three; one being the minor axis bisecting primary and secondary jets (Plane A) and the others being the major axes of the primary (Plane C) and secondary (Plane B) jets. Figure 4.1 is a schematic diagram of the planes of visualised flow, which are similar to those used by Perry and Pleasance (1983a; 1983b) and Mullinger *et al.*, (2002).

The velocity of the primary jet was set to maintain a Reynolds number of 10,000, the flow rate through the secondary jets were varied to provide the velocity ratios. This resulted in the Reynolds number of the secondary jet varying between 3720 and 24,928 (Table 3.3). The operating velocity ratios of the jets in the boilers have been determined in section 3.3.2.

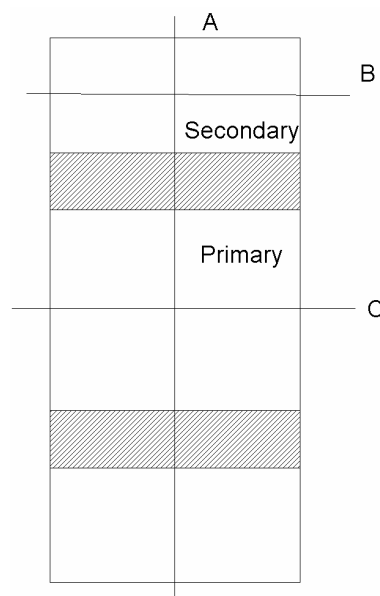
As stated in Section 3.3.1, in the industrial application, the projected distance of the rectangular jets from inside the recess to the other side of the boiler is approximately 12 nozzle diameters, although the notion of free jets is no longer valid for approximately  $x/D > 5-6$ .

The laser sheet at its focal point (ie at its thinnest), is 182 mm wide meaning that only 6.12 nozzle diameters are imaged at one time. Consequently the sheet must be traversed down at least another 182 mm, in order to visualise up to 12 nozzle diameters.

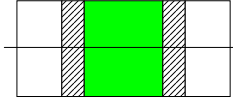
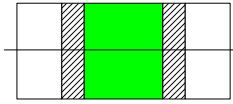
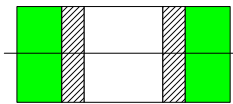
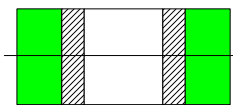
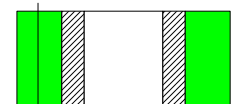
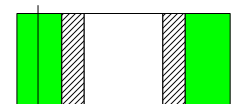
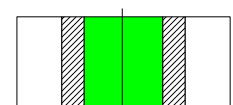
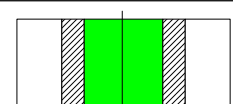
Either the primary or both secondary jets could be seeded with Sodium Fluorescein. Table 4.1 is a full summary of the experimental conditions depicting the conditions of which flows were seeded with which velocity ratio and laser orientation.

The secondary to primary momentum flux ratio,  $\gamma$  and momentum ratio  $\kappa$ , are directly related to the velocity ratio in the present study since a fixed working fluid of constant density was used. Table 4.2 shows the momentum flux and momentum ratios of the experimental conditions.

The lower resolution sequential images were recorded with a 12-bit Sony digital video camcorder delivering an image of 720\*576 pixels and the high resolution still images were captured with a Canon E60 SLR camera which delivered an image resolution of 3072\*2048 pixels.



**Figure 4.1** Generic Laser Orientation and Nomenclature of Plane of Visualised Flow.

Dye and Laser Orientation	$x/D$	Secondary to Primary velocity ratio, ( $\lambda$ )
	$0 < x/D < 6.12$	0, 0.55, 1.4, 2.8, 3.6
	$6.12 < x/D < 12.24$	0, 0.55, 1.4, 2.8, 3.6
	$0 < x/D < 6.12$	0, 0.55, 1.4, 2.8, 3.6
	$6.12 < x/D < 12.24$	0, 0.55, 1.4, 2.8, 3.6
	$0 < x/D < 6.12$	0.55, 1.4, 2.8, 3.6, $\infty$
	$6.12 < x/D < 12.24$	0.55, 1.4, 2.8, 3.6, $\infty$
	$0 < x/D < 6.12$	0, 0.55, 1.4, 2.8, 3.6
	$6.12 < x/D < 12.24$	0, 0.55, 1.4, 2.8, 3.6

**Table 4.1:** Laser orientation and marked stream, the shaded green indicates the marking of either the primary or secondary jet, the horizontal or vertical line highlights the laser orientation.

Velocity Ratio, $\lambda$	Momentum Flux ratio, $\gamma$	Momentum ratio, $\kappa$
0	0	0
0.55	0.30	0.1815
1.4	1.96	1.176
2.8	7.84	4.704
3.6	12.96	7.776

**Table 4.2:** The calculated Momentum Flux and Momentum ratios for each experimental velocity ratio.

### 4.3 Flow Visualisation Results

Video images presented in the following sections were extracted using the image processing toolbox and movie reading function in Matlab version 6.5 (Mathworks, 2004). For images with poor definition the contrast was increased digitally to improve clarity.

#### 4.3.1 Primary Jet

Figures 4.2 to 4.11 present sequences of video images of the primary jet at time intervals of 0.08 seconds with the laser aligned to pass through the axis of all three jets (Plane A) for  $0 < x/D < 6$  and  $6 < x/D < 12$  respectively. Velocity ratios of 0, 0.55, 1.4, 2.8 and 3.6 are illustrated. Figures 4.23 to 4.32 present video sequences of the primary jet through plane C under the same conditions. High-resolution instantaneous images of the primary jet through planes A and C are presented in Figures 4.12-16 and 4.33-4.37 respectively.

##### 4.3.1.1 Plane A

The primary jet operating alone ( $\lambda=0$ ) is visualised in Figure 4.2 and at higher resolution in Figure 4.12. Small scale structures in the shear layer appear at about 1 diameter downstream from the nozzle exit. These structures are dominated by velocity fluctuations and are enhanced by sharp corners (Toyoda and Hussein, 1989 and Schadow *et al.*, 1988). Larger scale structures more commonly known as ‘rings’ typically play a major role in the growth of the shear layer, and hereby appear between 4 and 5 diameters downstream (Gutmark and Grinstein, 1999). Large scale motions in turbulent flow for unexcited and excited round jets have been examined by Dimotakis *et al.*, (1983) and identified the large scale structure to move in a helical motion. Yoda *et al.*, (1994) repeated Dimotakis’s experiments and failed to detect the helical motion and stated that the large scale structures moved in a ‘zig-zig’ or ‘sinuous’ motion. The flow visualisation experiments in this chapter do not identify whether the trajectories of the large-scale flow structures are helical, but sinuous motion of some form are present in the flows.

An interpretation of this sinuous motion in the primary jet between  $6.12 < x/D < 12.24$  (Figure 4.3) is highlighted with a white line. The sinuous motion is easily identified in Figure 4.3 because growth of the coherent motions through entrainment and increasing the size of the shear layer causes structures to increase in size and slow down, making them easier to distinguish and track. This phenomena is also caused by the presence of the braids in the ring structure and appear between each deformation and interact with the shear layer to expel jet fluid through the plane A (minor axis) causing the jet to expand (Hart, 2004, Gutmark and Grinstien, 1999).

In the time sequenced images for  $\lambda=0.55$ , (Figures 4.4.and 4.5) and the high-resolution instantaneous image in Figure 4.13, it is evident that the presence of the secondary jet causes a deformation of the structures in the shear layer, inhibiting or distorting their development. The white lines in Figure 4.5 again show the sinuous motion of the main jet structure and  $A$  is the amplitude of the sinusoidal wave and  $l$  the wavelength. When white lines representing the sinuous motion in Figures 4.5, 4.7, 4.9 and 4.11 are compared with Figure 4.3, the amplitude and the oscillation of the structure appears to have changed. These images show that even a velocity ratio of  $\lambda=0.55$  and a momentum ratio of  $\gamma=0.3$ , is sufficient to distort the coherent motions, including presumably the ring structure. Although the maximum and minimum values of  $A$  and  $l$  are time dependant (varying from frame to frame) observations suggest that they also vary with velocity ratio. Greater differences between the maximum and minimum values of  $A$  and  $l$  results in a more unstable flow.

Stronger effects of the higher secondary velocity become more apparent for  $\lambda=1.4$  ( $\gamma=1.96$ ,  $\kappa=1.18$ ) illustrated in Figures 4.6 and 4.7 and the increased momentum of the secondary jet alters the large structures in the primary jet from about  $x/D=4$  in Figure 4.6 and 4.14, similarly further downstream (Figure 4.7) greater cross-stream motion in the  $y$ -direction of the larger structures is observed. The white lines in Figure 4.7 highlights the sinuous motion of the main structure of the primary jet, with larger fluctuations of the value of the maximum and minimum values of  $A$  with respect to Figure 4.5,  $\lambda=0.55$  (justifying the greater cross-stream motion in the  $y$ -direction). Larger fluctuations of maximum and minimum values of  $l$  in Figure 4.7 are also observed, indicating that a higher velocity ratio is increasing the main structure to flap in the  $x$ -direction.

The time sequenced images in Figures 4.8 to 4.11 and the high resolution instantaneous images in Figures 4.15 and 4.16 show that there is a clear change in near and far field flow structures as the velocity ratio is raised to 2.8 and 3.6 ( $\gamma=7.84$  &  $12.96$ ,  $\kappa=4.7$  &  $7.8$ ). The once orderly

structure observed for  $\lambda = 0$  and 0.55 is no-longer present as more intense fine scale mixing is observed at higher velocity ratios. The main primary structures as seen in Figures 4.15 and 4.16 decreases in size with increasing secondary velocity. In longer time sequences than are shown here it has also been observed that the frequency of flapping of the primary jet increases with increasing  $\lambda$ . The observed sinuous motions in Figures 4.9 and 4.11 ( $\lambda=2.8$  and 3.6) show that the amplitudes  $A$  and the wavelengths  $l$  for both cases  $\lambda=2.8$  and 3.6, show greater fluctuations when compared to the sinuous motions in Figure 4.7 at  $\lambda=1.4$ . This observation concludes that coherent motion of the main structure of the primary jet is heavily influenced by velocity of the secondary jet. Figure 4.17 reports the values of  $l/D$  and  $A/D$  versus velocity ratio, where  $l$  and  $A$  were taken over ten frames and then averaged. The amplitude of the sinuous movement of the main coherent flow structure increases with  $\lambda$  to eventually maximise at  $\lambda=2.8$ . The wavelength of the sinuous motion shows two increases to a first maximum at  $\lambda=0.55$  and drops at  $\lambda=1.4$  to increase at  $\lambda=2.8$  and thereafter.

The effects of the bluff body are more evident for  $\lambda = 2.8$  and 3.6 than for  $\lambda=0, 0.55$  and 1.4. Here they exert a significant effect on the flow structure of the shear layer in the near nozzle region around  $x/D < 1$ . It can be deduced that the region downstream from the bluff-body has developed a low-pressure region causing entrained fluid (which is not dyed) to re-circulate. This characteristic is present in steady turbulent flows behind bluff bodies such as plates or cylinders. The streamline representation of the time-averaged steady flow behind a bluff body is well-represented by Oertel (1990) where the wake region of a blunt plate (similar to the bluff body between the primary and secondary jets) is depicted by two zones of recirculation rotating in opposite directions. Figure 4.18 presents an analogous time-averaged diagram of the deduced re-circulation behind the bluff body between the primary and secondary jets. The nature of the re-circulation is heavily dependant on velocity ratio. For  $\lambda=1$ , two equally acting and counter acting zones of re-circulation can be expected to form in the wake region. For  $\lambda < 1$ , where the velocity of the primary jet is greater, the length scale of the re-circulation on the primary jet side is greater than on the secondary side, causing the whole wake area to deviate from the geometric axis. Conversely for  $\lambda > 1$  the re-circulation zone on the secondary jet side is larger and deviates the wake region in the opposite direction.

Another schematic representation of the large scale coherent structures in the primary jet are illustrated in Figure 4.19. These diagrams are based on the large scale coherent motion representation for round jets by Dahm and Dimotakis (1987). Using this representation, three



diagrams are representative of the 5 experimental conditions because it was concluded from the instantaneous analysis that the qualitative features in the flow are similar for all cases for  $\lambda > 1.4$ . The distance between each structure is a function of the equivalent diameter, the general shape of the structures change, from a sharp conical form to a broader rounded structure, as  $\lambda$  is increased. For  $\lambda = 0$  the typical spacing between successive structures is  $\alpha/D$  (where  $\alpha$  is a “constant” of proportionality). When the secondary flow is introduced at  $\lambda = 0.55$ , the spacing between structures causes  $\alpha$  to reduce and further reduction is observed between  $\lambda = 1.4$  to  $3.6$ . Figure 4.20 is an averaged measurement (over ten frames) of  $\alpha/D$  versus  $\lambda$ , illustrating how higher secondary jet co-flow ratios shorten the spacing between coherent structures.

The nature of the coherent structures on the edge of the shear layer also changes with  $\lambda$ . Specifically, changes in the shear layer especially in the near nozzle region may also affect the entrainment mechanisms and consequently the amount of fluid entrained into the primary or secondary jet. Figure 4.21 is a schematic depiction of the nature of the intermediate structures in the shear layer for velocity ratios of 0 to 0.55, 1.4 and 2.8 to 3.6. The structures in the shear layer at  $\lambda = 0$  in Figure 4.21a) order themselves outwards from the bulk jet flow, anti-clockwise on the left hand side and clockwise on the right hand side. However, for  $\lambda = 0.55$ -1.4 (Figure 4.21b) the structures re-align themselves facing the opposite directions due to the higher external velocity exerted by the secondary jet. For higher velocity ratios such as  $\lambda = 2.8$ –3.6, the eddies with a length scale similar to the spacing between primary and secondary jets appear at about  $x/D = 0.8$ . Figure 4.21c) is a diagram of the relatively larger eddies in proximity to the nozzle which appears at  $\lambda = 2.8$ -3.6.

The nature of the shear layer determines the mechanisms of entrainment. Using the same sketching principle as Mungal and Hollingsworth (1989) Figures 4.22a) and 4.22b) are illustrations of the instantaneous and time-averaged entrainment mechanisms into the primary jet for  $\lambda = 0$ -0.55 and  $\lambda = 1.4$ -3.6 respectively. For  $\lambda = 0$ -0.55 the orientation of the streamlines shown in Figure 4.22a) show how the structures in the shear layer convolute so that part of the primary fluid is entrained into the primary jet and the rest being re-circulated by the shear layer. For  $\lambda = 1.4$ -3.6 in Figure 4.22b) the streamlines show how the fluid in the primary jet shear layer is being re-directed into the direction of the secondary jets to accommodate its higher appetite for entrainment.

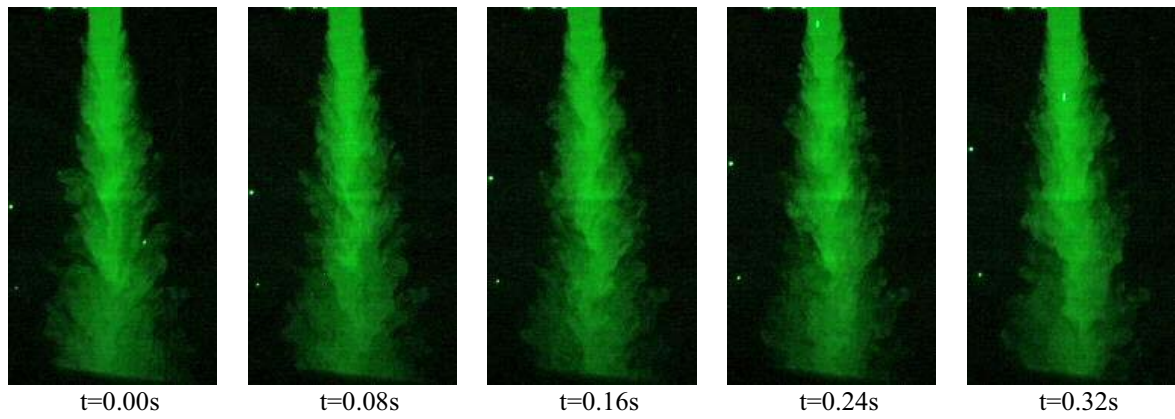


**Figure 4.2:** Video images of the primary jet at 0.08 second intervals with the laser orientated through Plane A. Velocity ratio is  $\lambda=0$ , flow region is  $0 < x/D < 6$ .

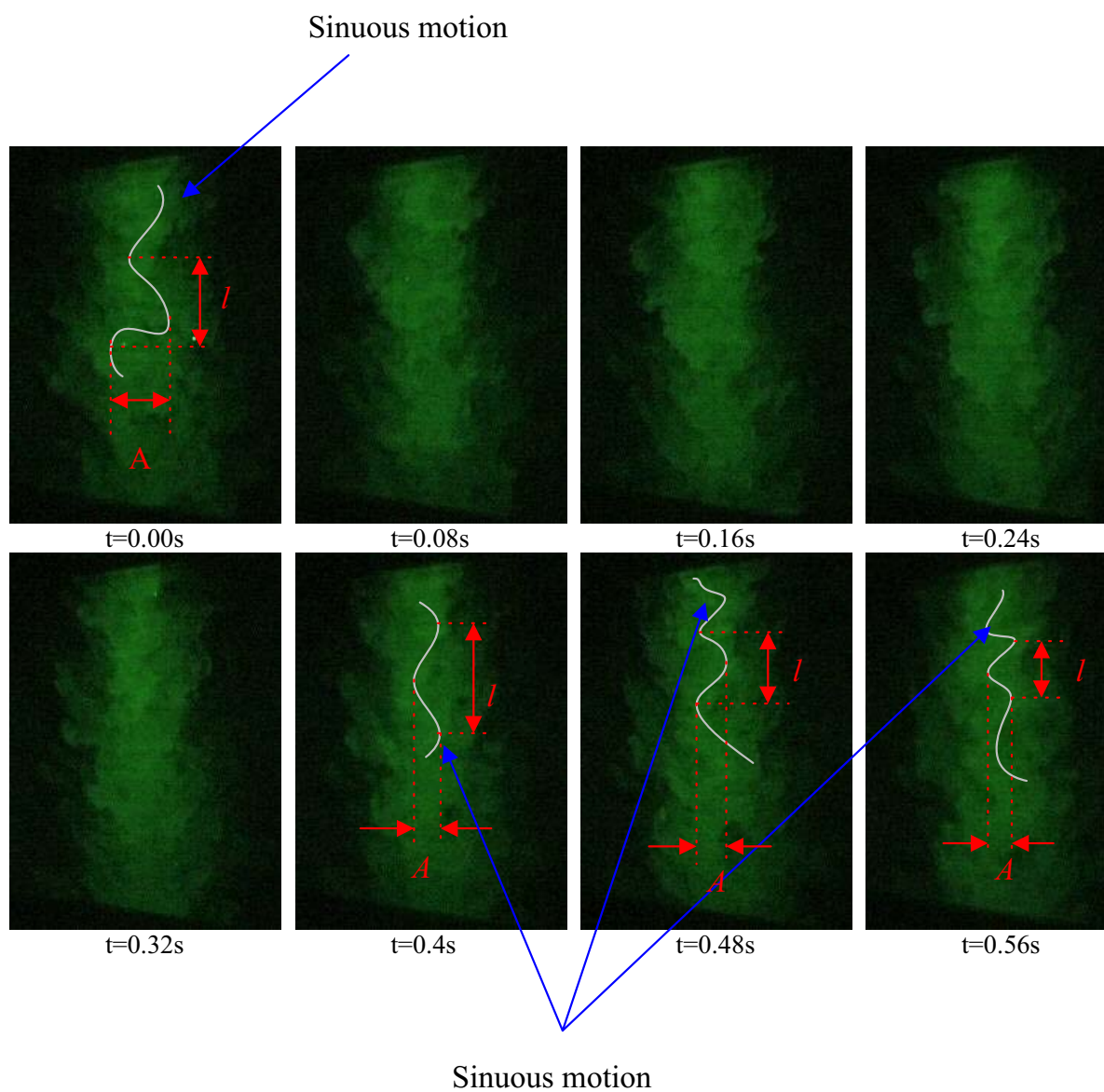


**Figure 4.3:** Video images of the primary jet at 0.08 second intervals with the laser orientated through Plane A. Velocity ratio is  $\lambda=0$ , flow region is  $6 < x/D < 12$ . The white lines highlight the sinuous motion of the main coherent structure,  $A$  an estimate of the amplitude and  $l$ , an estimate of the wavelength.

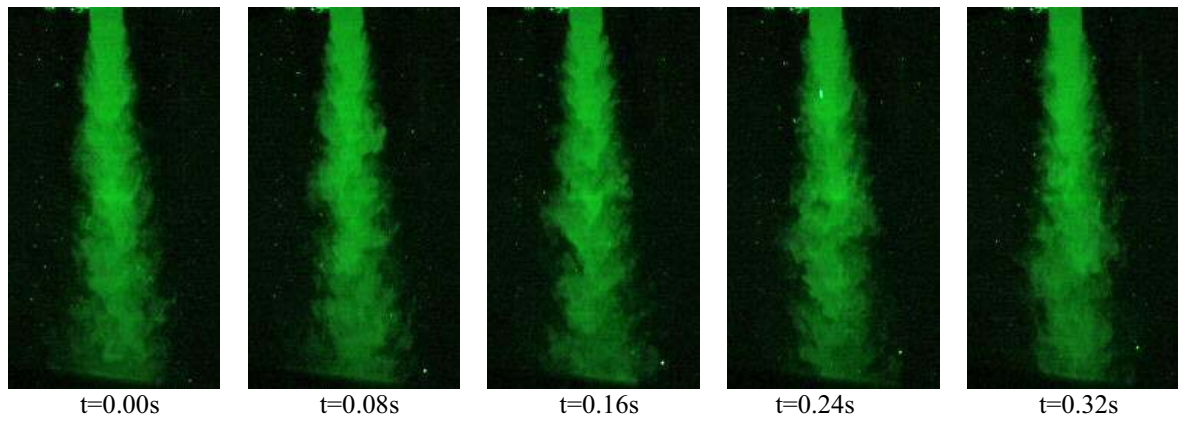


**Figure 4.4:** Video images of the primary jet at 0.08 second intervals with the laser orientated through Plane A. Velocity ratio is  $\lambda=0.55$ , flow region is  $0 < x/D < 6$ .

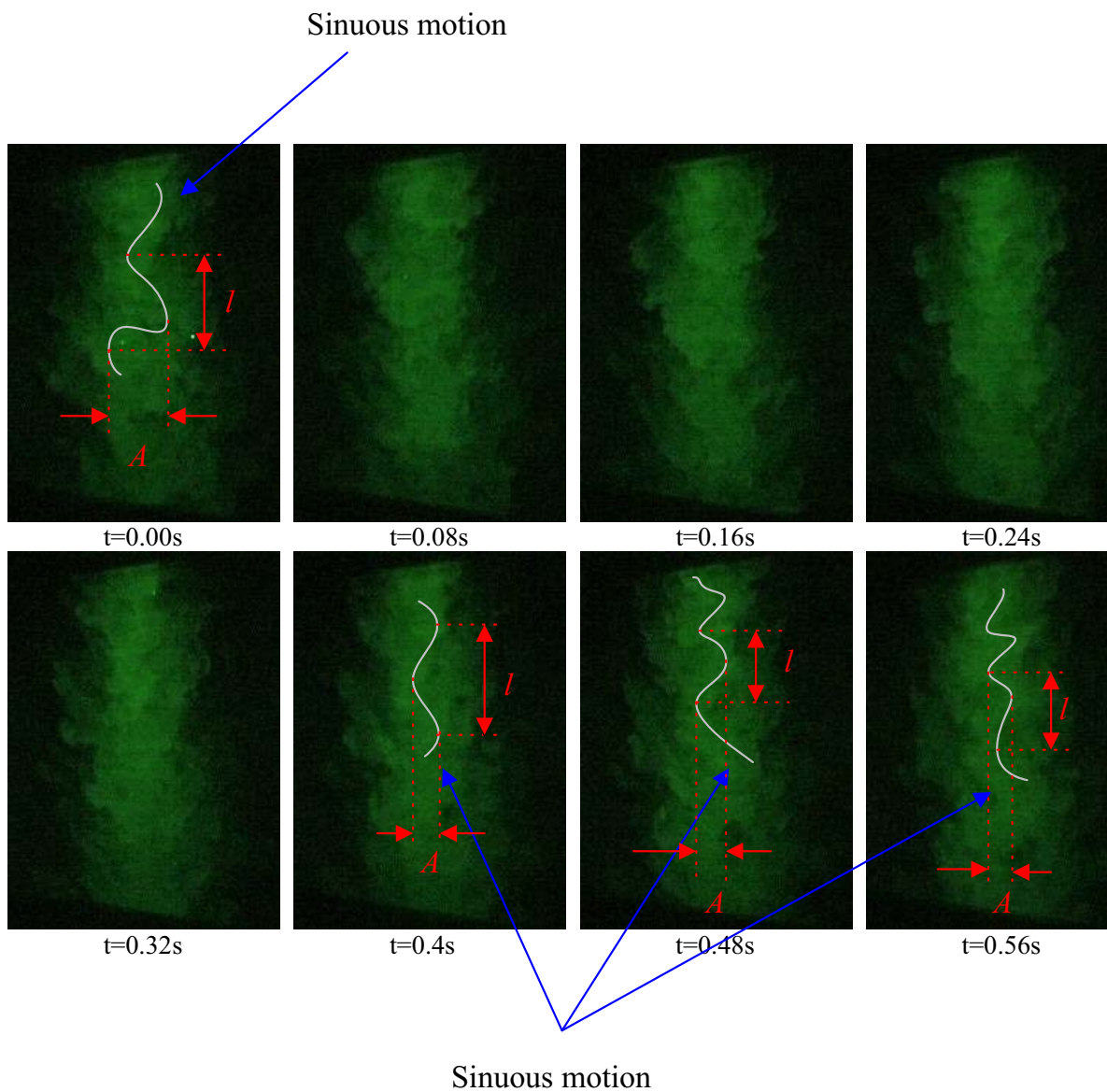


**Figure 4.5:** Video images of the primary jet at 0.08 second intervals with the laser orientated through Plane A. Velocity ratio is  $\lambda=0.55$ , flow region is  $6 < x/D < 12$ . The white lines highlight the sinuous motion of the main coherent structure,  $A$  an estimate of the amplitude and  $l$ , an estimate of the wavelength.

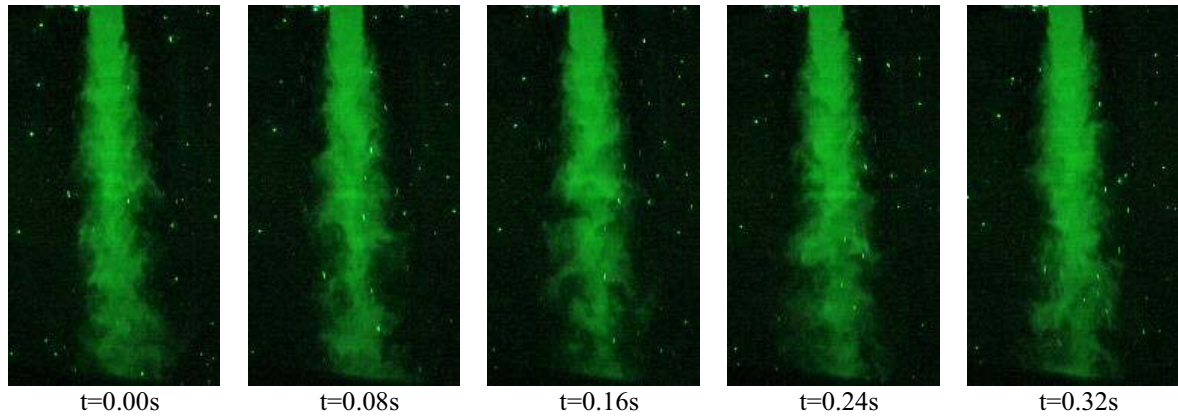


**Figure 4.6:** Video images of the primary jet at 0.08 second intervals with the laser orientated through Plane A. Velocity ratio is  $\lambda=1.4$ , flow region is  $0 < x/D < 6$ .

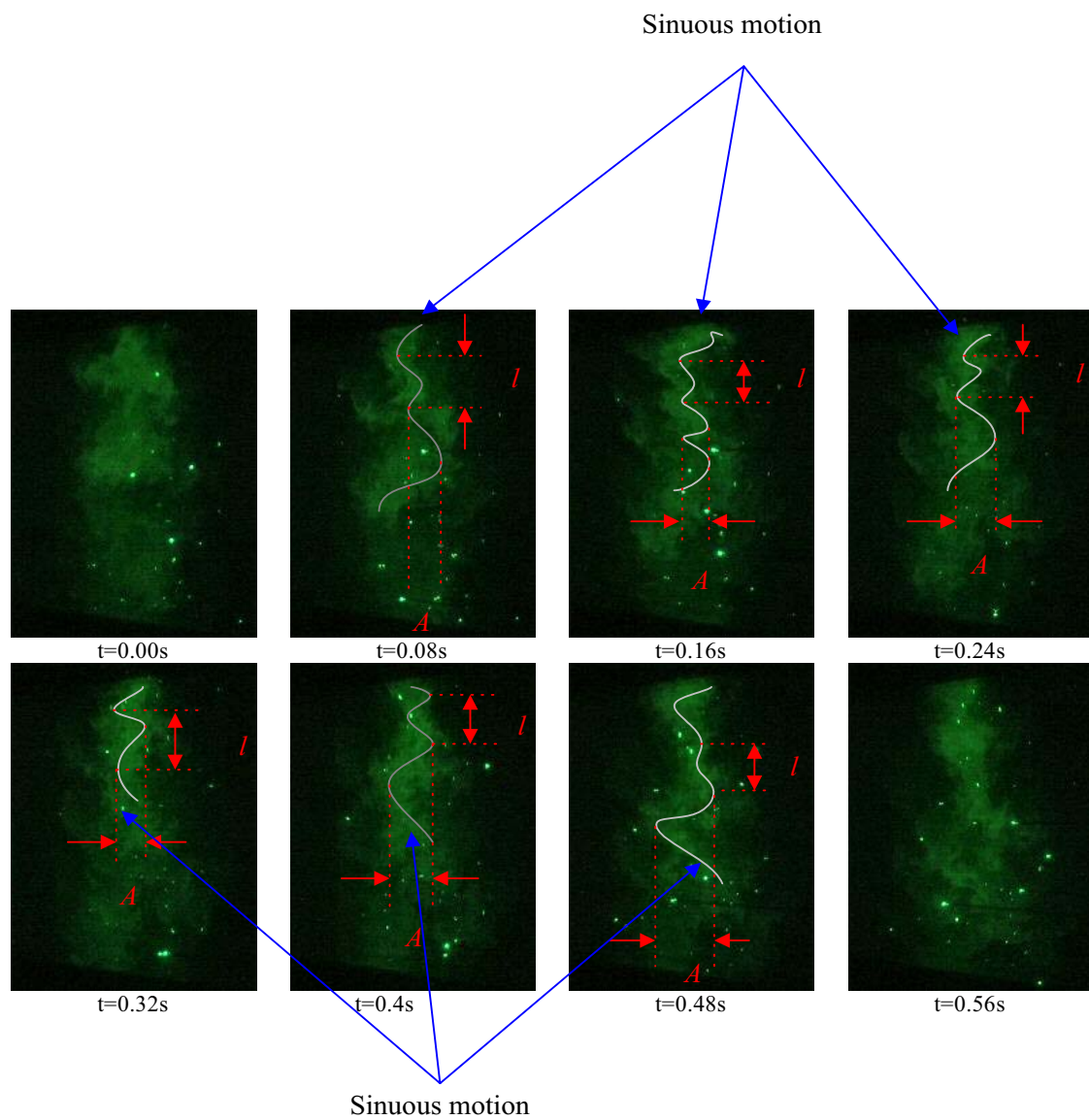


**Figure 4.7:** Video images of the primary jet at 0.08 second intervals with the laser orientated through Plane A. Velocity ratio is  $\lambda=1.4$ , flow region is  $6 < x/D < 12$ . The white lines highlight the sinuous motion of the main coherent structure,  $A$  an estimate of the amplitude and  $l$ , an estimate of the wavelength.

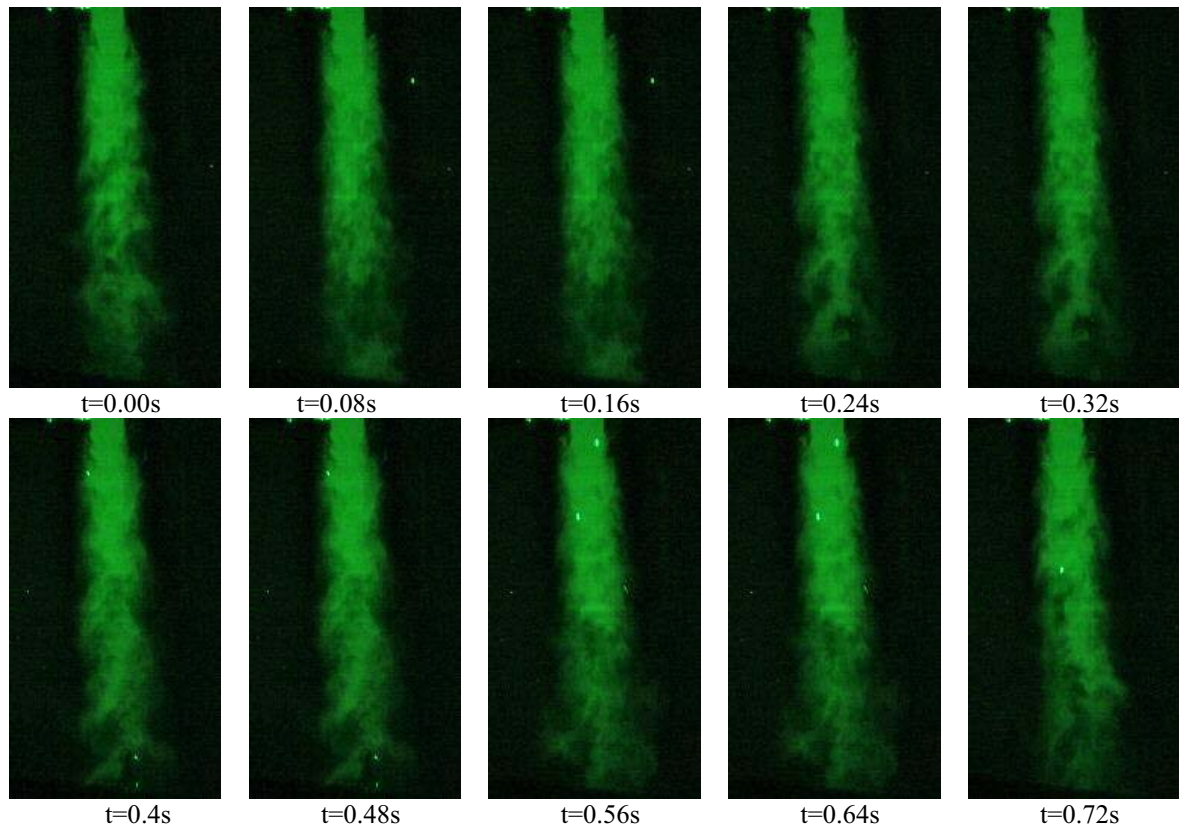


**Figure 4.8:** Video images of the primary jet at 0.08 second intervals with the laser orientated through Plane A. Velocity ratio is  $\lambda=2.8$ , flow region is  $0 < x/D < 6$ .

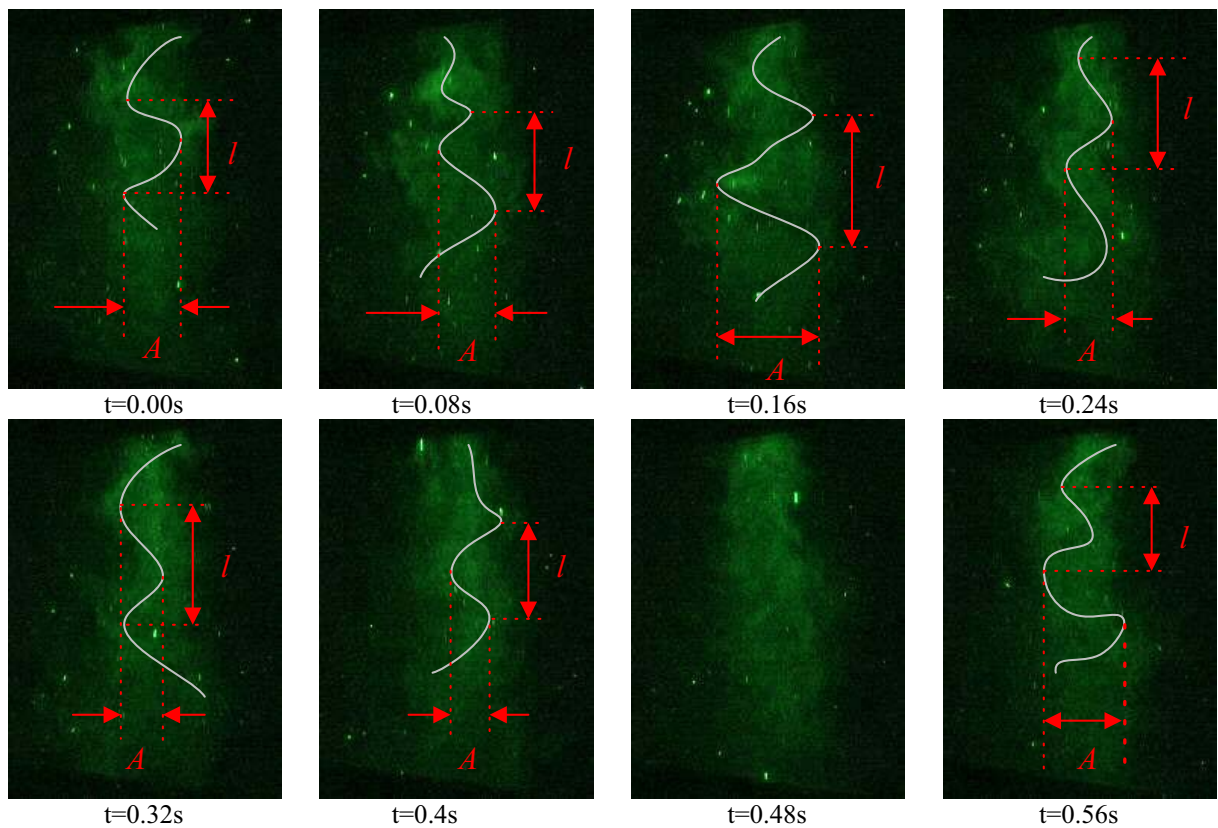


**Figure 4.9:** Video images of the primary jet at 0.08 second intervals with the laser orientated through Plane A. Velocity ratio is  $\lambda=2.8$ , flow region is  $6 < x/D < 12$ . The white lines highlight the sinuous motion of the main coherent structure,  $A$  an estimate of the amplitude and  $l$ , an estimate of the wavelength.

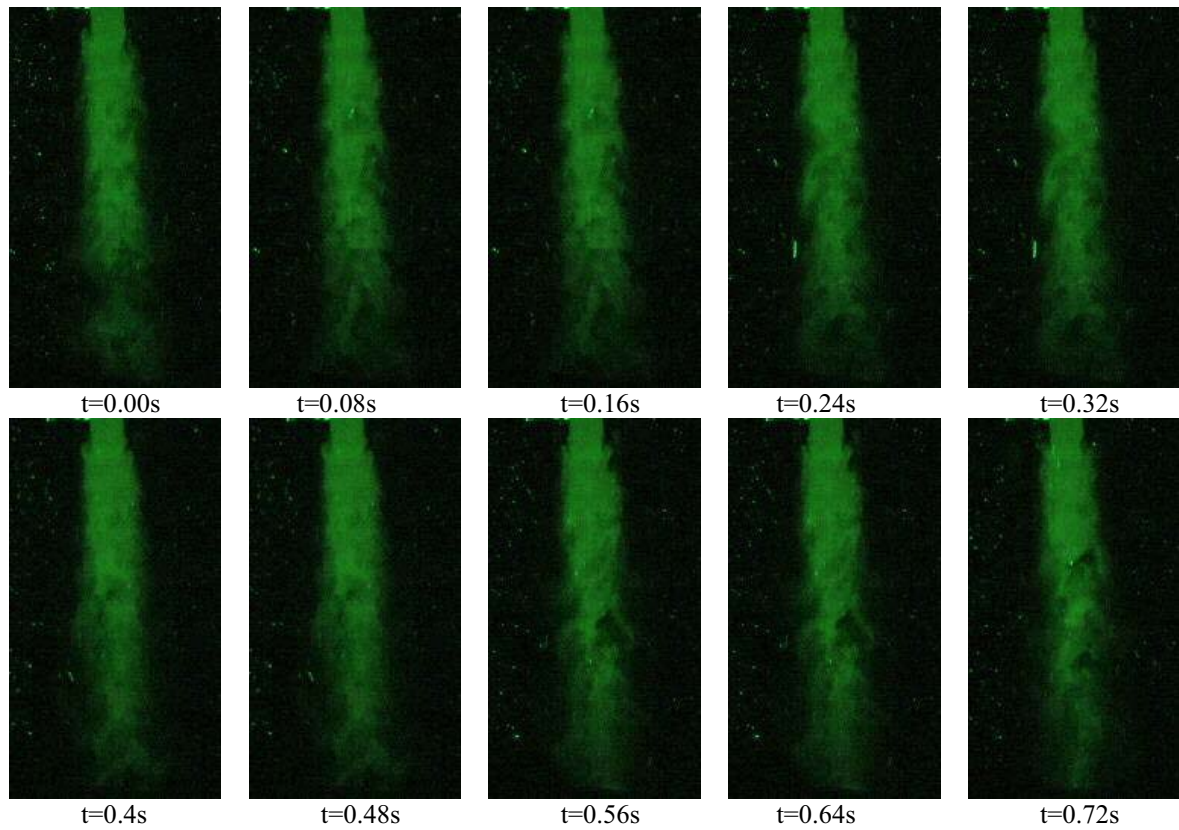


**Figure 4.10:** Video images of the primary jet at 0.08 second intervals with the laser orientated through Plane A. Velocity ratio is  $\lambda=3.6$ , flow region is  $0 < x/D < 6$ .

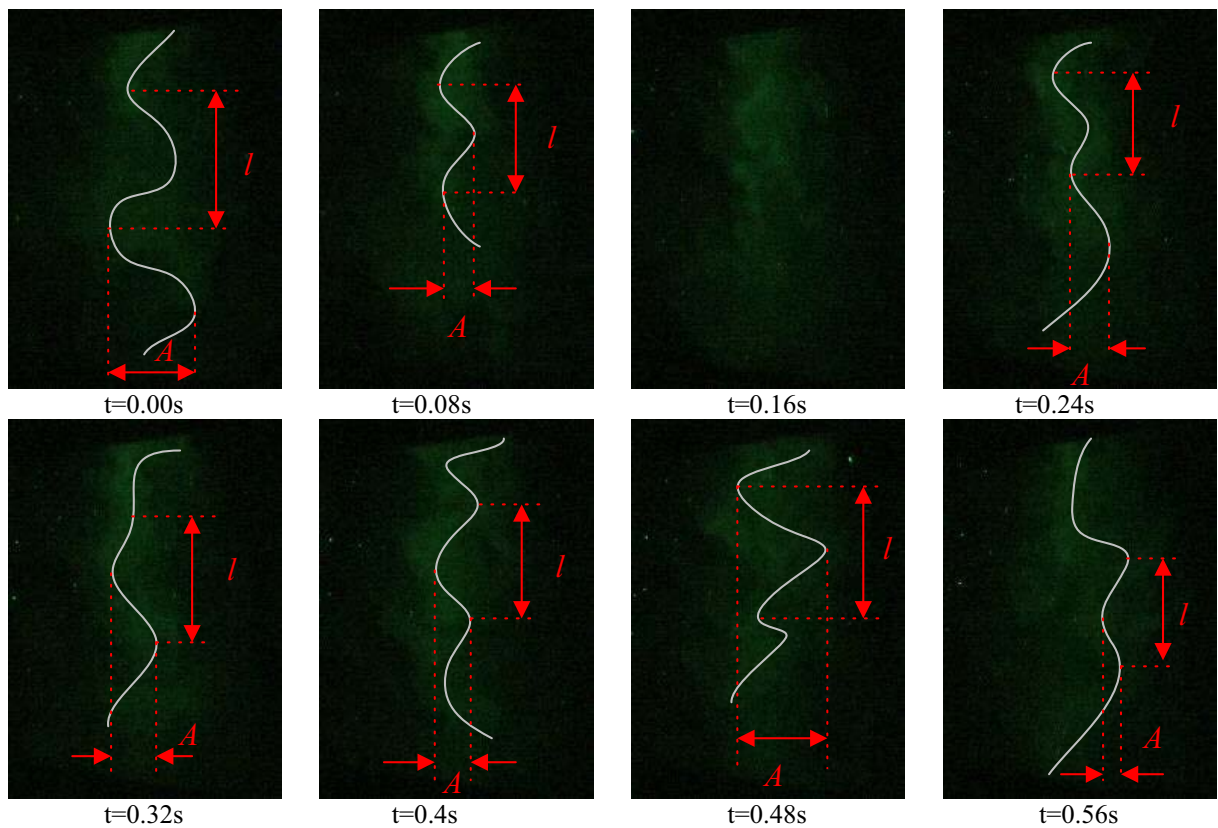


**Figure 4.11:** Video images of the primary jet at 0.08 second intervals with the laser orientated through Plane A. Velocity ratio is  $\lambda=3.6$ , flow region is  $6 < x/D < 12$ . The white lines highlight the sinuous motion of the main coherent structure,  $A$  an estimate of the amplitude and  $l$ , an estimate of the wavelength.

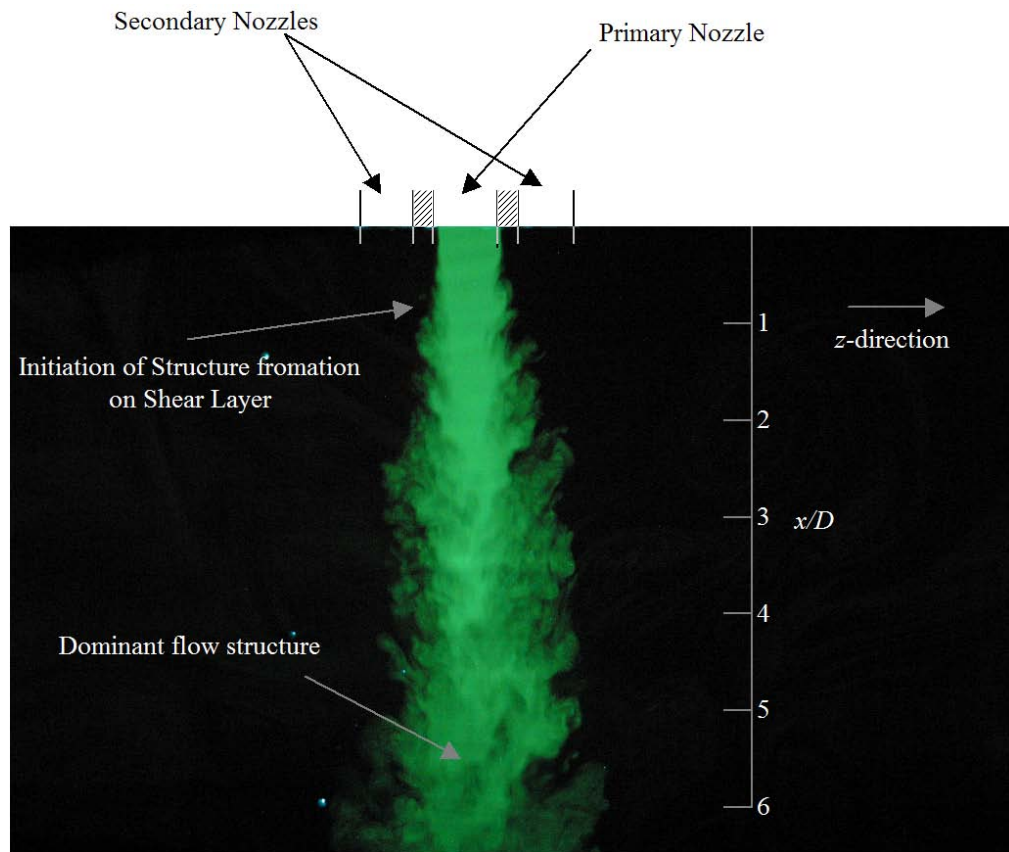


**Figure 4.12:** High resolution image of the instantaneous flow field of the primary jet through plane A, for  $\lambda=0$ , and  $0 < x/D < 6$ .

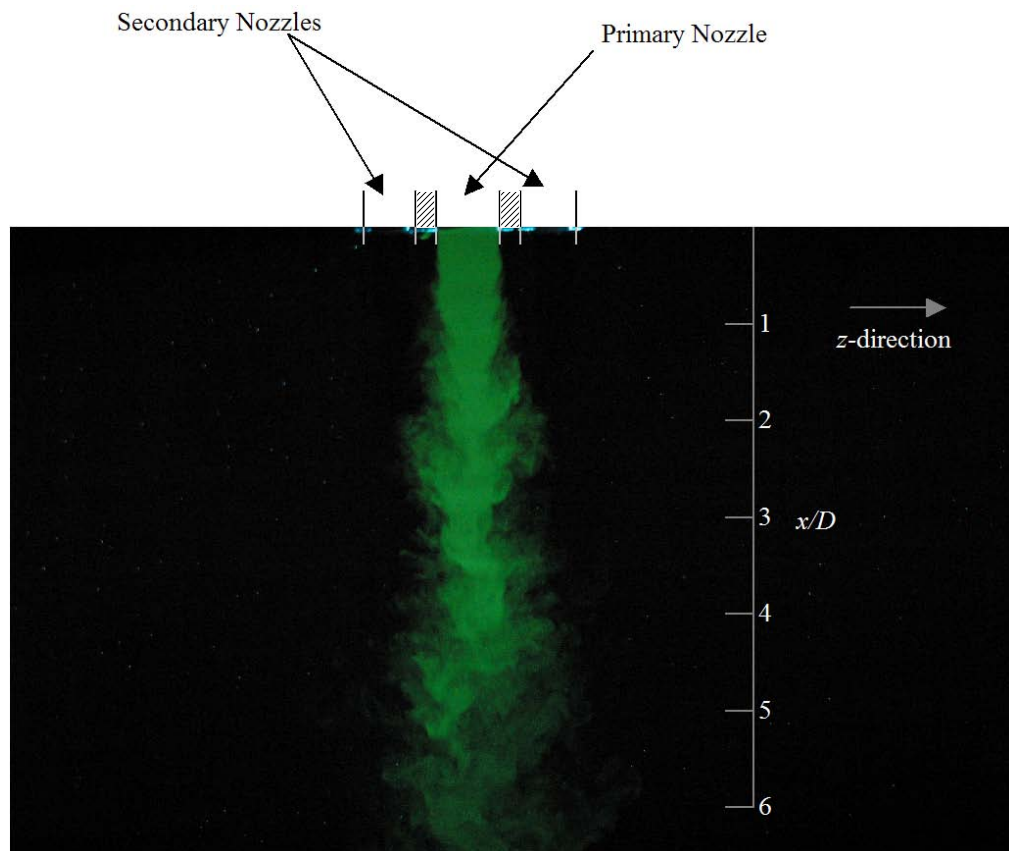


**Figure 4.13:** High resolution image of the instantaneous flow field of the primary jet through plane A, for  $\lambda=0.55$ , and  $0 < x/D < 6$ .

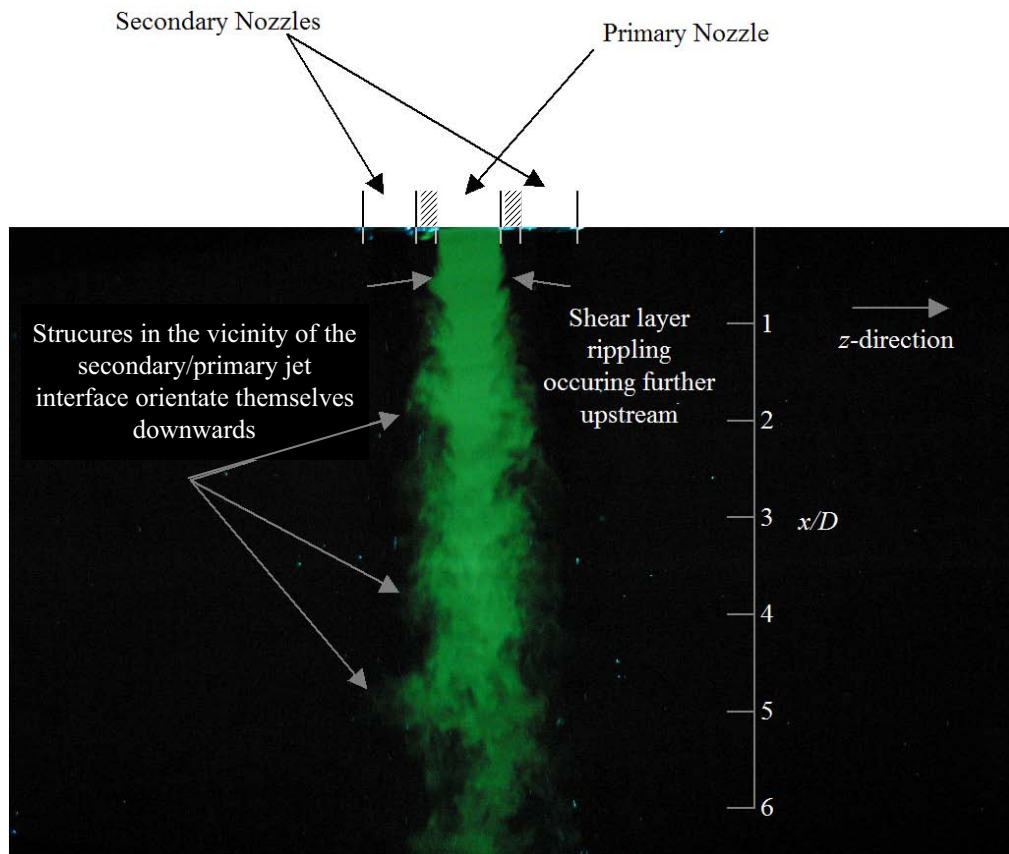


**Figure 4.14:** High resolution image of the instantaneous flow field of the primary jet through plane A, and  $\lambda=1.4$ , and  $0 < x/D < 6$ .

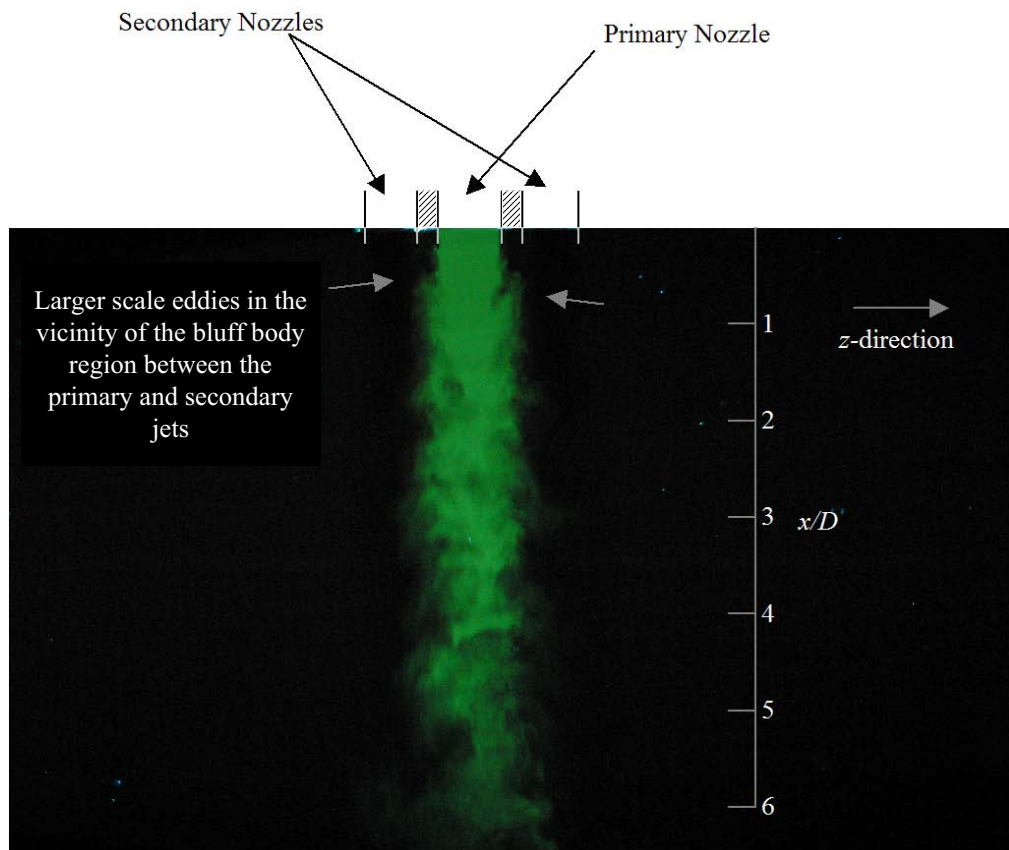


**Figure 4.15:** High resolution image of the instantaneous flow field of the primary jet through plane A, for  $\lambda=2.8$ , and  $0 < x/D < 6$ .



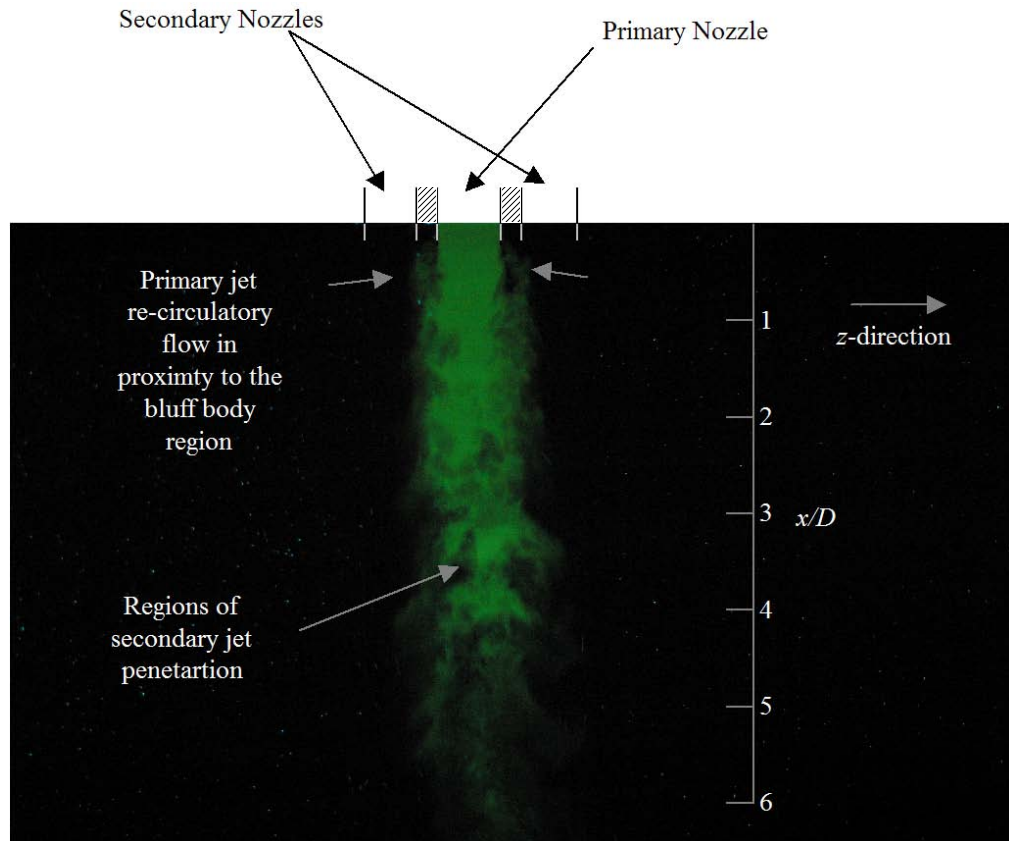


**Figure 4.16:** High resolution image of the instantaneous flow field of the primary jet through plane A, for  $\lambda=3.6$ , and  $0 < x/D < 6$ .

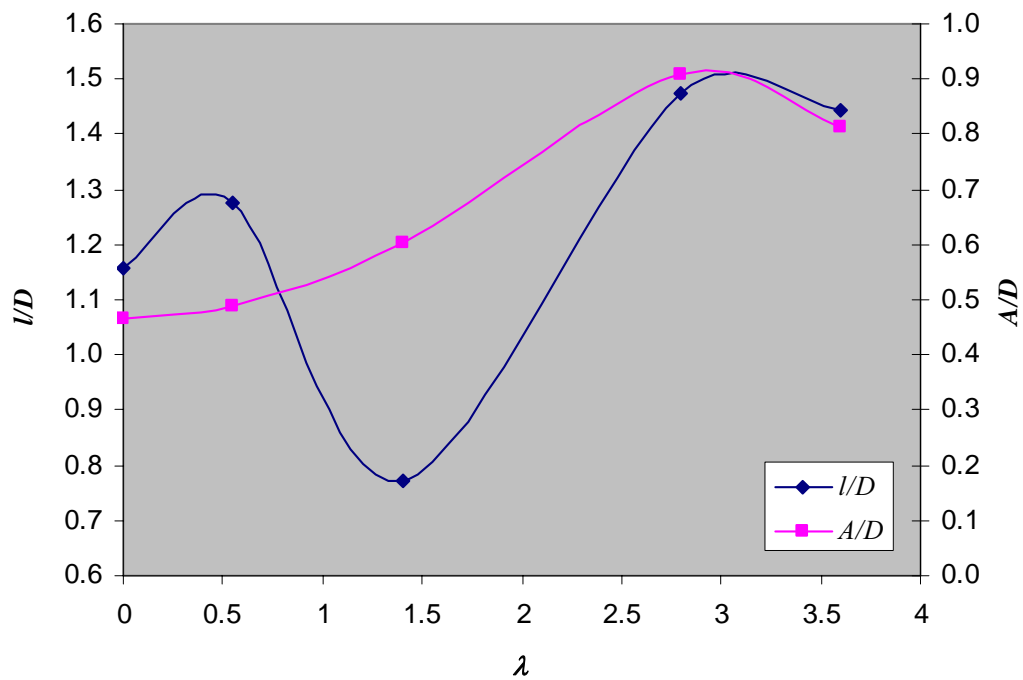


**Figure 4.17:** Dependence on the velocity ratio of the dimensionless wavelength,  $l/D$  and amplitude,  $A/D$  of the sinuous motion of the main coherent structure of the primary jet through Plane A, as estimated visually and time averaged over ten sequential frames.

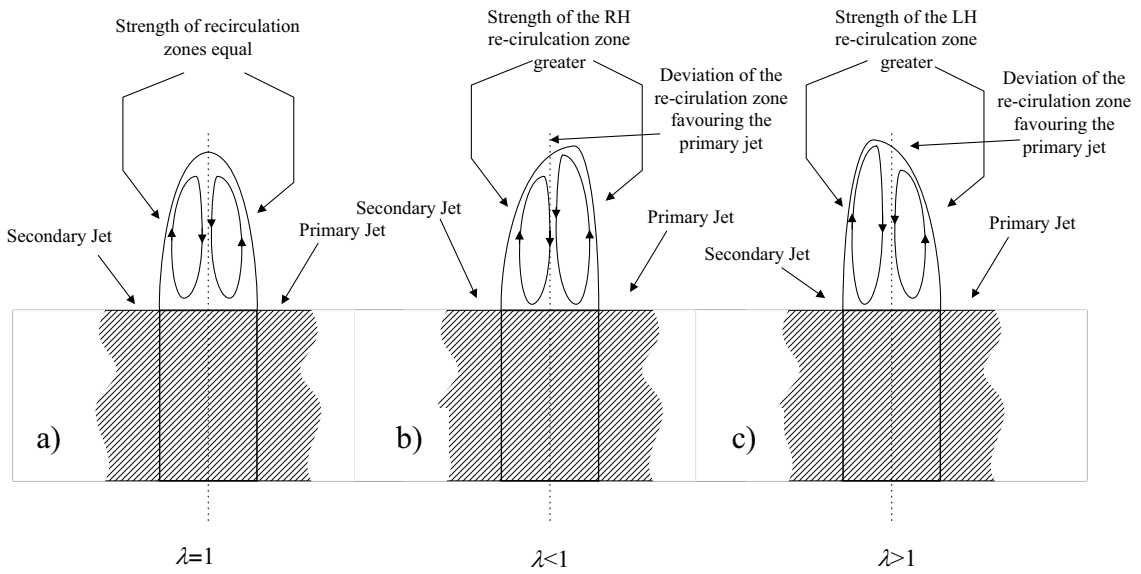


**Figure 4.18:** Wake region in the vicinity of the bluff body between the primary and secondary jets, a)  $\lambda=0$ , b)  $\lambda < 1$ , c)  $\lambda > 1$ .

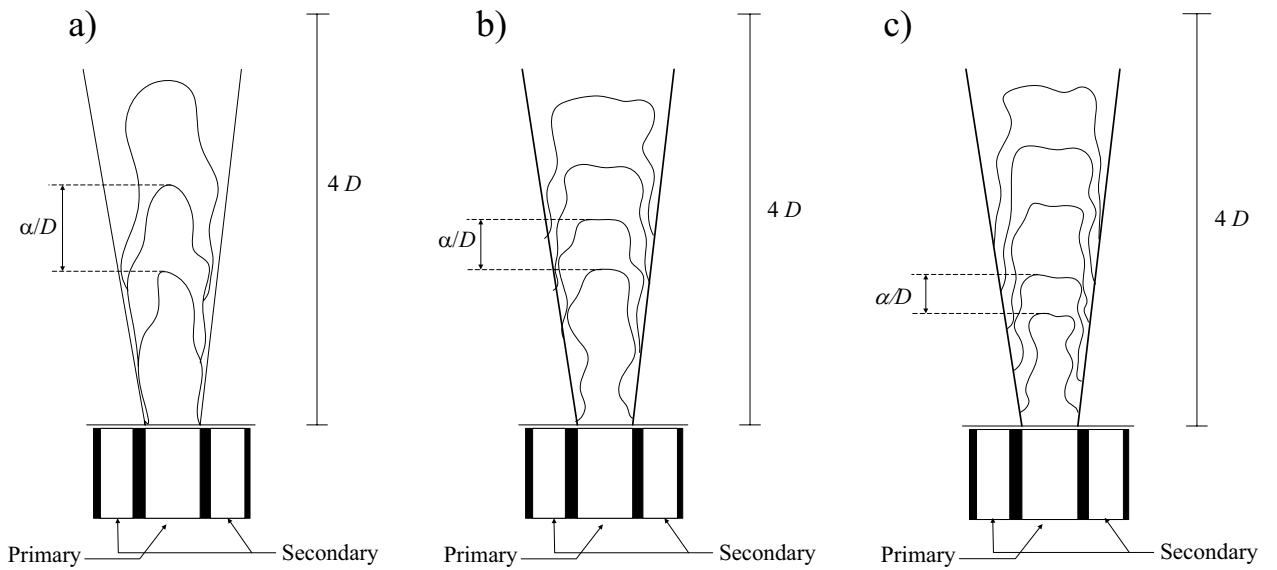


**Figure 4.19:** Schematic diagrams of the first order analysis of large-scale structures of the primary jet through Plane A, a)  $\lambda=0$ , b)  $\lambda=0.55$ , c)  $\lambda=1.4-3.6$ .

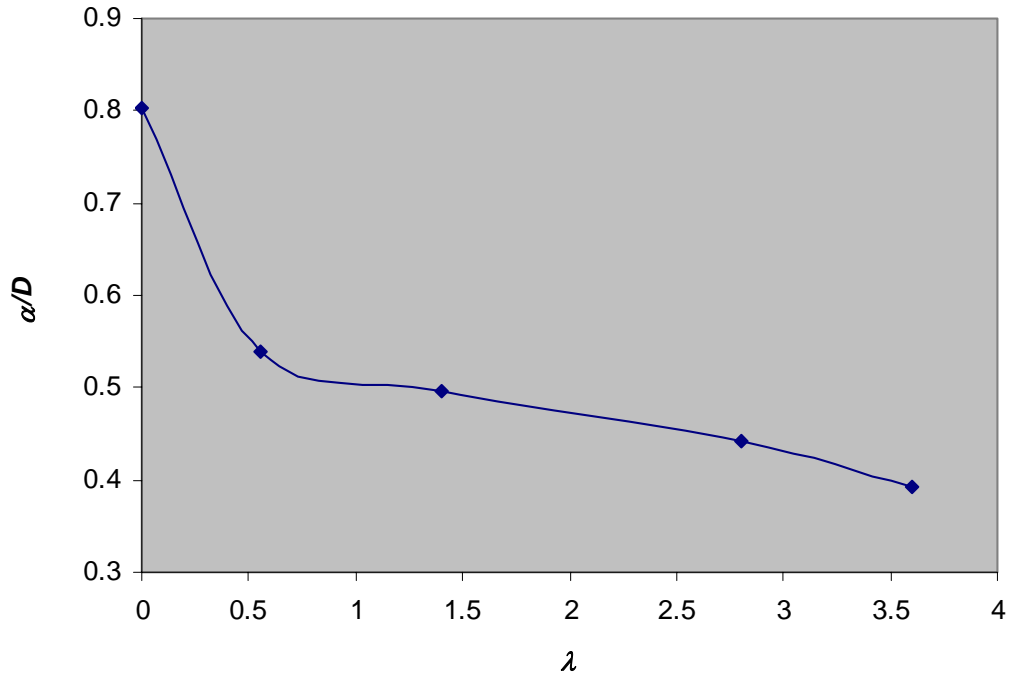


**Figure 4.20:**  $\alpha/D$  versus  $\lambda$  for the primary jet through plane A.  $\alpha/D$  was measured over ten frames of sequential footage and then time-averaged.

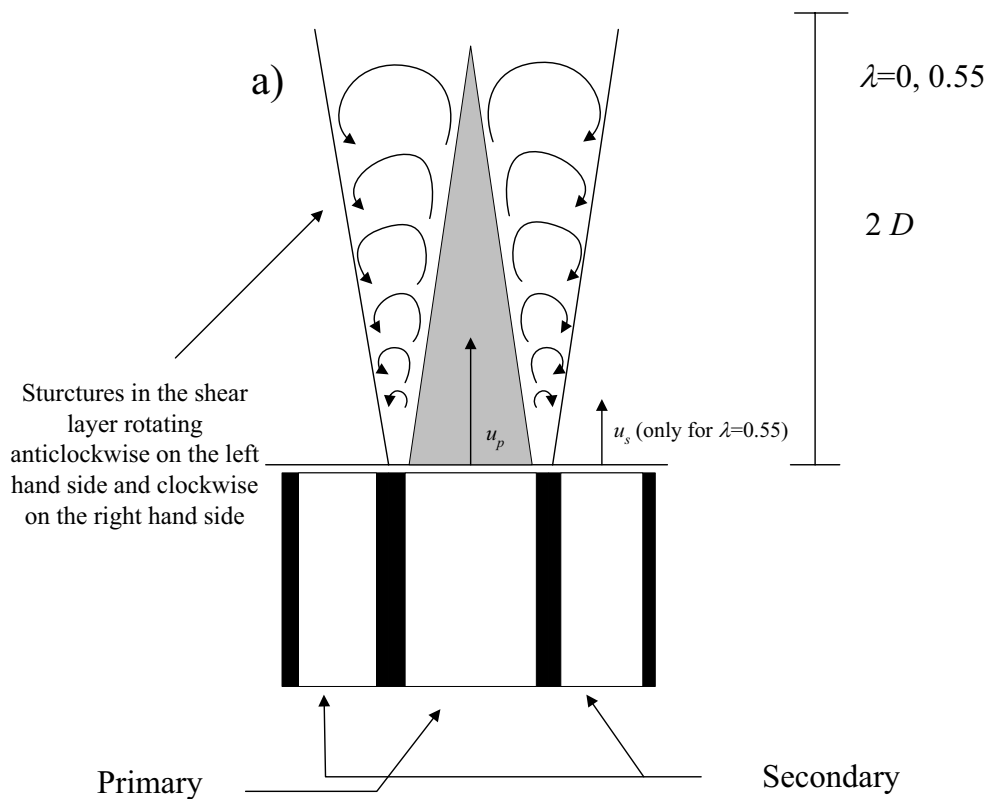


**Figure 4.21:** Schematic diagrams of the second order analysis of intermediate-scale structures of the primary jet through Plane A, a),  $\lambda=0-0.55$ , b),  $\lambda=1.4$ , c),  $\lambda=2.8-3.6$ .

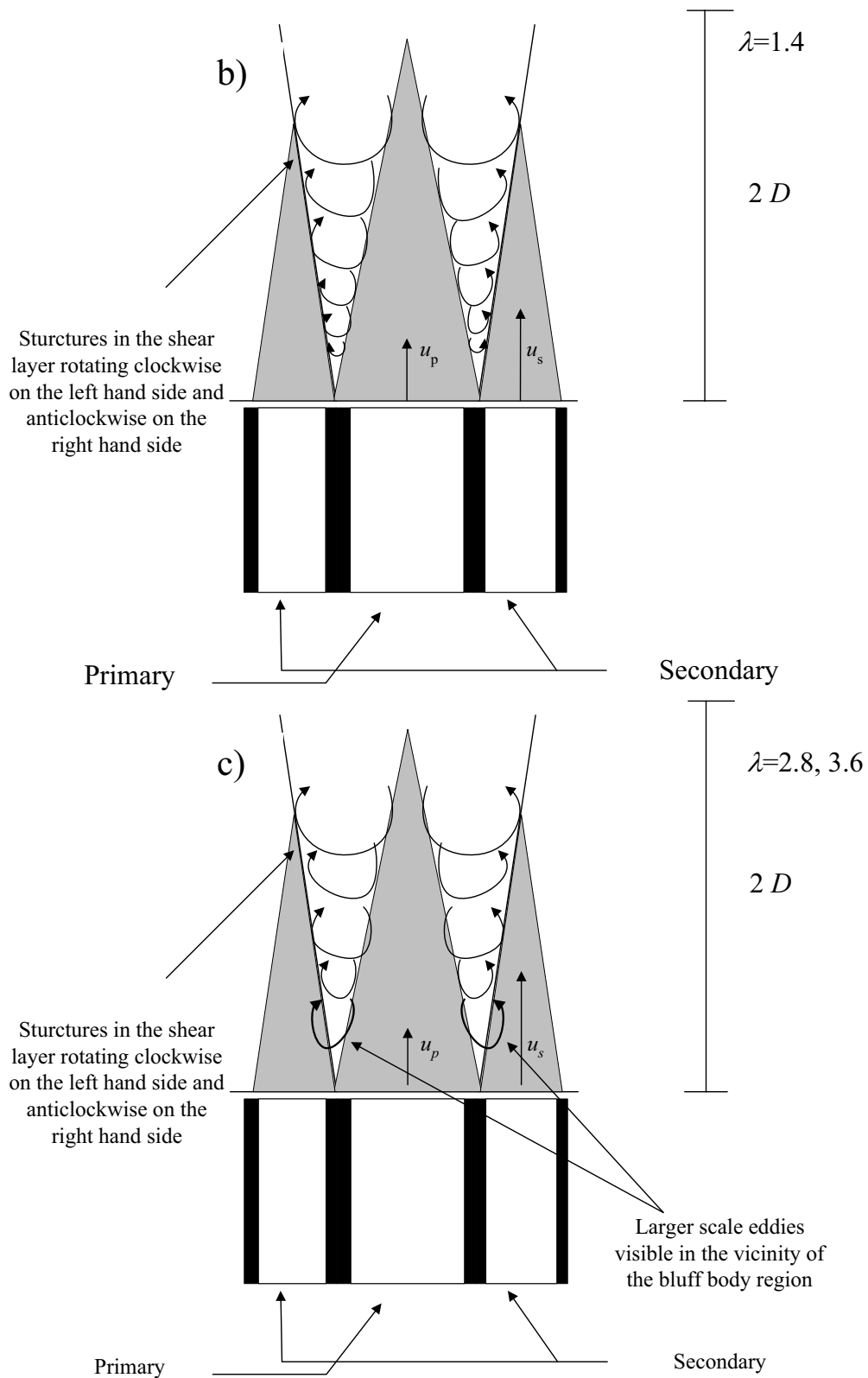


**Figure 4.21:** Schematic diagrams of the second order analysis of intermediate-scale structures of the primary jet through Plane A, a),  $\lambda=0-0.55$ , b),  $\lambda=1.4$ , c),  $\lambda=2.8-3.6$ .

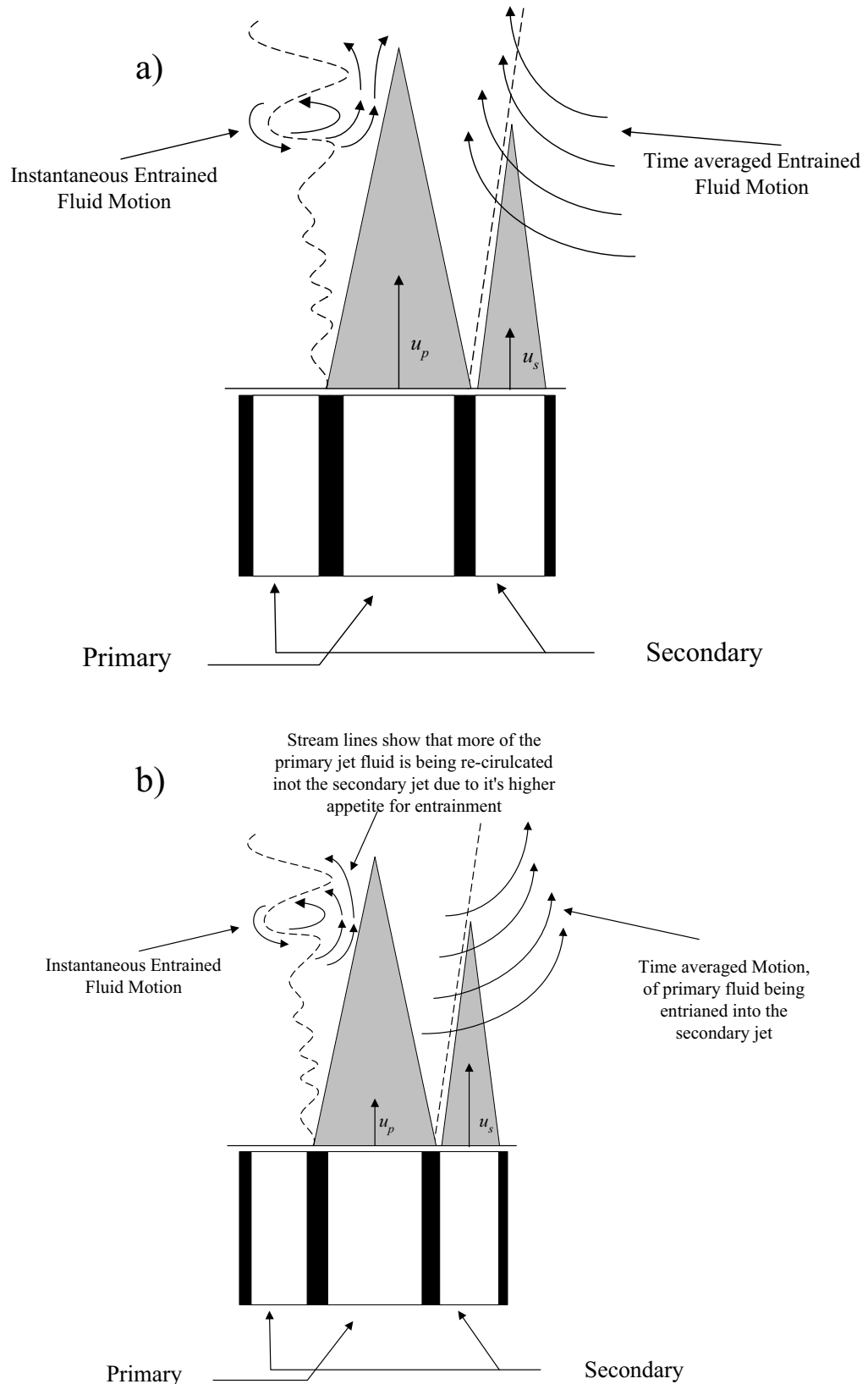


**Figure 4.22:** Schematic Diagrams for the instantaneous and time-averaged entrainment mechanisms for the primary jet at  $\lambda=0-0.55$  a), and  $\lambda=1.4-3.6$  b).

### 4.3.1.2 Plane C

The primary jet operated alone ( $\lambda = 0$ ) through plane C is shown in a sequence of images in Figures 4.23 and 4.24 with a high resolution image in Figure 4.33. The mixing patterns in the near field are similar to those in Plane A (Figures 4.2, 4.3 and 4.12) as expected for the nearly square aspect ratio of the jet ( $AR = 1.2$ ).

The presence of the secondary jet at  $\lambda=0.55$  in Figures 4.25, 4.26 and 4.34 shows that although the secondary jet has insufficient velocity and momentum to dominate mixing patterns it does increase the sinuous motion of the primary jet as pointed out in Figure 4.34.

Figures 4.27-4.28 and 4.35 illustrate how the higher momentum of the secondary jet at  $\lambda = 1.4$  increases the scale of the sinuous motion. This sinuous motion is not only larger in the  $z$ -direction with respect to  $\lambda=0.55$ , but also occurs further upstream with the velocity ratio increasing from  $\lambda=1.4$  to 2.8 and 3.6 as seen in Figures 4.27-4.32 and 4.35-4.37. It is also evident that the flapping frequency has also increased for  $\lambda=3.6$ , as illustrated in Figure 4.37. Analysis of the sinuous motion of the main coherent structures also reveals that the scale and amplitude of the sinuous motion is affected by velocity ratio. This is proof that the co-flowing velocity ratio also affects the motion of the main coherent structure of the primary jet through plane C. Figure 4.38 shows that the time-averaged amplitude and wavelength of the sinuous motion of the primary jet through plane C decreases with  $\lambda$ .

Unlike the structures visualised in the shear layer through Plane A, their rotational direction is not affected by the speed of the secondary jet.

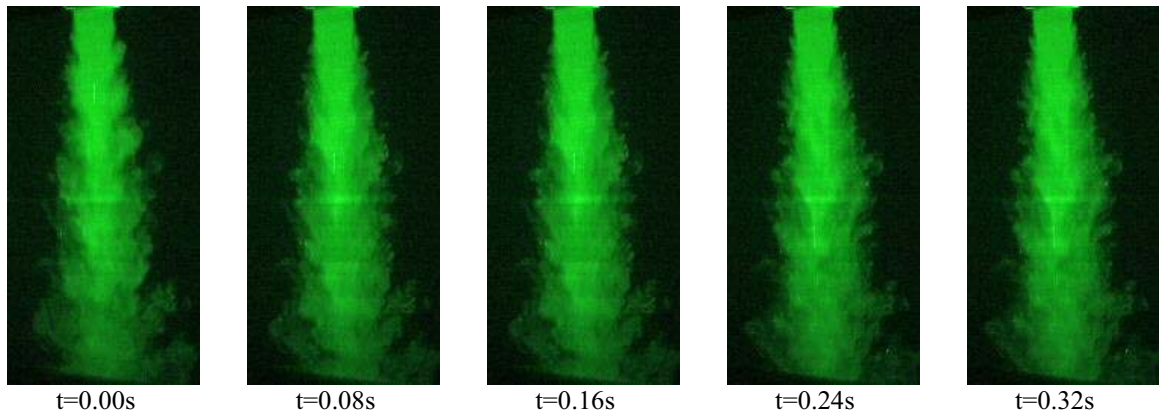


**Figure 4.23:** A sequence of video images of the primary jet with the laser orientated through Plane C at 0.08 second intervals. Velocity ratio:  $\lambda=0$ , flow region:  $0 < x/D < 6$ .

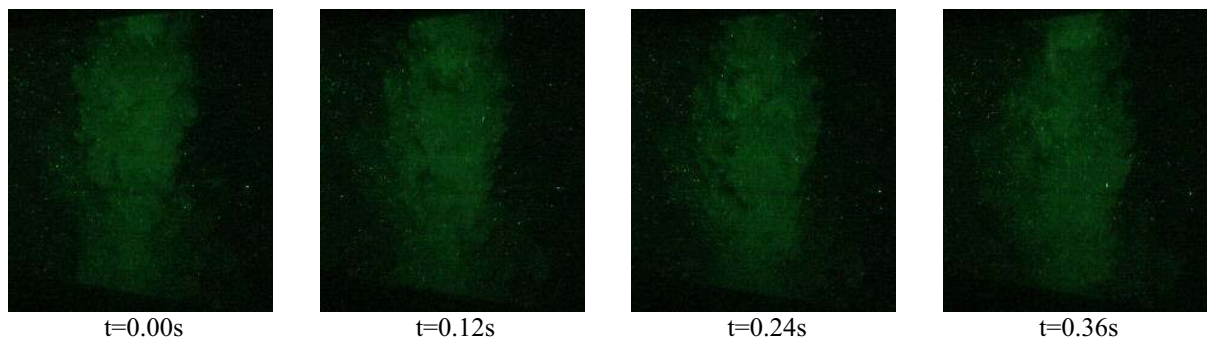


**Figure 4.24:** A sequence of video images of the primary jet at 0.12 second intervals with the laser orientated through Plane C. Velocity ratio:  $\lambda=0$ , flow region:  $6 < x/D < 12$ .

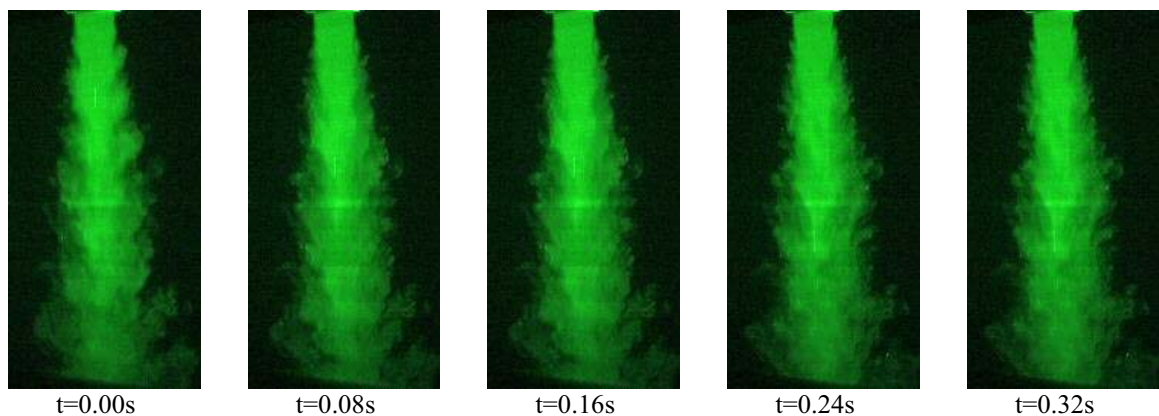


**Figure 4.25:** A sequence of Video images of the primary jet with the laser orientated through Plane C at 0.08 second intervals. Velocity ratio:  $\lambda=0.55$ , flow region:  $0 < x/D < 6$ .

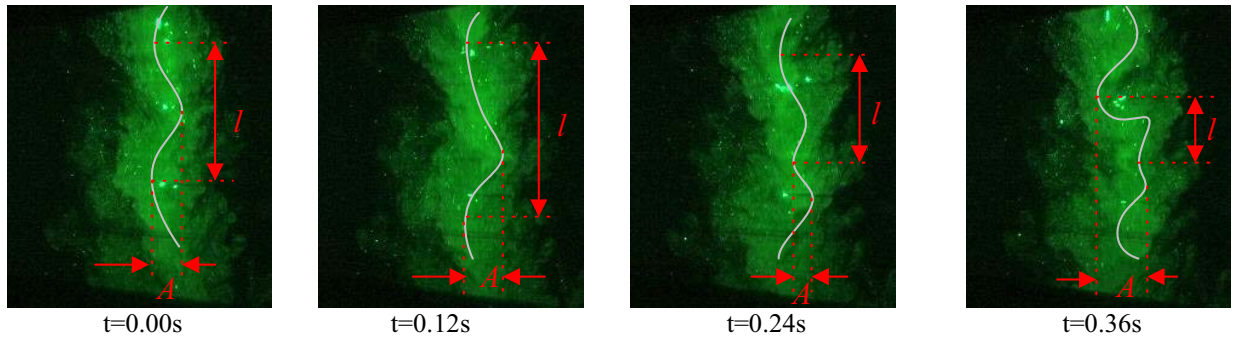


**Figure 4.26:** A sequence of Video images of the primary jet at 0.12 second intervals with the laser orientated through Plane C. Velocity ratio:  $\lambda=0.55$ , flow region:  $6 < x/D < 12$ . The white lines highlight the sinuous motion of the main coherent structure,  $A$  being the amplitude and  $l$ , being the wavelength.

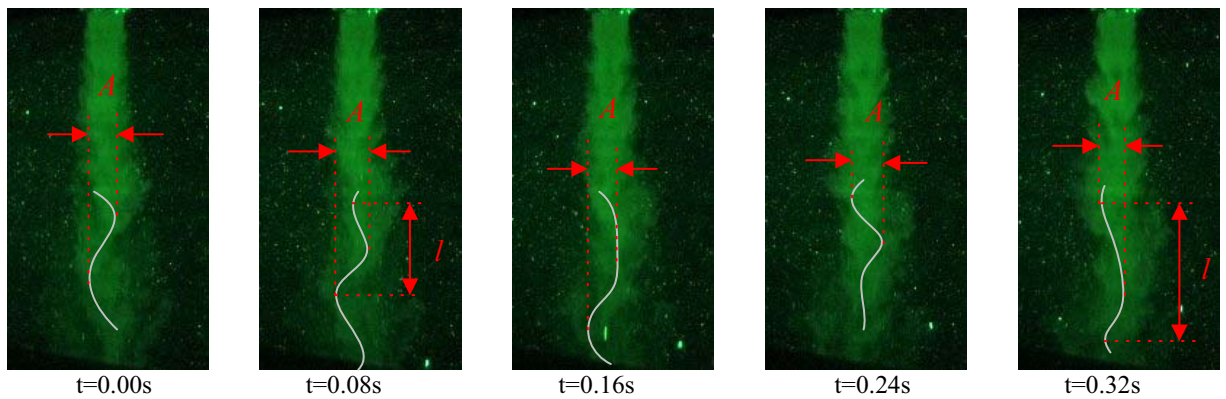


**Figure 4.27:** A sequence of Video images of the primary jet at 0.08 second intervals with the laser orientated through Plane C. Velocity ratio:  $\lambda=1.4$ , flow region:  $0 < x/D < 6$ . The white lines highlight the sinuous motion of the main coherent structure,  $A$  being the amplitude and  $l$ , being the wavelength.

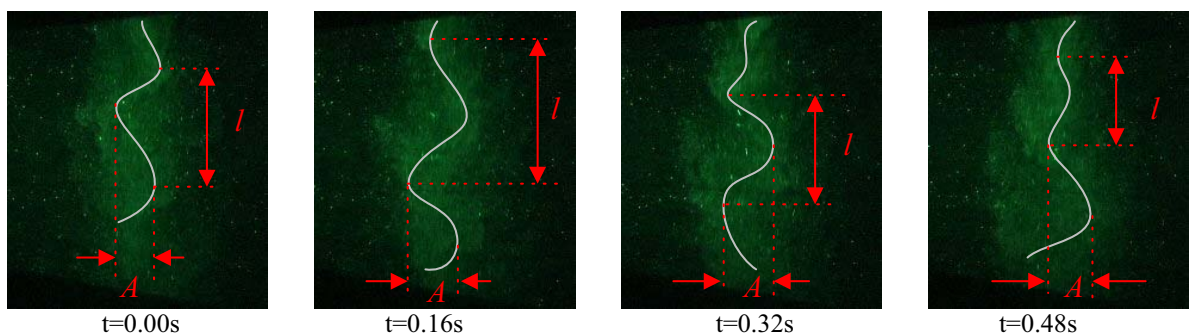


**Figure 4.28:** A sequence of Video images of the primary jet at 0.16 second intervals with the laser orientated through Plane C. Velocity ratio:  $\lambda=1.4$ , flow region:  $6 < x/D < 12$ . The white lines highlight the sinuous motion of the main coherent structure,  $A$  being the amplitude and  $l$ , being the wavelength.



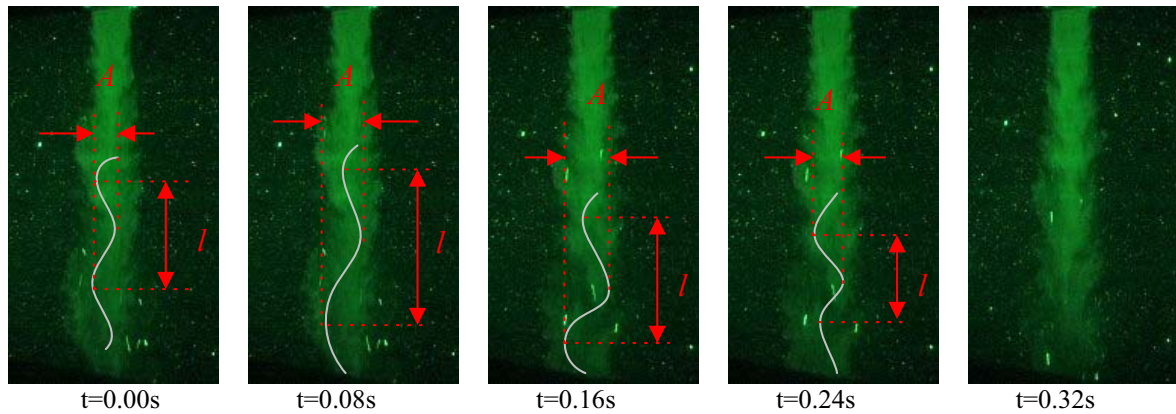


**Figure 4.29:** A sequence of Video images of the primary jet with the laser orientated through Plane C at 0.08 second intervals. Velocity ratio:  $\lambda=2.8$ , flow region:  $0 < x/D < 6$ . The white lines highlight the sinuous motion of the main coherent structure,  $A$  being the amplitude and  $l$ , being the wavelength.

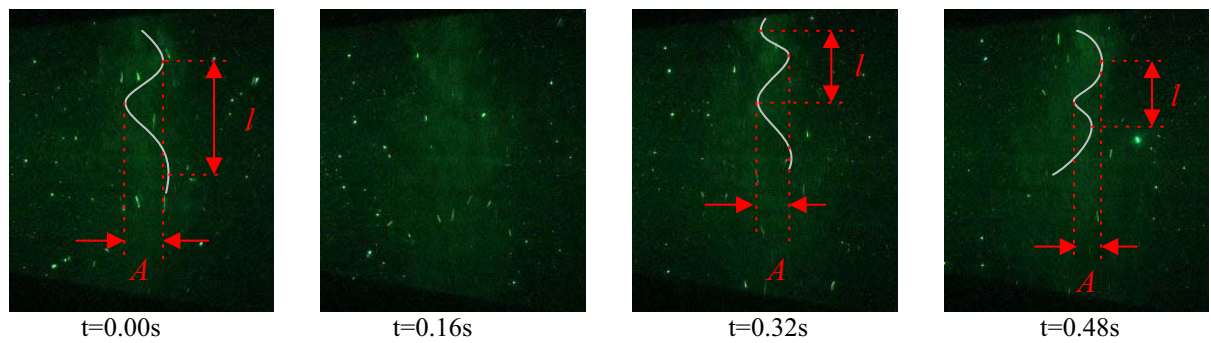


**Figure 4.30:** A sequence of Video images of the primary jet at 0.16 second intervals with the laser orientated through Plane C. Velocity ratio:  $\lambda=2.8$ , flow region:  $6 < x/D < 12$ . The white lines highlight the sinuous motion of the main coherent structure,  $A$  being the amplitude and  $l$ , being the wavelength.

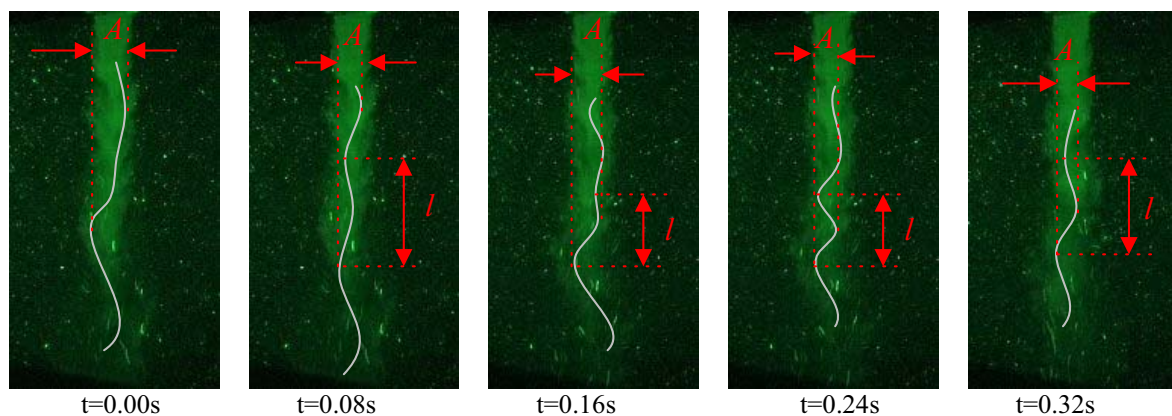


**Figure 4.31:** A sequence of Video images of the primary jet at 0.08 second intervals with the laser orientated through Plane C. Velocity ratio:  $\lambda=3.6$ , flow region:  $0 < x/D < 6$ . The white lines highlight the sinuous motion of the main coherent structure,  $A$  being the amplitude and  $l$ , being the wavelength.

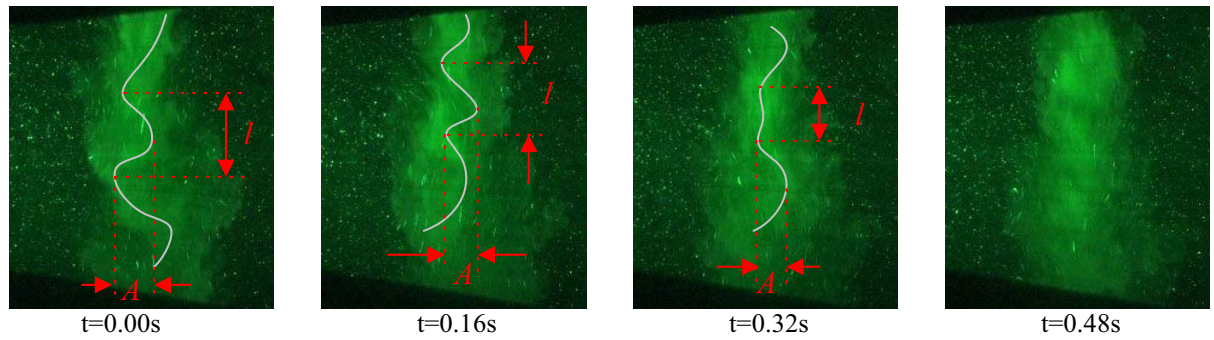


**Figure 4.32:** A sequence of Video images of the primary jet at 0.16 second intervals with the laser orientated through Plane C. Velocity ratio:  $\lambda=3.6$ , flow region:  $6 < x/D < 12$ . The white lines highlight the sinuous motion of the main coherent structure,  $A$  being the amplitude and  $l$ , being the wavelength.

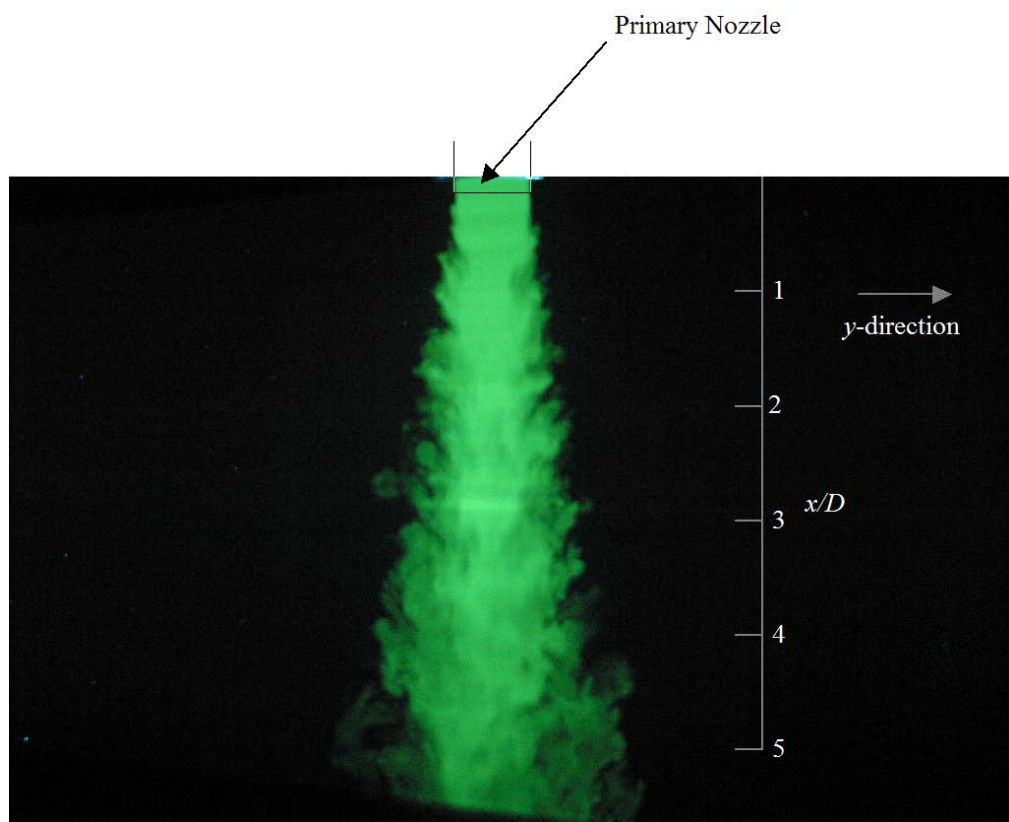


**Figure 4.33:** High resolution image of the instantaneous flow field of the primary jet through plane C, for  $\lambda=0$ , and  $0 < x/D < 6$ .

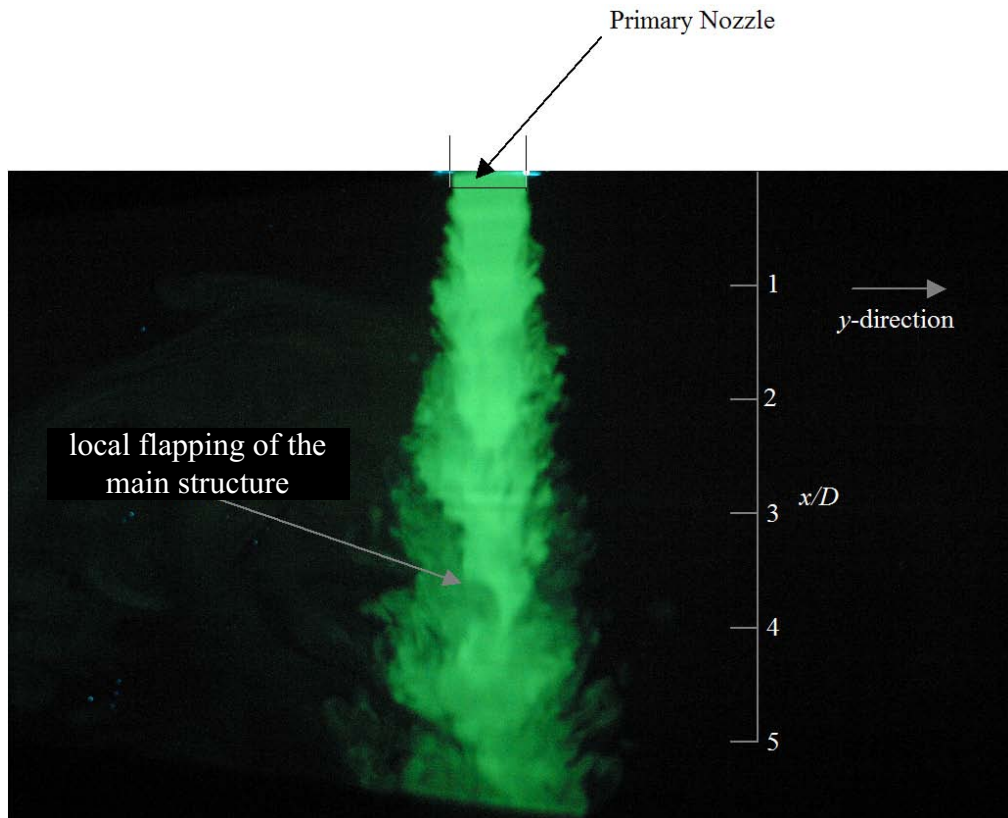


**Figure 4.34:** High resolution image of the instantaneous flow field of the primary jet through plane C, for  $\lambda=0.55$ , and  $0 < x/D < 6$ .

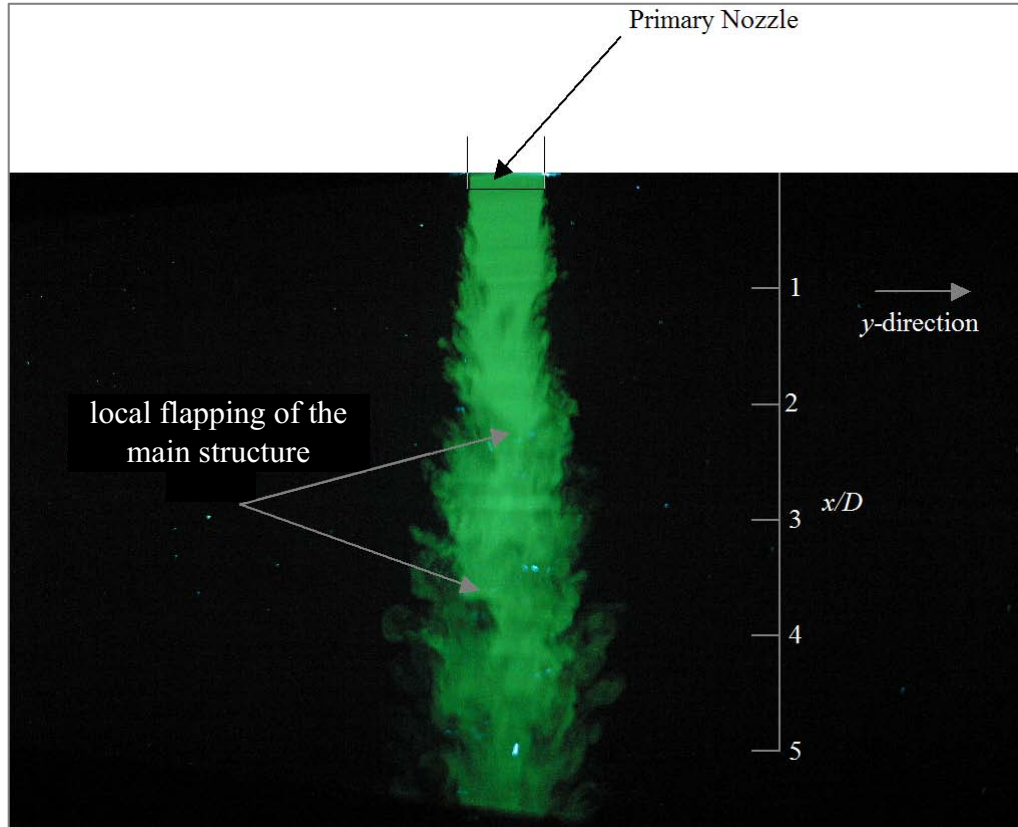


**Figure 4.35:** High resolution image of the instantaneous flow field of the primary jet through plane C, for  $\lambda=1.4$ , and  $0 < x/D < 6$ .

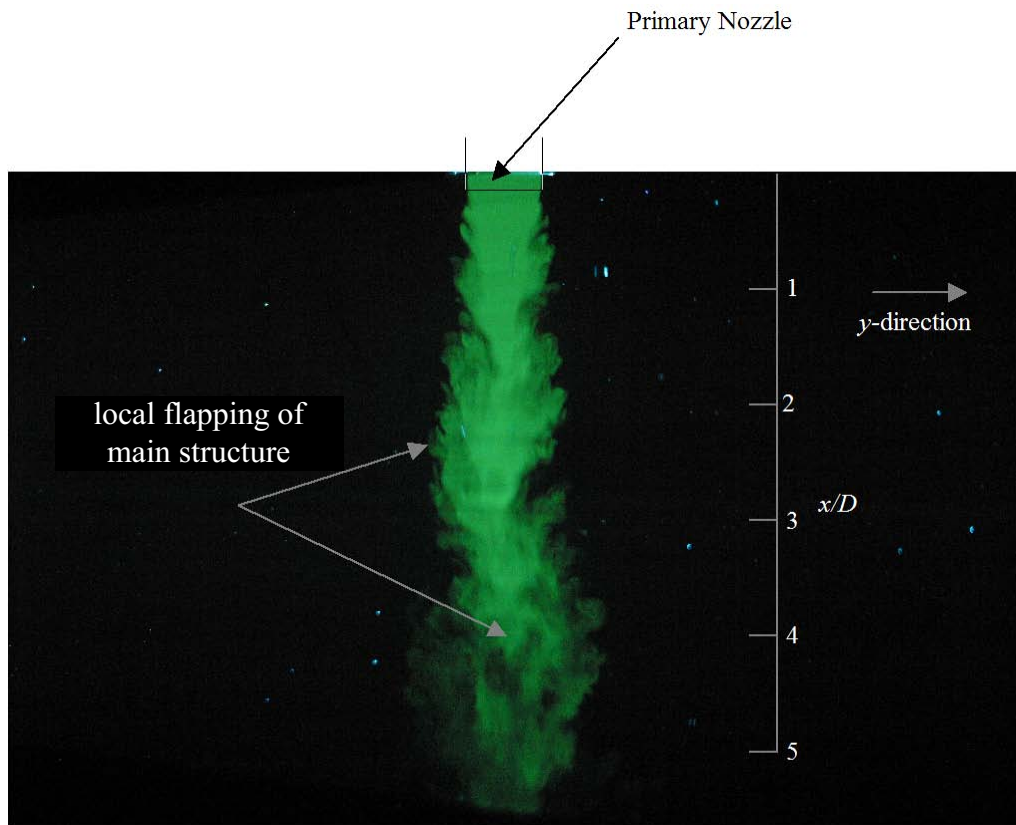


**Figure 4.36:** High resolution image of the instantaneous flow field of the primary jet through plane C, for  $\lambda=2.8$ , and  $0 < x/D < 6$ .

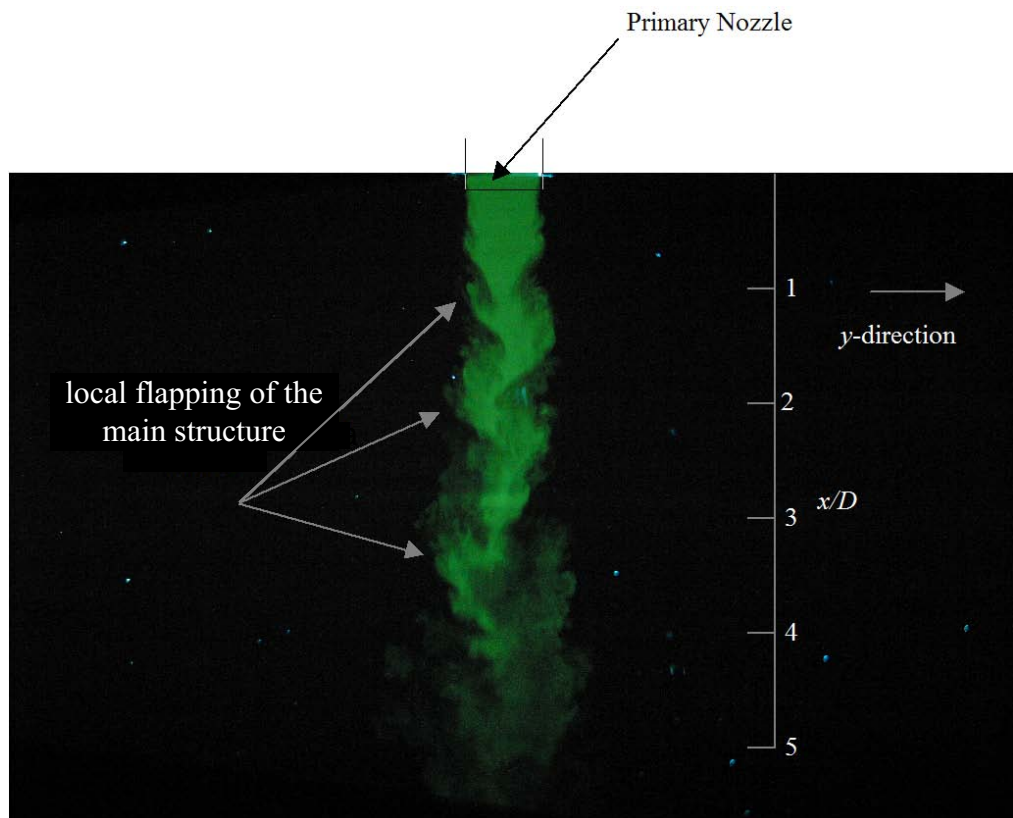


**Figure 4.37:** High resolution image of the instantaneous flow field of the primary jet through plane C, and  $\lambda=3.6$ , between  $0 < x/D < 6$ .

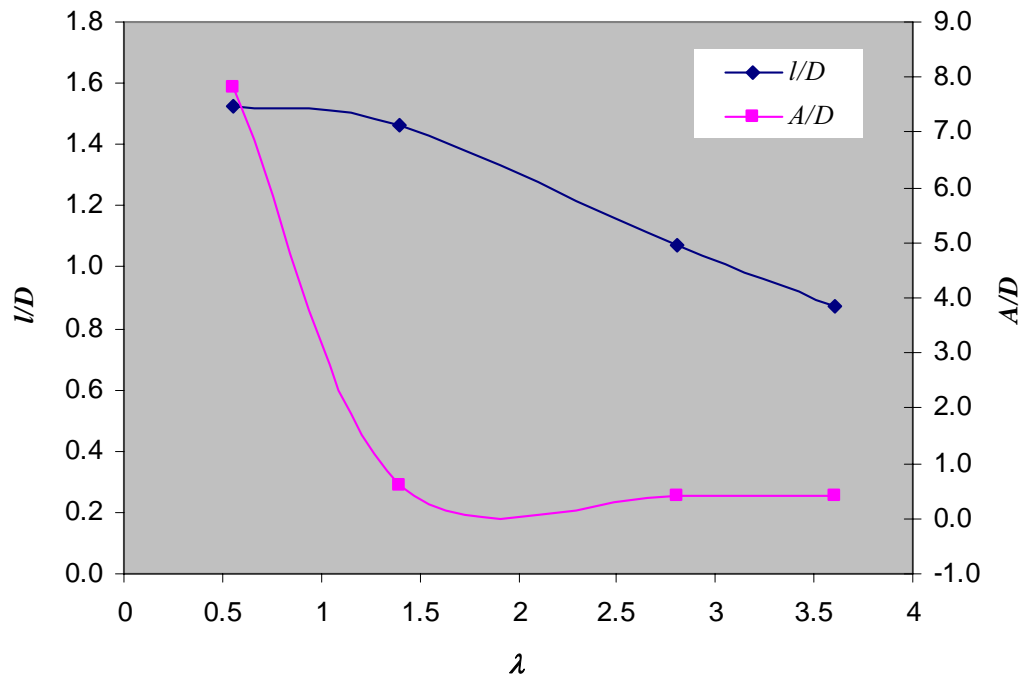


**Figure 4.38:** Dependency on the velocity ratio of the dimensionless wavelength,  $l/D$  and amplitude  $A/D$  of the sinuous motion of the main coherent structure of the primary jet through Plane C, as estimated visually and time averaged over ten sequential frames.

## 4.3.2 Secondary Jet

### 4.3.2.1 Plane A

In Figure 4.39, for  $\lambda=0.55$ , the velocity of the primary jet is sufficient to alter the shear layer as well as the bulk fluid flow. The secondary jet shear layer adjacent to the primary jet is also influenced by the velocity of the primary stream, particularly for  $\lambda=0.55$ . Figures 4.39 and 4.44 show that as the secondary fluid is entrained into the primary, the opposite shear layer grows in size as a counter effect, causing large-scale oscillation at about  $x/D=1$ .

As the velocity ratio is increased from  $\lambda=1.4$  to 2.8 and 3.6 (Figures 4.40-4.42 and 4.45-4.47) the large-scale sinuous oscillation becomes less apparent. For  $\lambda=\infty$  (Figure 4.43 and 4.48) the size of structures in the shear layers is very similar on each side before merging. Note that the size of the bluff-body now spans the entire distance between the two secondary jets. Mutual

entrainment of the jets causes them to deviate from their geometric axes towards each other as illustrated in the high-resolution image in Figure 4.48.

The main coherent structures of the secondary jet also shows visibly different movement with variation in  $\lambda$ . The white lines in Figures 4.39-4.43 highlight the sinuous oscillation of the main coherent structure, which appears to oscillate with greater amplitude and wavelength at  $\lambda=0.55$  and  $\lambda=\infty$ . Figure 4.49 illustrates the variation of the dimensionless amplitude ( $A/D$ ) and wavelength ( $l/D$ ) with the inverse velocity ratio  $1/\lambda$ , particularly at the higher amplitudes at  $\lambda=0.55$  and  $\lambda=\infty$ , which highlights greater oscillation of the main coherent structure of the secondary jet through plane B.

The length scale of the structures in the shear layer, as well as the offset of jet axis from the geometrical axes, depend heavily on velocity ratio as schematically depicted in Figures 4.50 a) b) and c). Figure 4.50 a) shows for  $\lambda < 1$  the higher velocity of the primary jet causes the jet axes of the secondary jets to offset from the geometric axes inclining them towards the primary jets due to their higher appetite for entrainment. In turn, this increases the length scale of the structures in the shear layer not sharing an interface with the primary jet. Figure 4.50 b) illustrates the nature of the secondary jets for  $\lambda > 1$  where the secondary jets have sufficient velocity and momentum to not have their trajectory influenced by the primary jet. Figure 4.50 c) shows what happens when  $\lambda = \infty$  where the secondary jets are drawn in towards one another, which is being created by a low-pressure region due to the absence of the primary jet.

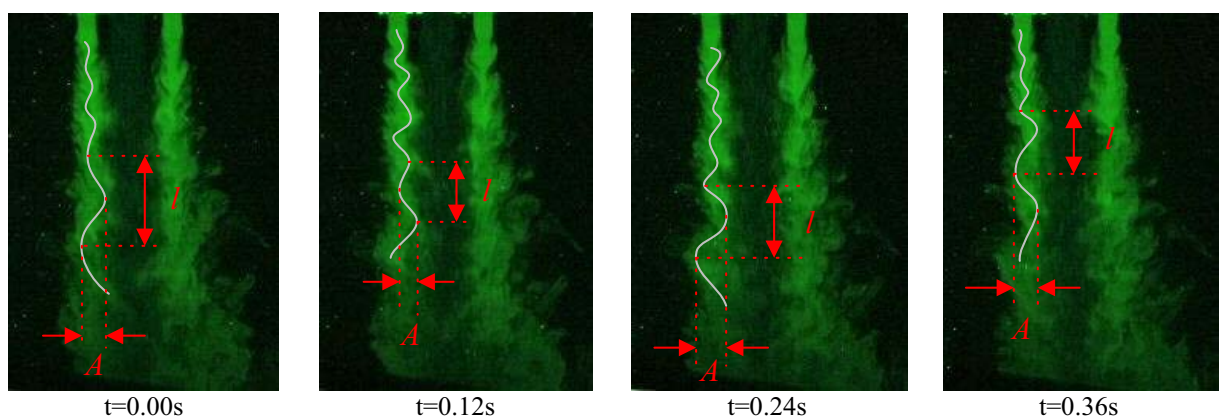


**Figure 4.39:** Video images of the secondary jet at 0.12 second intervals with the laser orientated through Plane A. Velocity ratio is  $\lambda=0.55$ , flow region is  $0 < x/D < 6$ . The white lines highlight the sinuous motion of the main coherent structure,  $A$  being the amplitude and  $l$ , being the wavelength.

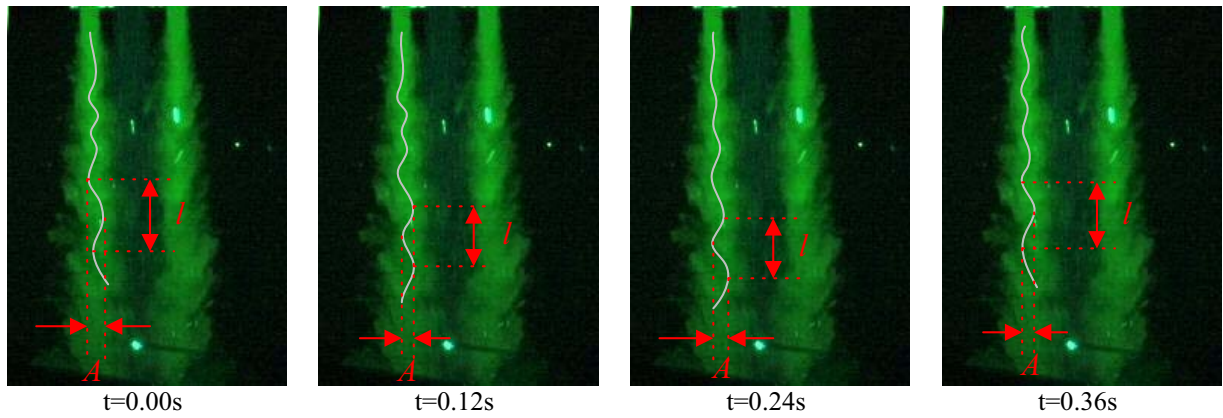


**Figure 4.40:** Video images of the secondary jet at 0.12 second intervals with the laser orientated through Plane A. Velocity ratio is  $\lambda=1.4$ , flow region is  $0 < x/D < 6$ . The white lines highlight the sinuous motion of the main coherent structure,  $A$  being the amplitude and  $l$ , being the wavelength.

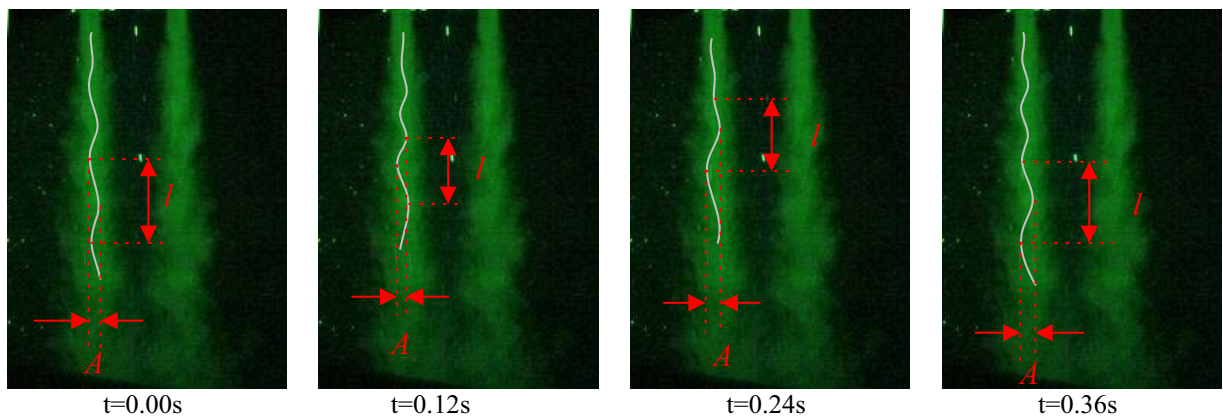


**Figure 4.41:** Video images of the secondary jet at 0.12 second intervals with the laser orientated through Plane A. Velocity ratio is  $\lambda=2.8$ , flow region is  $0 < x/D < 6$ . The white lines highlight the sinuous motion of the main coherent structure,  $A$  being the amplitude and  $l$ , being the wavelength.

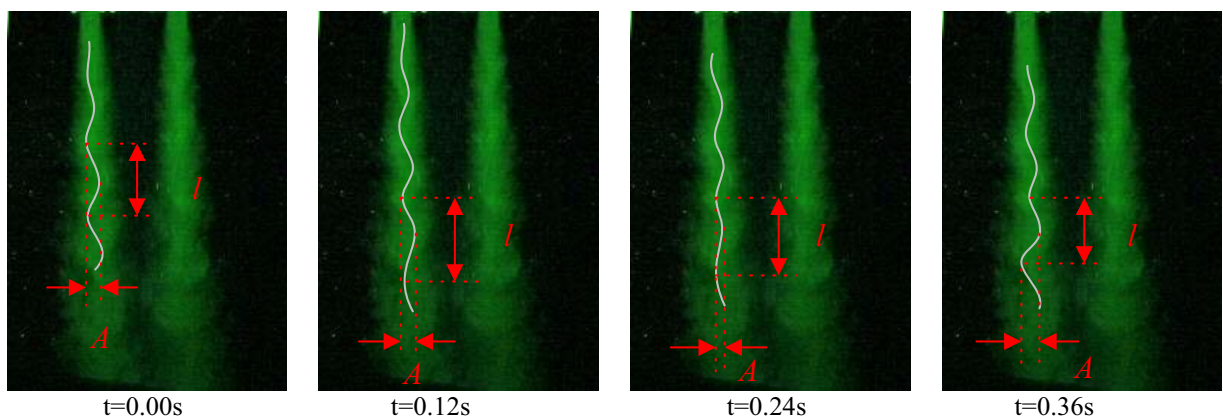


**Figure 4.42:** Video images of the secondary jet at 0.12 second intervals with the laser orientated through Plane A. Velocity ratio is  $\lambda=3.6$ , flow region is  $0 < x/D < 6$ . The white lines highlight the sinuous motion of the main coherent structure,  $A$  being the amplitude and  $l$ , being the wavelength.

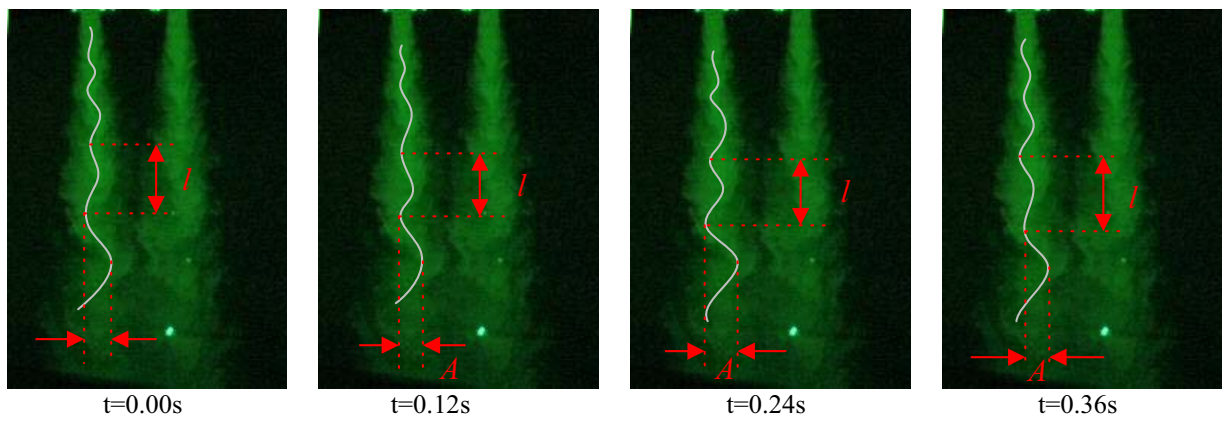


**Figure 4.43:** Video images of the secondary jet at 0.12 second intervals with the laser orientated through Plane A. Velocity ratio is  $\lambda=\infty$ , flow region is  $0 < x/D < 6$ . The white lines highlight the sinuous motion of the main coherent structure,  $A$  being the amplitude and  $l$ , being the wavelength.

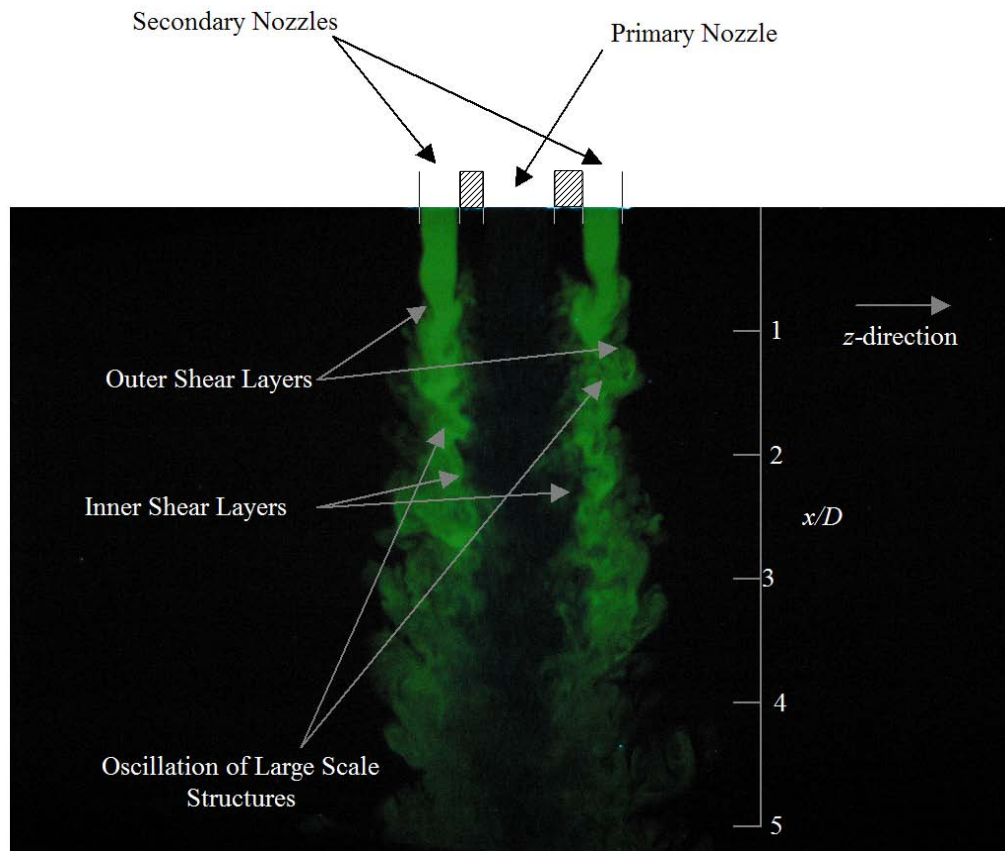


**Figure 4.44:** High resolution image of the instantaneous flow field of the secondary jet through plane A, and  $\lambda=0.55$ , between  $0 < x/D < 6$ .



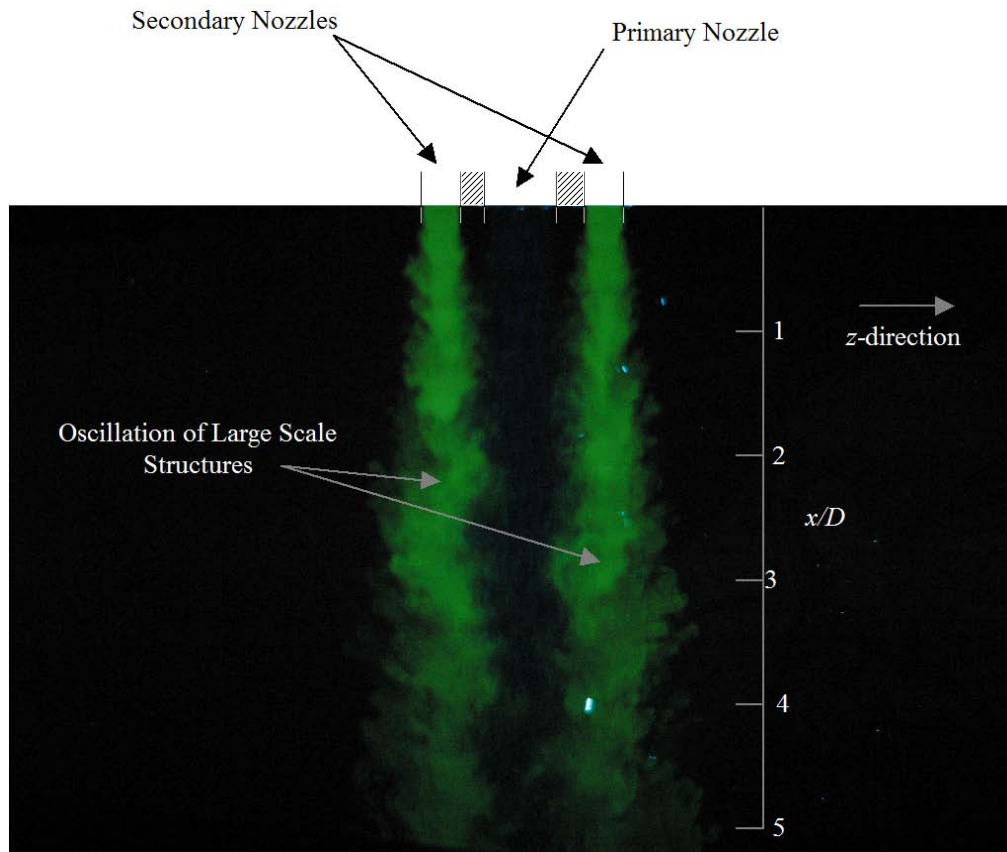


**Figure 4.45:** High resolution image of the instantaneous flow field of the secondary jet through plane A, and  $\lambda=1.4$ , between  $0 < x/D < 6$ .

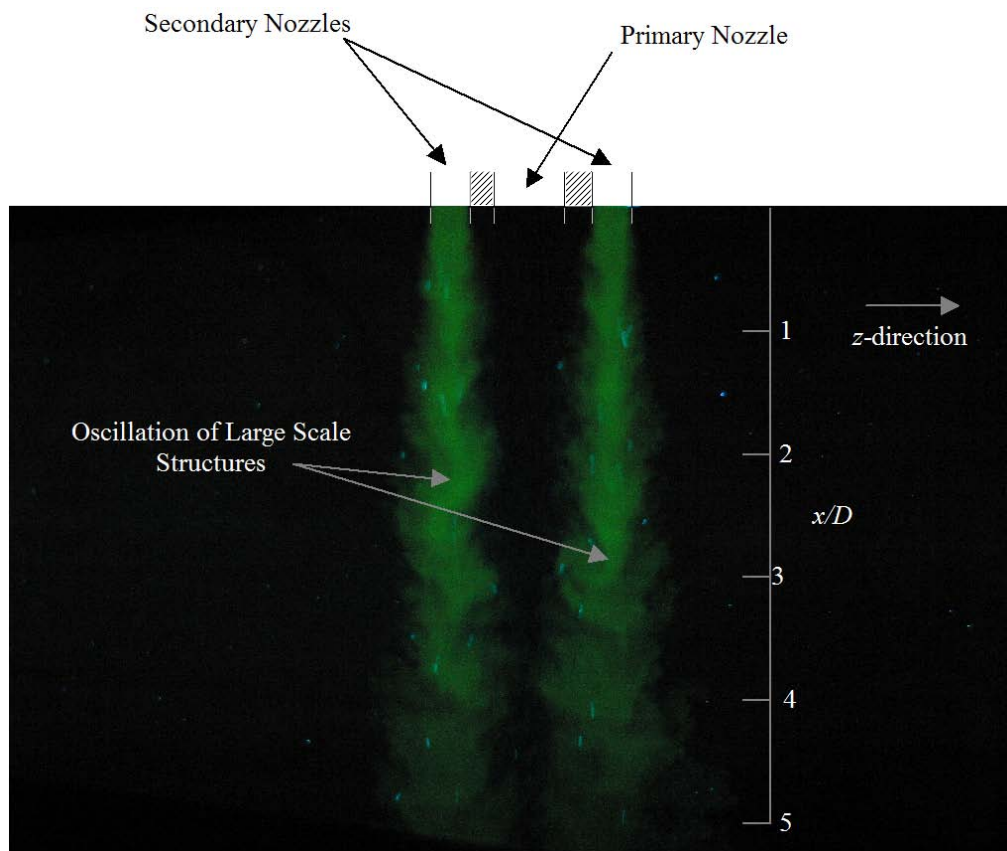


**Figure 4.46:** High resolution image of the instantaneous flow field of the secondary jet through plane A, and  $\lambda=2.8$ , between  $0 < x/D < 6$ .

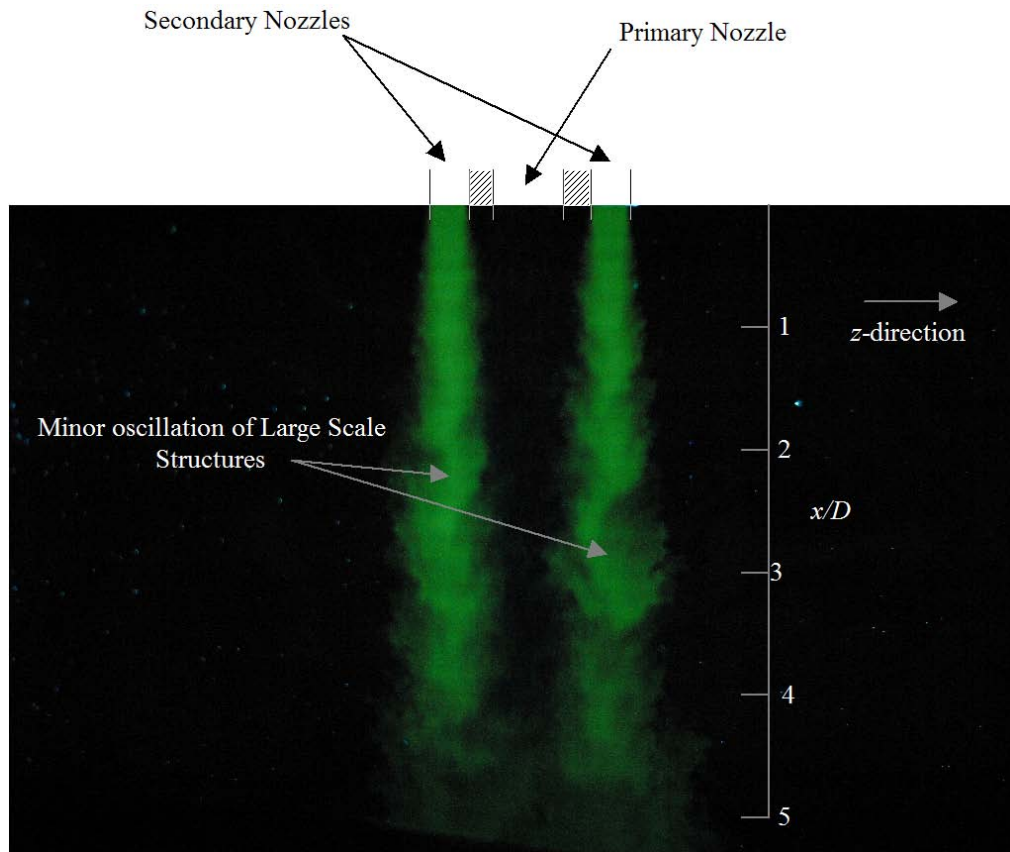


**Figure 4.47:** High resolution image of the instantaneous flow field of the secondary jet through plane A, and  $\lambda=3.6$ , between  $0 < x/D < 6$ .

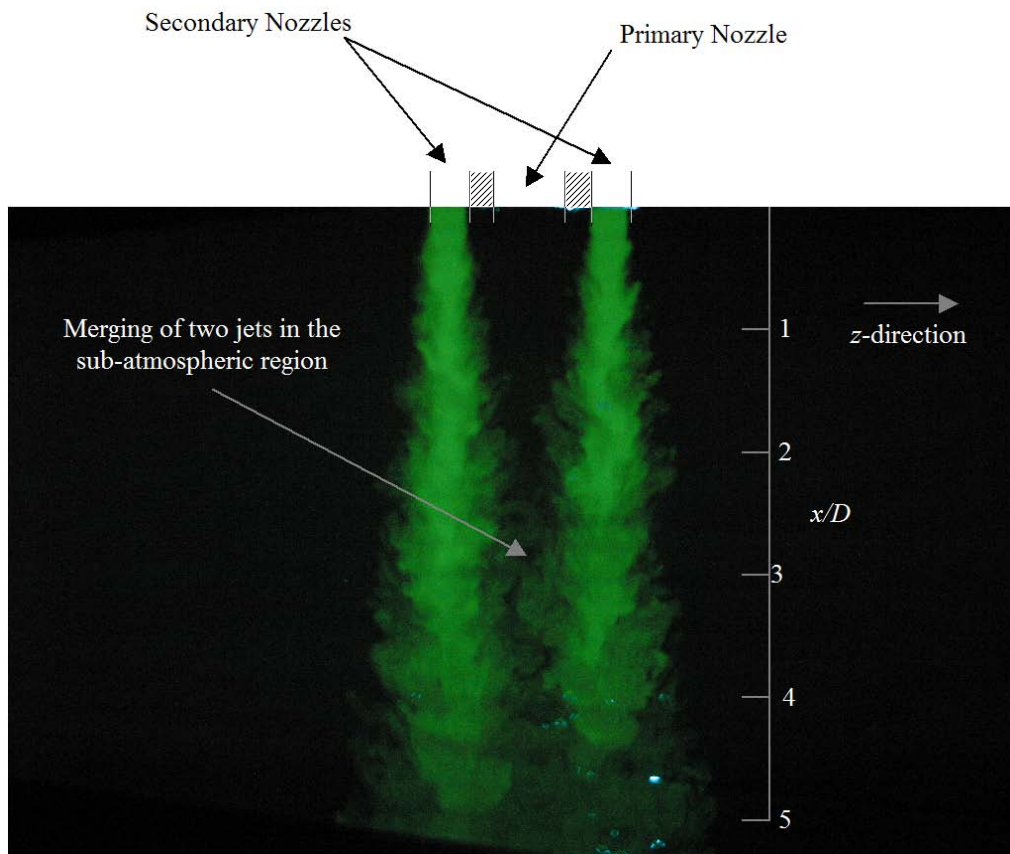


**Figure 4.48:** High resolution image of the instantaneous flow field of the secondary jet through plane A, and  $\lambda=\infty$ , between  $0 < x/D < 6$ .

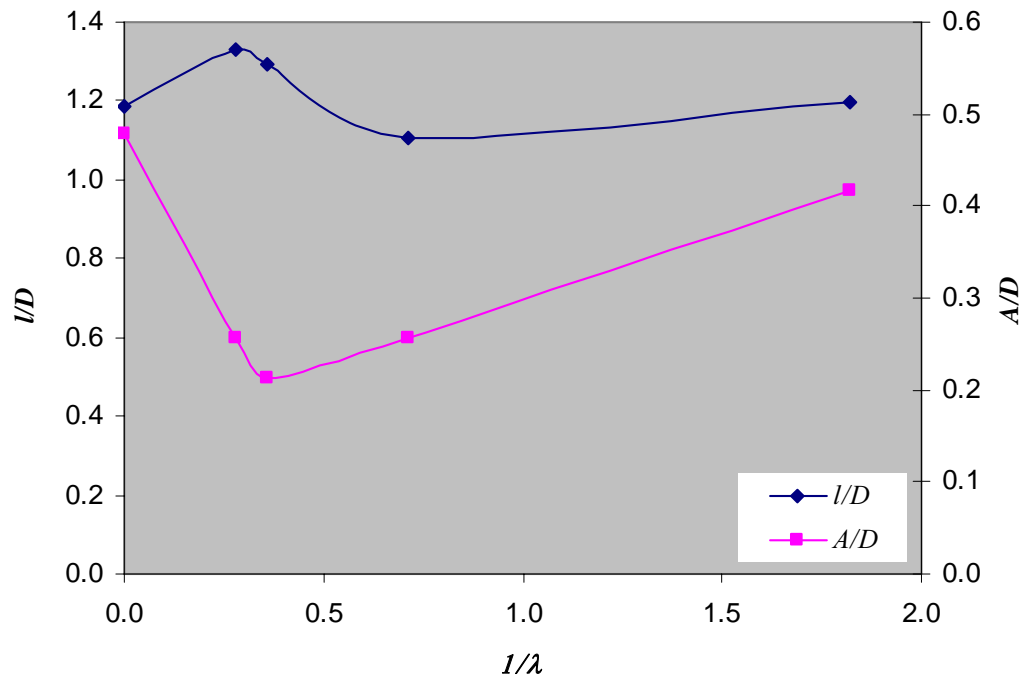


**Figure 4.49:** Dependency on the velocity ratio of the dimensionless wavelength,  $l/D$  and amplitude  $A/D$ , of the sinuous motion of the main coherent structure of the secondary jet through Plane A, as estimated visually and time averaged over ten sequential frames.

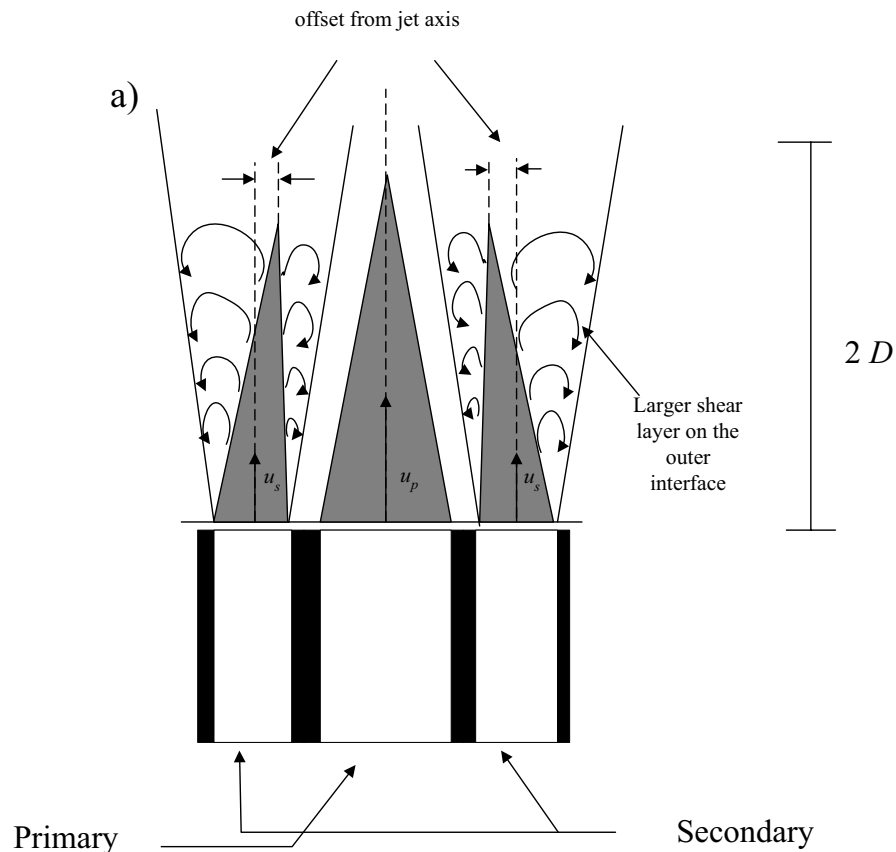


**Figure 4.50:** Schematic diagram of the nature of the shear layer between the primary and secondary jet for the cases when a)  $\lambda = 0.55$ , b)  $1.4 \leq \lambda \leq 3.6$  and c)  $\lambda = \infty$ .

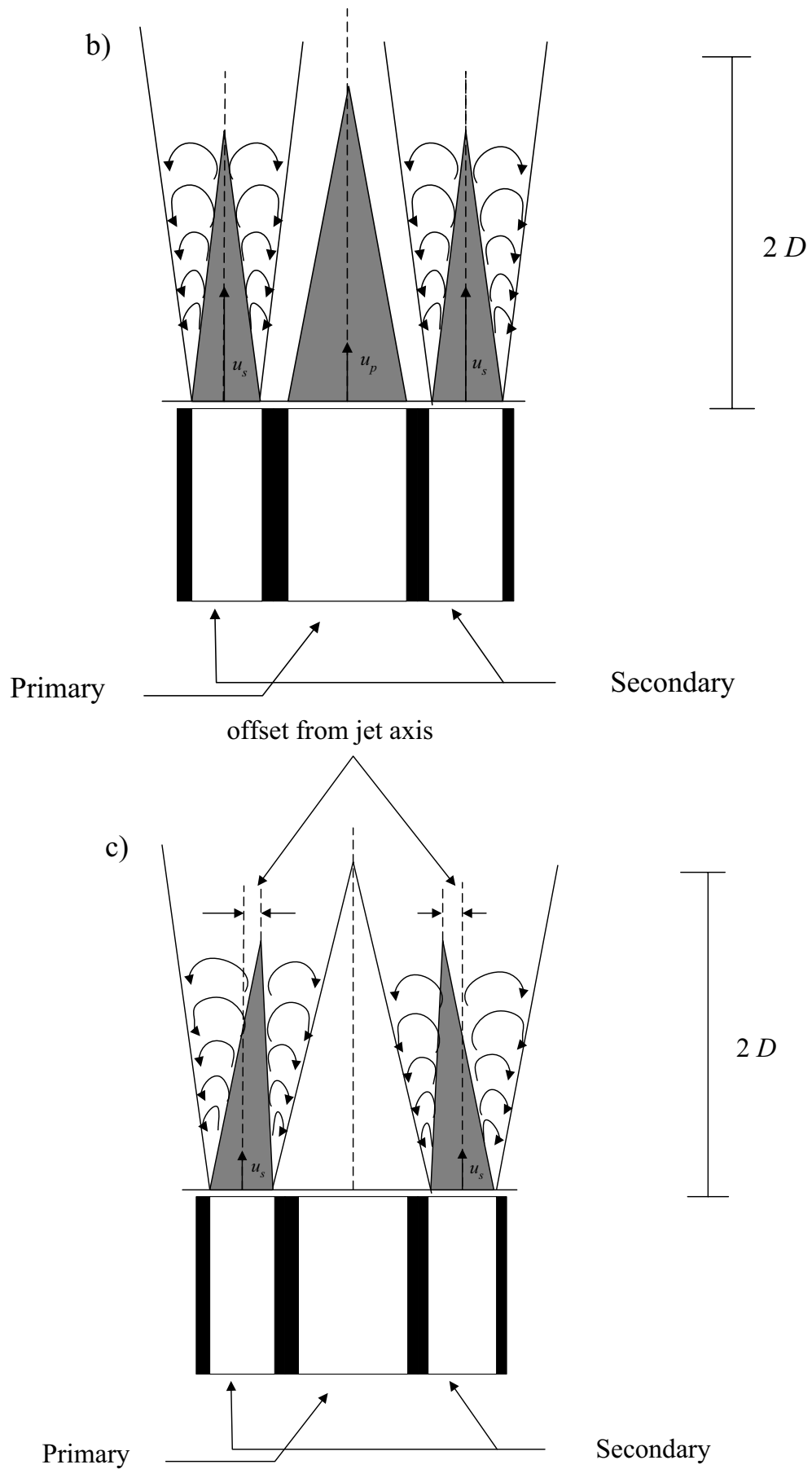


**Figure 4.50:** Schematic diagram of the nature of the shear layer between the primary and secondary jet for the cases when a)  $\lambda = 0.55$ , b)  $1.4 \leq \lambda \leq 3.6$  and c)  $\lambda = \infty$ .

### 4.3.2.2 Plane B

The flow visualisation and interpretations performed on the secondary stream through Plane B are presented in Figures 4.51 to 4.60. The figures show of an influence of the primary jet or velocity ratio on flow through plane B. The change in the sinuous motion with velocity ratio outlined in sections 4.3.1.1, 4.3.1.2 and 4.3.2.1 is also outlined here, with white lines depicting the instantaneous trajectory of the large coherent structure of the secondary jet through plane B. Figure 4.61 is a graph of the dimensionless amplitude and wavelength versus the inverse velocity ratio  $1/\lambda$ , which shows that an increase in velocity ratio causes a reduction in the amplitude and wavelength of the sinuous motion of the main coherent structure of the secondary jet.

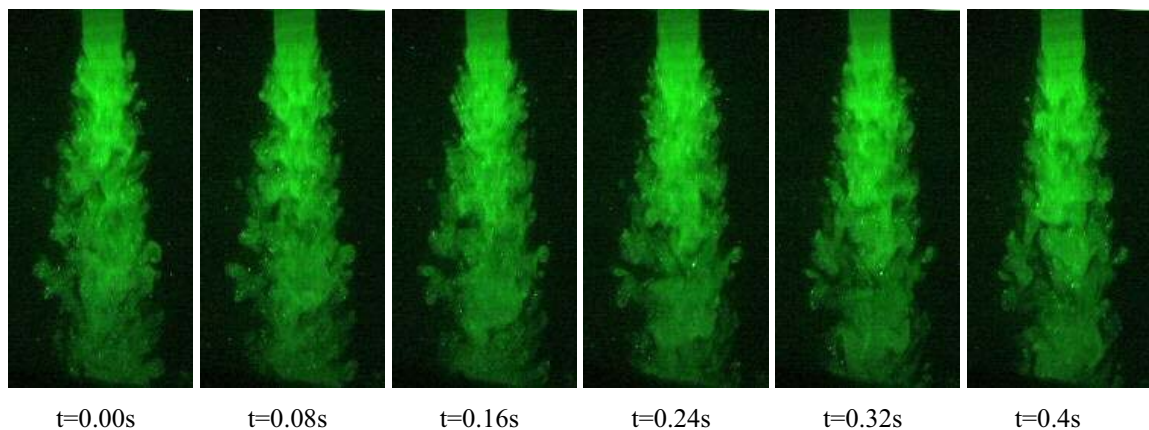


**Figure 4.51:** Video images of the secondary jet at 0.08 second intervals with the laser orientated through Plane B. Velocity ratio is  $\lambda=0.55$ , flow region is  $0 < x/D < 6$ .

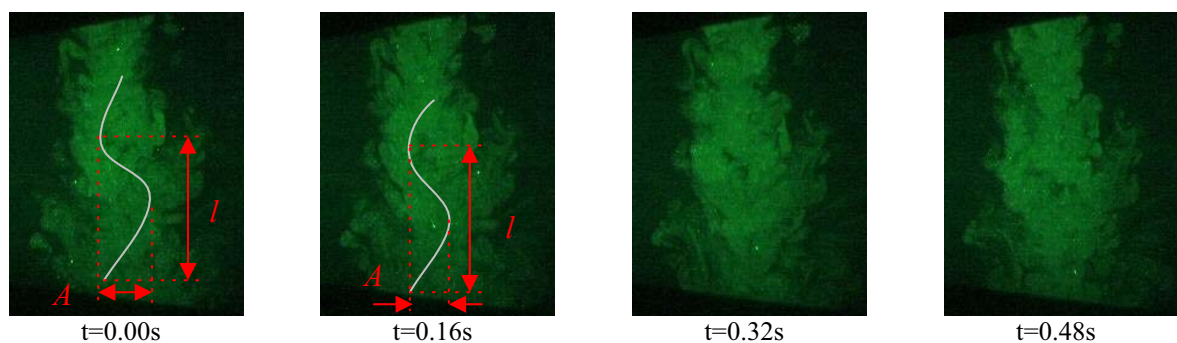


**Figure 4.52:** Video images of the secondary jet at 0.16 second intervals with the laser orientated through Plane B. Velocity ratio is  $\lambda=0.55$ , flow region is  $6 < x/D < 12$ . The white lines highlight the sinuous motion of the main coherent structure,  $A$  being the amplitude and  $l$ , being the wavelength.

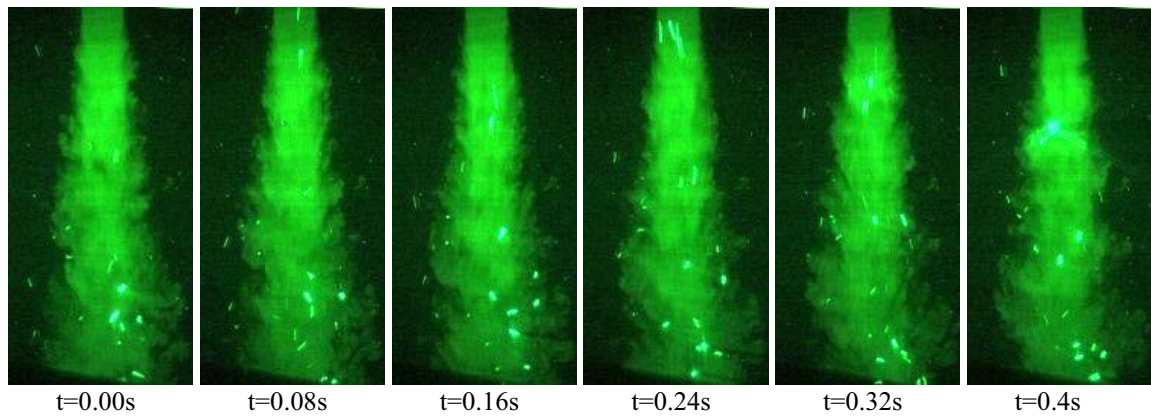


**Figure 4.53:** Video images of the secondary jet at 0.08 second intervals with the laser orientated through Plane B. Velocity ratio is  $\lambda=1.4$ , flow region is  $0 < x/D < 6$ .

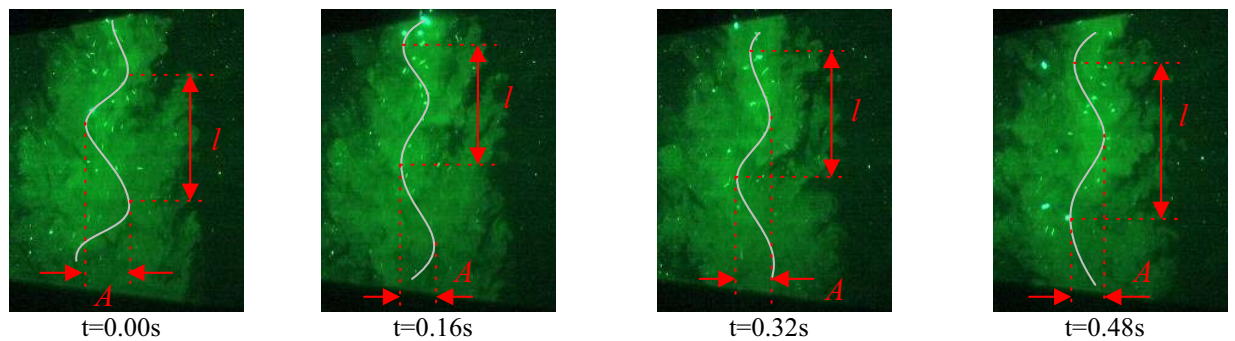


**Figure 4.54:** Video images of the secondary jet at 0.16 second intervals with the laser orientated through Plane B. Velocity ratio is  $\lambda=1.4$ , flow region is  $6 < x/D < 12$ . The white lines highlight the sinuous motion of the main coherent structure,  $A$  being the amplitude and  $l$ , being the wavelength.

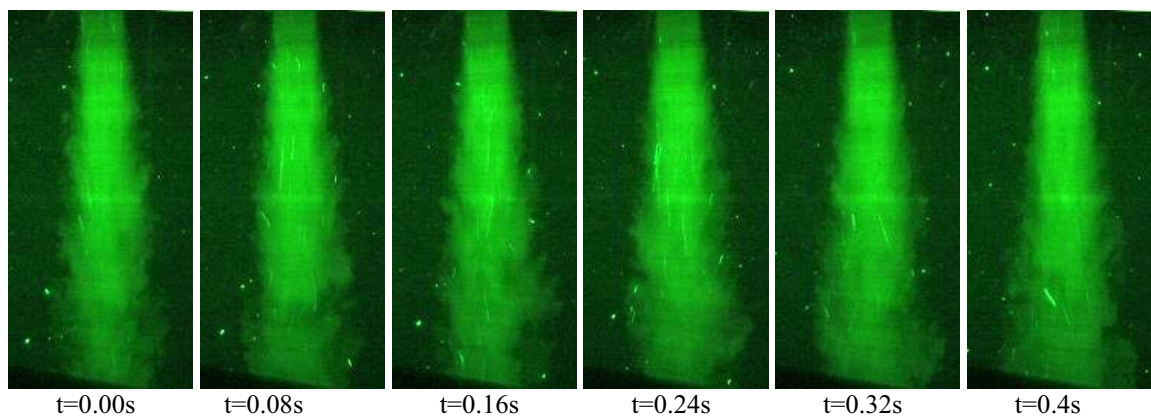


**Figure 4.55:** Video images of the secondary jet at 0.08 second intervals with the laser orientated through Plane B. Velocity ratio is  $\lambda=2.8$ , flow region is  $0 < x/D < 6$ .

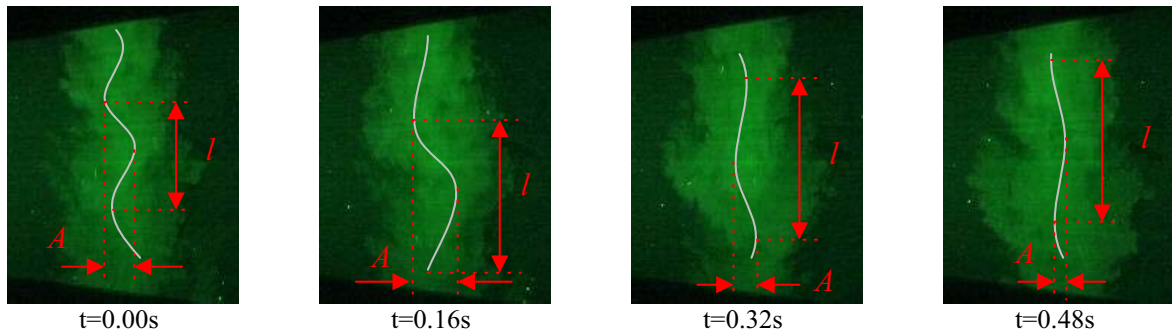


**Figure 4.56:** Video images of the secondary jet at 0.16 second intervals with the laser orientated through Plane B. Velocity ratio is  $\lambda=2.8$ , flow region is  $6 < x/D < 12$ . The white lines highlight the sinuous motion of the main coherent structure,  $A$  being the amplitude and  $l$ , being the wavelength.

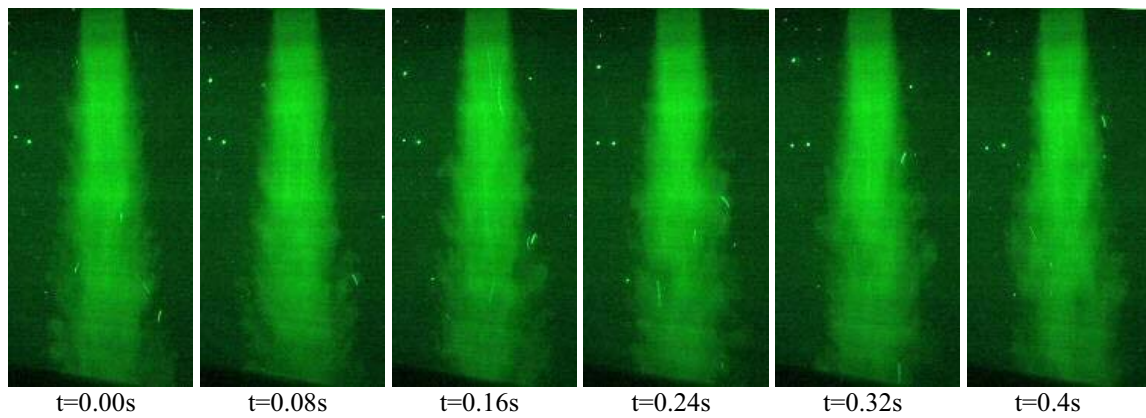


**Figure 4.57:** Video images of the secondary jet at 0.08 second intervals with the laser orientated through Plane B. Velocity ratio is  $\lambda=3.6$ , flow region is  $0 < x/D < 6$ .

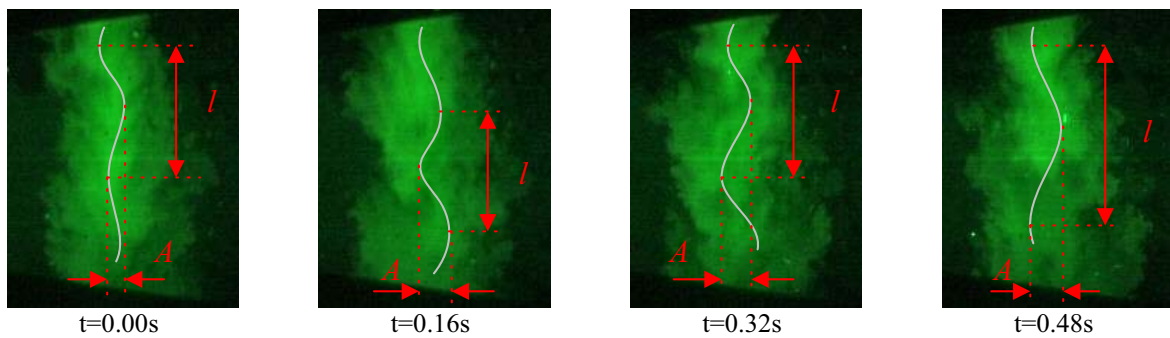


**Figure 4.58:** Video images of the secondary jet at 0.16 second intervals with the laser orientated through Plane B. Velocity ratio is  $\lambda=3.6$ , flow region is  $6 < x/D < 12$ . The white lines highlight the sinuous motion of the main coherent structure,  $A$  being the amplitude and  $l$ , being the wavelength.

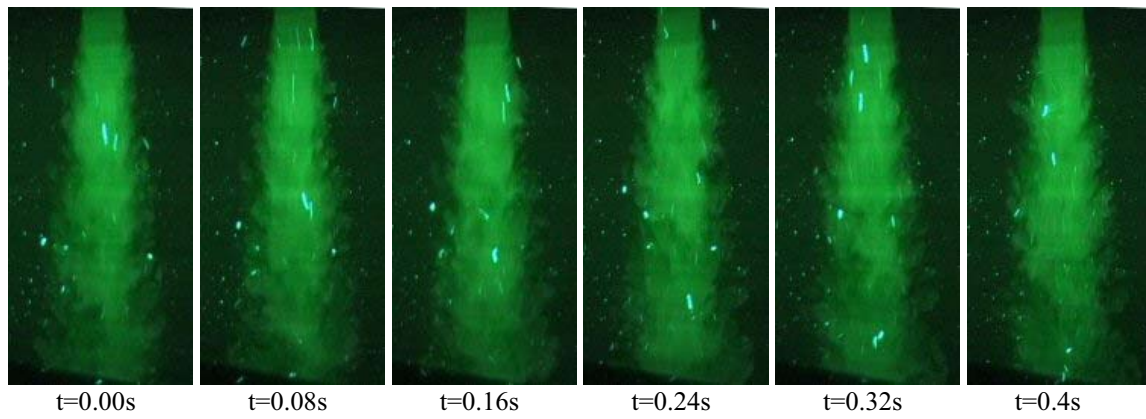


**Figure 4.59:** Video images of the secondary jet at 0.08 second intervals with the laser orientated through Plane B. Velocity ratio is  $\lambda=\infty$ , flow region is  $0 < x/D < 6$ .

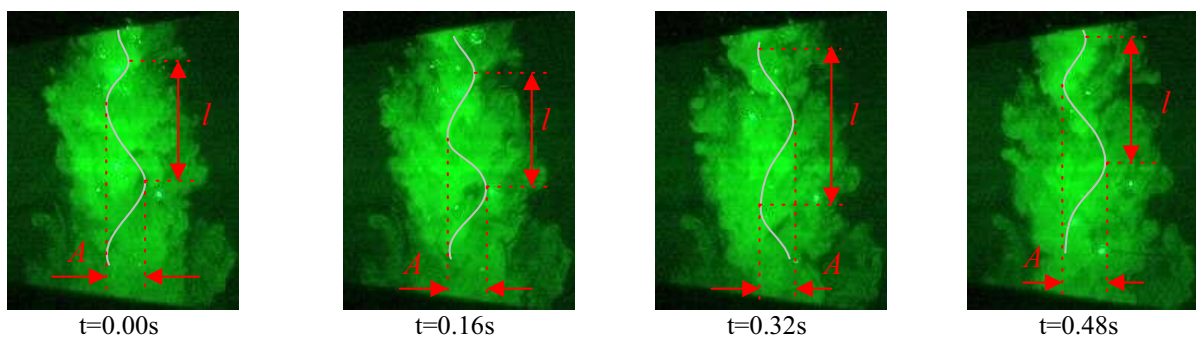


**Figure 4.60:** Video images of the secondary jet at 0.16-second intervals with the laser orientated through Plane B. Velocity ratio is  $\lambda=\infty$ , flow region is  $6 < x/D < 12$ . The white lines highlight the sinuous motion of the main coherent structure,  $A$  being the amplitude and  $l$ , being the wavelength.



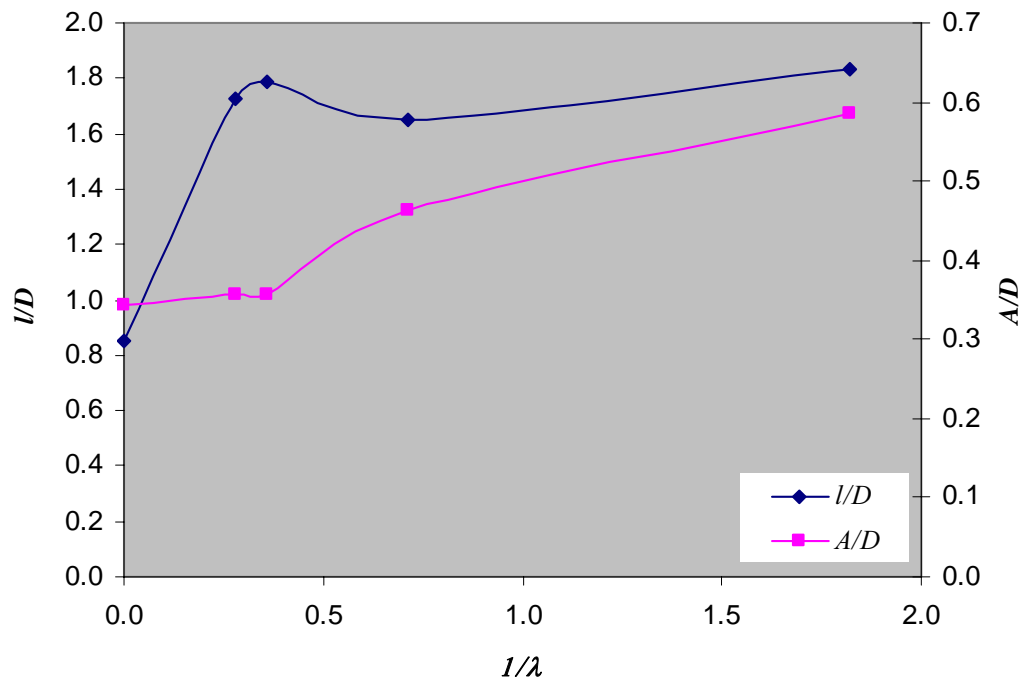


**Figure 4.61:** Dependency on the velocity ratio of the dimensionless wavelength,  $l/D$  and amplitude,  $A/D$  of the sinuous motion of the main coherent structure of the secondary jet through Plane B, as estimated visually and time averaged over ten sequential frames.

### 4.3.3 Discussion

The dominant feature of the coherent motions in a rectangular jet is the vortex ring (Gutmark and Grinstein, 1999). The presence of the ring causes near field axis rotation, a characteristic which enhances the formation of intermediate structures or ‘braids’ between each ring as it deforms with distance downstream. This three dimensional deformation of the rings is a typical characteristic of low aspect ratio rectangular jets ( $AR < 4$ , Grinstein, 1995). The main structure of the primary jet flaps at  $\lambda=0$  due to the turbulent nature of the jet and continues to do so for  $\lambda=0.55$  as shown in Figures 4.4, 4.5 and 4.13. The vortex rings causes entrained fluid from the shear layer to be transferred into the bulk jet flow, hence the process of entrainment. The braids play a major role in axis switching and are responsible for jet entrainment on the minor side and fluid expulsion on the major side (Hart *et al.*, 2004). This cycle of fluid entrainment by the vortex ring and entrainment/expulsion by the braids adjacent to the minor and major sides respectively, is responsible for the natural turbulent growth of bluff rectangular jets ( $AR < 5$ , Rajaratnam, 1976). The vortex ring is the structure mainly responsible for momentum transport (Gutmark and Grinstein, 1999) whereas the braids and smaller structures developing from the

shear layer possess very little momentum. The presence of a co-flowing stream with greater momentum such as the secondary jets for  $\lambda > 0.6$  ( $\kappa > 1$ ) most certainly altered the nature of the vortex ring of the primary jet and thus primary jet itself. The primary jet undergoes increased flapping as the velocity ratio is raised from 1.4 to 2.8 to 3.6 in Figures 4.6-4.11 and 4.14-4.16. The increased flapping commences at approximately  $x/D \sim 1$ , ie at approximately the same distance at which the rings begin to develop (Hart, 2001) and at which the different momentum bearing vortex rings between the primary and secondary jet start to interact. The main-coherent structures follow a oscillating movement, this ‘sinuous’ movement as defined by Yoda *et al.*, (1994) has a well defined wavelength and amplitude. It has been demonstrated that these properties vary with velocity ratio. Also, an analysis of the time averaged distance between the main coherent structures of the primary jet through plane A, similar to that of Mungal and Hollingsworth (1989) shows that the distance between each structure diminishes with an increase in velocity ratio.

It can only be hypothesized that the driving force of the mixing between the primary and secondary jet is controlled by the difference in momentum or by the secondary to primary jet momentum exchange because the momentum ratio has not been independently varied with velocity ratio. However, there is a clear influence of the co-flowing conditions on the main coherent structure of either the primary or secondary jet through all planes. The main coherent structure identified in Sections 4.3 is most probably the vortex ring, which in turn is responsible for momentum transfer. The mechanism for the instability of the primary jet at the higher velocity ratios is unclear; a realistic scenario is related to the mixing cycle arranged between the ring and braids;

An increase in velocity ratio causes the secondary jet vortex rings to dominate other structures present in the primary jet due to the favourable momentum transfer. The secondary vortex ring having higher momentum may immediately dominate all low momentum structures in the primary jet, such as structures in the shear layer and the braids. This phenomena alters the natural ring-braid development of stable primary jet development thus inducing a change in the flow conditions.

It is only speculative at this stage that the behaviour of the main coherent structures of the primary and secondary jet are controlled by momentum ratio and momentum exchange between the primary and secondary jets. There is strong evidence suggesting that the higher velocity ratios alter the nature of the flapping of the primary jet and lower velocity ratios alter the nature

of the flapping of the secondary jet. However, whether or not the primary and secondary flows are controlled by momentum is uncertain without independently varying the momentum ratio from the velocity ratio.

At  $\lambda > 2.8$ , larger scale eddies appear in the vicinity of the nozzles (primary jet, plane A) showing irregular shear layer growth. It is possible that these eddies are a bi-product of the re-circulatory phenomena depicted in Figure 4.18. The re-circulatory phenomena occurs due to the bluff bodies present between the primary and secondary jets which is observed only in the immediate vicinity of the nozzle exit plane, where ring development has not yet occurred. Previous studies in the literature (Dahm *et al.*, 1992 Namazian and Kelly, 1992 Ko and Kwan, 1976 Buresti *et al.*, 1998 and Champagne and Wygnanski, 1971 Alpinieri, 1964, Chigier and Beer, 1964 in Beer and Chigier, 1972) suggest that velocity rather than momentum is responsible for re-circulation in the near nozzle regions of co-annular or coaxial systems. The shear layer of the secondary jet through plane A is also subject to change with velocity ratio, due to an antisymmetric nature of the secondary jets through plane A. The secondary jets tend to deviate from their geometric axes towards the primary jet axis at  $\lambda < 1$  and  $\lambda = \infty$ . This causes the structures in the shear layer not sharing an interface with the primary jet to grow in size with respect to the same shear layer at  $\lambda > 1$ .

It is uncertain whether or not the change in flow structure with velocity ratio ( $\lambda$ ) will actually be observed in the main burners of full scale boilers. Comparison of the experimental velocity ratios, the momentum flux and momentum ratios and secondary to primary velocity and momentum differences of the experimental conditions to the conditions inside the Yallourn W1 boilers are illustrated in Tables 4.3 and 4.4. The data used for calculation of furnace conditions was retrieved from Perry and Pleasance (1983b). This Comparison suggests that momentum and momentum flux ratio are very similar between the experiments and the boilers. Comparison of the velocity and momentum differences however, suggest that, if they are the responsible driving force for the major flow features in the flow visualisation experiments rather than the velocity, momentum flux and momentum ratios, the developed flow structures may be different in the main burners of an industrial furnace.

Velocity ratio, $\lambda$	Momentum flux ratio, $\gamma$	Momentum ratio, $\kappa$	Velocity difference (sec-prim), m/s	Momentum difference (sec-prim), Newton
0.55	0.38	0.18	-6.71	-113.62
1.4	2.48	1.14	5.96	19.2
2.8	9.93	4.56	26.82	490.38
3.6	16.42	7.53	38.74	900.66

**Table 4.3:** Secondary to primary, velocity ratio, momentum flux ratio, momentum ratio, velocity and momentum gradients for the Yallourn W1 using velocity ratio similarity.

Velocity ratio, $\lambda$	Momentum flux ratio, $\gamma$	Momentum ratio, $\kappa$	Velocity difference (sec-prim), m/s	Momentum difference (sec-prim), Newton
0.55	0.30	0.1815	-0.19	-0.03
1.4	1.96	1.176	0.17	0.01
2.8	7.84	4.704	0.77	0.13
3.6	12.96	7.776	1.12	0.24

**Table 4.4:** Secondary to primary, velocity ratio, momentum flux ratio, momentum ratio, velocity and momentum gradients for the experimental conditions.

## 4.4 Time Averaged Analysis

### 4.4.1 Introduction

The flow visualisation of the rectangular jets can be extended to provide some measurements of the time-averaged properties of the jet. The images cannot be used to calculate mixture fractions of the flow because they have not been corrected for the background signal, laser beam profile and fluorescent laser response. However, they can be used to determine jet spread (e.g. half widths) because the variation in laser intensity in the cross stream direction is small relative to the variation in the downstream direction.

### 4.4.2 Image Processing Technique

The video footage captured in the flow-visualisation experiments was digitally transferred using Windows Movie maker into a 20 second 576x720 pixel video for Windows movie file. The pixel resolution varied between 0.35 to 0.37 mm per pixel depending on the camera zoom. The image

processing was done by developing a code in the Matlab environment using Matlab's Image processing toolbox. The resultant time averaged images were compiled from 300 independent images using footage captured at a standard 25 frames per second.

The rate of spreading of any jet is quantified by determining the position of the half-width or half radius, which is the position at which the concentration is half that on the centreline. The half-width is a relative measure of the largest turbulent structures in the flow (Tennekes and Lumley, 1972). This may be the largest structures which dominate the flow, for example large eddies deriving from round jets with high blockage ratio bluff bodies (Huang and Lin 2000, Balachandar *et al.*, 1997). In the case of rectangular jets, the dominant large scale flow feature is the vortex ring.

The intensity of each pixel in the time-averaged image was the normalised locally with respect to the maximum pixel intensity in the same row, (ie at the same downstream distance).

#### 4.4.3 Time Averaged Results

The time-averaged results delivered satisfactory delineation of the half width contour for each condition. Figures 4.62 to 4.68 present the normalised intensity profiles for the primary and secondary jets through planes A, B and C using the conditions specified in Table 4.1. The colour contours of each normalised image were manipulated so that pure background fluid corresponds to blue and pure jet fluid to red. The concentration profile at half the maximum value is shown in white, and the half-widths have been delineated with a faint black line, over the white background.

The effect of velocity ratio on the shaping of the primary jet is clearly evident in Figure 4.62. The near nozzle region is clearly affected by the presence of the bluff body. The recirculation zone behind the bluff bodies becomes a significant feature for  $z/D=0.5$  and  $-0.5$  for  $x/D<0.5$ . The primary jet contracts at  $2<x/D<5$  and then expands in the far field as velocity ratio is increased (Figure 4.63).

It was concluded in Section 4.3, that it is highly likely that the majority of the mixing between the primary and secondary fluid occurs through plane A. However, as illustrated in Figure 4.64, higher velocity ratios also cause a reduction in jet spread of the primary jet through plane C in

the region between  $2 < x/D < 5$ . The reduction in jet spread may be attributed to the fact that the secondary jet has sufficient momentum to affect the small-scale structures of the primary jet, through all planes, even through plane C. The contraction then results in greater rates of spread in the far field for  $x/D > 6$  (Figure 4.65).

A change in velocity ratio does not affect the spread of the secondary jet, in either plane A (Figure 4.66) or B (Figures 4.67 and 4.68). The notion of jet half-width is only viable before jet merging plane A and not for merged jets, hence the discussion will be restricted to the near field region for the secondary jet. For  $\lambda = \infty$  (Figure 4.66e) the inner half-widths of the two jets merge at a distance of approximately  $x/D = 3.7$ . It can be deduced that when the primary jet is present (Figures 4.66 a-d) the primary momentum prevents the secondary streams merging until  $x/D = 5.2$ . The time averaged analysis through plane B (Figure 4.67 and 4.68) indicates that increasing velocity ratio widens the secondary jet.

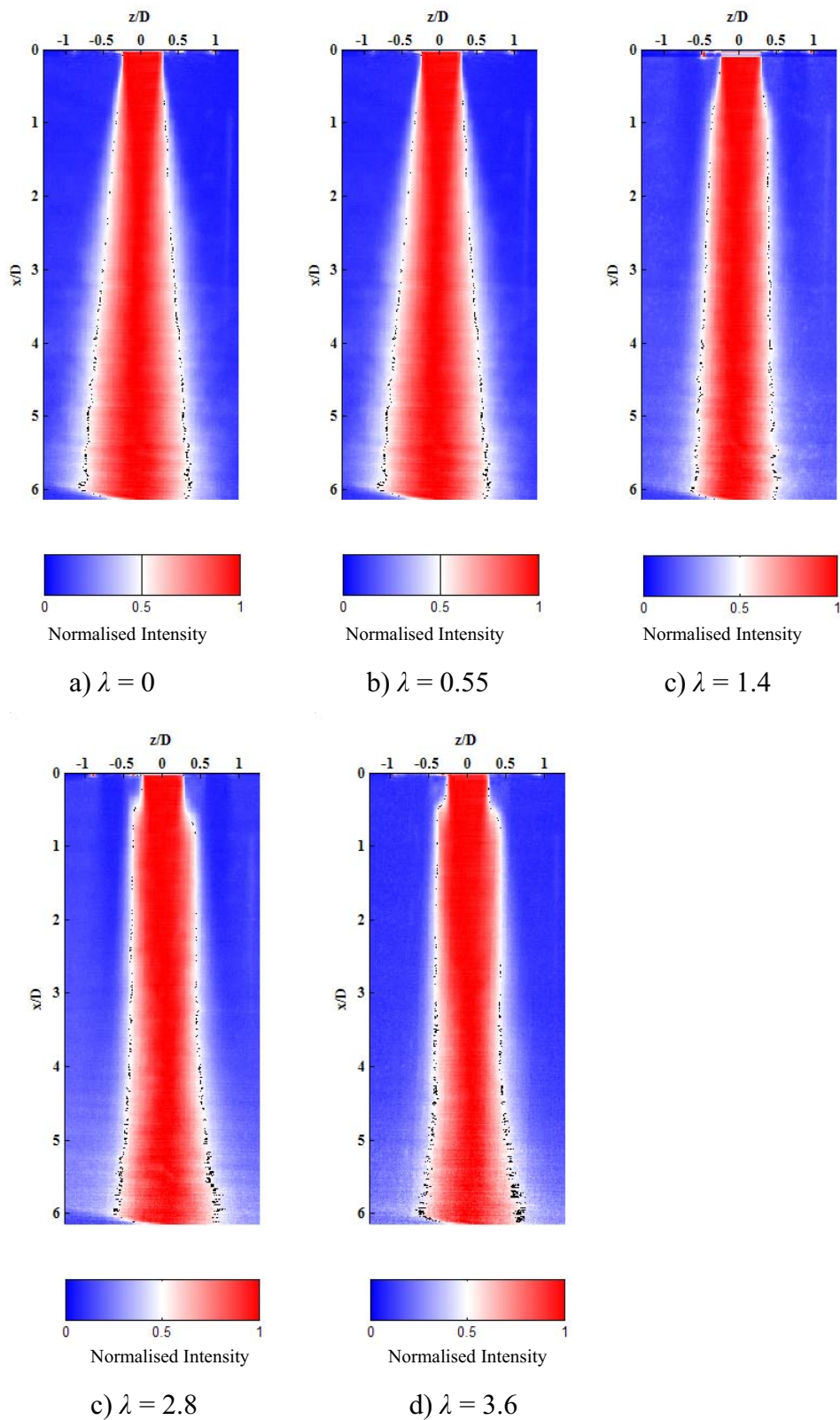


**Figure 4.62:** Normalised intensity for the primary jet with the laser orientated through Plane A in the region between  $0 < x/D < 6$ . Refer to Table 4.2 for jet conditions.

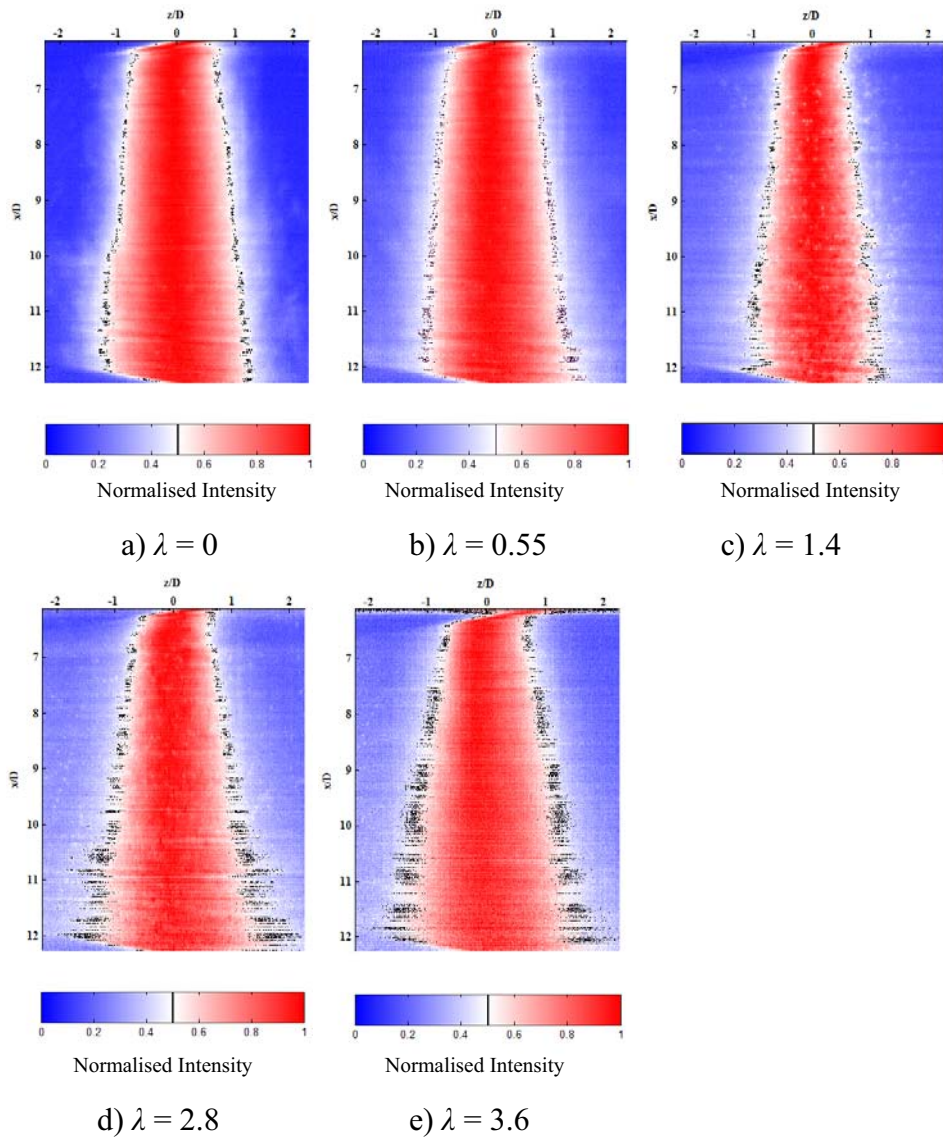


**Figure 4.63:** Normalised intensity for the primary jet with the laser orientated through Plane A in the region between  $6 < x/D < 12$ . Refer to Table 4.2 for jet conditions.



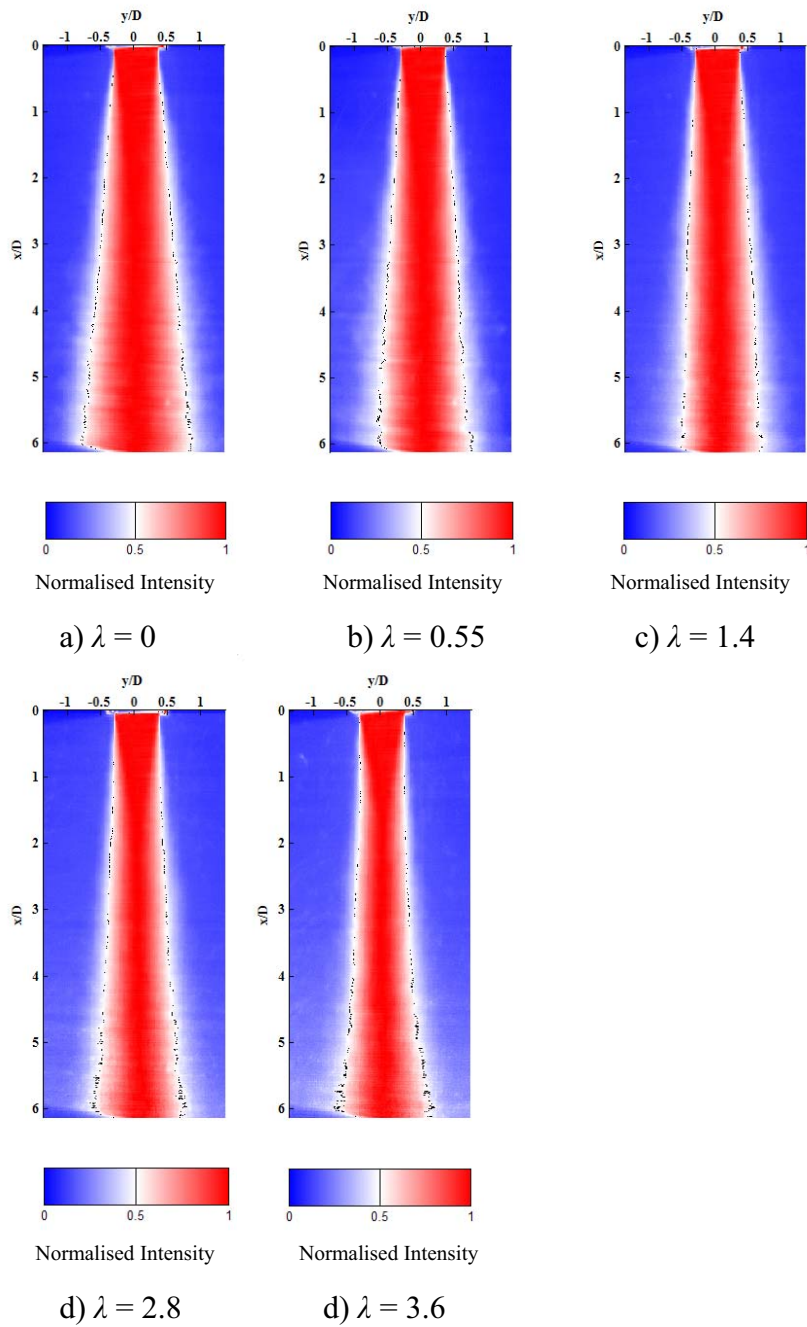


**Figure 4.64:** Normalised intensity for the primary jet with the laser orientated through Plane C in the region between  $0 < x/D < 6$ . Refer to Table 4.2 for jet conditions.

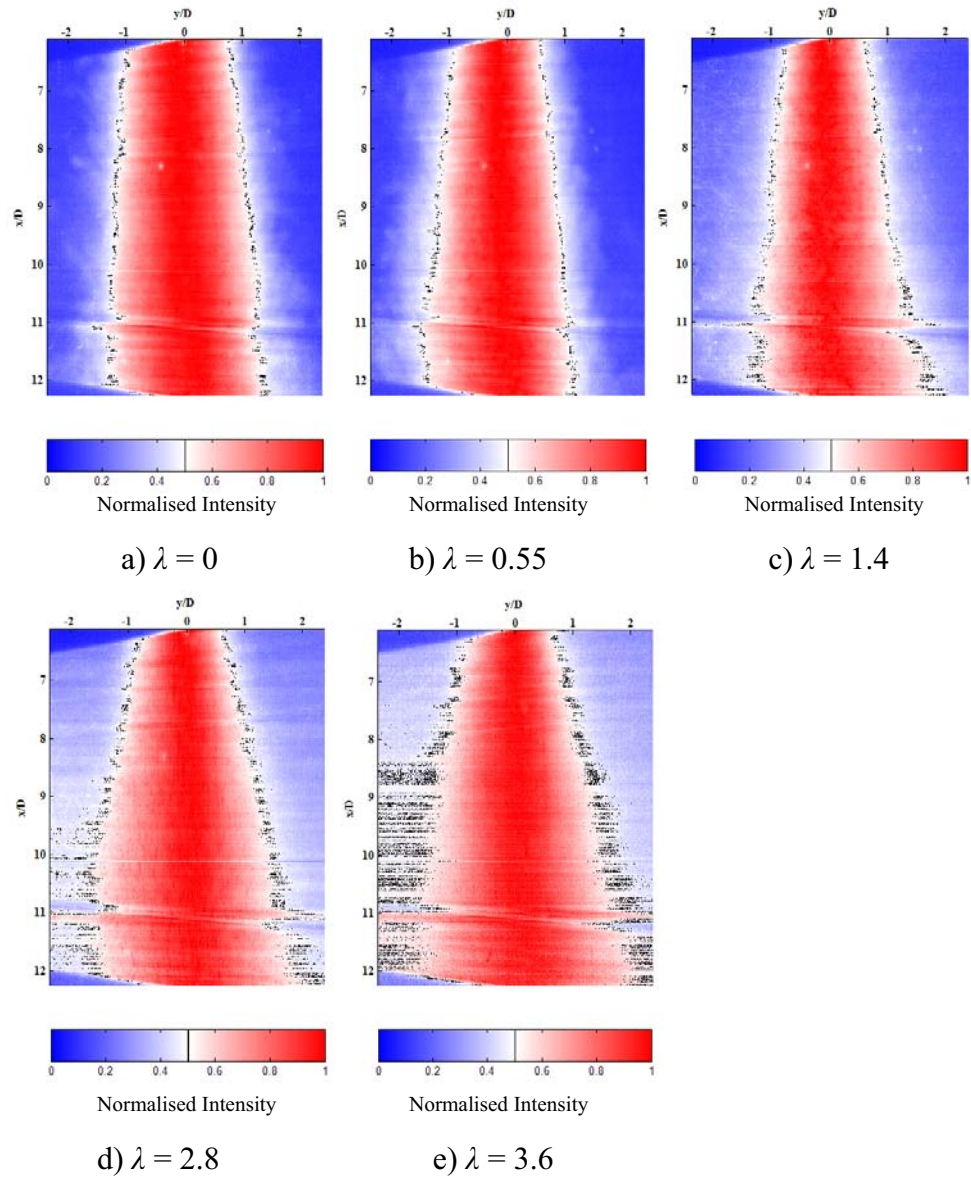


**Figure 4.65:** Normalised intensity for the primary jet with the laser orientated through Plane C in the region between  $6 < x/D < 12$ . Refer to Table 4.2 for jet conditions.

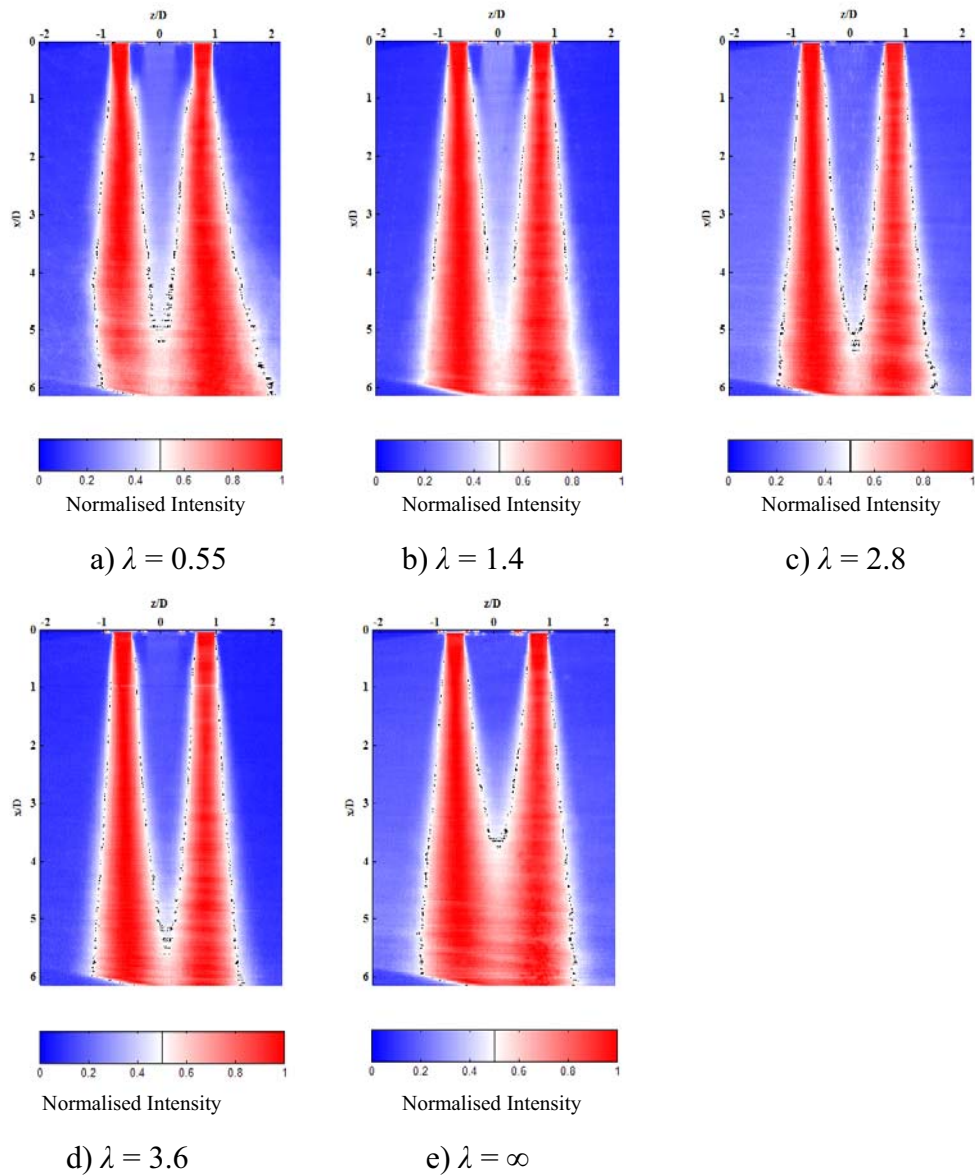


**Figure 4.66:** Normalised intensity for the secondary jet with the laser orientated through Plane A in the region between  $0 < x/D < 6$ . Refer to Table 4.2 for jet conditions.

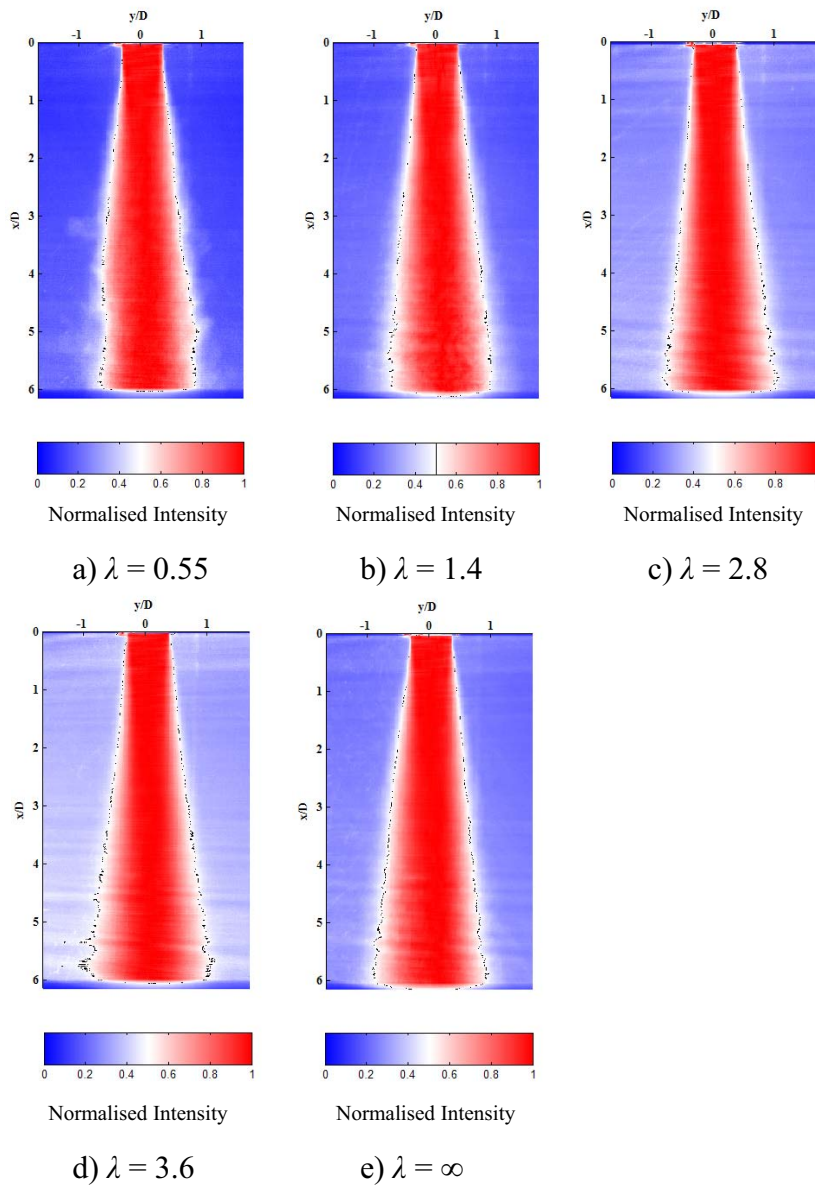


**Figure 4.67:** Normalised intensity for the secondary jet with the laser orientated through Plane B in the region between  $0 < x/D < 6$ . Refer to Table 4.2 for jet conditions.

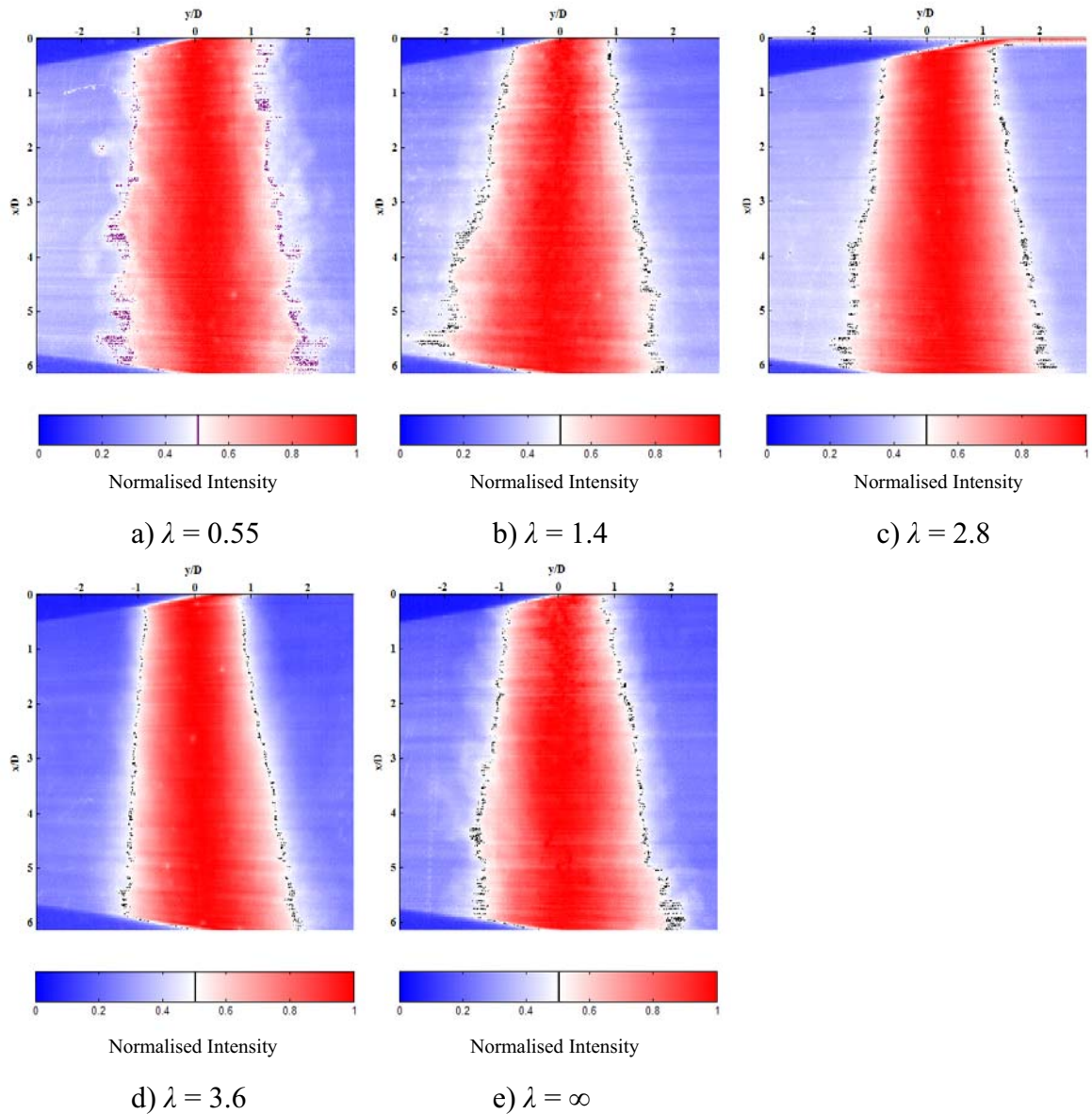


**Figure 4.68:** Normalised intensity for the secondary jet with the laser orientated through Plane B in the region between  $6 < x/D < 12$ . Refer to Table 4.2 for jet conditions.

#### 4.4.4 Statistical Analysis

Figures 4.69 to 4.72 show the normalised half widths ( $r_{1/2}/D$ ) of the primary jet through planes A and C, and of the secondary jet through planes A and B. The primary jet half-width is clearly affected by the velocity ratio in the near field in both plane A and plane C. Preliminary work (Mullinger *et al.*, 2002) was not able to resolve this effect, and was limited to velocity ratios between 0 and 2.

Equation 2.25 can be used to evaluate the half-width spread constant,  $K_2$  and virtual origin  $x_{o,2}/D$ . Comparison can then be made with the spread of the better understood round jet. In order to evaluate these parameters a line of best fit was applied for each measurement. The spreading patterns of the primary jet in planes A and C and the secondary jet in plane B are symmetrical. Consequently the values of  $K_2$  and  $x_{o,2}/D$  were averaged from both sides of the jet (positive and negative regions in Figures 4.69, 4.70 and 4.72). However, this was not applicable for a single secondary jet (Figure 4.71) in plane A, since there is no symmetry.

Figures 4.73 and 4.74 shows the values of the half-width spread constant,  $K_2$  and secondary virtual origin,  $x_{o,2}/D$  as a function of the velocity ratio. The value of  $K_2$  in the primary jet decreases when  $\lambda$  is increased from 0 to 0.55 in both planes A and C. With a further increase in  $\lambda$  ( $\lambda > 1$ ), the primary jet is dominated by a higher momentum flux from the secondary jet, thus increasing jet spread rate. The dimensionless virtual origin  $x_{o,2}/D$  plotted in Figure 4.73 for the primary jet on planes A and C has a maximum situated on  $\lambda = 0.55$  and generally, much lower values for other  $\lambda$ .

The values of  $K_2$  of the secondary jet are quite different to those of the primary jet. Note that in Figure 4.74, the inverse velocity ratio is used so that the term  $\lambda = \infty$  can be plotted. Through plane A, where the secondary jet shares an interface with the primary, a drop in  $K_2$  with  $1/\lambda$  is incurred between  $0 < 1/\lambda < 0.714$  (or  $1.4 < \lambda < \infty$ ). However, where the secondary jet interfaces with stagnant fluid there is little change with  $1/\lambda$ . The magnitude of  $K_2$  is similar to values from the literature. For instance, Dahm and Dimotakis (1990) used PLIF with a pipe jet in water and  $K_2$  as 0.104, Law and Wang (2000) under similar conditions, observed  $K_2 = 0.108$ .

The virtual origin of the secondary jet on the primary jet side (Figure 4.74) experiences an exponential rise from  $1/\lambda = 0$  to  $1/\lambda = 0.71$  ( $\lambda = 0.55$ ). This trend is observed for both planes A and C. The virtual origin of the rectangular jets varies between 1 and 7 depending on the jet plane of visualisation and velocity ratio. In comparison a pipe jet has  $x_{o,2}/D = 2.57$  (Papanicolaou and List, 1988). Together with the analysis of  $K_2$ , the main conclusion that can be drawn is that a change in velocity ratio plays a major role in jet spread of the primary jet, and a weaker influence on the secondary.

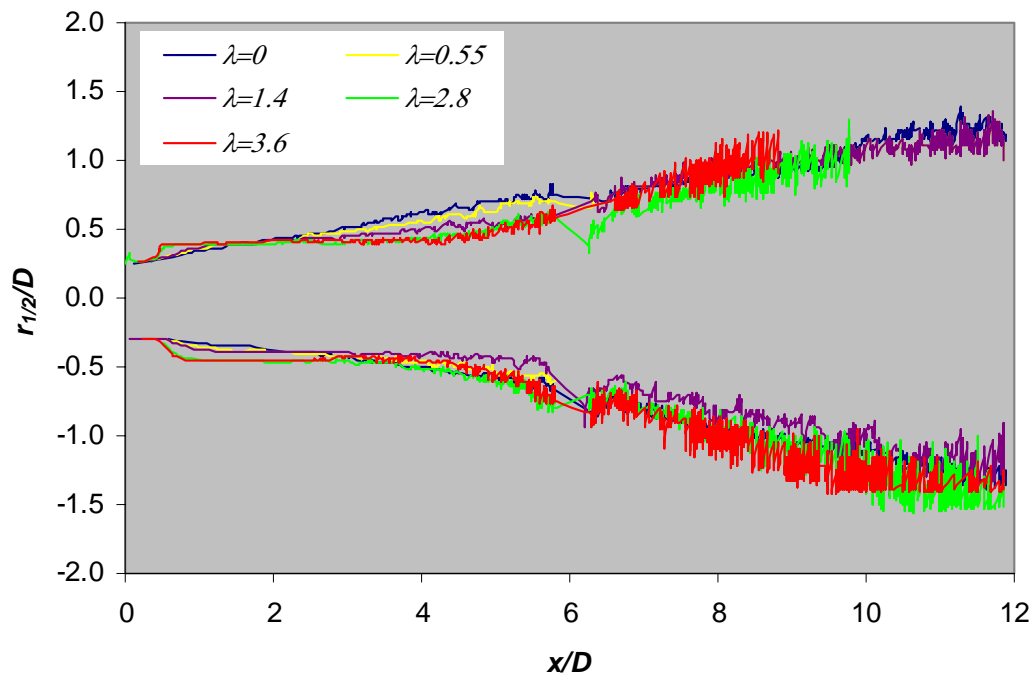


**Figure 4.69:** Normalised half width versus axial distance for the primary jet on plane A. Refer to Table 4.2 for jet conditions.

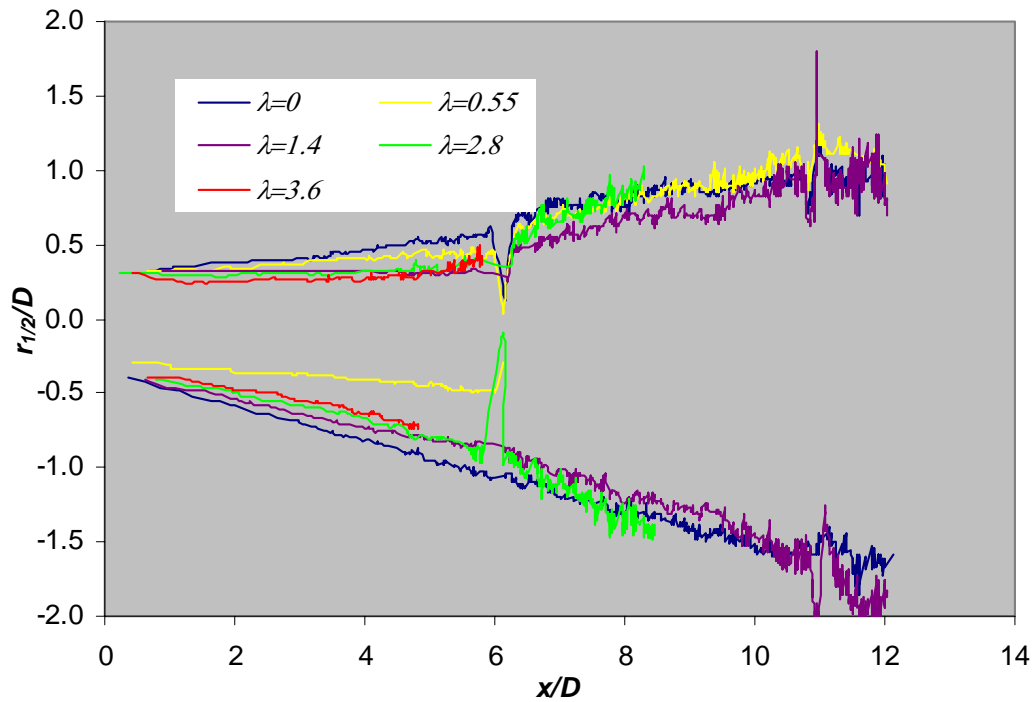


**Figure 4.70:** Normalised half width versus axial distance for the primary jet on plane C. Refer to Table 4.2 for jet conditions.

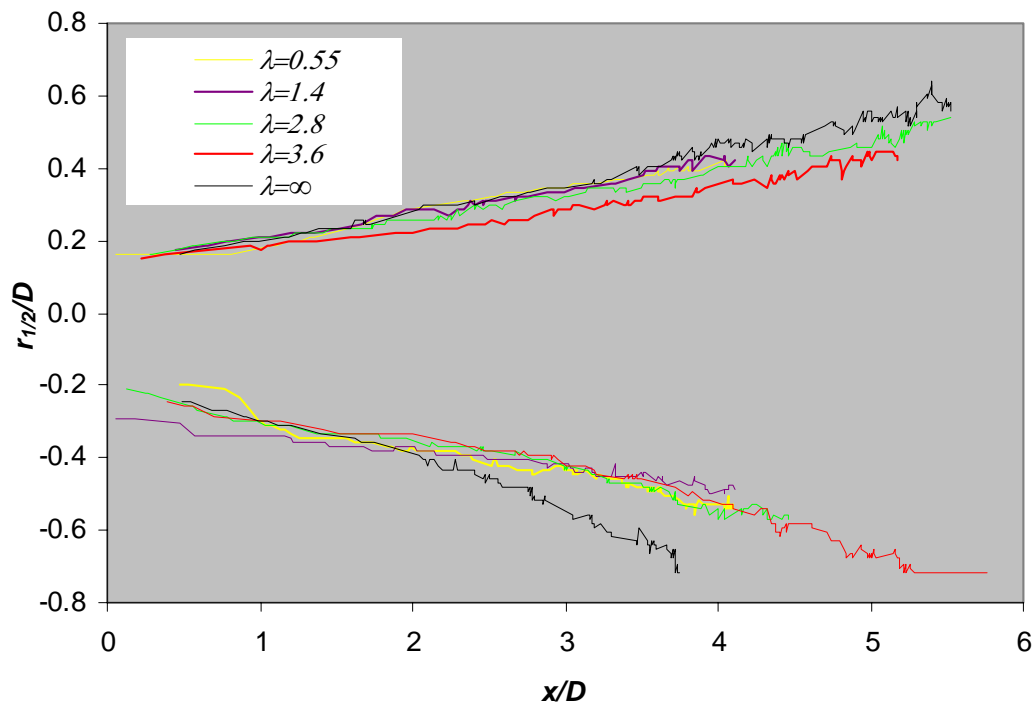


**Figure 4.71:** Normalised half width versus axial distance for the secondary jet on plane A, with the origin positioned on the axis of the secondary jets. The side sharing an interface with the primary jet is  $r_{1/2}/D < 0$ . Refer to Table 4.2 for jet conditions.



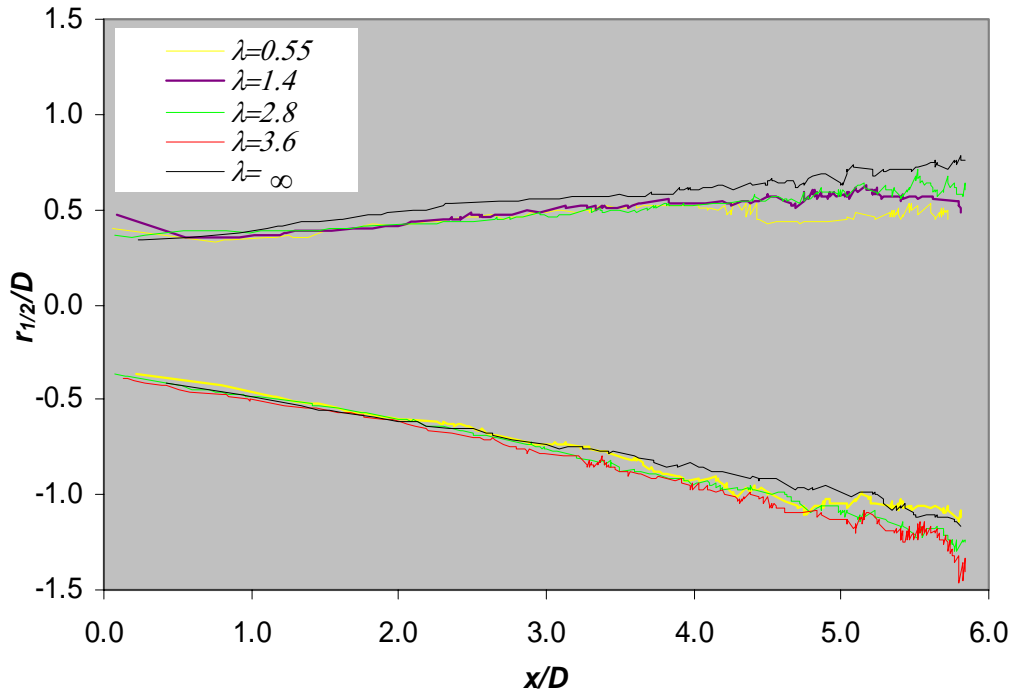


**Figure 4.72:** Summary and comparison of the normalised half width versus axial distance of the secondary jet on plane B. Refer to Table 4.2 for jet conditions.

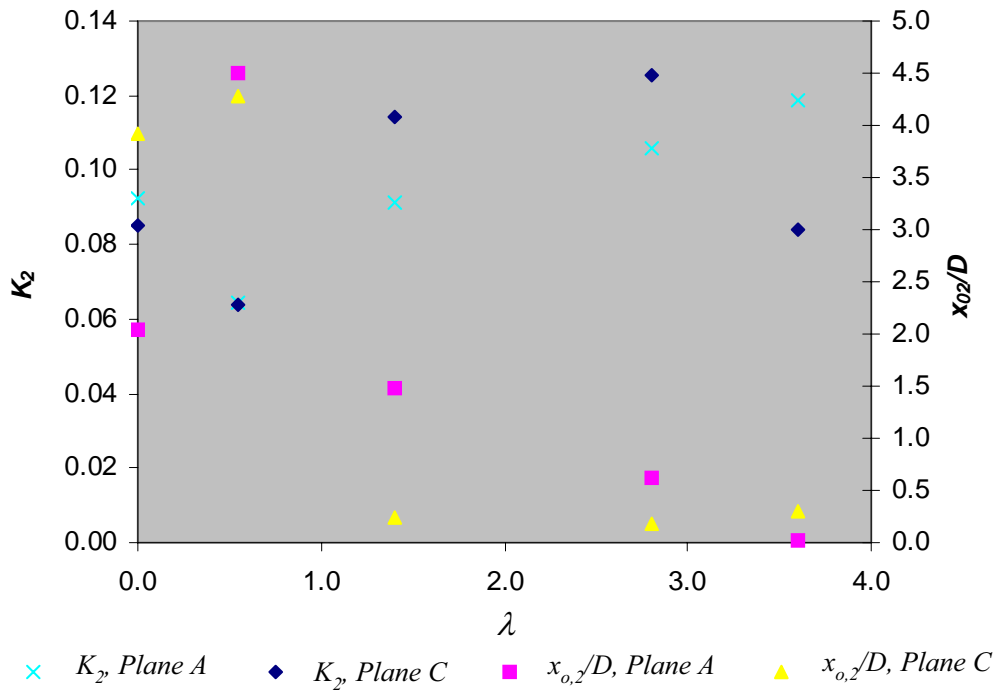


**Figure 4.73:** The half-width spread constant for the secondary jet,  $K_2$ , and spread virtual origin,  $x_{o,2}/D$ , for the primary jet on planes A and C.

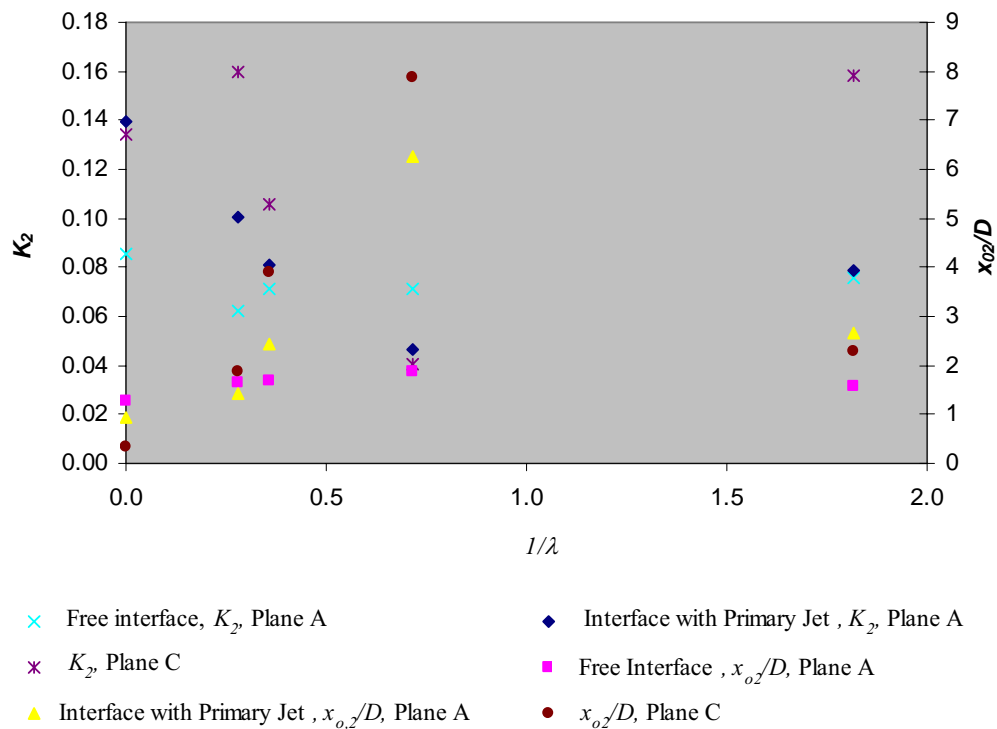


**Figure 4.74:** The half-width spread constant,  $K_2$  and spread virtual origin,  $x_{0,2}/D$ , of the secondary jet interfacing with the primary jet and stagnant fluid on plane A and plane B.

## 4.5 Conclusions

A flow visualisation technique has been used to assess the effects of large and small scale turbulent motions in a geometrically scaled version of burner jets used in brown coal fired boilers. The instantaneous images show that the presence of a secondary jet has a dramatic effect on the flow characteristics of the primary. The majority of these changes occur through plane A and become more noticeable as the secondary to primary velocity ratio ( $\lambda$ ) is increased. The presence of the secondary jet causes primary jet fluid to be entrained, which alters the deformation process of the vortex ring in the primary jet. The natural oscillation of the vortex ring forms braids which participate in the development of the shear layer. However, it is possible that these braids are altered in length and frequency by the co-flowing conditions provided by the secondary stream thus interrupting the natural formation of the primary jet which very well could be the flapping of the primary jet witnessed in Section 4.3.1.

Further downstream the secondary stream interacts with large structures in the primary jet causing further instability. The amplitude of the oscillation of the main structure of the primary

jet increases with  $\lambda$ . Higher  $\lambda$  also changes the nature of the developing shear layer, causing the outer structures to follow the direction of the secondary jet, especially for  $\lambda=2.8-3.6$ . The presence of the bluff body between the two jets also contributes to jet development particularly at  $\lambda=2.8-3.6$ , where pulsating structures occur slightly downstream from the re-circulation zone.

Changes in flow characteristics were also observed for the secondary jet through plane A. The structures in the shear layer sharing an interface with the primary jet are dominated by those associated with the flow with the greater momentum. For  $\lambda=0.55$ , the participating shear layers have the adjacent structures re-directed into the primary stream, whilst those of the shear layers sharing an interface with the free fluid, evolve in their natural direction. This disparity is a source of instability of the flow, not witnessed with the other velocity ratios.

The effect of velocity ratio on the main coherent structure of the primary and secondary jets through planes B and C, has been assessed and the dependency proved. The change in the main coherent flow structure, or the vortex ring, of either primary or secondary jet with velocity ratio may suggest that the dominant mixing structures of these rectangular jets may be momentum controlled. The change in the behaviour of the main coherent structures dictate the nature of shear layer of the primary and secondary jets, particularly through plane A.

The time-averaged analysis reveals that the half-width of the primary jet changes with  $\lambda$ . To be more specific, for  $\lambda=2.8-3.6$  the recirculation in the near field of the primary jet through plane A causes an expansion of the jet. The large entrainment appetite of the secondary jet causes the primary to contract between  $2 < x/D < 4$  with a subsequent rapid expansion. This contraction effect is also observed through plane C. The secondary jets appear to widen with increasing  $\lambda$ . For  $\lambda=\infty$ , viewed through plane A, the absence of the primary jet causes the two secondaries to merge further upstream than in other cases. Statistically the values of  $K_2$  and  $x_{0,2}/D$  are comparable to those found in the round jet. Their variation depends on the velocity ratio and plane of flow.

# Chapter 5

## 5 Quantitative Methodology

### 5.1 Introduction

The mixing and entrainment characteristics of Ricou and Spalding, (1961) and Becker *et al.*, (1967) of free round and confined jets have been widely studied. The data has been used in predictive combustion and radiative heat transfer models (Jenkins and Moles, 1981). However, insufficient data is available to model rectangular jets, and especially a number of interacting rectangular jets. The round turbulent mixing models are inadequate due to the fundamentally different nature of interacting rectangular jets.

The PLIF technique used in the current chapter to quantitatively measure the concentration of both primary and secondary rectangular jets is a passive scalar technique. Passive scalar techniques have been widely used to map the concentration of round jets (Becker *et al.*, 1967) and rectangular jets (Grandmaison and Pollard, 1991). The use of two-dimensional techniques permits not only sampling of large quantities of data per experiment but may also allow for three-dimensional re-construction of the flow field.

### 5.2 Quantitative PLIF

Planar Laser Induced Fluorescence is a powerful non-intrusive technique, suitable for diagnosing the time averaged, instantaneous and fluctuating statistics of flows. PLIF is a developed diagnostic tool for reacting and non-reacting flows and has been used extensively in the quantitative determination of concentration from round jets. Quantitative measurements in water include the work of Papanicolau and List (1988) Chu *et al.*, (1986) Dahm and Dimotakis (1990) and Law and Wang (2000).

The current study employed a continuous wave (CW) Coherent Innova 90 Argon Ion Laser. Continuous wave lasers have been used in the past by a number of experimentalists: Koochesfahani and Dimotakis (1985) measured the concentration of the vortical structures in a plane shear layer and Walker (1987) measured the fluorescent response of fluorescein whilst varying the fluid pH. Although not as powerful as pulsed Nd:yag Lasers, PLIF with CW lasers can be used to quantitatively diagnose the time averaged scalar mixing of the jets. CW laser cannot, however, be used to resolve the temporal scale of high speed structures. The current technique focusses on obtaining mean data and so it does not require time-dependent monitoring. The CW laser is relatively simplistic and does not possess the optical dangers associated with pulsing beams.

### 5.3 Quantitative PLIF Image Processing Fundamentals

An expression initially developed by Karasso (1994) and also applied by Parham (2000) in precessing jets expresses the total signal emitted by a fluorescent source as a function of background light  $B_{i,j}$ , Laser distribution  $I_{i,j}$  and fluid concentration  $C_{ij}$ .

$$S_{i,j} = B_{i,j} + I_{i,j}(\phi C_{i,j}) + R \quad \text{Equation 5.1}$$

The indices  $i$  and  $j$  respectively represent the rows and columns of a two dimensional measurement,  $R$  is the accumulated background signal and  $\phi$  is the quantum yield.

Assuming that the concentration of fluorescent dye is in the linear response region (Arcoumanis *et al.*, 1990) and the quantum yield unity, rearrangement of Equation 5.1 yields the local concentration (Equation 5.2) and mixture fraction (Equation 5.3);

$$C_{i,j} = \frac{S_{i,j} - B_{i,j}}{I_{i,j}} \quad \text{Equation 5.2}$$

$$\xi_{i,j} = \frac{C_{i,j} - R}{C_{ref} - R} \quad \text{Equation 5.3}$$

where  $C_{ref}$  is the concentration of 100% jet fluid. In order to determine the concentration or mixture fraction it is required to measure  $B_{ij}$ ,  $I_{ij}$  and  $R$ .

## 5.4 Quantitative PLIF Technique

### 5.4.1 Experimental

Chapter 3 described the use of PLIF to qualitatively diagnose the flow with the laser sheet orientated along the jet axis. For quantitative measurements of the concentration, the laser sheet was orientated at  $90^\circ$  to the flow. This orientation of the laser sheet allows for measurement of concentration of both the primary and secondary streams in one image. Two dimensional mapping at different axial stations provides data for modelling the flow (Chapter 8) and doubles as a flow visualisation tool for the developing cross section of the jet.

A detailed description of the apparatus is given in Chapter 3. The rectangular jet nozzles were immersed 60 cm below the water surface in a 0.75x0.75x1.5 m water tank; Fluorescent dye and water were stored in supply tanks so that either the primary or secondary fluid could be seeded in the tank. Primary and secondary flows were each pumped using a 0.5 hp Onga pump and controlled using a manual control valve and a Solartron Mobrey 2000 rotameter. A horizontal Laser sheet was employed from a Coherent Innova 90 Continuous Wave Argon ion Laser operated at 2.28 watts and a wave length of 488 nm in constant light mode. The fluoresced signal was captured by a mirror positioned below the tank at 45 degrees and then relayed on to a 8 bit Phantom 4.1 camera. The shutter speed was  $1/50^{\text{th}}$  of a second and data was automatically digitised in the camera's internal memory at 50 frames per second. Experiments were repeated for each experimental velocity ratio (Table 3.3) as well as for each downstream station ( $x/D = 0.1, 0.2, 0.5, 1, 2, 6$  and  $8$ ).

### 5.4.2 Image Processing Technique

An image processing procedure has been developed including the corrections described in 5.4.2.1 and 5.4.2.2. Several errors occur when using fluorescence and lasers as a diagnostic tool for quantitative measurements, which must be corrected for:

- Camera background noise; background light
- Background concentration in an image
- Camera gain effects (only valid for gain controlled cameras)
- Correction for Laser Spatial Intensity. The spatial intensity of a laser beam or laser sheet varies with position and assumes a Gaussian distribution. The intensity is also distorted through scratches and uneven consistencies in the Perspex tank
- Variation in Fluorescent response of the dye with varying laser power.

#### **5.4.2.1 Correction for Background**

Two measurements for background noise corrections were required: The first, for background light in the room, was performed with the room darkened, the laser off and camera at the fixed shutter speed and lens aperture used in the experiments. The second was for effects produced by the tank and the water inside it, with the laser on, tank purged with water and re-filled so that all traces of dye could be eliminated. A total of 20 seconds of footage were recorded at 50 fps for each background measurement, 300 images were required for image processing.

#### **5.4.2.2 Correction for Laser Spatial Intensity**

The spatial distribution of laser sheet intensity varies significantly, especially when using cylindrical lenses. Failure to account for this phenomena would contribute to erroneous measurements. Measurements were conducted with the water tank containing a solution of 0.1 mg/L of sodium fluorescein, a concentration of the same order of that to be used in the jets in the following experiments. The fluorescein, which was diluted from a 500 mg/L stock solution. Dilution of the solution was done after the tank had been completely purged of residual dye and the water level was at its minimum so that the addition of further water would provide sufficient agitation to ensure a uniform concentration. Once the tank was full the solution was left for 20 minutes so a uniform concentration was achieved. The technique assumes that the dye does not stratify due to gravity. To check this the concentration at the top and the bottom of the tank were compared. A total of 1000 images were collected with the laser on, 300 of these were used in the image processing procedure.

Monitoring of the reference solution was not done simultaneously with the jet experiments as is common practice with a Nd:Yag Laser because the intensity of the continuous wave laser, such as the Innova 90, does not need to be monitored over time. To verify this, an evaluation of the rms fluctuations of the CW laser power over a 1 minute period was undertaken with a Sony handheld DVC. Fluctuations did not vary by more than  $\pm 1\%$  rise from over the time-averaged mean.

### 5.4.2.3 Image Processing Procedure

Figure 5.1 shows the mean 300 images with a) laser off, with b) laser on and c) fluorescent response of a uniform 0.1mg/L fluorescein solution in the tank. The intensity of the laser sheet appears to be Gaussian and maximum peak intensity is located on the sheet centreline and drops off towards the boundaries (Figure 5.1 c). The fluorescent signal emitted by the dye varies in proportion to the laser sheet intensity. Hence with reference to Figure 5.2, the intensity of the fluoresced signal would be subject to large experimental errors in the  $x$ -direction (axial direction).

At a fixed shutter speed the recorded movie images are digitised into video for windows format so it they could be read and processed using MATLAB's image processing toolbox. Although the Phantom 4.1 is a black and white camera, the resulting footage is digitised, as a 24-bit RGB image.

Three hundred instantaneous images were used to obtain a one time averaged image. This is considered to be a sufficient number of images to reduce the level of uncertainty less than 5% (Yoda *et al.*, 1994). Equations 5.3, 5.4 and 5.6 are for time averaging the background signals with the laser on, and laser off, and the fluorescent response for a 0.1mg/L solution, respectively.

$$\overline{B_{on,i,j}} = \frac{1}{K} \sum_{k=1}^K B_{on,i,j,k} \quad \text{Equation 5.4}$$

$$\overline{B_{off,i,j}} = \frac{1}{K} \sum_{k=1}^K B_{off,i,j,k} \quad \text{Equation 5.5}$$



$$\overline{C_{0.1mg/L,i,j}} = \frac{1}{K} \sum_{k=1}^K C_{0.1,i,j,k} \quad \text{Equation 5.6}$$

Subscripts,  $i, j$  and  $k$  refer to the row, column and image number of the digitised sequence, and  $K$  is the total number of images. The corrected fluorescence response is then calculated by subtracting  $\overline{C_{0.1mg/L,i,j}}$  from the background signal with the laser off  $\overline{B_{off,i,j}}$ ;

$$A_{i,j} = \overline{C_{0.1mg/L,i,j}} - \overline{B_{off,i,j}} \quad \text{Equation 5.7}$$

Since for the corrected fluorescence response, the laser intensity and fluorescent response varies mainly with  $j$  (ie the axial direction,  $x$ ) the average of each column is determined so that a correction matrix may be calculated;

$$M_{i,j} = \frac{A_{i,j}}{X_{1,j}} \quad \text{Equation 5.8}$$

$X_{1,j}$  is the average of  $j^{\text{th}}$  column of  $A_{i,j}$  and  $M_{i,j}$  is the correction matrix. A recorded image of the jet in operation will be denoted as  $P_{i,j,k}$ , the background noise is removed by subtracting  $\overline{B_{on,i,j}}$ , and the resultant matrix is then divided by the correction matrix;

$$P'_{i,j,k} = \frac{(P_{i,j,k} - \overline{B_{on,i,j}})}{M_{i,j}} \quad \text{Equation 5.9}$$

The instantaneous background concentration is determined for each image, where no jet fluid is present, and is then averaged over the designated area with dimensions  $W \times H$ ;

$$R_{1,1,k} = \frac{1}{WH} \sum_i^W \sum_j^H P_{i,j,k} \quad \text{Equation 5.10}$$

The instantaneous signal, which is proportional to the amount of jet fluid, is then determined as;

$$C_{i,j,k} = P'_{i,j,k} - R_{1,1,k} \quad \text{Equation 5.11}$$

If  $W \times H$  defines a region where 100% jet fluid is present, the average signal proportional when 100% jet fluid is present is defined as;

$$\overline{C_{o,i,j,k}} = \frac{1}{W \times H} \sum_i^W \sum_j^H C_{i,j,k} \quad \text{Equation 5.12}$$

The ratio between the terms on the RHS in Equations 5.11 and 5.12 is the instantaneous mixture fraction;

$$\xi_{i,j,k} = \frac{C_{i,j,k}}{\overline{C_{o,i,j,k}}} \quad \text{Equation 5.13}$$

The time-average mixture fraction is then defined as;

$$\overline{\xi_{i,j}} = \frac{1}{K} \sum_{k=1}^K \xi_{i,j,k} \quad \text{Equation 5.14}$$

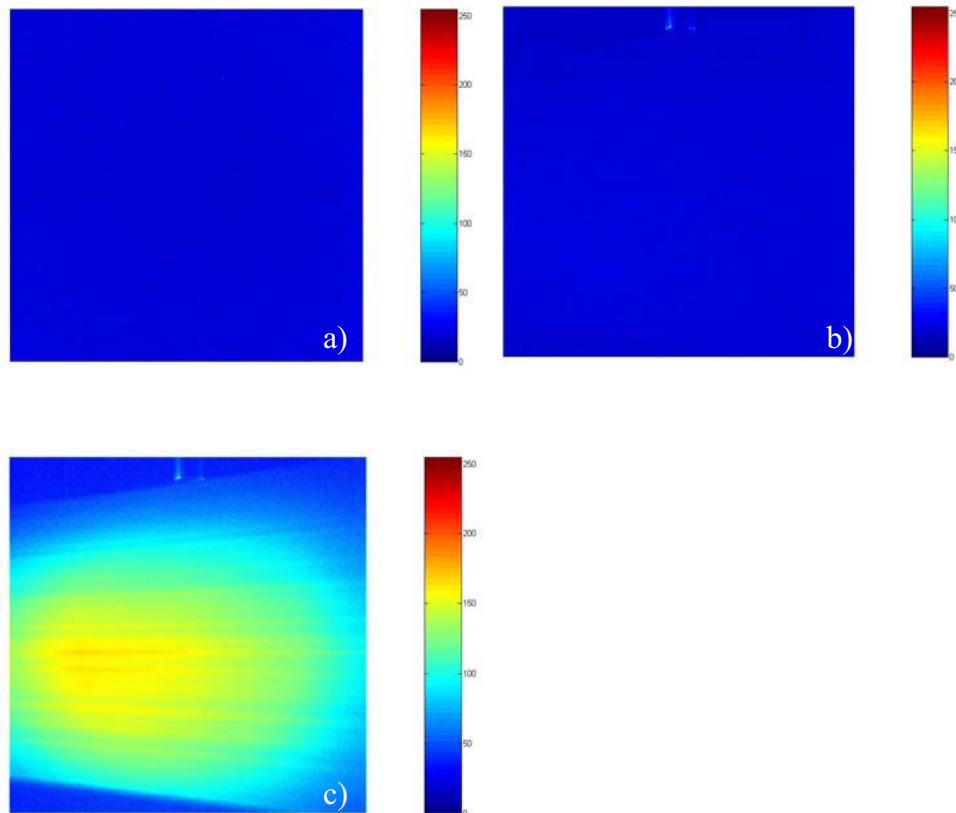


**Figure 5.1:** Time averaged background corrections with a) laser off, with b) laser on and c) fluorescent response for a 0.1mg/L Flourescein solution.

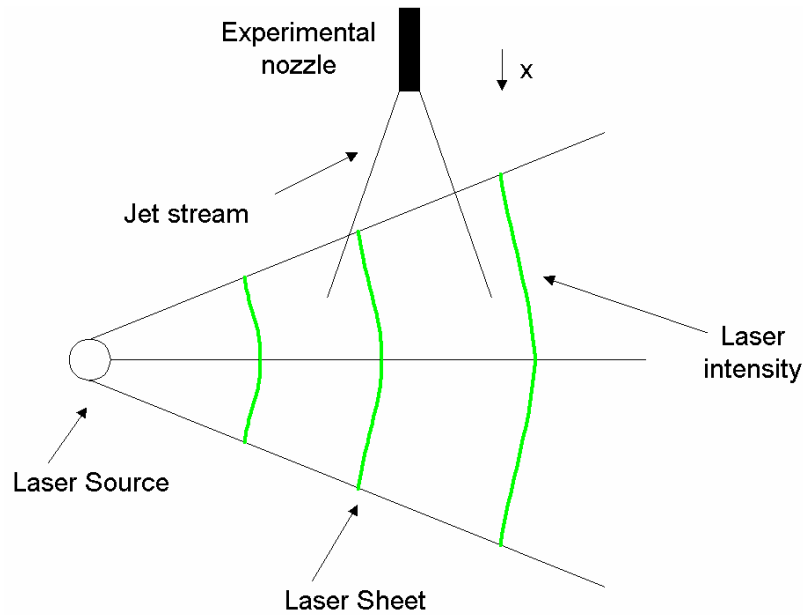


**Figure 5.2:** Laser sheet intensity profile, with respect to the direction of flow

### 5.4.3 Experimental Procedure

The experimental procedure was based upon the image processing requirements; essentially four measurements were required in order to conduct a series of experiments on a particular axial station ( $x/D$ ). Below is the summary of experimental procedure to evaluate the scalar field for the primary and secondary jet for a particular  $x/D$ .

#### Preparation

- Optics were aligned.
- The manual traverse was used to position the optics at the desired downstream distance with laser on.
- Laser power was set to 2.28 watts in light control mode.
- The primary or secondary supply tank was filled with 0.1 mg/L of sodium fluorescein.
- Pumps were turned on and valves adjusted so that a minimum amount of jet fluid was injected into the tank.
- The mirror angle camera position and zoom were then adjusted, after which the pumps were turned off and control valves shut immediately.

## Experimental

- The desired flow conditions were selected and the fluorescent signal recorded (every 2 runs required tank fluid to be dumped and re-filled to avoid accumulation of background dye).

## Background and Laser Intensity Measurements

- Once the primary and secondary experiments at all conditions were concluded, the laser was turned off and the background signal with laser off was then recorded.
- Fresh water was introduced into the tank whilst water contaminated with fluorescein was discharged via a pump through the bottom, at the same rate. The purge was continued until all residual dye was removed from the tank. At the end of the purging procedure the tank was refilled with fresh water. A second background signal was then recorded with the laser on.
- The tank was then emptied, and re-filled with a calculated volume of 500 mg/L stock standard solution of fluorescein in order to achieve 0.1 mg/L. The Laser intensity distribution and fluorescent response was then recorded.

### 5.4.4 Sources of Error

#### 5.4.4.1 Spatial Resolution

The concept of turbulent scales has been introduced with specific definitions in Chapter 2, however briefly; the Kolomogrov and Batchelor scales represent the smallest lengths associated with turbulent flow and scalar dissipation and are defined as:

$$\lambda_K = \left( \frac{v^3}{\varepsilon} \right)^{1/4}$$

Equation 5.15

$$\lambda_B = \lambda_K Sc^{-0.5} \quad \text{Equation 5.16}$$

where  $\nu$  is the kinematic viscosity,  $\varepsilon$  the rate of turbulent dissipation and  $Sc$  the Schmidt number, which is the ratio of kinematic viscosity to molecular diffusivity.

Several empirical relationships for the determination of the Kolomogrov scale exist for round turbulent jets in the self-similar region, for instance Antonia *et al*, (1980):

$$\frac{\lambda_k}{D} = (48 * Re^3)^{-0.25} \frac{x}{D} \quad \text{Equation 5.17}$$

where  $Re$  is the Reynolds number at nozzle exit,  $x$ , is the axial distance downstream from the nozzle exit and  $D$ , is the nozzle diameter.

a more accurate prediction is also available which covers all the downstream positions;

$$\lambda_k = 2.3b_v Re_{b_v}^{-0.75} \quad \text{Equation 5.18}$$

where  $Re_{b_v}$  is the local Reynolds number at any downstream distance, and  $b_v$  is the local velocity based half-width and is defined from;

$$Re_{b_v} = \frac{\overline{U_c} b_v}{\nu} \quad \text{Equation 5.19}$$

where  $\overline{U_c}$  is the time-averaged centreline velocity.

The Kolomogrov scale represents the length scale of the smallest turbulent fluctuations, which for a jet, increases with downstream distance. The size of these length scales depends on outlet velocity and jet diameter. The largest physical length of the probe size (this being a unit cell, of the laser/optics/camera arrangement) in the current work is the thickness of the laser sheet, which is 0.8 mm. Therefore this technique can only resolve for scales greater than 0.8 mm. The use of water models as a flow visualising tool represents a problem when attempting to fully resolve the scalar field, due to the high value of Schmidt number of soluble dyes in water (Fluorescein,  $Sc =$

1930) which implies that the Batchelor scale is some 43 times smaller than the Kolomogrov scale. Hence alternative techniques are required to resolve the instantaneous scalar field. Figure 5.3, is a plot of the calculated ratios of laser sheet thickness to Batchelor scale and Kolomogrov scale versus dimensionless axial distance for a 15 mm round jet operating at  $Re = 10,000$ .

Fully resolving the turbulent or scalar field in flow imaging diagnostics depends on the physical size of the probe being used. In the case of hot wire or cold wire anemometry the probe size is the wire thickness and in the case of laser diagnostics it is the larger of the thickness of the light sheet and the dimensions of each pixel in the planar flow field, which depends on the camera's zoom and position. If the probe size is smaller than the value of the Kolomogrov scale for turbulent resolution and/or Batchelor scale for scalar resolution at a given position, then the turbulent and/or scalar field is known to be 'fully resolved'. Total spatial resolution of the turbulent system is not always required. For instance, generation of mean scalar data does not require resolution of the Batchelor scale (Mi, *et al.*,2001a) but resolution of rms field and scalar dissipation does (Mi *et al.*,2003). Determination of the rms field at a resolution ten times the Batchelor scale will yield an error of about 4% between the measured and true value (Mi *et al.*, 2003). Determination of the scalar dissipation at the same resolution will yield an 86 % error (Mi *et al.*, 2003).

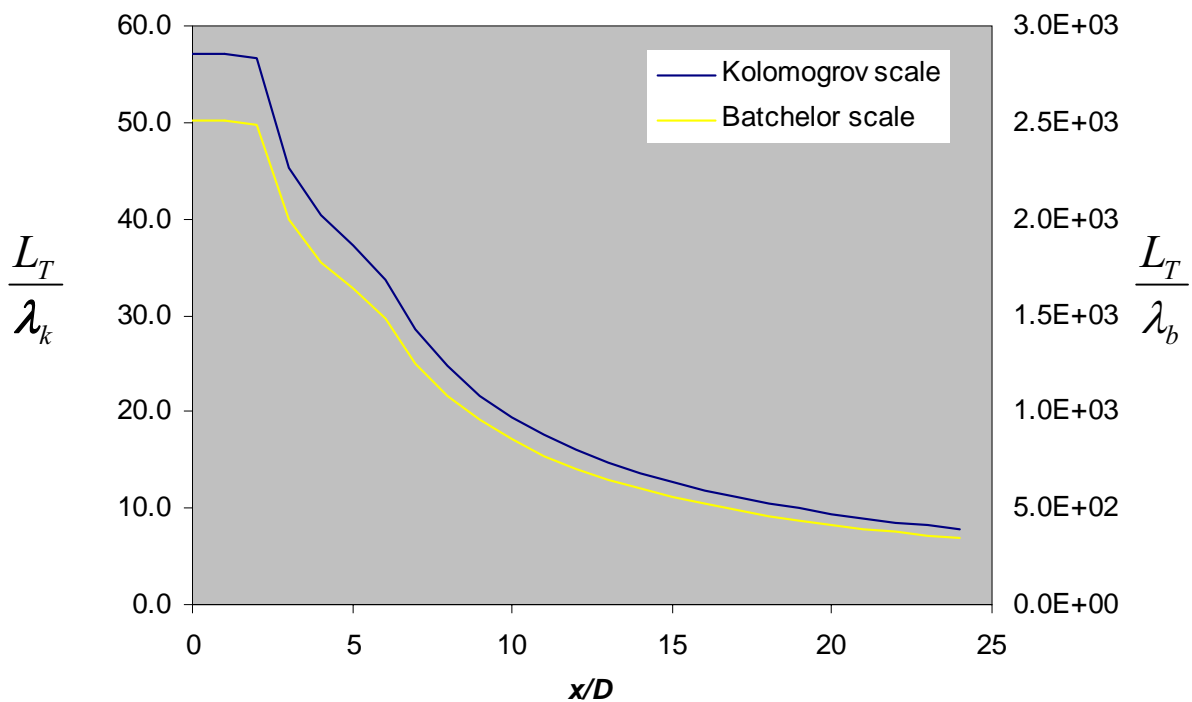


**Figure 5.3** Ratio between probe size and Kolomogrov and Batchelor scales versus axial distance, for a 15 mm round jet operated at  $Re = 10,000$ .

#### 5.4.4.2 Temporal Resolution

The other fundamental resolution issue in flow visualisation is temporal resolution. The temporal resolution required to resolve the Batchelor length scale is defined by the Batchelor time scale,  $\tau_B$ ;

$$\tau_B = \frac{\lambda_B}{\bar{u}} \quad \text{Equation 5.20}$$

where  $\bar{u}$  is the local time-averaged velocity, which in the case of a turbulent jet is usually approximated to the centreline velocity  $\bar{u}_c$ .

Resolution of the scalar temporal scale implies that the sampling time of the flow field must be less than the scalar temporal scale. The sampling time in continuous laser diagnostics is characterised by the shutter speed of the camera. Operation of cameras at fast shutter speeds restricts the amount of light being introduced to the charged couple array, thus decreasing signal intensity and lowering the signal to noise ratio. In the current experiments the camera was operated at a shutter speed of 1/50<sup>th</sup> of a second so that the signal to noise ratio was not compromised. Analysis of the signal to noise ratio is explained in detail in Section 5.4.4.8.

For good resolution of the mean flow field it is also important to allow sufficient time for many independent fluctuating flow cycles to be recorded. In the case of turbulent jets the largest jet structure is the order of the jet half-widths,  $r_{1/2}$  (Tennekes and Lumley, 1972). A useful rule of thumb is that sufficient recording time must be allowed so that approximately 100 independent flow cycles are measured of the largest flow structure;

$$\tau_{\text{recording}} \approx 100 \frac{r_{1/2}}{U_c} \quad \text{Equation 5.21}$$

The phantom v4.1 camera has an internal memory of 254 megabytes and can store a maximum of 1000 frames at 0.254 megabytes per frame, meaning that only 10 seconds of footage may be

stored at 100 frames per second, 20 at 50 fps and 50 at 20 fps (note that the maximum achievable shutter speed can be no more than the frame sample rate). Using the round jet velocity half-width data and centreline velocity decay of Boguslawski and Popiel (1979) the calculated minimum recording time was accommodated by the phantom camera.

#### 5.4.4.3 Measurement Length

Equation 5.21 defined the required duration of the flow measurement. The relationship between the number of independent PLIF images and the statistical significance of the image processing procedure is best illustrated by Yoda *et al.*, (1994) who developed an expression which estimates the level of uncertainty associated with a finite number of measurements;

$$\mu = 2 \left( \frac{\sigma}{\sqrt{N}} \right) * 100\% \quad \text{Equation 5.22}$$

where  $\mu$  is the level of uncertainty,  $\sigma$  is the standard deviation between measurements and  $N$  is the total number of collected/processed images. The present experiments for the round pipe jet indicate that  $\sigma$  is approximately 0.5 for  $x/D > 8$ , delivering a level of uncertainty of 5.7% for 300 images.

#### 5.4.4.4 Laser Sheet Distribution and Power

The correction for the spatial distribution of power within a laser sheet is normally by far the largest source of error when conducting Laser Induced Fluorescence experiments. The mathematical correction procedure has been detailed in Section 5.4.2.3.

#### 5.4.4.5 Photobleaching

Photobleaching is the decrease in fluorescent intensity of water-soluble dyes with continuous exposure to a laser. It has been demonstrated that significant photobleaching occurs on the millisecond time-scale (Saylor, 1995). The residence time of dye in the laser sheet is dependent on the local velocity. A technique has even been developed to determine localised velocities



based on the photobleaching effects of sodium fluorescein (Ricka, 1987). A comparison of the photobleaching tendencies of common fluorescent dyes used with CW argon lasers has been conducted by Saylor (1995) and Crimaldi (1997) with both concluding that Fluorescein is a dye with greater susceptibility to this phenomena than Rhodamine 6G. However, Crimaldi (1997) showed that the photobleaching only becomes significant when the localised velocity normal to the laser sheet or beam is less than 50 cm/s. The lowest velocity in the current experiments occurs for the secondary jet when  $\lambda = 0.55$  and is approximately 200 cm/s at the nozzle exit plane (Table 3.3).

#### 5.4.4.6 Absorbance

The absorbance of a linear laser dye system is characterised by the Beer-Lambert law. Karasso and Mungal (1997b) concluded that absorbance of a carboxy-dichlorofluorescein with a Nd:Yag Laser pulsed at 532nm in a seeded flow was significant. The carboxy-dichlorofluorescein, Nd:Yag Laser coupling peak absorbance occurs at a similar wavelength to the incident light. Sodium Fluorescein coupled with a CW Argon Ion Laser operating 488 nm emits a Fluorescent spectra peaking at 520 nm, in contrast to the peak of the absorbance spectra which occurs at 490 nm (Brungart *et al.*, 1991) resulting in a minimal effect of absorbance on measurements.

#### 5.4.4.7 Mie Scattering

Mie scattering is the phenomena of scattering of incident light by spherical particles and is used as a proven quantitative technique to diagnose the concentration of marked flows (Hanson, 1986, Eckbreth, 1988). It can however become a nuisance when trying to diagnose flows using water as the medium, if air bubbles are accidentally introduced into the flow region. The relative signal strength of Mie scattering is an order of magnitude higher than that of Laser Induced Fluorescence (Eckbreth, 1988). Because of the different wavelengths of scattered and fluoresced signals a long-pass filter is usually placed in front of the detection device to exclude the Mie Scattering signal at the expense of signal strength. This option was trialled in the current set of experiments but gave poor signal to noise ratio and poor quality LIF imaging. The imaging device was not capable of gain increase, consequently experiments were conducted without filters and air traps were placed at specific points in the water supply hoses. A digital filter was incorporated into the image processing procedure to eliminate any pixels that possessed an

intensity above a certain cut-off value. The results of these efforts were to considerably reduce Mie-scattering effects in the time-averaged images (Chapter 6).

#### 5.4.4.8 Signal to Noise Ratio

The signal to noise ratio is the ratio between the emitted fluorescent signal and the background noise. Achieving good signal to noise operation with any laser diagnostic technique requires experience and trial and error. Factors that effect the signal to noise are laser power, source concentration (concentration of fluorescent dye) camera shutter speed, lens aperture, build up of background dye and presence of bubbles. The current experiments achieved signal to noise ratios between 8 and 14, whereas the signal to noise ratio achieved by superior imaging systems, such as the pulsed Nd:yag Laser coupled with a Kodak megaplus camera used by Parham (2000) typically vary between 20 and 25.

#### 5.4.4.9 Water Quality

The quality of the water used during the experiments is of some importance and worth some consideration. It is important that the chemical and physical properties of the water remain constant throughout the experimental program. Sodium fluorescein in aqueous solution creates a surplus of anions by dissociating water to form  $OH^-$  ions in equilibria creating a slightly alkaline solution (Walker, 1987). The dissociation of sodium (represented by  $NaF_2$ ) fluorescein in water is as follows;



The negatively charged fluorescein ions then progressively react in water;



It is the  $F^{2-}$  anion which contributes to the excitation and its concentration is heavily dependant on pH. In fact the relative fluorescence of Sodium Flourescein between the pH levels of 2 and 8 varies by 90 % (Walker, 1987). The variation of  $F^{2-}$  concentration with pH has been exploited to visualise reacting flows (Dimotakis *et al.*, 1978) however, it also implies that great caution must be taken when using large quantities of tap water over a period of time. Mains water to the Lab's domicile had a pH of approximately 7.3 through 2004 and 2005 and varied between 7.2 and 7.8 (SA Water, 2006).

Due to the large quantities of water used per experiment (at least  $1\text{m}^3$  per run) it was decided not to control temperature and pH but instead to continuously monitor pH during the experiments. Monitoring revealed that occasional fluctuations of  $pH = \pm 0.01$  were observed, which is at the limit of resolution of the pH meter.

## 5.5 Experiment Validation

### 5.5.1 Introduction

The present technique is validated against previous investigations of round turbulent jets. Concentration measurements in round pipe jets issuing into a stagnant environment have been widely performed due to the significant industrial applications of round jets. The properties of round turbulent jets are explained in detail in Section 2.4.1.

### 5.5.2 Schmidt Number Effects on Turbulent Mixing

It has been explained how the Schmidt number effects spatial and temporal resolution in Sections 5.4.4.1 and 5.4.4.2, but it is also important to outline the implications this may have when using techniques such as water modelling where Reynolds number similarity is achieved but Schmidt number similarity is not. In laser diagnostics the Schmidt number is representative of the marker used, seeing that this is the detected. High Schmidt numbers are not only encountered in water modelling, but also in air modelling, for example  $Sc = 38,000$  was calculated for Mie-scattering using olive oil fog as the marker (Nobes, 1997). The Schmidt number is defined as the ratio of viscous to molecular diffusion;

$$Sc = \frac{\nu}{D}$$

Equation 5.26

hence the Schmidt number is a measure of how molecular diffusion or mixing can affect a flow in motion. The effect of small scale turbulent mixing is influenced by molecular diffusivity (Broadwell and Mungal, 1991) (high diffusivity low Schmidt number). If the flow is characterised by large scale structures the effect of Schmidt number on the flow will be minimal. However in a reacting flow, where the rate of reaction is quasi-instantaneous when compared to the mixing rates, molecular diffusion plays a significant role (Dahm *et al.*, 1990). Broadwell and Mungal, (1991) adopted a Lagrangian approach to study the effects of Schmidt number and concluded that  $Sc$  has an effect on bulk mixing in a shear layer, but does not alter the mixing on the centreline of a jet. The influence of  $Sc$  on Jet entrainment or mean scalar mixing on a jet centreline has not been established, however it does alter the rms and fluctuating field (Miller and Dimotakis, 1991).

A different approach is from first principles by using the governing equations for turbulent mass transport reduced to one-dimensional flow;

$$-\left(\frac{\partial}{\partial x} \overline{Cu}\right) - \left(\frac{\partial}{\partial x} \overline{C'u'}\right) + D_f \left(\frac{\partial^2}{\partial x^2} \overline{C}\right) = 0$$

Equation 5.27

where  $\overline{C}$  and  $\overline{u}$  are the time-averaged values of the concentration and velocity, and the value  $\overline{C'u'}$  is the time averaged product of the concentration and velocity fluctuations.

Equation 5.27 is then made dimensionless by using the following relationships

$$\overline{U} = \frac{\overline{u}}{U_o}, \overline{C} = \frac{\overline{C}}{C_o}, \overline{x} = \frac{x}{L}, \overline{U'} = \frac{\overline{u'}}{U_o}, \text{Re}_0 = \frac{\overline{U_o}L}{\nu}, \text{Sc}_0 = \frac{\nu}{D_f} \text{ where terms } \overline{U_o} \text{ and } \overline{C_o} \text{ are}$$

reference velocity and concentration, in the case of a jet they would be at the nozzle exit plane,  $L$  is a characteristic length scale, which would be nozzle diameter. Inserting these relationships into Equation 5.27 and rearranging yields;

$$\left(\frac{\partial \overline{\overline{Cu}}}{\partial x}\right) + \left(\frac{\partial \overline{\overline{C'u'}}}{\partial x}\right) = \frac{1}{Re_o Sc_o} \left(\frac{\partial^2 \overline{\overline{C}}}{\partial x^2}\right) \quad \text{Equation 5.28}$$

The product  $Re * Sc$  is more commonly known as the Peclet number ( $Pe$ ). According to Equation 5.28, if the Reynolds number is sufficiently high the term on the RHS will be deemed negligible, and hence the Schmidt number will have little effect on the flow. From this analysis it may seem a trivial task to determine whether or not the Peclet number has any effect on the flow, but this is not the case. Mi *et al.*, (2001a) performed hot wire measurements of the scalar field of a flow issuing from a round pipe and a smooth contraction and compared the mean scalar fields to those in the literature. The constant  $K_I$  in Equation 2.23 was a parameter used to assess the degree of mean scalar mixing. The values of  $K_I$  for a round pipe and a smooth contraction respectively are illustrated in Tables 5.1 and 5.2.

Author	$Sc_o$	$Re_o$	$Pe_o$	$K_I$	$\frac{x_{o,2}}{D}$
Richards <i>et al.</i> , (1993)	1	25000	25000	4.81	2.1
Pitts (1991).	1	3960	3960	4.42	-0.35
Dyer (1979).	1	9790	9790	4.5	
Antonia <i>et al.</i> , (1976)	0.7	23500	16450	4.16	
Mi <i>et al.</i> , (2001a)	0.7	16000	11200	4.64	4.91
Law and Wang (2000)	1000	12700	1.27E7	5.31	0

**Table 5.1:** Values of  $K_I$  for different nozzle exit conditions for a pipe flow issuing into a stagnant fluid.

Author	$Sc_o$	$Re_o$	$Pe_o$	$K_I$	$\frac{x_{o,2}}{D}$
Richards <i>and Pitts</i> (1993)	1	25000	25000	4.76	1.6
Dowling and Dimotakis (1990)	1.2	16000	19200	4.73	
Mi <i>et al.</i> , (2001a)	0.7	16000	11200	4.48	4.25
Grandmaison, <i>et al.</i> (1982)	38000	2.7E+5	1.03E+10	5.43	1.67
Becker, <i>et al.</i> (1967)	38000	54000	2.05E+09	5.59	2.4
Nobes. (1997)	38000	16400	6.23E+08	5.52	0.75
Kristmanson and Danckwerts (1964)	500	10000	5E+7	4.78	0
Dahm <i>et al.</i> , (1990)	600	5000	3E+6	5.41	
Papanicolau and List (1987)	1000	16700	1.67E+7	5.49	
Papanicolau and List (1988)	1000	11000	1.1E+7	6.34	4.35

**Table 5.2:** Values of  $K_I$  for different nozzle exit conditions for a fluid issuing from a smooth contraction into a stagnant fluid.

### 5.5.3 Validation Experiments

The equipment and procedures are the same as those described in sections 3.5.3 and 5.4.3 respectively, with the only difference being that a 1200 mm long round pipe was immersed 600 mm into the water tank instead of the rectangular jets illustrated in Figures 3.4 and 3.5.

### 5.5.4 Results of Validation Experiments

#### 5.5.4.1 Planar Data

The spatial distribution of the scalar mixing field is characterised by the instantaneous and time-averaged concentration field. Figures 5.4 and 5.5 are the instantaneous and time-averaged mixture fraction of the 15 mm round jet at a Reynolds number of 10,000, taken at a shutter speed of  $1/50^{\text{th}}$  of a second. The planar data is shown for  $0 < x/D < 12.79$  in Figure 5.4 and for  $12.79 < x/D < 25.58$  in Figure 5.5. A consistent colour map represents the mixture fraction, where blue is pure unmixed fluid and red is pure jet fluid.

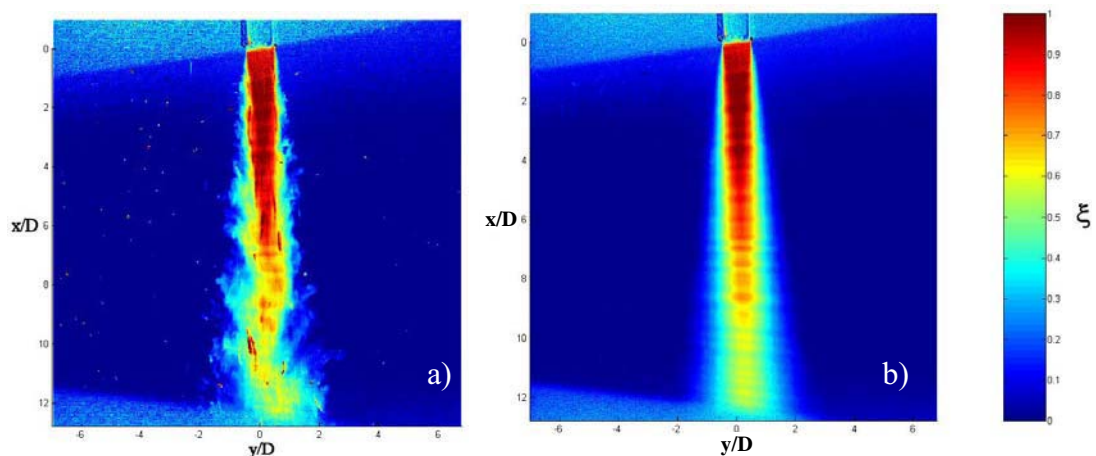


**Figure 5.4:** Instantaneous a) and time-averaged b) mixture fraction of the 15 mm round jet at,  $x/D < 12.79$ ,  $Re = 10,000$ ,  $\tau_{\text{shutter}} = 1/50$  secs.

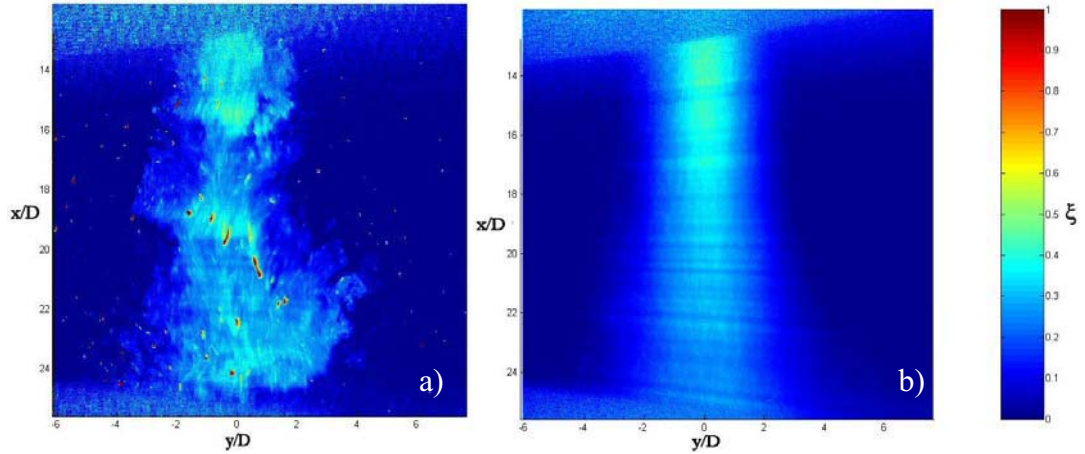


**Figure 5.5** Instantaneous a) and time-averaged b) mixture fraction of the 15 mm round jet at,  $12.79 < x/D < 25.58$ ,  $Re = 10,000$ ,  $\tau_{shutter} = 1/50$  secs.

#### 5.5.4.2 Statistical Analysis and Validation

Figure 5.6 plots the inverse mixture fraction on the jet centreline ( $1/\bar{\xi}_c$ ) versus dimensionless axial distance ( $x/D$ ). It also compares the present results with other data using pipe jets in water ( $Sc \sim 1000$ ) and air ( $Sc \sim 1$ ). The results demonstrate the expected inversely proportional relationship with downstream distance. A line of best fit through the data in the linear region ( $x/D > 5$ ) defines the relationship between centreline mixture fraction and downstream distance to be;

$$\frac{1}{\bar{\xi}_c} = \frac{1}{6.86} \left( \frac{x}{D} + 1.925 \right) \quad \text{Equation 5.29}$$

The value of the concentration decay constant  $K_I$ , and virtual origin,  $x_{0,I}/D$  which were determined to be 6.86 and 1.925 respectively, are comparable to other values reported in Tables 5.1 and 5.2 at similar Schmidt numbers. However,  $K_I$  is slightly above the upper end of the range of literature data. Many factors could have contributed to a moderately higher  $K_I$  such as imperfections of the nozzle at the exit plane or counter current effects due to tank overflow whilst the nozzle was in operation.

The jet spread is quantified by determining the dimensionless concentration half-width  $r_{1/2}/D$ , which was calculated using the average values on each side of the centreline. Figure 5.7 is a comparison of the present jet data with that of a round pipe jet operating in a high Schmidt



number fluid, which illustrates a distinct linear relationship taken with a pulsed Nd:Yag Laser technique.

The linear relationship used to fit the jet spread of the present data is;

$$\frac{r_{1/2}}{D} = 0.0725 \left( \frac{x}{D} + 4.044 \right) \quad \text{Equation 5.30}$$

The rate of jet growth is also comparable to that of other high Schmidt number jets (Law *et al.*, 2000, Parham, 2000) and also comparable to the lower end of the rates determined from gaseous jet experiments which vary between 0.089 to 0.132 (Antonia *et al.*, 1976 Dyer, 1979 Pitts, 1991 and Richards *et al.*, 1993).

The radial profile of the mean concentration field normalised with respect to the centreline value, is shown in Figure 5.8 with data from other researchers shown for comparison. The radial coordinate ‘ $\eta$ ’ is defined as  $\frac{r}{x - x_{0,2}}$ , where  $r$  is the radial value,  $x$ , the downstream value and  $x_{0,2}$  is the virtual origin of the scalar half-width.

The values of the numerical constants in Equations 5.29 and 5.30 are also heavily dependent on the upstream geometry and ducting of the jets. Little information exists in the literature on such effects. However, the studies of Mi *et al.*, (2001b) comparing the scalar characteristics of a free round jet issuing from a long pipe with that of a jet issuing from a smooth contraction suggests that the difference in turbulent structure in the near field dictates the downstream flow conditions. This observation is supported by Xu and Antonia (2002) who stated that the flow from the smooth contraction develops closer to the nozzle exit plane. Observations of the exit velocity profiles from both conformations suggest that the pipe jet has a typical Gaussian bell-shape profile, whereas the smooth contraction possesses a steep near plug-flow/top-hat profile, implying that greater shear and turbulence intensity are developed in the mixing layer causing it to reach a self-similar state further upstream. Other examples of alterations in upstream geometry do exist in the literature such as Ferdman *et al.*, (2000) who compared the long pipe jet, with a pipe jet having a 90 degree bend 11 diameters upstream or Mi *et al.*, (2006) who studied the frequency of jet precession from a precessing jet issuing from a pipe, orifice and smooth contraction.

The value of  $K_I$  in the current experiments is similar to that from other experiments at high Schmidt numbers (Table 5.2, Parham, 2000, Nakamura et al., 1982, Chua and Antonia, 1986, Dahm and Dimotakis, 1990 and Law and Wang, 2000) which varies between 5.26 and 5.41. Similar geometries used at low Schmidt numbers (Birch *et al.*, 1978, Richards and Pitts, 1993, Pitts and Takashi, 1984, Pitts, 1991) yielded lower values; 4.44 to 4.64. In the case of the study of the smooth contracting nozzle high  $Sc$  experiments yielded  $K_I$  values between 4.75 to 6.34 (Kristmanson and Danckwerts, P.V., 1964, Papanicolaou and List, 1987, Papanicolaou and List, 1988) whereas low  $Sc$  experiments yielded  $K_I$  values between 3.26 and 5.59 (Richards and Pitts, 1993, Dowling and Dimotakis, 1990, Grandmaison *et al.*, 1982, Becker *et al.*, 1967, Ebrahimi and Kliene, 1977, Chua and Antonia 1986, Corrsin and Kislter 1955). These observations lead the author to believe that molecular diffusivity does affect the bulk mixing, as does the exit velocity profile. The effect of increasing  $Sc$  number is to increase  $K_I$ , which implies a reduced rate of concentration decay, i.e. slower mixing. In other words, to achieve the same level of mixing, increased turbulence is likely to be required to overcome the reduction in molecular diffusivity.

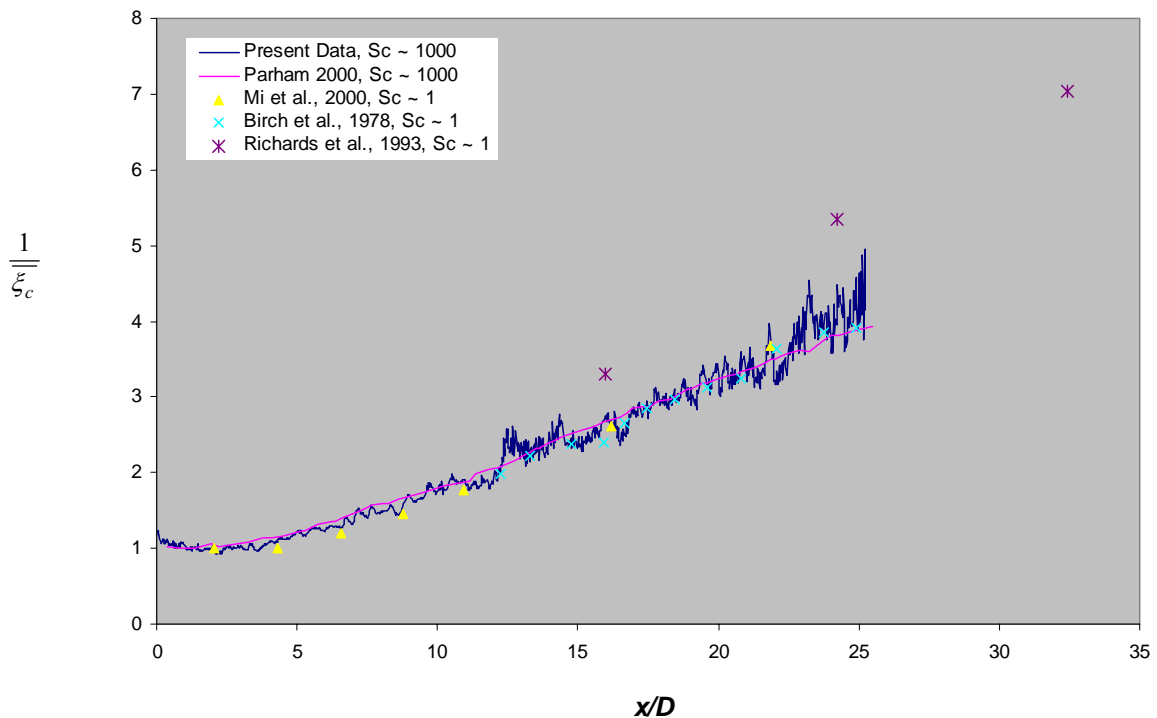


**Figure 5.6** Time-averaged centreline mixture fraction of the 15 mm jet at compared with the results of other liquid ( $Sc \sim 1000$ ) and gaseous ( $Sc \sim 1$ ) pipe jets.

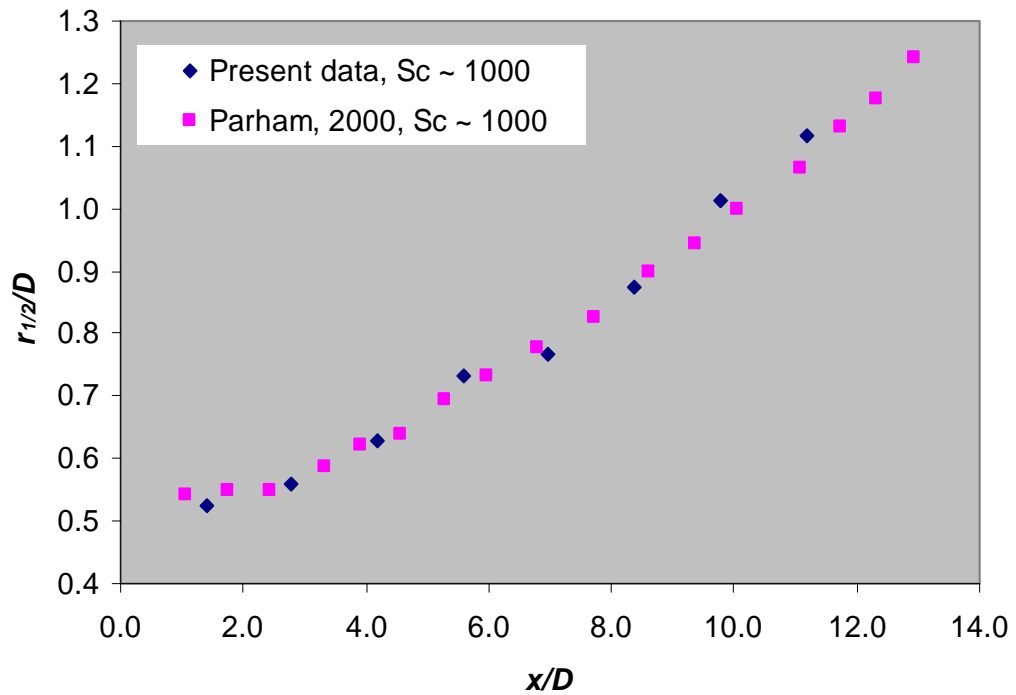


**Figure 5.7:** Jet spread of the 15 mm jet at compared with the results of a other liquid ( $Sc \sim 1000$ ) jet.

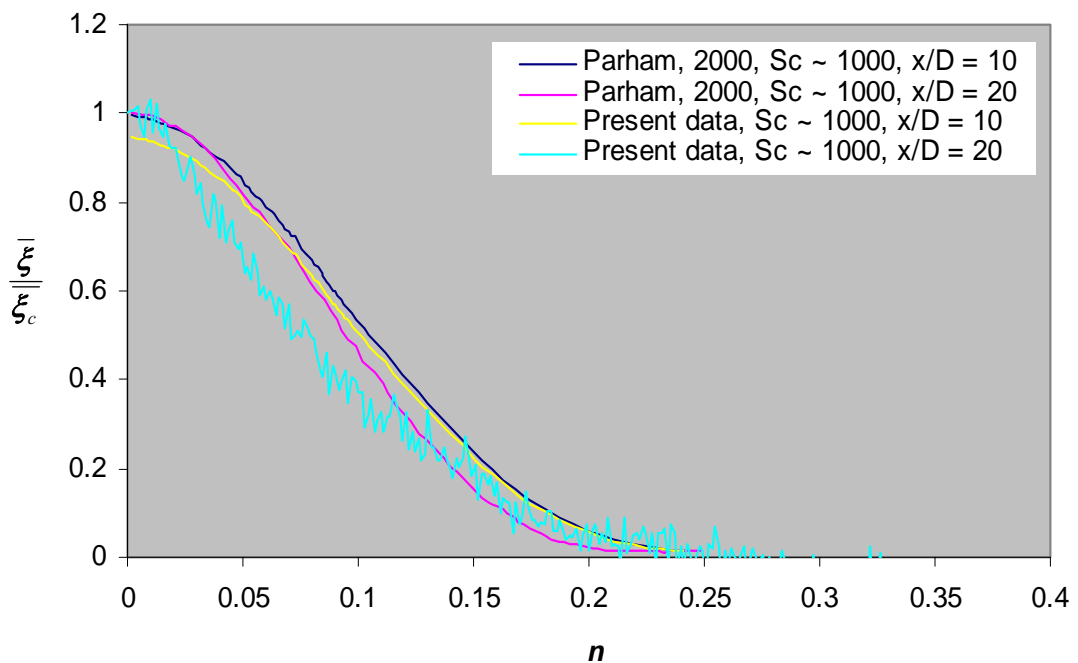


**Figure 5.8** Radial profiles of the mean jet concentration normalised to the centreline value. Comparison between data for high Schmidt number jets.

## 5.6 Conclusion

The current technique possesses the ability to measure the time-averaged concentration field with a good degree of accuracy. Three background measurements, of 300 captured images each are required to correct the time averaged flow field. The sources of error associated with the experimental procedure and equipment have been addressed; these are; background light, Laser sheet intensity, photobleaching, measurement length, absorbance and water quality.

It has been established through the literature that upstream geometry does have an effect on jet development and that simple jets deriving from a smooth contraction will develop more rapidly than pipe jets. The influence of molecular diffusivity on bulk jet mixing is apparent, however it's effects are dependant on turbulence intensity. More importantly, the values of  $K_1$  and  $r_{1/2}$  for the simple pipe jet used in the validation experiments are similar to those in the literature, showing that the present technique is valid.